2023

Bond Behaviour between Carbon Fibre Strand and Mortar under Marine Environment

Ji, Jie

UNIVERSITY OF
PLYMOUTH

BOND BEHAVIOUR BETWEEN CARBON FIBRE STRAND AND MORTAR UNDER MARINE ENVIRONMENT

by

JIE JI

A thesis submitted to the University of Plymouth
in partial fulfilment for the degree of

DOCTOR OF PHILOSOPHY

School of Engineering, Computing and Mathematics

July 2022

ACKNOWLEDGEMENTS

With time passing by, I get an insight into how to do scientific research and gradually understand the significance of this PhD career to my life. Many people give their kindest help to me during this period. I would like to engrave them in my mind, especially my supervisors. Their guidance is deemed as the key to my research work in these years.

My supervisor, Dr. Shanshan Cheng, is a very respectable and patient guide for my life. When I started the research several years ago, I was confronted with lots of problems I could not imagine before. She led me to overcome those problems one by one. I do really appreciate her support for me. Her support becomes my confidence and courage to achieve the ultimate goal in my PhD candidate career.

My supervisors, Prof. Long-yuan Li and Prof. Neil James, are highly experienced scientists who provide a great deal of helps and supports for me. The guidance from Prof. Long-yuan Li is beneficial to my development in the academic ability. The discussion with him usually broadens my horizons about my research field. Prof. Neil James gives me many valuable suggestions when I design experiments and write thesis.

I am also grateful to all technicians who support my research work during the period of my PhD study. Two times of campus lockdown due to Covid-19 pandemic caused big difficulties to my long-term experiments. Their efforts help my work back on track after then.

Finally, I appreciate University of Plymouth and School of Engineering, Computing and Mathematics. Facilities provided by them are essential for me to carry out research.

AUTHOR'S DECLARATION

At no time during the registration for the degree of Doctor of Philosophy has the author been registered for any other University award without prior agreement of the Doctoral College Quality Sub-Committee.

Work submitted for this research degree at the University of Plymouth has not formed part of any other degree either at the University of Plymouth or at another establishment.

This study was financed with the aid of a studentship from the University of Plymouth.

Publication:

Cheng, S., Ji, J. and Meng, M. (2020). Interfacial response of fibre-to-matrix in textile reinforced concrete between two cracks: Analytical solution. Composite Structures, 245, 112380. (DOI number: 10.1016/j.compstruct.2020.112380)

Presentation at conference:

Use of Carbon Fibre Textile Reinforced Concretes in Marine Constructions. The 6th Partnership for Research in Marine Renewable Energy (PRIMaRE) conference 2019. 3rd-4th July 2019, Cardiff University, Cardiff, UK.

Word count of main body of thesis: **54711**

Signed: Jie Ji

Date : 22th July 2022

Bond Behaviour between Carbon Fibre Strand and Mortar under Marine Environment

Jie Ji

ABSTRACT

Owing to the steel corrosion in traditional steel reinforced concrete structures exposed to marine environment, the present study explores carbon fibre textile reinforced mortar (TRM) as the alternative construction material. Moreover, sea sand and seawater can be used in casting mortar in this study, because carbon fibre is non-corrosive. Focusing on the long-term bond degradation at the interface between the carbon fibre strand (CFS) and mortar in carbon fibre TRM under marine environments, experimental and numerical investigations have been carried out by using single CFS-reinforced mortar (CFSRM) specimens.

Interfacial debonding is one of the key failure modes in TRM, due to the poor bonding between CFS and mortar compared with traditional steel rebar to mortar. Since the pull-out performance is selected to assess the interfacial durability of TRM, this thesis derived an analytical solution of interfacial bond-slip behaviour during the pull-out process. The moisture-induced degradation has also been discussed in this research, with a particular focus on the effects of hygroscopic expansion and interfacial ageing.

Considering that there exists a scientific challenge of understanding CFSRM durability before it can be applied to practice extensively, this study focuses on the real working condition in the offshore area and thus investigates its durability problems by coupling two different degradation mechanisms altogether, namely hygroscopic expansion and interfacial ageing. Although each of them has been individually studied in literature so

far, this study innovatively takes them into account simultaneously to investigate the coupling effect. At last, a long-term prediction model based on multiphysics is proposed to estimate its interfacial degradation behaviour under marine environment.

The present study includes both experimental work and numerical testing. A total of 125 samples are tested in experiments. Mortar samples are used for strength, flowability and diffusion tests, containing 24 cubes (100 mm), 24 cylinders (200×100 mm height/diameter), three prisms (40×40×160 mm), fresh mortar and eight small cylinders (50×20 mm height/diameter). 28 CFS samples are used for mechanical and physical tests. 32 CFSRM cylinders (50×20 mm height/diameter) are used for pull-out tests. All above-mentioned tests are carried out in University of Plymouth. According to material parameters acquired from experiments, COMSOL Multiphysics software is used to build the multi-field numerical model which simulates the coupling effects of water diffusion, hygroscopic expansion, and immersion temperature on the bond degradation of CFSRM. As the present thesis proposes a three-parameter durability (TPD) model based on Arrhenius Law to predict the interfacial ageing over time, TPD model is further used in the numerical testing and then validated by the experimental records. Finally, the present thesis proposes a hand calculation method of pull-out force retention under long-term conditioning, based on above-mentioned experimental and numerical analyses altogether.

Key words:

carbon fibre strand; sea sand and seawater mortar; marine environments; long-term durability; textile reinforced mortar; carbon fibre strand reinforced mortar (CFSRM) specimens;

TABLE OF CONTENTS

LIST OF FIGURES

LIST OF TABLES

ANNOTATIONS

Abbreviations

- AFRP — aramid fibre reinforced polymer
- BFRP — basalt fibre reinforced polymer
- CFRP — carbon fibre reinforced polymer
- CFS — carbon fibre strand
- CFSRM — carbon fibre strand reinforced mortar
- CV — coefficient of variation
- CZM — cohesive zone model
- FM — freshwater mortar
- FRP — fibre reinforced polymer
- GFRP — glass fibre reinforced polymer
- GGBS — ground granulated blast-furnace slag
- HPC — high performance concrete
- OPC — ordinary performance concrete
- PFA — pulverised fuel ash
- RC — reinforced concrete
- SM — seawater mortar
- SF — silica fume
- SWSSC — seawater and sea sand concrete
- TPD — three-parameter durability model of pull-out performance
- TRC — textile reinforced concrete
- TRM — textile reinforced mortar

- TSF — time-shift factor of interfacial ageing reaction rate constant as per Arrhenius Law

Notations

- A — pre-exponential factor of Arrhenius Equation
- A_{Al} — cross-sectional area of aluminium tube used in CFS anchorage region
- A_{CFS} — measured CFS cross-sectional area in the initial dry state
- A'_{CFS} — measured CFS cross-sectional area in the moisture saturation state
- A_{mo} — cross-sectional area of mortar of idealised mechanical model
- A_{es} — cross-sectional area of epoxy resin used in CFS anchorage region
- A_{fi} — cross-sectional area of fibre of idealised mechanical model
- C — moisture concentration used in ageing kinetics and TPD model
- C_{CFS} — concentration of water in CFS medium
- C'_{CFS} — saturation concentration of water in CFS medium
- C_{SM} — concentration of water in SM medium
- C'_{SM} — saturation concentration of water in SM medium
- D — interfacial adhesive contact damage for an arbitrary point in CZM
- D_{CFSr} — radial diffusion coefficient of CFS material
- D_{CFSz} — axial diffusion coefficient of CFS material
- D_{CFSr20} — radial diffusion coefficient of CFS immersed in 20 °C seawater
- D_{CFSz20} — axial diffusion coefficient of CFS immersed in 20 °C seawater
- D_{SM} — diffusion coefficient of SM material
- D_{SM20} — diffusion coefficient of SM material at 20 °C
- E_a — apparent activation energy of Arrhenius Equation

- E_{aMW} — water diffusion activation energy of SM
- E_{aFWr} — radial water diffusion activation energy of CFS
- E_{aFWz} — axial water diffusion activation energy of CFS
- E_{Al} — elastic modulus of aluminium material
- E_{CFSr} — radial elastic modulus of CFS
- E_{CFSz} — uniaxial tensile elastic modulus of CFS material
- E_{mo} — Young's modulus of mortar of idealised mechanical model
- E_{es} — elastic modulus of epoxy resin
- E_{fi} — Young's modulus of fibre of idealised mechanical model
- E_{SM} — uniaxial compressive elastic modulus of SM after 28 days of curing
- F_{HE} — decrease in pull-out force on account of hygroscopic expansion singly
- F_{IA} — decrease in pull-out force on account of interfacial ageing singly
- F_{PI} — initial pull-out force of intact CFSRM specimens
- F_{PR} — measured pull-out force retention after a certain duration of conditioning
- fu_{CFS} — ultimate tensile strength of CFS material
- G_{CFSr} — transverse shear modulus of CFS
- G_{CFSz} — axial shear modulus of CFS
- G_{el} — elastic fracture toughness of CZM
- G_r — shear energy release rate of CZM
- G_{so} — interface softening fracture toughness of CZM
- G_t — total fracture toughness of CZM
- k — reaction rate constant of Arrhenius Equation
- k_s — interfacial shear stiffness of CZM suffering from adhesive contact damage
- K_τ — interfacial shear stiffness of CZM
- $[K_{CFS}^{el}]$ — elastic stiffness matrix of CFS material

- L — length of interfacial bond of idealised mechanical model
- l_{pa} — length of CFSRM anchorage zone beyond jig's grip in pull-out test
- l_{pj} — length of CFSRM junction zone between mortar and anchor structure
- M_{CFS} — current water absorption in CFS
- M'_{CFS} — saturated water absorption in CFS
- $M_{FSL}(t)$ — moisture absorption mass growth for a group of 60 CFS samples with 240 mm length at an arbitrary time t
- M'_{FSL} — maximum moisture uptake at the saturation status for a group of 60 CFS samples with 240 mm length
- M_{FSLd} — initial mass of a group of 60 CFS samples with 240 mm length, after complete drying treatment
- M_{SM} — current water absorption in SM
- M'_{SM} — saturated water absorption in SM
- M'_{SMC} — saturated water absorption within the entire SM cylindrical specimen
- M_{SMCd} — initial mass of SM cylindrical specimen after complete drying treatment
- $M_{SMC}(t)$ — the current mass growth of water uptake for SM cylindrical specimen at an arbitrary time t
- M_w — molar mass of water
- P — pull-out force acting upon the loading end
- P_1 — loading acting upon right end of fibre in idealised mechanical model
- P_2 — loading acting upon left end of fibre in idealised mechanical model
- P_3 — reaction force from right support of mortar in idealised mechanical model
- P_4 — reaction force from left support of mortar in idealised mechanical model
- PA_{CFS} — percentage of water absorption that accounts for the mass of CFS material under its dry condition

- PA'_{CFS} — percentage of saturated water absorption that accounts for the mass of CFS material under its dry condition
- PA_{CFS28} — PA_{CFS} at the 28th curing day for CFS embedded in CFSRM specimen
- PA'_{SM} — percentage of saturated water absorption that accounts for the mass of SM material under its dry condition
- R — universal gas constant
- r_{CFS} — radius of CFS
- r_R — radius of CFSRM specimen
- $S_{CFS}(t)$ — current moisture saturation of CFS at any time t
- $S_{SMC}(t)$ — current moisture saturation of SM cylindrical specimen at any time t
- t — time
- T — temperature
- u — local relative slip for an arbitrary point in CZM interfacial elements
- u_{mo} — absolute displacement of mortar of idealised mechanical model
- u_{da} — displacement of pull-out force P applying to the anchorage end of CFSRM
- u_{fi} — absolute displacement of fibre of idealised mechanical model
- u_p — slip corresponding to τ_p in CZM interfacial elements
- u_p^{age} — retention of u_p after an ageing duration related to Y
- u_{st} — actual interfacial slip at the loading end of CFSRM
- u_{td} — critical slip before the total decohesion occurs at a point in CZM
- u_{td}^{age} — retention of u_{td} after an ageing duration related to Y
- v_{CFSr} — transverse Poisson's ratio of CFS
- v_{CFSz} — axial Poisson's ratio of CFS
- v_{SM} — Poisson's ratio of SM
- Y — property retention

- Y_∞ — final retention of bond property after interfacial ageing of infinite time
- z_h — half length of CFSRM specimen
- α_T — shift factor of time-temperature superposition used for water diffusion
- β_{CHE} — coefficient of hygroscopic expansion for the transverse swelling of CFS material
- β_{sr} — swelling ratio, namely the ratio of dilatation strain to current moisture concentration in CFS
- δ — relative displacement between fibre and mortar of idealised mechanical model
- δ_1 — slip corresponding to τ_f of local bond-slip relationship
- δ_2 — slip corresponding to τ_r of local bond-slip relationship
- Δl_{pe} — tensile deformation of CFSRM junction zone and anchorage zone beyond jig's grip
- ε_{CFS}^{el} — elastic strain existing in CFS
- ε_{CFS}^{t} — total strain existing in CFS
- ε_{mo} — mortar strain of idealised mechanical model
- ε_{fi} — fibre strain of idealised mechanical model
- ε_{HE} — transverse hygroscopic expansion strain of CFS material
- ε_{HE}' — maximum transverse hygroscopic expansion strain of CFS material in the state of moisture saturation
- σ_{CFS} — stress existing in CFS
- σ_{mo} — axial stress in mortar of idealised mechanical model
- σ_{fi} — axial stress in fibre of idealised mechanical model
- σ_r — transverse compressive stress in CFSRM
- σ_z — axial stress in CFSRM
- τ — bond stress along the interface of idealised mechanical model

- τ_f — maximum shear stress of local bond-slip relationship
- τ_p — peak shear stress in CZM interfacial elements
- τ_p^{age} — retention of τ_p after an ageing duration related to Y
- τ_r — residual shear stress of local bond-slip relationship
- τ_s — interface shear stress between CFS and SM
- $\emptyset$ — diameter of fibre of idealised mechanical model

1 INTRODUCTION

1.1 Background

There has been an increasing demand on marine structures in modern development, including seawalls, port and harbour, offshore structures such as sea bridges, oil & gas platforms, offshore renewable energy devices and so on. Seaborne trade activities and the utilisation of various marine energy resources would be impossible without the support of the relevant infrastructural construction which involves the extensive use of reinforced concrete (RC).

However, the traditional RC-based construction materials exposed to the marine environment proves to be not as durable as it is used on land (Page, 1975; Melchers, 2020). On the one hand, chloride ions in marine environment can penetrate into RC, which can lead steel reinforcement corrosion (Wei et al., 2012). On the other hand, oxides would generate inside the RC material immersed in saline water and cause expansion cracks (Andrade et al., 2016). Subsequently, the crack damage further worsens the steel reinforcement corrosion because the protection from the concrete cover is not intact any more (Andrade et al., 2016). Apart from the erosion of reinforcement, conventional concrete that only adopts normal Portland cement as the cementitious material is prone to the damage stemming from marine environmental erosion as well (Qu et al., 2021). Fig.1-1 illustrates the representative degradation phenomena of RC structures due to seawater erosion (Mohammed, 2015; Nolan et al., 2021). As a result, the long-term durability problem of traditional RC materials used in marine environments causes the expensive maintenance costs and the potential safety risks, thereby restricting the future development of construction industry in marine areas.

(a) (b)

Fig.1-1 Degradation of RC structures due to seawater erosion and steel reinforcement corrosion: (a) bridge column (Mohammed, 2015); (b) seawall (Nolan et al., 2021).

Other problems that generally limit the development of construction industry are related to resource utilisation and environmental protection. As the global construction industry consumes 40 to 50 billion tonnes of sand every year, the shortage of natural sand becomes more serious recently (Cousins, 2019). Meanwhile, the production of traditional RC materials has consumed a large amount of freshwater. From the perspective of natural ecology, the excessive exploitation of natural sand and freshwater resources are usually followed by the damage to ecological environments. The carbon emissions during large-scale production of Portland cement aggravate the global greenhouse effect.

To improve the durability of marine concretes, diverse approaches have been proposed in practice. The introduction of mineral admixtures is one of the frequently used methods to prevent the corrosion. Existing research indicates that taking advantage of pulverised fuel ash (PFA) and ground granulated blast-furnace slag (GGBS) as cement substitutes can effectively improve the concrete durability under seawater and retard the interior pentration of chloride ions (Sengul and Tasdemir, 2009; Swaroop et al., 2013). Another method is to apply corrosion inhibitors to the concrete substrate. However, the inhibitors

would gradually lose their protective action over time owing to the migration and leaching out mechanism during the long-term water immersion period (Vazques, 1990; Vaysburd and Emmons, 2004; Topçu and Uzunömeroğlu, 2020). In recent years, people turn their attention to the search for substitute materials. Unlike steel bars, fibre reinforced polymer (FRP) materials would not corrode when used in marine conditions. Many studies have focused on the durability of FRP materials (Sen, 2015; Guo et al., 2018). Existing research demonstrates that carbon fibre reinforced polymer (CFRP) usually has a better performance than basalt fibre reinforced polymer (BFRP) or glass fibre reinforced polymer (GFRP) in long-term ageing tests (Guo et al., 2018).

To protect the ecological environments and reduce the consumption of natural resources, seawater and sea sand can replace freshwater and natural sand respectively in concrete if the construction adopts FRP materials as the reinforcement instead of traditional steel rebar (Ahmed et al., 2020). They are readily available from marine areas with relative cheaper costs. Industrial by-products such as PFA and GGBS are eco-friendly alternatives to blend with Portland cement. They act as supplementary cementitious materials used in concrete and thus reduce the requirement of Portland cement, thereby help minimising CO_2 emissions. However, more studies should be done to further understand the change and reformation of the reinforced concrete improved in this way, thus facilitating its wide applications to engineering practice under marine environments.

1.2 Research aim and objectives

Compared with conventional FRP bar or plate, carbon fibre textile is a new type of reinforcement for concrete, which is gaining popularity rapidly. The reinforced concrete produced by the combination of using carbon fibre textile reinforcement, sea sand,

seawater and other eco-friendly admixtures is deemed as a highly promising construction material, particularly for marine environment. However, there still exists a research gap in this material before realising its extensive application to marine construction. In order to have a better understanding about carbon fibre textile reinforced concrete, especially its long-term performance, the present thesis focuses on the long-term interfacial bond behaviour between carbon fibre textile and concrete, based on the degradation mechanisms including water diffusion, hygroscopic expansion, interfacial ageing and interfacial failure which determine the durability performance of such a construction material exposed to the marine environment.

In this study, the interfacial contact between the fibre textile and concrete can be simplified to the single interface between CFS and mortar, as explained in Fig.1-2 wherein CFS is the basic element that comprises the fibre textile while mortar is the main component that directly contacts the reinforcement in concrete. In this way, the specific research objectives of the thesis can be listed as follows,

- To study the water diffusion and absorption behaviour of carbon fibre textile and the textile reinforced mortar specimens under different temperature conditions.
- To study the hygroscopic expansion behaviour of single CFS embedded in mortar and its effect on the pull-out performance.
- To study the long-term interfacial bond behaviour between CFS and mortar with respect to its pull-out performance, and the effect of ageing treatment.
- To understand the entire interfacial degradation process of CFSRM specimens by developing a multi-field numerical model which couples the theoretical mechanisms of water diffusion, hygroscopic expansion, interfacial ageing and pull-out behaviour altogether.

- To predict and evaluate the long-term durability of the interfacial bond between CFS and mortar in CFSRM under various exposure conditions in marine environment.

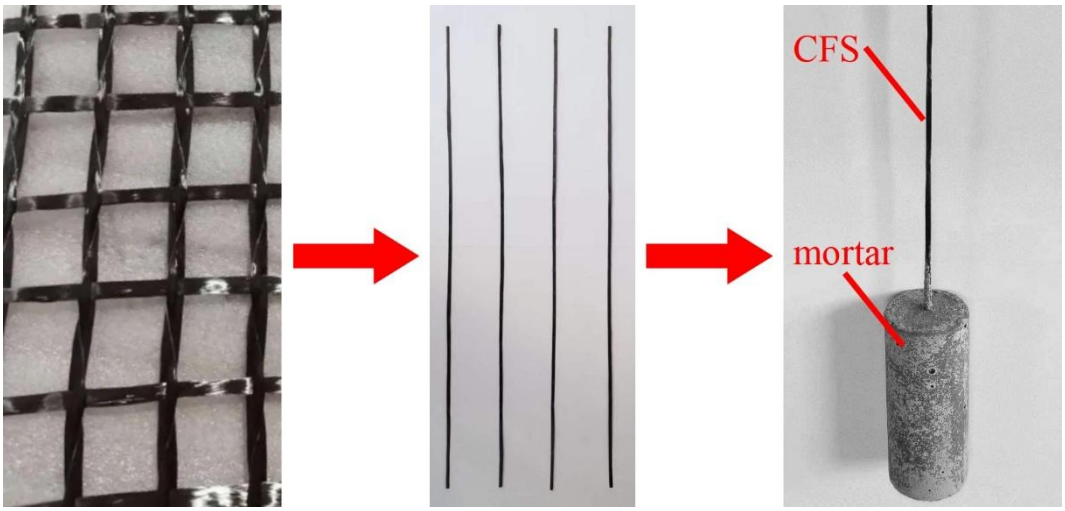

(a) (b) (c)

Fig.1-2 Research object and its composition: (a) carbon fibre textile; (b) CFS directly extracted from the textile; (c) CFSRM specimen that contains CFS and mortar contacted each other by a single interface.

1.3 Research Methodology

The general degradation mechanisms of carbon fibre textile reinforced mortar exposed to marine environment can be roughly estimated by sorting out the existing literature in the related research field, from which the present thesis decided to focus on hygroscopic expansion and interfacial ageing as two key contributing factors.

In order to carry out the study on the coupling effect of the above-mentioned two different degradation mechanisms, the present thesis focused on their mutual precondition first, namely water diffusion which drove the whole degradation process. Both experimental work and numerical testing were adopted to investigate the water diffusion behaviour.

Once the diffusion coefficients and the moisture absorption ratio were measured by experiments with eight cylindrical mortar specimens (50×20 mm height/diameter) and 16 groups of CFS specimens (6&240 mm length), they were further used to build the numerical model of water diffusion field. Then the diffusion behaviour at any temperature and time could be analysed.

In order to understand the hygroscopic expansion occurred inside CFSRM specimen, simulation method was adopted to analyse the swelling stress and consequent interfacial slip, owing to the fact that such a phenomenon could not be experimentally observed. By applying this simulation method to calculating the swelling behaviour of the research case from the published paper and then comparing the calculation results with the published data, the simulation method used in this study was validated.

In order to understand the interfacial ageing behaviour, the experimental method based on accelerated ageing treatment on 32 CFSRM cylindrical specimens (50×20 mm height/diameter) was conducted to analyse its durability performance changes within the limited duration, given that the interfacial degradation process was extremely slow at room temperature. The multiphysics numerical simulation by using COMSOL software was adopted to further analyse the ageing experimental records whereby the TPD theoretical model proposed by this thesis was numerically realised to estimate the interfacial ageing behaviour under different time, temperature and moisture content.

In the meanwhile, the theoretical analysis of the fundamental interfacial failure process between mortar and CFS was also necessary to carry out, in order to provide the theoretical support for conducting pull-out tests as well as simulating pull-out processes which investigated the coupling effects of hygroscopic expansion and interfacial ageing.

In order to realise the estimate of long-term degradation behaviour, the present thesis combined all aforementioned research achievements together and thereby derived the long-term durability prediction model which used the indicator of residual pull-out force to showed the bond degradation process at CFS/mortar interface inside CFSRM under different environmental exposure.

1.4 Thesis structure and outline

By using a flowchart, Fig.1-3 gives a brief illustration of the thesis outline and how the thesis assigns its structure.

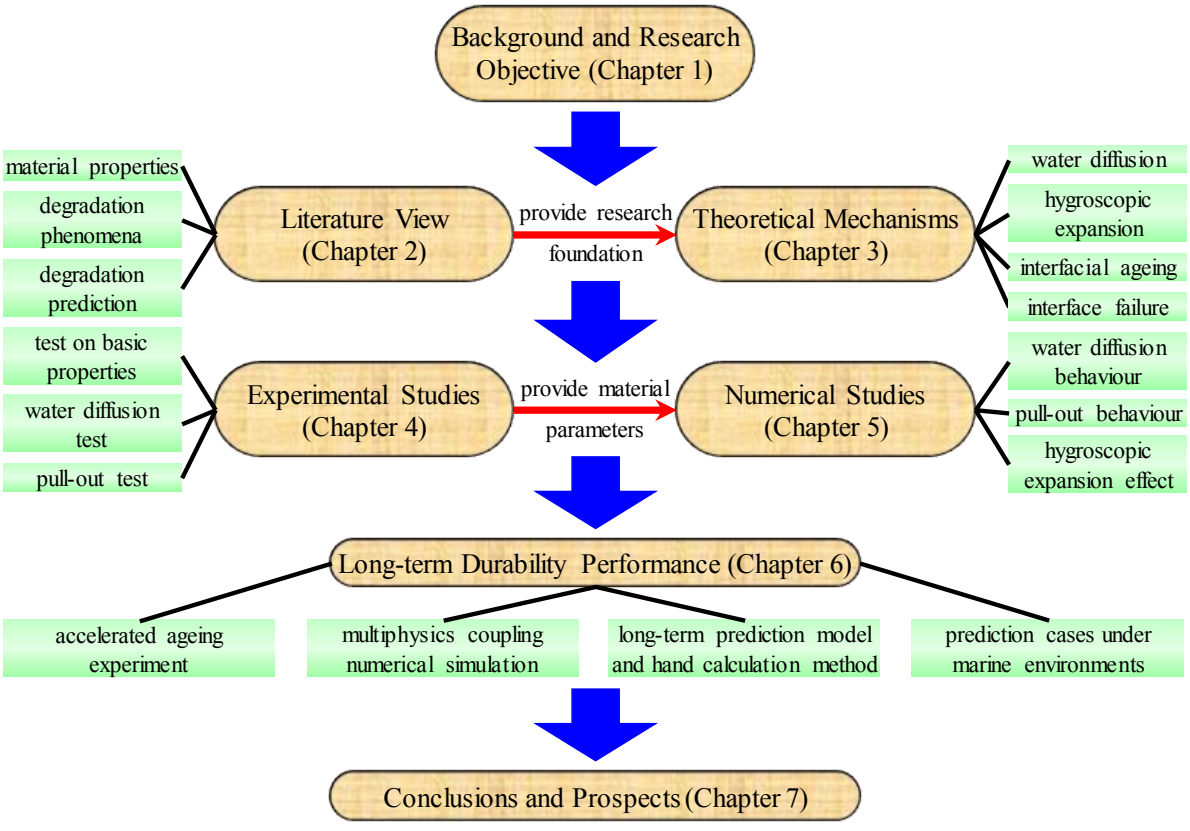

Fig.1-3 Flowchart of thesis structure and outline.

2 LITERATURE REVIEW

2.1 Fibre composites as reinforcement

2.1.1 Historical background

Although the exploitation of fibre materials and relevant products has existed back to antiquity, the majority of them during ancient times are in the scope of natural fibres, along with handmade products such as jute rope and straw reinforced soil based on the collection of natural fibres (Bauer and Halim, 1987; Khan et al., 2018). Those primitive materials with low strength and durability were gradually incapable of reinforcing constructions with the development of civil engineering especially after the invention of cement. Fibre and fibre based composites thus were not considered as the reinforcement for modern constructions until the 20th century, when a series of innovations and technological breakthroughs were achieved in respect of high-strength synthetic fibres including glass fibre and carbon fibre, along with continuous improvements on techniques of the large-scale manufacture for them (Bhatt et al., 2018).

Carbon fibre already existed in embryo in 1860s when Sir Joseph Wilson Swan first invented the filaments made by carbon fibre material (Seymour et al., 2012), but the significant improvement on this material occurred in 1960s when Dr. Akio Shindo, working at Agency of Industrial Science and Technology in Japan, used polyacrylonitrile (PAN) to create the carbon fibre with the carbon volume fraction ratio more than 50% and a large drop in manufacturing cost (Lu, 2021). Then carbon fibre material gradually attracted interest from modern industry. After many decades of development, now carbon

fibre material has been widely exploited in various fields such as civil engineering, aerospace engineering and mechanical engineering (Techno, 2016).

As another popular fibre material, glass fibre has its history of development, similar to the carbon fibre. The prototype of modern glass fibre was invented by Games Slayter working at Owens-Illinois in 1930s (Babar et al., 2019). Over World War II, many technological breakthroughs in its mass production occurred, leading the glass fibre to engineering practice from scientific study (Bhatt et al., 2018). Now the application of glass fibre can be found not only in traditional industries but also in some emerging fields, such as renewable energy, 3D printing and biomimetic material (Masselter and Speck, 2011; Javaid et al., 2016; Shahrubudin et al., 2019).

With the development of material science and manufacturing technology, more and more types of synthetic fibres were invented and introduced into civil engineering since the mid-20th century (Khatib, 2016; Naaman, 2018). Apart from above-mentioned fibre types, modern construction industry takes advantages of aramid fibre, basalt fibre and polypropylene fibre as well, with the time of occurrence that can be traced back to 1960s (Madhavi et al., 2014).

The structure of continuous fibre materials is featured as a large quantity of fibre filaments aligned parallel. The interconnections among different filaments are loose without resin matrix to bind them together. Although each filament has a high mechanical strength, the stress transfer among the loose interconnections limits the global mechanical properties (Hegger et al., 2004).

In order to make better use of fibre materials, a composite material called FRP was invented as an alternative for the direct usage of loose fibre filaments in industrial fields. It generally has two phases containing fibres and polymer matrix acting like glue to bind loose fibre filaments together. Fig.2-1 illustrates the structure of FRP from a microscopic point of view.

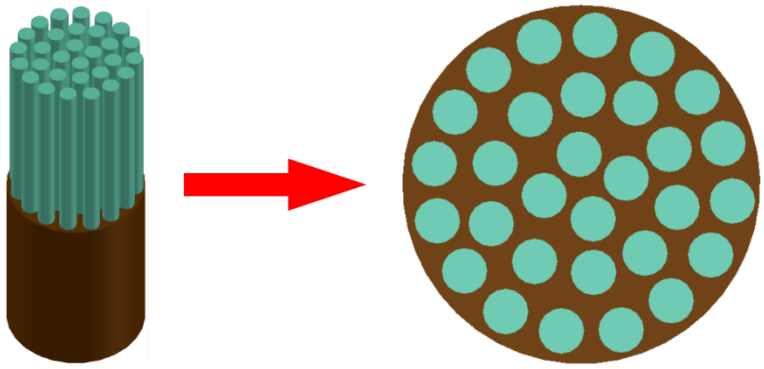

(a) (b)

Fig.2-1 Microstructure of FRP material: (a) three-dimensional view; (b) cross-sectional view.

The origin of FRP can be traced back to 1930s when the company, Owens Corning, started to manufacture glass fibre, and in the meanwhile Carleton Ellis, as the chemical engineer of Dupont Company, patented unsaturated polyester resin in 1936 (PASĂRE et al., 2019; Godara et al., 2021). Coupled with resin as the matrix for fibre reinforcement, the original glass fibre reinforced polymer was thus invented by DuPont Company in the same year (Faruk et al., 2017). During World War II, the development of FPR materials was booming as materials with light weight and high strength were increasingly demanded (Nagavally, 2017). After decades of scientific research and commercial exploitation, FRP materials had been widely used in aerospace, automotive industry and shipbuilding by 1980s (PASĂRE et al., 2019; Godara et al., 2021). Civil engineering is also a major field for the application of FRP. In 1975, GFRP bar was first used as the

reinforcement for concrete substrate in Russia (Shrivastava, 2018). Based on more applications of FRP to construction industry overtime, Japan in 1996 published the first engineering guideline for FRP reinforced concrete structures (Shrivastava, 2018). More relevant standards and specifications were compiled and updated when it came into 21th century (Nanni et al., 2014; Prince-Lund Engineering, PLC, 2018). Those codes and guidelines are stemming from the practice of utilising FRP in construction industry, and in turn further promote its development. Now engineering practice adopting FRP material as the reinforcement can be found all over the world. The exploration of FRP materials along with FRP-based structures is deemed a state-of-the-art scientific field.

2.1.2 Material properties of fibre composites

Compared with traditional materials used in civil engineering, FRP has a series of advantages. As the reinforcement, it has a higher mechanical strength than normal steel bar but it is much more lightweight than steel reinforcement. In addition, it is featured as an excellent durable material, especially the moisture resistance, anti-corrosion of chloride ions and oxidation resistance when FPR replaces steel reinforcement to work in harsh environments (Afshar et al., 2016; Cousin et al., 2019). On account of its special two-phase structure consisting of soft fibre filaments and resin matrix to fix them, FRP materials are easy to shape into any profiles to cater for the demand of components (Magna et al., 2016). Such superiority makes it highly flexible to design for diverse constructions with different purposes (Gemi et al., 2021). Based on its various shapes and design flexibility, components made by FRP are simple and fast to install for constructions (Živanovic et al., 2019). During the installation, they prove the convenience of handling (Santandrea et al., 2016). After the installation, they scarcely need maintenance or upkeep even under severe conditions (Živanovic et al., 2019). Apart from

those general benefits mentioned above, existing research suggests that the usage of CFRP can improve the fatigue resistance of components, particularly when it serves as the external reinforcement for the retrofit and rehabilitation (Yu and Wu, 2018). From the viewpoint of carbon neutrality, a high performance of electrochemical resistance makes FRP reinforcement able to decrease its cover thickness in concrete and thereby support a lightweight design of reinforced concrete components with the decline in the amount of concrete and carbon emissions (Spelter et al., 2018). Thus, FRP can be classified into eco-friendly construction material for sustainable civil infrastructures (Hota and Liang, 2011). Furthermore, replacing conventional steel reinforcement by FRP helps remove the restriction of concrete mix design owing to its anti-corrosion property exposed to chloride-rich environments, thereby making lots of environmental friendly raw materials feasible to introduce into concrete, such as sea sand and seawater as the alternatives of river sand and freshwater respectively (Bazli et al., 2020).

However, as a newly developing construction material, FRP still has many drawbacks that cannot be ignored up to now. Although FRP reinforced concrete has a higher durability performance than traditional steel reinforced concrete, its long-term degradation problem cannot be totally avoided, especially at the bonding interface between FRP and concrete substrate (Sen, 2015; Li et al., 2019). Compared with conventional construction materials, relevant experimental studies, basic research and engineering experiences are not adequate to support the wide application of FRP in construction industry (Chin et al., 2015; Kim, 2019). On account of its short application history, there is a lack of long-term durability records neither from laboratory investigation nor from engineering practice (Portal et al., 2016; Liang et al., 2018). Those problems would be likely to cause the irrationality of structural design and the difficulty of lifespan evaluation in regard to FRP reinforced concrete. On top of adverse factors

mentioned above, the material costs of FRP reinforcement are generally higher than conventional steel reinforcement.

2.1.3 Commercialised fibre types

Many fibres have been proved viable to be used in FRP. This section introduces some most commonly used fibres that are successfully commercialised and frequently used in recent years.

2.1.3.1 Aramid fibre

Aramid fibre can be classified into organic fibre composed of long molecular chains with a high rigidity that has at least 85% of amide linkages attached to two cyclobenzene (Chatzi and Koenig, 1987). According to the specific molecular structures, there are two kinds of aramid fibres commonly used today. One is called Nomex, with its molecular structure shown in Fig.2-2 (The University of Southern Mississippi, 2022a). The other is called Kevlar, with a greater popularity and the molecular structure shown in Fig.2-2 (The University of Southern Mississippi, 2022a). The former was invented by DuPont Company in 1961 and commercialised in 1967 (Weber et al., 1992; Baker, 2018), while the latter was invented by the same company in 1965 and commercialised in 1971 (Kabir and Ferdous, 2012).

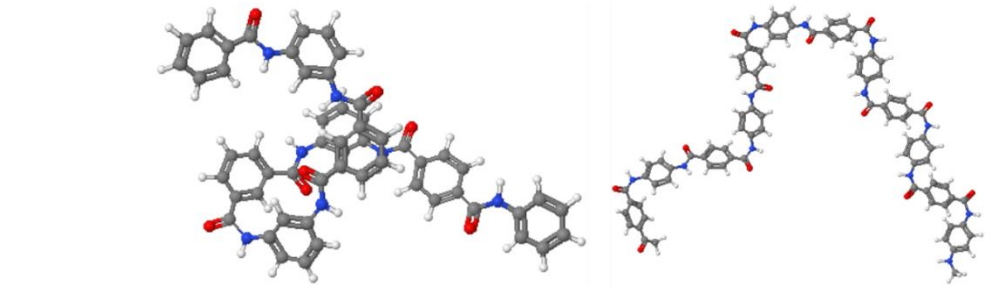

(a) (b)

Fig.2-2 Three-dimensional model of micromolecular structures: (a) Nomex aramid fibre; (b) Kevlar aramid fibre (The University of Southern Mississippi, 2022a).

Aramid fibre is featured as a lightweight and high tensile strength material with the density of 1.45 g/cm^3 and the ultimate tensile strength of 2.06 GPa (Mathavan and Patnaik, 2020; Dharmavarapu and S, 2021; Kulagina and Zhelezina, 2022). It has the high-temperature resistance as well, exhibiting stability under 200 °C (Zhou et al., 2020). However, existing literature indicates that aramid fibre is prone to damage owing to moisture exposure (Kaya et al., 2018). To date, many marketable products made by aramid fibre can be found in engineering practice, including aeronautical engineering, automotive engineering and even sport industry (Ma et al., 2020; Dharmavarapu and S, 2021).

2.1.3.2 Basalt fibre

Basalt fibre can be classified into inorganic synthetic fibre composed of a number of oxide including silicon dioxide (SiO_2), aluminium oxide (Al_2O_3), calcium oxide (CaO), magnesium oxide (MgO), etc. that form the network structures of silicate molecules (Alagirusamy and Das, 2010; Xing et al., 2019). Fig.2-3 plots five different molecular structures of cumulative silicate (Xing et al., 2019).

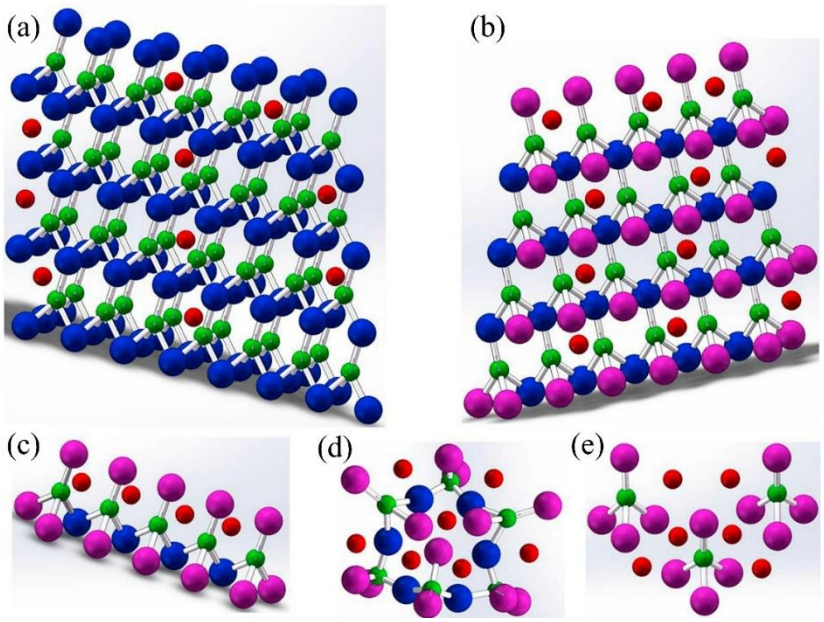

Fig.2-3 Micro-molecular structures of basalt fibre: (a) tectosilicate; (b) phyllosilicate; (c) inosilicate; (d) ring silicate; (e) nesosilicate (Xing et al., 2019).

Although the first exploration of basalt fibre material could be traced back to 1920s, scientists did not pay much attention to it until 1960s (Jamshaid and Mishra, 2016). Since many studies concentrating on this newly developing material have been done over time, people gradually find its superiority, including the chemical inertness, outstanding ability of sustaining elevated temperature and high mechanical strength (Jamshaid and Mishra, 2016). In the meanwhile, the shortcomings of its intrinsic properties are gradually revealed as well, such as the deficiency in toughness, poor behaviour when withstanding bending force and the energy-intensive manufacturing process (Zhang et al., 2012; Fonseca et al., 2020). After rapid development over several decades, basalt fibre has been widely used in modern industries to date, containing high performance constructions, power engineering, environmental protection etc. (Jamshaid and Mishra, 2016).

2.1.3.3 Carbon fibre

Carbon fibre belongs to inorganic synthetic fibre. Its microstructure is characterised as carbon atoms that align parallel to the longitudinal direction of fibre (Khurshid et al., 2019). Moreover, carbon atoms are bonded together in crystals on each layer (Khurshid et al., 2019). The diagram of its microstructure is illustrated in Fig.2-4, wherein the atomic layer of carbon fibre is featured as the laminar alignment of crystal structure (Chung, 2019).

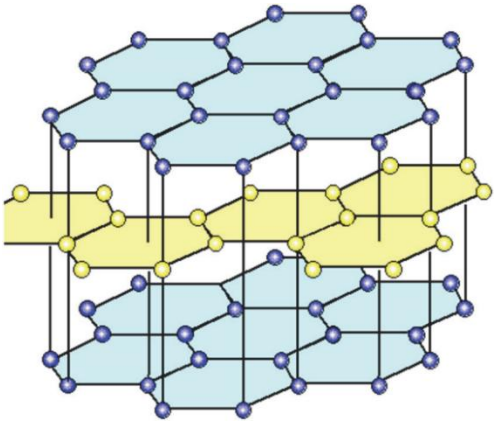

Fig.2-4 Microstructure of carbon fibre in terms of atomic layers (Chung, 2019).

Since large amount of research involving carbon fibre material has been conducted during the past several decades, more and more advantages of carbon fibre have been found out and exploited in the engineering practice. Carbon fibre material has high tensile strength of 2.5 to 4 GPa and low density of 1.8 g/cm^3 (Kaur and Keith Millington, 2016; Manu et al., 2019). It is usually utilised as the reinforcement in construction industry and lap joint for aircraft manufacturing. Its electrochemical resistance makes it possible to work well in various harsh conditions including long-term seawater immersion, loading cycles and continuous alkaline/acid corrosion (Graham-Jones and Summerscales, 2015; Backe and Balle, 2016; Tao and Zhang, 2016; Yu, 2020). Considering the further large-scale

application of carbon fibre to diverse industries, relevant basic research, experimental investigations and practical experience of modern engineering, however, are still needed to support the rational utilisation of this emerging material, owing to its relatively short history of application when compared with those conventional construction materials (Carra and Carvelli, 2015; Chin et al., 2015; Kim, 2019). Based on the same reason, the general consensus about assessment methods of service life have not been achieved until now, leading to the difficulty in durability evaluation (Carra and Carvelli, 2015). As a consequence, carbon fibre material still suffers from the deficiency in relevant standard or specification to guide the structural design, especially under tough conditions (Kafodya et al., 2015; Emparanza et al., 2017).

2.1.3.4 Glass fibre

Glass fibre belongs to inorganic synthetic fibre. For normal E-glass fibre, SiO_2 is the essential chemical composition that occupies more than 58% of total mass, while other components contain a series of oxide including Al_2O_3, CaO, Fe_2O_3, etc. (Deák and Czigány, 2009). As a non-crystalline material, it has the basic molecular structural element of tetrahedron network with each silicon atom shared by four oxygen atoms, as shown in Fig.2-5 (Park and Seo, 2011). Thus, glass fibre can be seen as the integration of those basic elements by means of the chemical bond between external silicon atom and internal oxygen atom at the corner (The University of Southern Mississippi, 2022b).

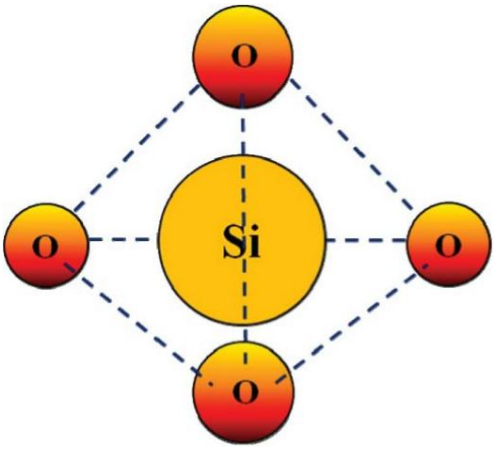

Fig.2-5 Microstructure of glass fibre in terms of basic molecular element (Park and Seo, 2011).

After continuous development over nearly one century, a variety of glass fibre types have been invented and commercialised according to different purposes and working conditions. E-glass fibre is the initial type first invented and introduced into market. C-glass fibre is deemed a low-priced alternative of E-glass fibre, due to its relatively simple manufacturing processes (Richet et al., 2021). AR-glass fibre is well-known for its alkaline resistance and thus can be used in concrete. S-glass fibre was invented in 1960s, applied to special conditions with higher demands for strength and elevated-temperature performance (Richet et al., 2021). Besides, there are D-glass fibre, R-glass fibre and ECR-glass fibre that are derived from E-glass fibre, widely used all over the world. Based on numerous studies and practical applications, its disadvantages are exposed as well. It has a poor abrasive behaviour (Demirci and Düzcükoğlu, 2014). It is more susceptible to deterioration than other inorganic synthetic fibres such as carbon fibre, owing to the lack of thermostability and chemical stability (Joshi and Purnima, 2010; Benmokrane et al., 2015). Another drawback is that the mechanical property of glass fibre is liable to intrinsic defect derived from its manufacturing process (Zhong et al., 2019).

2.1.4 Reinforcement produced by fibre composites

Based on the flexibility in shape and structural design, a wide range of FRP reinforcement has been developed to meet the needs from construction industry, such as bar, plate, tube and mesh (Spadea et al., 2017; Tran et al., 2019). Coupled with concrete substrate, they serve as the reinforcement for structures. Besides, they can be applied to the surface of existing structures for rehabilitation, retrofit and strengthening. Note that the present study here does not discuss those discontinuous fibre composites, namely short fibre composites, working as the secondary reinforcement to refine mechanical properties of concrete members.

The first category introduced herein is FRP bar, in which fibres (glass, carbon, aramid or basalt) are bound together with resin. Fig.2-6 displays BFRP, GFRP and CFRP bars made by basalt, glass and carbon fibre respectively (Wang et al., 2017a). They have the diameter of 6 mm which is also frequently adopted by the steel rebar in the engineering application. As the reinforcement to sustain load, FRP bar is commonly embedded in the tensile area of concrete components. It is known as the substitute for conventional steel bar, particularly under harsh environmental conditions.

Fig.2-6 Types of commonly used FRP bar (Wang et al., 2017a).

The second category is FRP plate. Generally, it has the thickness ranging from 1.2 mm to 1.5 mm (Rao et al., 2012; Mohee et al., 2016; Wang et al., 2018). Similar to FRP bar, it

is able to act as the tensile reinforcement for concrete beam and slab for construction (Awad et al., 2012). Fig.2-7 displays the frequently used categories of FRP plates fabricated by CFRP, GFRP and BFRP, respectively (Rao et al., 2012; Mohee et al., 2016; Wang et al., 2018).

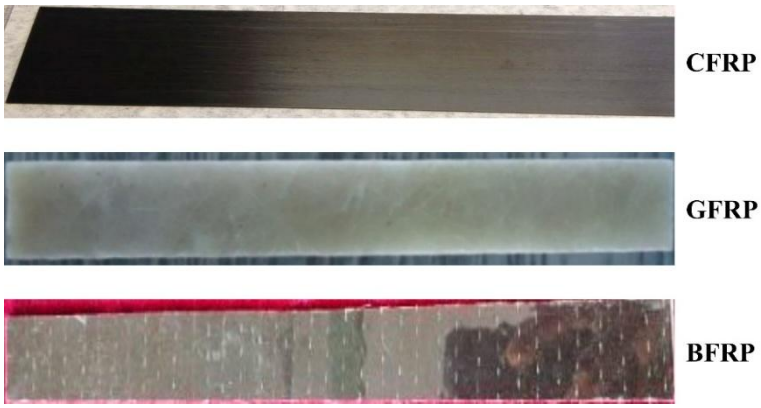

Fig.2-7 Frequently used FRP plates (Rao et al., 2012; Mohee et al., 2016; Wang et al., 2018).

FRP tube is another type of reinforcement used in construction industry, with high hoop strength and anti-corrosion performance. When FRP tube covers the exterior surface of cylindrical concrete substrate, it can not only serve as the external confinement to prevent concrete from cracking, but also protect the reinforced concrete from corrosion under hostile natural conditions (Bazli et al., 2020). Fig.2-8 displays the frequently used FRP tubes with the common thickness of 3 mm and the outer diameter of 16 cm, fabricated by CFRP, GFRP and BFRP, respectively (Bazli et al., 2020).

Fig.2-8 Frequently used FRP tubes (Bazli et al., 2020).

In recent years, fibre textile or mesh structure gradually attracts the attention of academics and industry. It is generally comprised of fibre strand aligned in two different orientations that are perpendicular to each other, namely the warp strand and the weft strand respectively. Hence, the fibre mesh can bear tensile stress both in longitudinal and latitudinal directions. Apart from the intrinsic superiority of FRP, the special net structure brings more advantages than those conventional structures, along with a more flexible application to construction industry. It becomes practical to design and produce high strength but lightweight concrete structures such as thin-walled sandwich panel or slender shell (Shams et al., 2014). A thin layer of fibre mesh is flexible in shape, thereby allowing reinforced concrete to have complex geometry or freeform profile like the curved roof with hyper-shell structure (Schumann et al., 2018). Furthermore, the adoption of textile reinforced concrete (TRC) can improve the ductility, namely a better property to resist a large deformation (Butler et al., 2009; Mesticou et al., 2017). On the other hand, if using fibre textile as the exterior strengthening or retrofitting for existing concrete members, their fatigue performance can be effectively enhanced because the utilisation of fibre textile effectively mitigates the crack propagation during fatigue cycles (Sheng et al., 2017).

Like other types of FRP reinforcement, the fabrication of fibre mesh with the common thickness ranging from 0.3 mm to 0.9 mm is based on commonly used fibre composites as well, including AFRP, BFRP, CFRP and GFRP as presented in Fig.2-9 (Jiang et al., 2019; Shi et al., 2019; Wei et al., 2020; Techbelt, 2022).

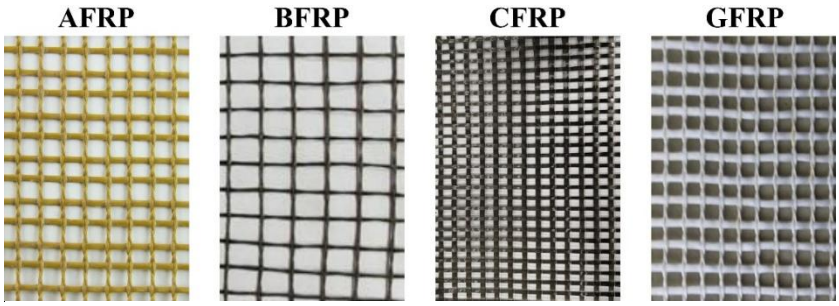

Fig.2-9 Frequently used fibre meshes in TRC (Jiang et al., 2019; Shi et al., 2019; Wei et al., 2020; Techbelt, 2022).

Benefitting from many advantages mentioned above, fibre mesh has gained popularity in engineering practice. To date, TRC has been widely applied to construction and manufacturing industry (Motavalli and Czaderski, 2007; Naaman, 2012). However, fundamental research related to TRC is still far from sufficiency to support its large-scale commercial practice (Mahboob et al., 2021). Based on the same reason, relevant codes, guidelines or regulations are not complete in this field (Donnini et al., 2019). As a result, when adopting fibre mesh as the reinforcement, there exist many uncertainties with respect to mechanical behaviour, optimum structural design, durability problem, etc. that are more likely to impede the rational design and constructing of TRC.

Fibre strand is the fundamental element in any fibre mesh. The interfacial properties between a single strand and its surrounding concrete are key for investigating the mechanical behaviour of TRC. Although there exist studies focusing on the interfacial adhesion, they usually only focus on the short-term pull-out mechanical behaviour rather

than the long-term durability (Cheng et al., 2020; Zhu et al., 2020). As a result, the lack of durability study on bond behaviour makes it difficult to assess or predict the long-term mechanical performance of TRC, particularly under harsh environments.

2.1.5 Fibre reinforcement surface treatment

It is known that fibre reinforcement material usually has a smooth surface. One of the representative problems about exploiting FRP reinforced concrete is the weakness of interfacial bonding between FRP and concrete (Lin et al., 2021). When conducting pull-out tests, interfacial debonding is a common failure mode. Many experimental studies showed that there were poor interfacial adhesion and weak mechanical interlocking at interface between the FRP and concrete (Esfandeh et al., 2009; Shrestha et al., 2015; Li et al., 2018).

Sand coating is one of the frequently used solutions to overcome the debonding problem mentioned above (Solyom and Balázs, 2020). As shown in Fig.2-10, the treatment of sand coating on FRP surface is often applied to different FRP materials including bar, mesh and strand, for enhancing the bond behaviour between FRP reinforcement and concrete substrate (Li and Xu, 2011; Donnini et al., 2018; Šenšelová et al., 2021). Fine-grained sand is a low-cost and easily accessible building material. Sand with fine particle size can be easily glued to FRP surface by means of adhesive such as epoxy resin (Solyom and Balázs, 2020). Experimental studies have demonstrated that after the introduction of sand coating on FRP surface, the bond strength at adhesive interface is significantly enhanced than those interfaces with a direct contact between smooth FRP surface and concrete substrate (Arias et al., 2012; Lee et al., 2013; Rolland et al., 2020). Arias et al. (2012) measured the interfacial shear strength between high performance concrete and GFRP bar

of 9 mm in diameter, and found that GFRP bar with smooth surface had an average bond strength nearly seven times lower than the corresponding sand coated bar, with the value of 1.47 MPa and 10.19 MPa, respectively (Arias et al., 2012). Likewise, Lee et al. (2013) used CFRP rod with smooth surface and sand coated surface to compare their pull-out force from concrete block. Their tests showed that CFRP rod after sand coating could enhance the critical pull-out force by more than five times, from 8.72 kN to 48.26 kN (Lee et al., 2013). Rolland et al. (2020) reported the similar results for GFRP rebar. Compared with the adhesive interface between concrete and smooth surface of GFRP rebar, the introduction of sand coating could provide the ultimate bond strength of 9.28 MPa at the interface, nearly five times higher than the former with 1.90 MPa (Rolland et al., 2020).

Fig.2-10 Sand coating treatment on FRP bar, mesh and strand (Li and Xu, 2011; Donnini et al., 2018; Šenšelová et al., 2021).

2.1.6 Brief summary

With the development of manufacturing technology, diverse types of fibre composite materials are produced to replace the traditional construction materials in engineering practice. The challenge that their long-term performance during service life is not clear hinders their extensive application, which has gained increasing research interests as well.

On the other hand, fibre composites acting as the reinforcement have many advantages compared with traditional steel rebar, including anti-corrosion of chloride ions and oxidation resistance. Furthermore, reinforcement made by fibre composites can have flexible structures such as bar, plate and tube. Carbon fibre textile is a relatively new type among them. It gains popularity in recent years when producing high strength but lightweight construction components such as the curved roof with hyper-shell structure.

However, there still exist many uncertainties with respect to its mechanical behaviour and structural design, especially under long-term harsh environment. Fundamental research is therefore urgently needed to facilitate the wide application of carbon fibre textile.

2.2 High performance concrete for marine applications

2.2.1 Overview of high performance concrete

Ordinary Portland cement concrete (OPC) with its mix design consisting of Portland cement, aggregate and water is one of the most frequently used building materials around the world. With the development of construction industry and the increasing demand for their working performance, OPC, however, gradually becomes less likely to meet the needs of engineering practice, particularly for those applications to strict working conditions. In order to cater for diverse demands during the practical engineering, OPC has been refined by means of changing mix design, introducing admixtures and additives, adjusting curing method, etc. With the improvement on one or several material properties, the high performance concrete (HPC) is a solution to special working conditions. Compared with the normal OPC, HPC has better material properties in one or more aspects as follows:

- High strength — By reducing water/binder ratio, the strength of concrete can be increased. The introduction of water reducer, also known as superplasticiser, can improve the flowability of fresh concrete during the mixing and promote hydration reaction. Additionally, some types of mineral admixtures such as silica fume (SF) can fill micropores inside concrete and improve its particle size gradation, thereby enhancing its mechanical behaviour containing compressive strength (Dong et al., 2020).
- Dimensional stability — In order to resist the concrete shrinkage or long-term deformation, one method is to reduce the cement content and the related paste volume by using mineral admixtures as the replacement, including PFA and GGBS (Ng and Kwan, 2016). Another method is to add expansive additive during concrete mixing, which can compensate the drying shrinkage of concrete and prevent crack from generating (Mo et al., 2012).
- Self-compacting — Concrete with a high self-compacting performance is featured as the filling ability and good flowability that help concrete fully fills moulds without vibrating. It has a strong segregation resistance as well. Self-compacting concrete can generally be produced by using proper admixtures and additives. For example, the usage of water reducer enhances its flowability. Aggregates possessing a continuous grading of particle-size distribution are also the important contributing factor (Skarendahl and Petersson, 1999).
- High durability — Concrete with high durability means a better long-term behaviour when working in severe environments due to chemical attacks, freeze-thaw cycles and even microbial activities. According to different hostile conditions, many ways are developed to improve its durability. As an illustration, replacing partial Portland cement by PFA or GGBS can obviously enhance its durability performance under marine environments (Swaroop et al., 2013). The adoption of dry-shake hardener as

the admixture for concrete is able to enhance its wear resistance (Mardani-Aghabaglou et al., 2021).

- Anti-penetration — Concrete that has a good performance of anti-permeability is more likely to provide a better protection for the interior reinforcement when it serves as the cover layer. Reducing water/binder ratio and the introduction of mineral particles as supplementary cementitious materials, such as marble powder, are effective ways to strengthen the anti-permeability property of concrete (Calvo et al., 2019).
- Low hydration heat — Hydration heat is detrimental to concrete casting and curing, particularly for those mass concrete structures. The adoption of supplementary cementitious materials such as PFA and GGBS to substitute a proportion of Portland cement helps decrease hydration heat. A mix design by using low water/binder ratio can also lessen the release of hydration heat (Zhang et al., 2002).

2.2.2 Eco-friendly alternatives for constituents of concrete applied to marine constructions

Although normal Portland cement has many advantages as the active cementitious ingredient used in concrete, its manufacturing process inevitably brings the adverse effect on global climate changes. It is known that the emission of carbon dioxide caused by producing cement occupies 5~8% of the global emissions of greenhouse gases (Teh et al., 2017).

On the other hand, with the rapid increase in the requirement of natural sand used for concrete over last twenty years, now the global construction industry consumes 40 to 50 billion tonnes of sand every year (Cousins, 2019). Consequently, there is a global shortage in the supply of sand (Kim et al., 2012).

Taking above mentioned into consideration, it is therefore necessary for construction industry to explore eco-friendly and sustainable substitutes for conventional concrete components. Those substitutes include PFA, GGBS and SF as shown in Fig.2-11.

(a) (b) (c)

Fig.2-11 Eco-friendly and sustainable substitutes: (a) pulverised fuel ash; (b) ground granulated blast-furnace slag; (c) silica fume.

2.2.2.1 Pulverised fuel ash

Pulverised fuel ash, also called as fly ash, is a frequently used supplementary cementitious material. It can react with water, namely the hydration reaction during the hardening process of concrete. Generally, it is characterised as small powdered particles with the colour of light or dark grey, as shown in Fig.2-11a. The particle size of PFA ranges from 0.3 to 250 μm (Li et al., 2014). As an eco-friendly material, it is collected from the emission of flue gases when traditional thermal power plants burn coal to generate electricity. The chemical composition of these fine particles mainly consists of SiO_2, Al_2O_3 and Fe_2O_3 (Ismail et al., 2007). The direct emission of flue gases full of PFA powder would not only pollute natural environments but also cause damage to human health. However, once PFA is filtered and captured from coal combustion residuals, it turns a valuable product used for the replacement of cement. Similar to Pozzolan, PFA is active during hydration reaction and forms cementitious compounds. Moreover, if PFA

is used as partial replacement of cement in concrete mix design, it is beneficial to the long-term hydration process of Portland cement (Feng et al., 2018).

PFA as the supplementary cementitious material is beneficial to concrete in many ways. One important contribution of PFA to concrete is the capacity to retard the diffusion and penetration of chloride ions in concrete (Liu et al., 2020). This is because the use of PFA in concrete can reduce the permeability of the concrete after its hardening. Furthermore, it is also demonstrated that the partial replacement of cement by using PFA can increases the compressive strength and flexural strength of concrete after the early age of curing (Feng et al., 2018). Meanwhile, using PFA can effectively lessen the hydration heat during concrete casting (Matos et al., 2020). In view of those contributing factors, PFA are widely used in the field of underwater engineering, especially for those mass concrete structures applied to marine constructions.

2.2.2.2 Ground granulated blast-furnace slag

Ground granulated blast-furnace slag is another eco-friendly alternative acting as the supplementary cementitious material in concrete. The physical appearance of GGBS is featured as fine powder with white or light grey colour, as shown in Fig.2-11b. GGBS has a high specific surface area ranging from 400 to 500 m^2/kg, with the average particle size of 9.2 μm (Divsholi et al., 2014; Ishak et al., 2017). In general, GGBS is the by-product when using blast furnace to smelt iron and steel. Although the glassy granules can be directly gathered from rapidly chilling molten iron slag, they need to be further dried and ground until those granules turn into fine powder completely, namely GGBS. The chemical composition of GGBS mainly consists of CaO, SiO_2 and Al_2O_3 that occupy more than 90% of all ingredients (Siddique, 2014). Like PFA, GGBS is the active

admixture used in concrete and thus is able to participate in the hydration reaction coupled with Portland cement. If introducing GGBS into the mix design, the initial hydration rate may be slower than the concrete that only uses cement as binder. However, GGBS can react with $Ca(OH)_2$ stemming from the hydration product of cement. Such a process is called secondary hydration reaction which further promotes the hydration of cement and thereby produces more cementitious gels of C-S-H (Dai et al., 2019).

The adoption of GGBS as the supplementary cementitious material can refine the concrete properties in many respects. One of the major functions of GGBS used in concrete is to reduce the chemical attacks induced by sulphate present in the ambient conditions, particularly in seawater environments (Suresh and Nagaraju, 2015). The usage of GGBS to replace a portion of cement decreases the content of $Ca(OH)_2$ and tricalcium aluminate ($Ca_3Al_2O_6$) in concrete, which are prone to react with sulphate ions and then generate ettringite (Qiao and Chen, 2019). By retarding the generation of ettringite, GGBS prevents the concrete from suffering internal stress and subsequent expansion-induced cracking owing to the expansive nature of the reaction products. In this way, concrete incorporated with GGBS is able to withstand the sulphate attack, which is particularly important when the concrete is exposed in marine environments. In addition, both the research and practice suggest that using GGBS can improve the workability of fresh concrete (Saranya et al., 2018).

2.2.2.3 Silica fume

Silica fume is also a frequently used binder material for concrete constituents, as shown in Fig.2-11c. It has another name as microsilica. SF is characterised as an ultrafine powder that belongs to the amorphous polymorph of SiO_2. Generally, SF comes from the by-

product during the smelting of ferrosilicon alloys, or more specifically, the collection of suspended SiO_2 powder full of industrial flue gases when using industrial furnace to smelt silicon and ferrosilicon materials. Compared with other components used in concrete, SF is featured as the extremely small particle size within the fluctuation between 100 nm and 200 nm (Pacheco-Torgal et al., 2018). As a superfine material, SF powder has a high specific surface area of 20 m^2/g (Pacheco-Torgal et al., 2018). Such a high specific surface area coupled with a high content of SiO_2 makes SF process pozzolanic properties with huge reactive surfaces.

As investigated by Lü et al. (2019) who used SF to replace 16% of cement in the concrete mix design, SF can increase the strength of hardened concrete by 38% and increase its anti-permeability by 63 times, because SF fills the interspace inside concrete structure and decreases the concrete porosity. Due to the fact that the particle size of SF is much smaller than ordinary Portland cement, the interspace among cement particles tends to be filled by the finer powder of SF, and thus forms a close compacting structure (Zhang et al., 2018). On the other hand, concrete blended with SF has a better performance to resist the alkali-aggregate reaction because the dispersed SF consumes alkaline ions in concrete and thereby inhibit the alkali-aggregate reaction between those alkaline ions and natural aggregate (Tavares et al., 2020). Meanwhile, concrete blended with SF has a lower hydration heat than the concrete only uses normal Portland cement. SF contributes to the improvement on abrasion resistance of concrete as well (Rashad et al., 2014). Overall, SF is a good eco-friendly admixture for concrete to enhance the mechanical properties and long-term durability.

2.2.2.4 Sea sand

As mentioned above, the insufficiency of natural sand resource becomes more serious with the development of construction industry. Moreover, the process of sand mining has the destructive effect on river bed and thus causes great damage to natural environments, as demonstrated in Fig.2-12 (Ako et al., 2014). Sea sand, as the replacement for river sand, has attracted a lot of interest from engineering practice, particularly for those located near the coastline.

Fig.2-12 The destruction of river ecosystem due to sand mining (Ako et al., 2014).

Direct utilisation of sea sand is prohibited for casting steel reinforced concrete structures due to its involvement of chlorides (Dong et al., 2018). Conventionally, sea sand has to be thoroughly washed by using freshwater to remove mineral salts before being used in reinforced concrete structures (Xiao et al., 2017). However, if FRP reinforcement is used this problem can be avoided because FRP does not have corrosion problem. Extensive research has been carried out recently on sea sand concrete structures reinforced by FRP materials (Xiao et al., 2017).

Compared with traditional river sand or manufactured sand like crushed rock, the relatively low economic costs can be considered to be another benefit of exploiting sea sand, particularly for marine applications. For one thing, with the consumption of river

sand existent in nature, the costs of extracting river sand climb year by year, which is higher than easily available sea sand. Moreover, the costs of long-distance transport could be saved if local sea sand is applied to the construction.

2.2.2.5 Seawater

Like sea sand, seawater cannot be used in traditional steel reinforced constructions. However, it has been found that concrete cast with seawater, namely seawater concrete, can hardly cause damage to FRP reinforcement (Xiao et al., 2017). Unlike steel reinforcement, FRP materials have an excellent electrochemical resistance and thus steadily keep their material properties under ambient conditions full of salt solution (Xiao et al., 2017). Therefore, it is an eco-friendly and economical choice for FRP reinforced concretes to use seawater as the substitute for freshwater, especially for coastal and marine applications.

2.2.3 FRP reinforced concrete under marine environment

Compared with ordinary terrestrial environments, marine environments have high requirement to the quality of concrete materials. This includes:

- Low permeability — Concrete with low permeability can not only prohibit the penetration of harmful ions that corrode the interior steel reinforcement of concrete, but also retard the free migration of water molecules which are more likely to damage the adhesion bond between reinforcement and concrete substrate (Shrestha et al., 2015).

- Corrosion resistance against salty solution — If concrete structures are directly subjected to seawater for a long time, it is inevitable that diverse categories of mineral salts dissolved in seawater intrude into the interior of concrete in the form of ions. Thus, alkali reactive aggregates are not recommended to use in marine concretes.
- Abrasion resistance — Concrete structures located at oceanic regions have to resist long-term abrasion and erosion stemming from seawater in terms of stormy waves. Therefore, marine concretes should have good abrasion resistance to keep the structural integrity during their service life.
- Anti-fatigue-fracture property — Marine concretes suffer cyclic loading from wave and wind, so good fatigue resistance is preferable.
- Long-term durability performance — Unlike inland structures, marine concrete materials should be durable under wet-dry and freeze-thaw cycles coupled with temperature changes, especially for those applied to splash or intertidal zones.
- Resistance to biological attack — Marine microorganisms widely exist in seawater and they are prone to diffuse into the interior of concrete through the porous microstructure of concrete. Microbial activities release hydrogen sulphide (H_2S) which finally converts into sulfuric acid (H_2SO_4) under marine condition. H_2SO_4 would gradually dissolve carbonates inside concrete, leading to the concrete deterioration including strength loss and volumetric expansion (Monteny et al., 2000).

Apart from above-mentioned requirements specifically for coastal and marine applications, modern construction industry also present higher demands on concrete materials than before, particularly for those involving mass concrete, innovative architecture or tough working conditions. Overall, those requirements include high mechanical strength, good workability of fresh concrete, low hydration heat, long-term volume stability, etc.

Compared with marine environments, the usage of fibre reinforcement does not give additional requirements on concrete properties. On the contrary, the introduction of fibre reinforcement to replace conventional steel reinforcement in concrete can remove some limitations on the concrete mix design, in particular on the chloride content requirement.

However, it is suggested that the concrete with high mechanical strength is more favourable to the efficient utilisation of fibre reinforcement materials (Pan and Leung, 2007; Godat et al., 2012; Godat et al., 2021). As fibre reinforcement is featured by its high tensile strength, long fibre reinforced concrete (FRP reinforced concrete or TRC) is more susceptible to the debonding failure at interface rather than the tensile rupture of reinforcement (Pan and Leung, 2007; Godat et al., 2012; Godat et al., 2021). In order to utilise the high mechanical strength of fibre materials, the interfacial properties should be improved. It has been proved that the strength of adhesive bonding is largely dependent on the tensile strength at concrete surface (Pan and Leung, 2007). The growth in concrete tensile strength is able to strengthen the bond property (Pan and Leung, 2007). Existing studies also indicate that the increase in concrete compressive strength is obviously beneficial to improve interfacial bond behaviour (Godat et al., 2012; Godat et al., 2021). Hence, for the same use of fibre reinforcement the high strength concrete would be better than ordinary concrete in terms of their global structural performance.

The aggregate size should also be considered if multiple layers of fibre reinforcement are used in concrete. Coarse aggregates with too big size which exceeds the fibre mesh size of 20 mm would affect the compatibility of concrete and lead to the poor concrete quality (Halvaei et al., 2020), because such coarse aggregates would be difficult to pass through the narrow fibre mesh during casting and thus could not be distributed among the

structural member evenly, especially when the structural member is reinforced by multiple layers of fibre mesh or textile (Ahmed and Ferhadi, 2016).

Taking those aforementioned into consideration, various mix designs have been developed for marine concretes, which are summarised in Table 2-1 and Table 2-2.

Table 2-1 Summary of mix designs applied to FRP reinforced concrete.

references	ratio of cementitious materials (%)				w/b (%)	concrete mix ratio (kg/m^3 or L/m^3)				
	C	PFA	GGBS	SF		binder	sand	gravel	water	WR
Triantafillou (2016)	67	30	—	3	30	822	1092	—	246	19.3
Triantafillou (2016)	30	65	—	5	40	700	1140	—	280	6.3
Kostova et al. (2013)	50	—	50	—	48	400	1150	770	190	—
Kostova et al. (2013)	80	—	20	—	48	400	1150	770	190	—
Benzecry et al. (2021)	80	20	—	—	38	404	728	979	152^S	0.63
Benzecry et al. (2021)	48	—	52	—	40	442	793	838	178	0.41
Won et al. (2008b)	75	15	—	10	22	727	581	865	160	16.7
Zeng et al. (2022)	72	18	—	10	19	899	617^S	1008	171^S	18
Lim and Ozbakkaloglu (2014)	84	—	—	16	52	450	710	1065	235	1.5
Zhang et al. (2021)	—	15	80	5	49	420	567^S	1260	206^S	—
Younis et al. (2020)	35	—	65	—	37	450	750^S	1190	165^S	4.46^L
Liang and Yin (2021)	70	30	—	—	38	714	626^S	467	271^S	6.23
Liang and Yin (2021)	70	—	30	—	38	714	626^S	467	271^S	6.23
Khayat and Meng (2014)	48	—	48	4	13	1138	1018	—	146	69.5^L
Khayat and Meng (2014)	52	—	48	—	15	1139	1002	—	174	54.2^L
Khayat and Meng (2014)	76	—	—	24	20	943	1231	—	189	29.2^L
Al-Hamrani et al. (2021)	65	15	—	20	37	400	750	1114	149	4.5

Note: (1) Cement is denoted by "C". (2) Water reducer is denoted by "WR". (3) Sea sand and seawater are labelled the superscript of "S"; if without "S", they denote normal building sand and freshwater, respectively. (4) w/b symbolises the ratio of water to binder. (5) The unit of water reducer can be both kg/m^3 and L/m^3 according to the specific references; when using L/m^3, it has the superscript of "L".

Table 2-2 Summary of mix designs for concrete subject to marine exposure.

references	ratio of cementitious materials (%)				w/b (%)	concrete mix ratio (kg/m^3 or L/m^3)				
	C	PFA	GGBS	SF		binder	sand	gravel	water	WR
Katano et al. (2013)	50	—	50	—	50	340	794^S	985	170^S	0.85
Katano et al. (2013)	45	—	45	10	50	338	782^S	985	169^S	0.85
Liu et al. (2021)	77	7	8	8	29	500	691	1177	145	11
Liu et al. (2021)	66	10	7	17	25	580	662	1128	145	14
Li et al. (2009)	37	20	40	3	35	437	689	1035	153	7.87
Saleh et al. (2019)	67	—	33	—	17	1200	1000^S	—	204^S	24
Saleh et al. (2019)	50	—	38	12	20	1200	1000^S	—	240^S	24
Li et al. (2013)	80	20	—	—	40	340	754^S	1180	136^S	3.4
Li et al. (2013)	70	30	—	—	35	488	593^S	1159	170^S	3.4
Preez and Alexander (2004)	93	—	—	7	54	364	762	1200	195	1.19^L
Patil and Dwivedi (2022)	50	25	25	—	36	460	817	1072	168^S	3.69
Patil and Dwivedi (2022)	50	20	30	—	36	460	820	1076	168^S	3.69
Sang et al. (2022)	55	18	27	—	28	550	662^S	993	155	4
Sang et al. (2022)	32	36	32	—	28	550	679^S	1072	155	3.5
Benli et al. (2017)	84	10	—	6	44	650	1176	—	286	8
Memon et al. (2002)	30	25	40	5	40	420	590	1220	170	1^L
Zhou et al. (2022)	95	—	—	5	33	525	562^S	1142	173^S	4.56
Dave et al. (2017)	50	30	10	10	38	440	603	1270	167	2.64
Liao et al. (2022)	72	18	—	10	19	899	617^S	1008	171^S	18

Note: (1) Cement is denoted by "C". (2) Water reducer is denoted by "WR". (3) Sea sand and seawater are labelled the superscript of "S"; if without "S", they denote normal building sand and freshwater respectively. (4) w/b symbolises the ratio of water to binder. (5) The unit of water reducer can be both kg/m^3 and L/m^3 according to the specific references; when using L/m^3, it has the superscript of "L".

As shown in Table 2-1 and Table 2-2, admixtures including PFA, GGBS and SF are often used to substitute a proportion of cement, and multiple admixtures are usually used together as the superposition of different admixtures with a proper ratio that can further optimise the physical structure of cementitious matrix and enhance the concrete performance (Gesoğlu et al., 2009; Guo et al., 2021). Apart from admixtures, Table 2-1 and Table 2-2 suggest that sea sand and seawater can be freely introduced to FRP reinforced concrete mix design, because their unfavourable effects on reinforcement or concrete can be effectively avoided.

2.2.4 Brief summary

The rapid development of modern construction industry especially under harsh environment puts forward higher demands on the working performance of concrete materials. To meet those requirements, HPC is introduced into engineering with various advantages such as high strength and enhanced durability exposed to seawater. During its production, eco-friendly admixtures like PFA and GGBS can be introduced into the mix design to improve its material properties in one or more aspects. Once FRP reinforcement replaces traditional steel rebar, sea sand and seawater can be utilised in the mix design because the corrosion problem due to chloride ion is negligible for fibre composites.

The present study adopted CFS from carbon fibre textile as the reinforcement while seawater, sea sand and multiple admixtures were used in the mortar casting. As existing studies had not investigated its performance yet, the present study needed to test its basic material properties first, before carrying out the research on the durability of interfacial bond between CFS and mortar used herein.

2.3 Degradation of fibre composites reinforced concrete along with its ageing behaviour

2.3.1 Overview of degradation in fibre composites reinforced concrete

Durability in regard to diverse types of FRP (including fibre mesh) materials used in concrete structures have aroused wide concern both in scientific research and engineering practice since 1980s when the viability and superiority of FRP composites replacing the traditional steel material in the construction industry were gradually recognised (Rizkalla et al., 2003; Balaguru et al., 2008; Imani et al., 2010; Lu and Ayoub, 2011). To date, the ageing behaviour of FRP reinforced concrete has been investigated in a number of studies, but no consensus has been reached owing to the different materials used in the tests, sample shapes, testing methods and evaluation indicators (Mumenya et al., 2010; Kafodya et al., 2015; Portal et al., 2016; Al-Lami et al., 2020). Some key affecting parameters have been summarised in the following sections.

2.3.2 Effect of fibre types on ageing behaviour

AFRP, BRRP, CFRP and GFRP are all commonly used with concrete substrate, but their ageing behaviour vary considerably from type to type due to different chemical composition involved (Sonnenschein et al., 2016; Li et al., 2019).

AFRP employs aramid fibre as the reinforcement. The major ingredient of aramid fibre is aromatic polyamide. It is not only susceptible to ultraviolet radiation that can deteriorate its chemical structure but also sensitive to moisture due to the hydrolysis reaction occurring at its macromolecular chains (Derombise et al., 2010; Sonnenschein et al., 2016). While AFRP is embedded in concrete, the deterioration by ultraviolet radiation is considered mild compared with the moisture ageing because the water molecules stemming from the concrete pore solution can continuously degenerate AFRP reinforcement especially when the concrete stays a moisture saturation condition (Wu et al., 2016; Oguz et al., 2021). According to the chemical structure of aramid fibre, such an ageing process can be illustrated by Fig.2-13 (Derombise et al., 2010).

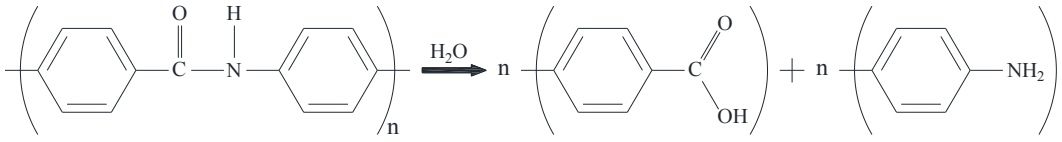

Fig.2-13 Aramid fibre degeneration subject to moisture (Derombise et al., 2010).

BFRP employs basalt fibre as the reinforcement. Basalt fibre is fabricated from natural basalt with pultrusion technology (Lu et al., 2015). Like basalt rock, basalt fibre is aluminosilicate fibre, mainly composed of oxides such as SiO_2, Al_2O_3, Fe_2O_3, etc. (Shi et al., 2020). It is prone to the damage from hydroxide ions present in the concrete pore solution and chloride ions if BFRP reinforced concrete is applied to the seawater environments (Wang et al., 2017b; Lu et al., 2021). The existence of silicon oxide framework in basalt fibre is likely to be broken by hydroxide ion attack as shown in Eq.2-1, while ferrous ions existing in basalt fibre are expected to react with both of chloride ions and hydroxide ions as presented in Eq.2-2 and Eq.2-3, respectively (Wang et al., 2017b; Lu et al., 2021).

$$\mathrm{—Si—O—Si— + OH^- \rightarrow —Si—OH + —Si—O^-} \quad (2\text{-}1)$$

$$Fe^{2+} + Cl^{-} \rightarrow [FeCl\ complex]^{-} \quad (2\text{-}2)$$

$$[FeCl\ complex]^{-} + OH^{-} \rightarrow Fe(OH)_2 + Cl^{-} \quad (2\text{-}3)$$

GFRP employs glass fibre as the reinforcement. Glass fibre is classified into inorganic non-metallic material and its major ingredient is silica. Existing studies have proved that it is liable to ageing in alkaline environments such as concrete pore solution (Larner et al., 1976; Bashir et al., 2018). Eq.2-1 can be used to characterise glass fibre ageing as well.

CFRP employs carbon fibre as the reinforcement. The percentage of carbon content in carbon fibre is more than 90% (Frank et al., 2012). Based on its manufacturing technology, carbon atoms are intensively aligned in the crystalline structure of regular hexagon (Huang, 2009; Frank et al., 2012). Such a firm structure alignment ensures carbon fibre is impermeable and almost corrosion-free during its service life under the possible normal service conditions including acid, alkaline, salt solution and moisture (Toumpanaki et al., 2015; Raman et al., 2020; Shen et al., 2021). Thus, carbon fibre can be seen as a chemically inert material in this study. Existing studies focusing on the FRP material ageing have demonstrated the corrosion-free property of carbon fibre (Guo et al., 2018; Wang et al., 2018; Bazli et al., 2020). Compared with basalt fibre or glass fibre, carbon fibre is able to keep its integrity to a full extent after ageing conditioning, as no visible corrosion pitting or etching can be found on its surface (Guo et al., 2018; Wang et al., 2018; Bazli et al., 2020).

According to the research results reported in the literature, carbon fibre has a higher performance of electrochemical resistance than other types of fibres and thus FRP composites made up by carbon fibre have a better durability performance, especially when exposed to harsh environment. Likewise, ageing phenomenon is unlikely to happen

on the carbon fibre embedded in concrete. Focusing on marine environment, carbon fibre composite was thus selected to reinforce the mortar in the present study.

However, existing literature listed here cannot proves that CFRP reinforced concrete is fully corrosion-free when exposed to marine environment. The polymer matrix that bonds fibre together and the adhesive interface between FRP and concrete would be subject to damage from those ageing environments and consequently may have macroscopic ageing degradation such as the decrease in the material mechanical performance (Alessi et al., 2014; Cui et al., 2021). The degradation mechanism of polymer under marine environment will be further discussed in Chapter 3.

2.3.3 Effect of concrete types on ageing behaviour

The exploitation of FRP materials widens the use of concrete raw materials that have been prohibited in conventional steel reinforced concrete products. However, different concrete may differ the ageing behaviour of FRP reinforced concrete. Three typical concrete types, i.e. normal OPC with its cementitious binder fully based on normal Portland cement, HPC and SWSSC, are discussed in this section.

In addition to normal OPC that has been commercially used in the FRP (including fibre mesh) reinforced structures since 1980s (Nanni et al., 2014), HPC has attracted a lot of interest in recent years as the combination of FRP and HPC can better utilise the material strength of both components (Tayeh et al., 2019; Wyrzykowski et al., 2020). As HPC usually replaces a portion of normal Portland cement with pulverised fuel ash, ground granulated blast furnace slag and silica fume (Kim et al., 2012), the alkalinity of HPC pore solution can decline considerably compared with normal OPC (Ahmed et al., 2020).

If the concrete pore solution has a relatively low alkaline concentration, basalt and glass fibre reinforcements are less likely to be attacked by hydroxide ions and thus show a better durability performance, while carbon fibre is barely affected by the alkalinity of concrete pore solution as discussed in Section 2.3.2. Although the usage of normal OPC or HPC does not deteriorate the long-term performance of carbon fibre itself, a high alkaline condition is still able to damage the polymer matrix and the adhesive interface, which plays an important part in the ageing behaviour of FRP reinforced concrete (Won et al., 2008a; Wang and Petrů, 2019).

SWSSC is a new type of concrete used together with FRP reinforcement. Compared with the conventional concrete using freshwater and river sand in the mix design, SWSSC due to the use of seawater and sea sand has high chloride ions content with 3.2 kg/m^3 in the concrete (Teng et al., 2019). It is well known that chloride ion is detrimental to steel reinforcement due to its acid nature, but no consensus has been agreed on its influence to the ageing behaviour of FRP reinforcement (Wang et al., 2017b; Ahmed et al., 2020). Based on the rather limited studies that have been found on the long-term durability of FRP reinforced SWSSC, CFRP reinforced SWSSC is usually reported to have a better durability performance than other types of FRP reinforced SWSSC (Li et al., 2018; Wang et al., 2018; Bazli et al., 2020). For example, Bazli et al. (2020) found that after 180 days of 60 °C ageing conditioning in SWSSC pore solution, the retention of hoop tensile strength for CFRP tube used to fill SWSSC is 48.3%, higher than GFRP and BFRP by 17.6% and 23.2%, respectively.

When HPC is utilised as the concrete substrate for FRP reinforcement, the relatively low alkalinity of the pore solution present in concrete is beneficial to the protection of the FRP reinforcement. In the meantime, seawater and sea sand can be introduced into the concrete

mix design as well. Additionally, owing to the intrinsic property of chemical inertness, carbon fibre is deemed to be durable working in HPC combined with sea sand and seawater. Based on the existing research (Toumpanaki et al., 2015; Guo et al., 2018; Li et al., 2018; Wang et al., 2018; Bazli et al., 2020; Raman et al., 2020; Shen et al., 2021), the carbon fibre itself hardly contribute to the ageing of CFRP reinforced concrete.

According to the literature listed above, HPC has a better durability performance exposed to marine environment than OPC does and it can also provide a better protection for FRP reinforcement embedded inside. Therefore, it is rational for the present study to use the mortar with the similar mix design of HPC when prepare CFSRM specimens. However, the basic mechanical properties of the mortar following this technology need to be experimentally tested, especially when sea sand and seawater are introduced into its mix design, as their effects on the bond behaviour between CFS and mortar remains unclear.

2.3.4 Effect of sample shapes, structures and testing approaches

A wide variety of FRP reinforcement types have been used in reinforced concrete, including bar, plate, tube and mesh. Depending on the different structural types and applications, they may present diverse ageing behaviour. In order to effectively evaluate the deterioration in their mechanical properties, tensile, compressive, bending, pull-out and pull-off tests are commonly used.

The tensile tests are usually conducted to study the long-term durability if the mechanical behaviour is dominated by the fibre tensile properties, such as the textile reinforced concrete plates or FRP laminate. Munck et al. (2018) treated GFRP reinforced laminate with heat-rain cycles and tested the tensile strength after treatment, as shown in Fig.2-14.

According to the test results, the authors found that the laminate tensile strength was reduced by 42% after the ageing conditioning, and the obvious damage caused by the ageing process could be observed on the surface of glass fibre reinforcement (Munck et al., 2018). Similar findings of tensile ageing behaviour were also reported based on glass fibre textile reinforced plate by Santis and Felice (2015) as well as Butler et al. (2010). However, such an ageing phenomenon is not obvious for CFRP reinforced plate. Spelter et al. (2019) immersed CFRP reinforced plate into 60 °C water over 6000 hours (250 days) but did not find the tensile strength reduction after the ageing treatment. The enduring tensile performance of CFRP reinforced concrete is attributed to the integrity of carbon fibre during the ageing process, because the mechanical property of tensile resistance is mainly determined by fibre reinforcement (Weitsman, 2012; Kafodya et al., 2015; Heshmati et al., 2016; Benmokrane and Ali, 2018).

Fig.2-14 Tensile test of a plate sample after ageing treatment (Munck et al., 2018).

If the ageing behaviour of sample is mainly dominated by the polymer matrix and the interfacial bonding, shear strength is a quantitative indicator conventionally used in the durability research (Weitsman, 2012; Kafodya et al., 2015; Heshmati et al., 2016; Benmokrane and Ali, 2018). Various testing methods have been proposed to study the shear-stress controlled ageing behaviour of FRP reinforced concrete, one of which is the pull-out test. It is usually adopted to test a FRP bar or rod embedded in cubic or cylindrical concrete substrate.

Fig.2-15 shows the FRP bar pull-out test carried out by Nepomuceno et al. (2021). Belarbi and Wang (2012) used the same method to study the CFRP bar reinforced concrete in salt water with cyclic temperature changes varying from 35 °C to 60 °C and found that the pull-out strength was reduced by 23% after the conditioning of 200 cycles with 160 minutes spent on each of them. Likewise, Wang et al. (2018) used the seawater immersion method at elevated-temperature of 60 °C and 80 °C to rapidly age CFRP bar reinforced concrete, and found a 59% decrease in the interfacial shear resistance on the 120th day of exposure conditioning.

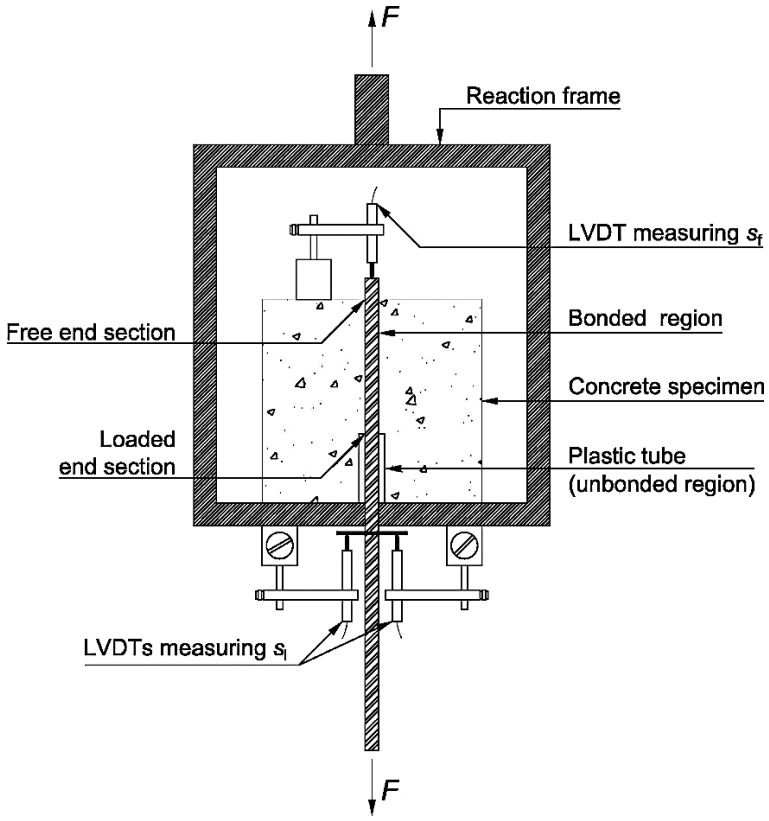

Fig.2-15 Pull-out test of FRP bar embedded in concrete block after ageing treatment (Nepomuceno et al., 2021).

Another testing approach is the pull-off test, as illustrated in Fig.2-16, which focuses on the in-plane shear bond strength between a FRP laminate and the substrate (Li et al., 2010). It is usually adopted for the durability study of thin-layer FRP laminate adhering to concrete surface. In compliance with this testing approach, the test results from Pan et al. (2015) revealed that the average value of the maximum shear force acting upon the FRP layer/concrete interface dropped to 67% after immersing in 50 °C water over two weeks.

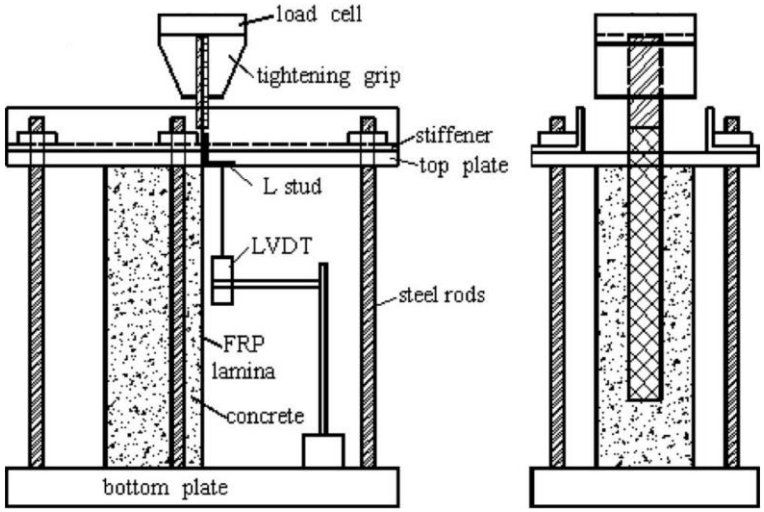

Fig.2-16 Pull-off test of FRP laminate adhering to concrete surface after ageing treatment: (a) lateral view; (b) front view (Li et al., 2010).

Tatar and Hamilton (2016) have carried out three-point bending tests to study the ageing behaviour of FRP reinforced beam as shown in Fig.2-17. FRP located at the tensile region of the beam carries both tensile force and interfacial shear force between FRP and concrete. Therefore, the bending resistance deterioration subject to the ageing environment can be attributed to not only the fibre or polymer itself, but also the FRP/substrate interface (Marouani et al., 2012; Tanks et al., 2017). Similarly, by conducting bending test, Dong et al. (2018) indicated that BFRP bar reinforced concrete beam had an obvious ageing behaviour as the maximum load applied to the beam fell by 21% after immersing in 50 °C seawater for nine months. In addition, the crack spacing during loading became wider with the increase of ageing duration, implying the interfacial bond strength degradation (Dong et al., 2018). Similar ageing behaviour was also found by Silva et al. (2013) who used CFRP strip as the external strengthening of the beam. After hygrothermal accelerated ageing in saline water over 3000 hours (125 days), the maximum shear force that the CFRP strip/concrete interface could sustain was reduced to 81% (Silva et al., 2013).

Fig.2-17 Bending test of FRP reinforced beam after ageing treatment (Tatar and Hamilton, 2016).

FRP tubes have been targeted to investigate the ageing behaviour as well. As shown in Fig.2-18, Eid and Paultre (2017) carried out experimental work to investigate the effect of ageing on the confinement of FRP tube to strengthen concrete columns. Similarly, Bazli et al. (2020) investigated the ageing behaviour of concrete-filled CFRP tube, and found that the compressive strength retention was 62% after six months of ageing conditioning, which was caused by the interface degradation between the exterior CFRP constriction and the interior concrete column while no damage was found on carbon fibre itself.

Fig.2-18 Axial compression test of FRP-confined reinforced concrete column after ageing treatment (Eid and Paultre, 2017).

Long-term degradation behaviour studies have been carried out on various types of FRP reinforced structures such as plate and beam, with different test methods. According to the existing research reports listed above, it can be found that unlike AFRP, BFRP or GFRP reinforced concrete materials, the ageing treatment of CFRP reinforced concrete hardly lead to the physical damage or mechanical property degradation of carbon fibre itself. Under the circumstance, the interfacial deterioration between the fibre reinforcement and the concrete substrate is deemed to be the major contributing factor that controls the ageing behaviour of CFRP reinforced structures.

2.3.5 Brief summary

The degradation behaviour of fibre composites reinforced concrete has raised wide concern both in scientific research and engineering practice. Compared with AFRP,

BFRP or GFRP, CFRP is found to have a better durability performance when serving as the reinforcement in concrete. On the other hand, HPC can provide a better protection for FRP reinforcement than OPC does. Above-mentioned conclusions can be found from relevant tests with diverse types of FRP reinforced structures such as plate and beam.

However, while many studies have been carried out on the ageing behaviour of conventional FRP reinforcement materials embedded in concrete, no research has been found on the durability performance of CFSRM composite material used in the present study under marine environments. In order to promote the use of such a new construction material, its ageing behaviour, especially when applied to marine environments, needs to be better understood.

2.4 Long-term durability prediction model

2.4.1 Overview of existing prediction models

The long-term durability performance needs to be well understood before a new material is applied to the construction industry, particularly under harsh conditions such as seawater immersion. Focusing on various FRP composite materials, many prediction models have been proposed so far. However, methodologies used in those models are diverse from each other. General consensus has not been achieved, leading to the prediction results varying considerably (Carra and Carvelli, 2015). The research on long-term properties of FRP reinforced concrete structures is still insufficient and thus makes it challenging to conduct a valid durability assessment. Among all the prediction models mentioned hereinafter, Arrhenius Law is the fundamental theory. Arrhenius Law, also

known as Arrhenius Equation as expressed by Eq.2-4, describes the relationship between reaction rate and reaction temperature:

$$k = Aexp\left(\frac{-E_a}{RT}\right) \quad (2\text{-}4)$$

where k is the reaction rate constant with the unit in s^{-1} or d^{-1}; A is generally called pre-exponential factor or frequency factor, which is a dimensionless temperature-independent constant and indicates the effective molecular collision frequency during a certain reaction; E_a is the apparent activation energy for the material and reaction type with the unit of $J \cdot mol^{-1}$ or $kJ \cdot mol^{-1}$, which indicates the minimum energy per mole of molecule needed for the reaction to occur and is also temperature independent; the higher the E_a, the harder a reaction occurs and progresses; R is the universal gas constant, which is 8.314 $J \cdot mol^{-1} \cdot K^{-1}$; and T is the absolute temperature with the unit of K.

Arrhenius Law was first proposed by Svante Arrhenius in 1889 and has been widely used in many scientific fields including mass diffusion, chemical reactions, creep relaxation and long-term material degradation (Tant et al., 1995; So et al., 2014; Zhang et al., 2015). It is known that the long-term changes in material properties at the micro level can be seen as the consequence of the thermal motion along with the interaction of molecules that constitute the material (Ito and Nagai, 2007; Kovalenko and Dobryakov, 2013). However, the molecular motion cannot be used to describe the macroscopic changes in material properties directly. As the thermal motion of molecules is temperature-dependent, Arrhenius Law explains the correlation between molecular motion and the variations in macroscopic material properties in terms of the reaction temperature, thus making it possible to calculate the macroscopic rate of physical or chemical changes based on the ambient temperature.

Taking that thermal motion of molecules is responsible for the degradation in macroscopic performance of FRP reinforced concrete (Lu et al., 2021), the theoretical long-term behaviour of FRP reinforced concrete could be derived from the short-term accelerated experiments based on the Arrhenius Law (Chen, 2007). By applying Arrhenius Law, it is assumed that the temperature change only affects the ageing rate of material properties rather than the degradation mechanism itself (Davalos et al., 2012b; Spelter et al., 2019). Therefore, E_a is independent of temperature (Moelwyn-Hughes, 1936; Robert et al., 2010), and as by definition it corresponds to a reaction mechanism.

2.4.2 Prediction Model I

Based on a large amount of ageing testing data about glass fibre reinforced concrete, Litherland et al. (1981) were the first to find out that there was a linear relationship between the retention of the composite material strength property and the logarithmic ageing duration. In accordance with this relationship, Bank et al. (2003) further developed an Arrhenius Law-based durability prediction model to characterise the FRP material performance reduction over time as shown in Eq.2-5. It is called Prediction Model I hereinafter.

$$Y = a\log(t) + b \tag{2-5}$$

where Y is defined as the retention of material properties; t is the ageing period; a and b are fitting coefficients for the model.

Although Prediction Model I has proved its viability to the durability study of FRP mechanical properties such as tension and creep (Robert et al., 2009; Robert and Benmokrane, 2013; Spelter et al., 2019), the experimental results from Oncu (2003) and Wu et al. (2015) indicate that the mechanical behaviour degradation curves derived from

Prediction Model I with different temperatures are not parallel to each other, which implies an obvious confliction to the basis of Arrhenius Equation.

Although Serbescu et al. (2015) refined Prediction Model I by defining a linear relationship with the logarithm of Y versus the logarithm of t, as presented in Eq.2-6, such a prediction model still stays at the level of phenomenological research directly based on experimental data and thereby lacks broad applicability to other materials or sample shapes (Davalos et al., 2012b; Wang et al., 2017b).

$$\log(Y) = a\log(t) + b \tag{2-6}$$

2.4.3 Prediction Model II

Focusing on the corrosion deterioration of GFRP in concrete pore solution, Purnell et al. (2001) first proposed a static fatigue model as shown in Eq.2-7, which is referred to as Prediction Model II,

$$Y = \frac{1}{\sqrt{1+gt}} \tag{2-7}$$

where g denotes an Arrhenius Law-based function of two variables containing the concentration of hydroxyl ions (C) and temperature (T), as presented in Eq.2-8.

$$g = \frac{k_C k_T C}{a_0} exp\left(\frac{-E_a}{RT}\right) \tag{2-8}$$

where k_C and k_T are the functions of C and T respectively, obtained from fitting test data; and a_0 is the length of initial flaw occurring on GFRP surface.

Although Prediction Model II has been used in many studies on GFRP reinforced concrete (Purnell et al., 2001; Purnell and Beddows, 2005; Butler et al., 2009), it is rarely used to evaluate the long-term behaviour of CFRP composites, because the fundamental theory

supporting Prediction Model II is the glass fibre corrosion in alkaline environments. Its ageing mechanism cannot explain the general deterioration of CFSRM specimens.

2.4.4 Prediction Model III

Prediction Model III stems from the empirical analysis of FRP material deterioration according to Prian and Barkatt (1999), as presented in Eq.2-9.

$$f = \beta t^{\alpha} \tag{2-9}$$

where f symbolises the deterioration rate; α and β are two fitting coefficients obtained from test data.

Derived from Eq.2-9, Davalos et al. (2012b) proposed Prediction Model III to characterise the relationship between the residual tensile resistance of GFRP bar and the exposure duration, as given in Eq.2-10.

$$Y = 100\left(1 - \frac{\int_0^t f\,dt}{r_0}\right)^2 = 100\left(1 - \frac{\beta t^{\alpha+1}}{(\alpha+1)r_0}\right)^2 = 100(1 - jt^{\alpha+1})^2 \tag{2-10}$$

where r_0 is the initial radius of GFRP bar; j is a model parameter explaining the ageing environmental factors and expected to vary with temperature based on Arrhenius Law.

Prediction Model III is designed to estimate the tensile property retention for FRP bar, rather than the interfacial shear performance reduction. The hypothesis of Prediction Model III is the decrease in the effective cross-sectional area of FRP bar over time, thereby causing its tensile resistance to reduce (Davalos et al., 2012b). Accordingly, it is not suitable to use Prediction Model III to study the interfacial bonding degradation.

2.4.5 Prediction Model IV

Unlike the aforementioned durability models, Prediction Model IV deems that the material degradation speed is fast at the beginning and significantly slows down over time. In other words, there is an exponential relationship between FRP material performance degradation and the exposure period. The degradation trend revealed by Prediction Model IV was first found by Phani and Bose (1986, 1987) via damage detection using ultrasonic waves. Then Chen et al. (2006) used this degradation model for describing the bonding degradation process at the interface between FRP and concrete. Based on their research findings, Prediction Model IV was finally proposed by Davalos et al. (2012b) to assess the durability behaviour of interfacial bonding, as given in Eq.2-15. The derivation of Prediction Model IV is presented by Eq.2-11 to Eq.2-14.

Defining that Y_∞ is the final retention of interfacial bonding performance with the ageing duration of infinity while the initial bonding performance is considered as 100, the chemical degradation kinetics of interfacial bonding can be expressed as Eq.2-11 in first-order reaction terms (Hukins et al., 2008; Mohanta et al., 2021).

$$-\frac{d(Y-Y_\infty)}{dt} = k(Y - Y_\infty) \tag{2-11}$$

where k is the reaction rate constant of interfacial degradation as per Arrhenius Law.

Integrating both sides of Eq.2-11 with respect to t, it yields,

$$\int -\frac{d(Y-Y_\infty)}{Y-Y_\infty} = \int k\, dt \tag{2-12}$$

Then Eq.2-12 can be transformed in terms of the logarithmic residual property excluding the final retention versus ageing period in linear scale, as given in Eq.2-13.

$$-\ln(Y - Y_\infty) = kt + b \tag{2-13}$$

where b is a constant of integration.

As the boundary condition of Eq.2-13 can be written as $Y - Y_\infty = 100 - Y_\infty$ when $t = 0$, the integration constant thus is determined as $b = -\ln(100 - Y_\infty)$.

Substituting the value of b into Eq.2-13, it becomes

$$\ln\left(\frac{Y-Y_\infty}{100-Y_\infty}\right) = -kt \tag{2-14}$$

Rewriting Eq.2-14 in exponential terms, the expression of Prediction Model IV is subsequently derived as

$$Y = (100 - Y_\infty)exp(-t/\tau) + Y_\infty \tag{2-15}$$

where $1/\tau$ is introduced to denote k by relevant references which usually defines τ as an experiment-based fitted coefficient for Prediction Model VI (Chen et al., 2006; Toumpanaki et al., 2015).

If the bonding performance retention falls to zero at the ageing period of infinity, namely $Y_\infty = 0$, the Prediction Model IV can be further simplified to Eq.2-16 (Chen et al., 2006; Wang et al., 2017b; Benmokrane and Ali, 2018).

$$Y = 100exp(-t/\tau) \tag{2-16}$$

Since Prediction Model IV was developed, it has been widely used in assessing the durability of interfacial bond behaviour and predicting the long-term deterioration in FRP materials with regard to interfacial shear performance (Davalos et al., 2012a; Benmokrane and Ali, 2018; Sang et al., 2018).

As Prediction Model IV cannot perfectly explain the bonding degradation trend over long-term exposure duration for all FRP shear test results, Tanks et al. (2017) proposed a refined model based on Prediction Model IV, as presented in Eq.2-17.

$$Y = (100 - Y_\infty)exp\left(-\gamma^\beta\right) + Y_\infty \quad (2\text{-}17)$$

where γ represents t/τ in Eq.2-15 and β is a model coefficient derived from fitting ageing test data.

The key parameter governing the prediction result of Prediction Model IV is $1/\tau$, which symbolises the Arrhenius reaction rate expression. According to Eq.2-4, $1/\tau$ is only controlled by environmental temperature and the intrinsic property of the material used in the test. However, many investigations revealed that the interfacial bonding degradation also largely depends on the concentration change in water molecules when they migrate across the interface and the polymer matrix inside FRP (Liang et al., 2019; Pan et al., 2019), which is not included in Prediction Model IV.

2.4.6 Prediction Model V

Taking into account the changes in moisture concentration during immersion conditioning, another prediction model was proposed by Papanicolaou et al. (2006), as presented in Eq.2-18. It is called residual property model (RPM) according to the author, namely Prediction Model V herein.

$$\frac{P_t}{P_0} = s + (1 - s)exp(-sM_t) \quad (2\text{-}18)$$

where P_t is the mechanical property retention; P_0 denotes the initial mechanical property; s is the ratio of finial residual property to intact property at the beginning; and M_t is the mass percentage of water absorption for test sample at an arbitrary time.

In Prediction Model V, moisture content M_t is the sole governing parameter that decides the degree of ageing within an arbitrary exposure duration. Toumpanaki et al. (2015) adopted Prediction Model V to assess the durability of CFRP shear behaviour in elevated-temperature distilled water, but found that the Prediction Model V does not provide reliable predictions for all experimental results. This is because the material degradation process would not stop after the moisture content inside the specimen reaches the maximum. Such a continuous degradation contributes to the gradually inaccurate durability assessment by Prediction Model V compared with the testing data.

2.4.7 Prediction Model VI

Prediction Model VI is an empirical method which is usually widely used in design guidelines, including ACI PRC-440.1-15 from America (American Concrete Institute, 2021), NS 3473: 2003 from Norway (Norwegian Council for Building Standardization, 2003), CAN/CSA S806 from Canada (Canadian Standards Association, 2021), JSCE-1997 from Japan (Japan Society of Civil Engineers, 1997), IStructE-1999 from UK (Institution of Structural Engineers, 1999) and CNR-DT 203/2006 from Italy (Italian National Research Council, 2006). This approach is convenient to use, because the material degradation within the service life can be quickly calculated using the environmental reduction factor given in the related specifications.

A typical prediction equation classified into Prediction Model VI is proposed by *fib* Task Group 9.3, Bulletin 40 (2007), as presented in Eq.2-19. It focuses on the tensile behaviour degradation and can be extended to other mechanical properties as well.

$$f_{fk,t} = f_{fk,1000h}/\eta_{env,t} \tag{2-19}$$

where $f_{fk,t}$ is the residual tensile property for the material exposed to a particular environmental conditioning over a certain period; $f_{fk,1000h}$ is the residual tensile property under the same ageing condition at the exposure time of 1000 hours; and $\eta_{env,t}$ is the tensile environmental reduction factor which can be expressed by Eq.2-20.

$$\eta_{env,t} = \frac{1}{\left(\frac{100-R_{10}}{100}\right)^n} \tag{2-20}$$

where R_{10} is the reduction of the material property in percentage during one logarithmic decade of conditioning; and n is the environmental influence determined by the synergy of moisture, temperature, structure size etc. Note that n is directly given by the design codes in accordance with the specifically defined environmental conditions.

As a decisive parameter in the prediction method based on Prediction Model IV, the environmental reduction factor is further explored by later studies to develop its reliability. Huang and Aboutaha (2010) proposed another definition of the reduction factor as shown in Eq.2-21.

$$\eta_E = 1 - [\Delta_1 - \rho \cdot log(DL \cdot TSF)] \cdot n_H \tag{2-21}$$

where η_E is the reduction factor; Δ_1 is the percentage of property reduction at the reference temperature during the first year; ρ is the slope of retention-time curve in double logarithmic scale; DL is the projection of design life without any environmental influence; and n_H is the degree of saturation.

Based on the research work with regard to Eq.2-21, Dong et al. (2017) modified the expression of η_E as presented in Eq.2-22.

$$\eta_E = 1 - \beta \cdot \left[\Delta_1 + \rho \cdot \log\left(\frac{DL}{\alpha \cdot TSF \cdot \eta}\right)\right] \tag{2-22}$$

where α, β and η are three correction coefficients related to experimental exposure.

After the refinement revolving around the diverse exposure conditions, the environmental reduction factors become more flexible to use in predicting the long-term behaviour in different scenarios (Huang and Aboutaha, 2010; Dong et al., 2017). However, using predetermined reduction factors is still rough and sometimes unconvincing, as the real environmental exposure is usually complicated. As a result, employing predetermined reduction factors to assess a new material durability would be questionable (Huang and Aboutaha, 2010).

2.4.8 Brief summary

The present study discussed the current prediction approaches to estimate the durability performance of FRP reinforced structures. There were six different prediction models introduced herein, all of which have been proved valid by means of the experimental records published in the relevant references.

However, each prediction model has its own limitations respectively. Prediction Model I and II stayed at the level of phenomenological research which restricted their scope of applications. Prediction Model III was suitable for the bar-shaped reinforcement but could hardly be applied to other shapes. Prediction Model IV did not consider the concentration changes in water molecules that was usually responsible for the water-induced deterioration in adhesive bonding, while Prediction Model V considered moisture as the single contributing factor to the contrary. Prediction Model VI along with the environmental reduction factors it proposed was essentially an empirical method, still rough for scientific research to predict the durability behaviour under various environments.

2.5 Summary

The literature review here introduced the FRP reinforced concrete along with its degradation behaviour under environmental conditioning. Although such a construction material attracted much attention in recent years, there is still lack of understanding, especially its long-term durability, neither from laboratory investigations nor from construction projects on account of its short application history.

The combination of fibre composite reinforcement and HPC can better utilise the material strength of both components. However, existing research is far from forming a complete system on this area. Rare studies focus on FRP reinforced concrete which possesses high performance as well as adopts seawater, sea sand and sustainable admixtures at the same time.

While a lot of durability research has been done on FRP reinforced materials exposed to severe conditioning, almost no quantitative conclusion has been reached due to the different materials used in the tests, sample shapes, testing methods and evaluation indicators. CFRP reinforced concrete generally has a better long-term performance than others when exposed to moisture environment, but the related literature has not considered carbon fibre textile reinforced concrete or mortar cast by sea sand, seawater and admixtures.

Although many prediction approaches have been proposed to estimate the durability performance of FRP reinforced structures, there are limits to their application ranges respectively, as reviewed in Section 2.4. Therefore, it is necessary for the present study

to further investigate the durability prediction method which is targeted at carbon fibre textile reinforced mortar applied to marine environment.

To sum up, FRP reinforced concrete/mortar that utilises sea sand, seawater and admixtures has superiority in construction industry compared with conventional steel reinforced materials, particularly under marine environment. Carbon fibre TRM is a new construction material belonging to the FRP reinforced material family. In order to make better use of it, more studies should be done to understand its long-term durability performance when it is exposed to marine environment.

3 DEGRADATION MECHANISMS OF TRM EXPOSED TO MARINE ENVIRONMENT

3.1 Overview

According to the literature review presented in Chapter 2, the long-term degradation of carbon fibre TRM is less likely to result from the mortar substrate or carbon fibre itself. HPC blended with the admixtures of PFA, GGBS and SF in this study has relatively low alkaline concentration in its pore solution and high corrosion resistance against seawater environments. Hence the mortar substrate adopted is unlikely to cause degradation in TRM. Likewise, carbon fibre itself proves to have the chemically inert behaviour as explained in Chapter 2. Relevant studies have suggested that the deterioration occurring in the polymer matrix that bonds carbon fibre together and the adhesive interface between fibre reinforcement and mortar are the main sources leading to the degradation. Meanwhile, moisture attack plays a key role in the long-term degradation process located in these areas.

This chapter conducts an in-depth study on the degradation mechanisms for TRM, offering the theoretical foundation for the later experimental and numerical investigations. The water diffusion mechanism for TRM, using CFSRM cylindrical specimens as adopted for the pull-out tests, will be discussed first. With the water uptake inside CFSRM, the moisture swelling of CFS reinforcement produces a negative effect on the bonding behaviour, while the adhesive interface and polymer matrix are under attack from water molecules continuously. In accordance with Arrhenius Equation, raising ambient temperature can obviously accelerate the above-mentioned process. Due to the fact that the above-mentioned degradation process is revealed by the pull-out performance decline

and both ends of fibre reinforced mortar are acted upon by loading in general engineering applications, this chapter proposes an analytical theory of 1D simplified bond-slip behaviour along with its interface failure mechanism under loading actions at both ends. Finally, this theoretical solution is used to analyse the entire process of pulling out carbon fibre strand from mortar in one direction, thereby providing the theoretical support for conducting pull-out tests as well as simulating pull-out processes in the later chapters that target the coupling effects of hygroscopic expansion and interfacial ageing.

3.2 Water diffusion mechanism

3.2.1 Cylindrical orthotropic water diffusion mechanism

Fick's Law is commonly used to describe the macro-level diffusion behaviour in gas, liquid or solid medium (Webb and Pruess, 2003; Donev et al., 2014; Díaz et al., 2016). In this study, Fick's Law is adopted to investigate the long-term water diffusion mechanism of seawater mortar (SM), CFS and CFSRM specimens by immersing them in seawater.

Both CFS and SM that used to make CFSRM specimens for water diffusion in this study feature a cylindrical shape (See the details in Chapter 4). Therefore, the axisymmetric geometry can be adopted to study the water uptake behaviour.

The SM is assumed uniform and thus possesses the isotropic physical properties including its water diffusion coefficient. Therefore, the cylindrical specimen has the same diffusion coefficient (D_{SM}) along its axial and radial directions.

Unlike SM material, CFS material has a feature of orthotropy (Ahmad et al., 2017; Tie et al., 2020). In terms of its water diffusion behaviour, the diffusion coefficient is higher in axial direction D_{CFSz} than in radial direction D_{CFSr} by up to ten times (Aoki et al., 2008; Barjasteh and Nutt, 2012; Huo et al., 2015; Li et al., 2018). Although theoretically the polymer matrix of carbon fibre is isotropic and has identical diffusion behaviour in any direction, there are voids and cracks generated at the interface between the fibre and the matrix inside CFS during its fabrication (Bao and Yee, 2002a). As voids and cracks are quickly filled with water during immersion, the apparent diffusion rate along axial direction inside CFS would be distinctly faster than that in radial direction (Bao and Yee, 2002a). For D_{CFSr}, it only shows the intrinsic diffusion behaviour in the polymer matrix (Bao and Yee, 2002b). As a result, the water uptake mechanism for CFS should consider the different diffusion coefficients of D_{CFSz} and D_{CFSr} at the same time.

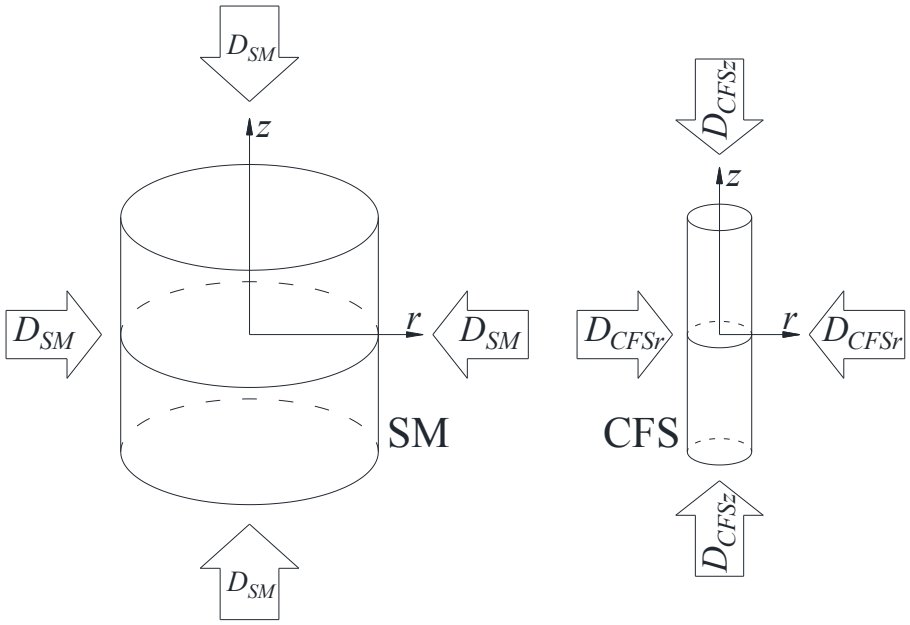

Fig.3-1 Diagram of diffusion mechanism: (a) cylindrical isotropic diffusion in SM material; (b) cylindrical orthotropic diffusion in CFS material.

As shown in Fig.3-1, cylindrical coordinates are more convenient to describe the diffusion mechanism mentioned above. Now define that the moisture concentration inside the cylinder at an arbitrary time and point is $C(r,z,t)$. Let the radius and the half height of the cylinder be denoted by r_R and z_h respectively. The mass function $M(t)$ that represents the total water absorption dependent on t can be written as Eq.3-1. Note that $C(r,z,t)$ here cannot exceed the saturated concentration C' which is independent of time.

$$M(t) = \int_0^{2\pi} d\theta \int_0^{r_R} r\, dr \int_{-z_h}^{z_h} C(r,z,t)\, dz \tag{3-1}$$

Combined with Fick's Law, the general form of $M(t)$ in a cylindrical orthotropic water diffusion field can be derived as Eq.3-2, which is adopted to study the diffusion mechanism in the cylindrical structure (Watson et al., 2010; Gagani et al., 2018).

$$M(t) = M'\left\{1 - \frac{32}{\pi^2}\sum_{m=1}^{\infty}\frac{1}{{\alpha_m}^2}\exp\left(-{\alpha_m}^2\frac{D_r}{{r_R}^2}t\right)\times \right.$$
$$\left.\sum_{n=0}^{\infty}\frac{1}{(2n+1)^2}\exp\left[-(2n+1)^2\pi^2\frac{D_z}{4{z_h}^2}t\right]\right\} \tag{3-2}$$

where M' is the water content at saturated concentration state; D_r and D_z are the diffusion coefficient in radial and axial direction, respectively; α_m are the roots of J_0 Bessel function, namely $J_0(\alpha_m) = 0$; and m gives the sequence of these roots, i.e. α_1 means the first root of J_0.

If the material is uniform and has an isotropic water diffusion coefficient D, Eq.3-2 can be simplified to

$$M(t) = M'\left\{1 - \frac{32}{\pi^2}\sum_{m=1}^{\infty}\frac{1}{{\alpha_m}^2}\exp\left(-{\alpha_m}^2\frac{D}{{r_R}^2}t\right)\times \right.$$
$$\left.\sum_{n=0}^{\infty}\frac{1}{(2n+1)^2}\exp\left[-(2n+1)^2\pi^2\frac{D}{4{z_h}^2}t\right]\right\} \tag{3-3}$$

Eq.3-2 illustrates the relationship between the water uptake and time in a cylindrical orthotropic water diffusion field, while Eq.3-3 describes their relationship in a cylindrical isotropic water diffusion field. It can be found that the total mass of water absorption at saturation state and the diffusion coefficients are the two critical parameters that decide the water diffusion behaviour. However, the behaviour is also influenced by the temperature of the solution used for immersing specimens, according to Arrhenius Law, which will be discussed in later sections.

3.2.2 Arrhenius Law and time-temperature superposition

This section adopts the Arrhenius Law to study the water diffusion mechanism, along with the effect of time-temperature superposition on the diffusion behaviour.

According to the basic form of Arrhenius Equation (Eq.2-4) as explained in Section 2.4.1, it can be found that once employing Arrhenius Law to study the rate of diffusion, the diffusion mechanism should comply with the default precondition that the variation in temperature only influences the water diffusion rate but not the diffusion mechanism itself.

Taking the natural logarithm of Eq.2-4, it yields

$$\ln\left(\frac{1}{k}\right) = \frac{E_a}{R}\frac{1}{T} - \ln(A) \tag{3-4}$$

As E_a, R and A are all temperature independent, Eq.3-4 indicates a linear relationship between $\ln\left(\frac{1}{k}\right)$ and $\frac{1}{T}$, where $\frac{E_a}{R}$ can be seen as the slope of the straight line and $-\ln(A)$ is the intercept on coordinate axis.

Eq.3-4 serves as the theoretical basis of time-temperature superposition principle (Tajvidi et al., 2005; Amiri et al., 2015). Once obtaining the values of k under two different temperatures of T_1 and T_2 within the same medium, they yield

$$\begin{cases} \ln\left(\frac{1}{k_1}\right) = \frac{E_a}{R}\frac{1}{T_1} - \ln(A) \\ \ln\left(\frac{1}{k_2}\right) = \frac{E_a}{R}\frac{1}{T_2} - \ln(A) \end{cases} \tag{3-5}$$

Then the slope of $\frac{E_a}{R}$ can be obtained. According to this superposition principle, the temperature-dependent water uptake behaviour can be manipulated by changing the ambient temperature. Therefore, a long-term water diffusion test can be accelerated by raising temperature. By defining M as the maximum mass of water uptake for a specimen, it yields

$$M(t_1, T_1) = M(t_2, T_2) \tag{3-6}$$

where t_1 and t_2 are the time required for reaching the saturated water absorption under the ambient temperature of T_1 and T_2, respectively.

Since the water diffusion rate varies with the ambient temperature, their relationship can be described as

$$\begin{cases} T_1 > T_2 \Leftrightarrow t_1 < t_2 \\ T_1 < T_2 \Leftrightarrow t_1 > t_2 \\ T_1 = T_2 \Leftrightarrow t_1 = t_2 \end{cases} \tag{3-7}$$

Eq.3-6 and Eq.3-7 can be further explained by the correlation of water diffusion coefficient D with the diffusion temperature T in terms of Arrhenius Law. During the water diffusion process, D is physically equal to k in Eq.3-4. Then the value of D at an arbitrary T can be derived as a function of T, namely $D(T)$. By introducing the initial diffusion coefficient D_0 as a baseline for the diffusion rate at the corresponding temperature of T_0, Eq.3-4 can be transformed as

$$D(T) = D_0 \exp\left[\frac{E_a}{R}\left(\frac{1}{T_0} - \frac{1}{T}\right)\right] \quad (3\text{-}8)$$

Using Eq.3-8, the shift factor α_T of time-temperature superposition can be derived as shown in Eq.3-9:

$$\ln(\alpha_T) = \ln\left(\frac{D}{D_0}\right) = \frac{E_a}{R}\left(\frac{1}{T_0} - \frac{1}{T}\right) \quad (3\text{-}9)$$

The mass increment for water uptake is usually extremely small during a limited testing period. Besides, mediums comprised of high performance mortar or polymer resin usually have a small D (Carra and Carvelli, 2015), and thus it takes a long duration of immersion for specimens made by those materials to attain saturation state at room temperature. To accelerate the water absorption process and quickly achieve the saturation, raising T is commonly used in many studies on water diffusion (Takiya et al., 2015; Li et al., 2018). It is a helpful method for those investigations into water uptake behaviour to overcome the limitation on test period and avoid the measurement deviation caused by the short time.

According to Eq.3-8 and Eq.3-9, at least two different immersion temperatures are always needed to solve α_T and E_a for studying the water uptake mechanism of a specimen. In addition, the selected immersion temperature ranges from room temperature and 60 °C (Robert et al., 2010; Jiang et al., 2014). Selecting too high temperature would be more likely to make the specimen, especially the polymer matrix used therein, fail to obey its original water diffusion mechanism based on Fick's Law and Arrhenius Law (Robert et al., 2010; Jiang et al., 2014). However, selecting too low temperature would make it more difficult to observe the water absorption increment within the immersion duration. Relevant contents about this part will be further discussed in Chapter 4.

3.3 Hygroscopic expansion

3.3.1 Hygroscopic expansion mechanism

CFS used herein is susceptible to moisture conditions due to its polymer matrix part that serves as the adhesive during the fabrication process of carbon fibre textile (Zhang et al., 2015). While its carbon fibre component resists the water ingress and thus would not be subject to the moisture-related effect (Tsai, 1988; Ibarra and Chamorro, 1991; Meng et al., 2015; Toscano et al., 2016), the other component of CFS, namely the polymer matrix, is sensitive to water molecules ingression, which would cause a series of physical and chemical changes such as swelling, osmotic cracking, plasticising, hydrolysis, polymer chain scission or polymer cross-link density reduction (Weitsman, 2011; Regazzi et al., 2016; Kari, 2017; Bahrololoumi et al., 2020). Consequently, the mechanical performance of CFSRM specimen is affected by ambient moisture. Although water uptake has multiple effects on this composite material, the mechanism of its interior hygroscopic expansion can be analysed separately. By using FEM tools in Chapter 5, the effect of CFS hygroscopic expansion on CFSRM pull-out behaviour can be decoupled from those multiple effects and further help analyse the experimental results in Chapter 6 quantitatively.

At the micro level, the onset of hygroscopic expansion often follows the water molecular movement from ambient environment to the inner space among macromolecular chain structures of the polymer matrix during the diffusion process (Pérez-Pacheco et al., 2013; Kafodya et al., 2015). Then the interior free volume of cross-linked polymer chain networks is occupied by absorbed water molecules gradually. With the water uptake going on, a portion of internal free water converts into bound water attached to polymer

chains, leading to the deformation and swelling of chain segments (Pérez-Pacheco et al., 2013; Amidi and Wang, 2016). As more and more water molecules are jammed into the inner space among polymer chains, these molecules are more likely to weaken or even break the Van der Waals interactions present in the cross-linked chain network structures, thereby giving polymer chains greater freedom and mobility to change its spatial morphology, especially for making the dilatation movement (Pérez-Pacheco et al., 2013; Bahrololoumi et al., 2020). The diagram of such a microscopic expansion mechanism based on water molecular movement is illustrated in Fig.3-2.

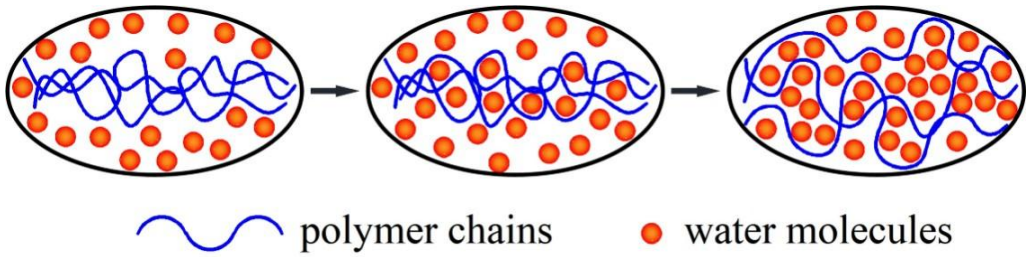

Fig.3-2 Diagram of microscopic hygroscopic expansion mechanism.

At the meso scale level, the porous structure of polymer matrix is another factor that contributes to its swelling when absorbing moisture (Toumpanaki et al., 2020). The interior of polymer matrix contains quantities of voids and pores (Fan, 2008). The ingress of water molecules into the polymer matrix is prone to enlarge those voids and pores, resulting in the swelling phenomenon (Shirangi, 2010; Amidi and Wang, 2016).

Above mentioned local hygroscopic expansion mechanisms are applicable to an arbitrary point inside the polymer matrix of CFS. At last, the macro swelling behaviour of CFS can be observed with increased water uptake.

Note that this swelling behaviour of CFS in the present study specifies its transverse swelling in particular. Compared with the transverse hygroscopic swelling ratio, the longitudinal swelling ratio of fibre reinforced polymer material is found to be insignificant according to the relevant experimental measurement in references (Tsai, 1988; Krauklis et al., 2019). Such an orthotropic dilatation characteristic of the composite material is due to the high elastic modulus of the carbon fibre reinforcement which is aligned with the axial direction of CFS but does not absorb water or swell, as well as the much lower elastic modulus of the polymer matrix itself (Meng et al., 2015). Thus, the global dilatation of CFS in its longitudinal orientation is anticipated to be negligible. To optimise the analysis method for the hygroscopic expansion mechanism, the present study only pays attention to the transverse swelling behaviour of CFS subject to water uptake. Without special emphasis, CFS swelling hereinafter only indicates the transverse swelling.

It has been proved by existing literature that the hygroscopic expansion of the polymer based material is directly proportional to its current moisture concentration if the mass percentage of water absorption does not exceed 2% (Shen and Springer, 1976; Cairns and Adams, 1983). Then the correlation between the dilatation strain and the moisture concentration yields

$$\varepsilon_{HE} = \beta_{sr} C_{CFS} \tag{3-10}$$

wherein ε_{HE} is the transverse hygroscopic expansion strain of CFS; and β_{sr} is the swelling ratio, namely the ratio of dilatation strain to current moisture concentration at a point in CFS.

As C_{CFS} cannot be directly measured by water uptake test or strictly describe the water content in CFS, the present study introduces the concept of mass concentration PA_{CFS} in percentage, namely the percentage of water absorption that occupies the mass of CFS

under its dry condition, along with the coefficient of hygroscopic expansion β_{CHE} to rephrase the relationship between hygroscopic expansion and moisture content as

$$\varepsilon_{HE} = \beta_{CHE} PA_{CFS} \tag{3-11}$$

Considering that C_{CFS} has the physical meaning of molar concentration equal to the ratio between molar quantities of water molecules and the volume of CFS material used, whereas PA_{CFS} represents the mass concentration equal to the mass ratio of water content to CFS material used, β_{CHE} can be transformed from β_{sr} by using Eq.3-12 which is deemed as the expression of their relationship derived from Eq.3-10 in combination with Eq.3-11.

$$\beta_{CHE} = \beta_{sr} \frac{C_{CFS}}{PA_{CFS}} = \beta_{sr} \frac{\rho_{CFS}}{M_w} \tag{3-12}$$

where ρ_{CFS} is the material density of CFS; $M_w = 18$ g/mol, denoting the molar mass of water.

However, once CFS possesses an initial moisture content to a certain degree before starting the test, the practical swelling strain during the test period should remove the initial dilatation value from the total dilatation value. In this study, CFS is embedded in fresh SM with 28 days of immersion curing before the test. The moisture stemming from its external SM substrate can easily diffuses into the interior of CFS reinforcement with a very small radius of 0.7 mm over one month of immersion in 20 °C seawater. Furthermore, SM used here has more than ten times the diameter of the central CFS and thus can provide adequate free water diffusing into CFS in the first 28 days after casting. In view of these factors, the present study considers that CFS embedded therein has an equal moisture concentration to the 28th day's concentration of its surrounding SM substrate. Excluding the initial expansion of CFS owing to its water content growth before

the specimen passes the standard curing time of 28 days, the practical hygroscopic expansion strain taking place in the test herein after 28 days can be written as

$$\varepsilon_{HE} = \beta_{CHE}(PA_{CFS} - PA_{CFS28}) \tag{3-13}$$

where PA_{CFS28} denotes the mass percent concentration of water absorption at the 28th curing day for CFS embedded in CFSRM specimen.

As per Hooke's Law, the elastic stress-strain constitutive relation for CFS can be defined as

$$\sigma_{CFS} = \left[K_{CFS}^{el}\right]\varepsilon_{CFS}^{el} \tag{3-14}$$

where σ_{CFS} symbolises the stress existing in CFS; $\left[K_{CFS}^{el}\right]$ symbolises the material elastic stiffness matrix for CFS; ε_{CFS}^{el} symbolises the elastic strain in CFS.

Note that ε_{CFS}^{el} herein is not equal to the total strain of CFS owing to the presence of swelling strain, as given in Eq.3-15

$$\varepsilon_{CFS}^{t} = \varepsilon_{CFS}^{el} + \varepsilon_{HE} \tag{3-15}$$

where ε_{CFS}^{t} represents the total strain in CFS.

Substituting Eq.3-13 and Eq.3-15 into Eq.3-14, the practical stress-strain relation of CFS when taking account of the occurrence of its hygroscopic expansion behaviour can be obtained as

$$\sigma_{CFS} = \left[K_{CFS}^{el}\right][\varepsilon_{CFS}^{t} - \beta_{CHE}(PA_{CFS} - PA_{CFS28})] \tag{3-16}$$

3.3.2 Research hypothesis about swelling effect on CFSRM specimens

If CFS is not acted upon by any constraint force during its swelling process, namely the free expansion, its total strain ε_{CFS}^{t} is expected to be the same as ε_{HE}, and thereby no stress

would occur. However, CFS reinforcement herein is embedded in hardened SM substrate when it suffers the seawater immersion curing along with the entire CFSRM specimen. Obviously, its hygroscopic expansion behaviour is restricted by the hoop of cylindrical SM, causing the occurrence of ε_{CFS}^{el} in Eq.3-15 and the corresponding σ_{CFS} which can be deemed as the swelling stress inside CFSRM.

The transverse elastic modulus of fibre reinforced polymer material is dependent on the polymer matrix and thus usually has a much lower value than the mortar elastic modulus especially for the high strength mortar (Sun et al., 2014; Faraj et al., 2019). On the other hand, the radius of SM cylindrical hoop herein is more than ten times longer compared with the CFS reinforcement. It can be found that the transverse compression stiffness of SM component is vastly higher than that of CFS component used herein. In consequence, the SM hoop tends to retain its original position subject to the swelling press from the CFS reinforcement. On account of Poisson effect, the transverse swelling strain of CFS is more likely to be converted into its axial strain inside CFSRM, particularly at both ends of CFS, when the lateral surface of CFS bears the restraining force provided by the surrounding SM substrate. The diagram of this phenomenon is illustrated in Fig.3-3.

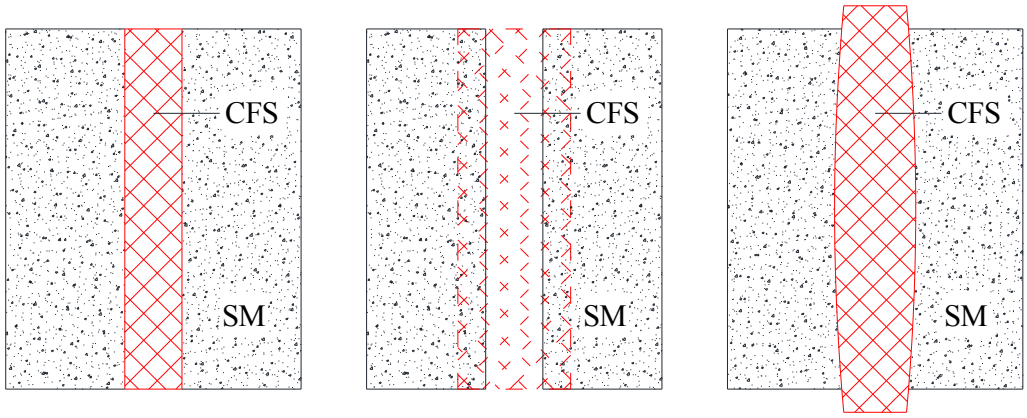

Fig.3-3 Swelling deformation diagram of CFS embedded in a CFSRM specimen: (a) before hygroscopic expansion; (b) assumed free hygroscopic deformation; (c) practical hygroscopic deformation for CFS under restraint conditions from surrounding SM.

With the axial deformation of CFS occurring, the interfacial slip between the deformed CFS and non-swelling SM material is anticipated to generate the interfacial shear stress. Relevant research regards it as the swelling shear stress present on the fibre composite/mortar interface and finds that it would increase following the moisture absorption in the fibre composite (Amidi and Wang, 2016).

To sum up, the hygroscopic expansion behaviour of CFS creates the internal pressure and further causes the interfacial shear stress when it is surrounded by hardened mortar and immersed in water. Once the CFS embedded in CFSRM is acted upon by a pull-out force with the presence of swelling deformation, such a swelling deformation is expected to redistribute the shear stress along the adhesive contact between CFS and SM and lead to the relative interfacial slip between them as well, thereby deteriorating the pull-out performance of CFSRM.

Additionally, the hygroscopic expansion mechanism introduced herein is subject to the ambient temperature when CFSRM is conditioned with water submersion until its internal CFS reaches the saturation condition. As discussed in Section 3.2, although the variation in temperature does not affect the maximum water absorption of CFS, it influences the water diffusion rate inside CFS (Shen and Springer, 1976; Vinson, 1978; Cairns and Adams, 1981; Springer, 1984). That is, temperature does not change the ultimate extent of CFS dilatation strain but it can accelerate or decelerate this expansion process by controlling the water absorption rate of CFS.

Chapter 5 further investigates the hygroscopic expansion mechanism mentioned above by utilising a numerical model with multi-physical fields. In the meantime, Chapter 6 uses related experimental data coupled with the simulation results to validate the effect of CFS hygroscopic expansion on its pull-out behaviour.

3.4 Interfacial ageing

3.4.1 Interfacial ageing induced deterioration

Unlike the mortar reinforced by aramid, basalt, or glass fibre composites, the ageing treatment of the mortar reinforced by carbon fibre composites proves to hardly lead to the physical damage or mechanical property degradation of carbon fibre itself according to the existing studies (Marouani et al., 2012; Toumpanaki et al., 2015; Spelter et al., 2019; Bazli et al., 2020). CFSRM specimen used herein employs CFS as the reinforcement embedded in the SM substrate. CFS/SM interfacial bonding and the polymer matrix in CFS play a critical role in force transfer mechanism between SM substrate and CFS reinforcement. Under the circumstance, their deterioration is deemed to be the major

contributing factor that controls the ageing behaviour of CFSRM in terms of the macroscopic mechanical performance. Once the integrity of the polymer matrix and the interfacial bonding degrade under ageing conditioning, the stress transfer inside CFSRM is expected to weaken gradually. With less load transferring to CFS, carbon fibres, particularly at the internal region, cannot be exploited effectively as the reinforcement for SM substrate. Moreover, the bonding performance decrease based on the polymer matrix is likely to cause the delamination among fibres when CFSRM bears external loads (Davalos et al., 2012b). As a result, the ageing behaviour of interfacial bonding reduces the ultimate load which CFSRM can sustain.

It is known that the degradation of fibre is reflected by tensile behaviour while that of polymer matrix and interface is reflected by shear behaviour (Weitsman, 2012; Kafodya et al., 2015; Heshmati et al., 2016; Benmokrane and Ali, 2018). However, the durability of CFS reinforced mortar material in terms of the interfacial shear behaviour is yet to be studied. Referring to existing studies on FRP/concrete bond property (Baena et al., 2009), CFSRM ageing behaviour concentrating on shear mechanical performance at the interface can be revealed by the pull-out process.

3.4.2 Microscopic ageing mechanism

Common ageing conditions occurring in natural environments include thermal ageing, oxidative ageing, ultraviolet radiation, moisture-induced ageing and their synergies (Maxwell et al., 2005). Considering that CFSRM herein is designed for the application in offshore environments, and the polymer matrix used in CFS is embedded in mortar substrate, water-induced ageing is particularly focused.

Once water molecules diffuse into the polymer matrix, they attack the polymer network and polymer chains continuously (Lekatou et al., 1997). This chemical degradation process is dynamic and irreversible (Nguyen et al., 2012; Sen, 2015; Shrestha et al., 2016). Water molecules age the polymer matrix through three kinds of micro mechanisms. As shown in Fig.3-4, one mechanism is the cross-link reduction in polymer matrix due to the water molecule attack (Bahrololoumi et al., 2020; Fulmali et al., 2021). The molecular structure of polymer materials is featured by long polymer chains. At the micro level, polymer chains are cross-linked and entangled with each other. On an arbitrary polymer chain, there are many points contacting other chains by cross-links and entanglements (Bahrololoumi et al., 2020). Additionally, these points may also bond to the molecular surface of other mediums, namely the fibre and mortar in the present study. The existence of water molecules in polymer is expected to dissolve cross-links and detach the entanglement at those points. According to the thermal motion of water molecules inside the polymer network, they continuously impact upon the polymer chains which compose the polymer matrix at the macro level (Pradas et al., 2001; Philip and AlAzzawi, 2018). Cross-link points on polymer chains are sensitive to the water molecular attack with time and thus prone to damage (Bahrololoumi et al., 2021; Shaafaey et al., 2022). Consequently, cross-link points are reduced under moisture attack. With the breakage of cross-links, the global cross-link density of polymer matrix decreases, leading to the degradation of its mechanical performance at the macro level (Manaila et al., 2018). Another mechanism is the dissolution of the original polymer network through cross-link detachment, as shown in Fig.3-4, which is more likely to increase the segment length of polymer chains between two network nodes (Bahrololoumi et al., 2020).

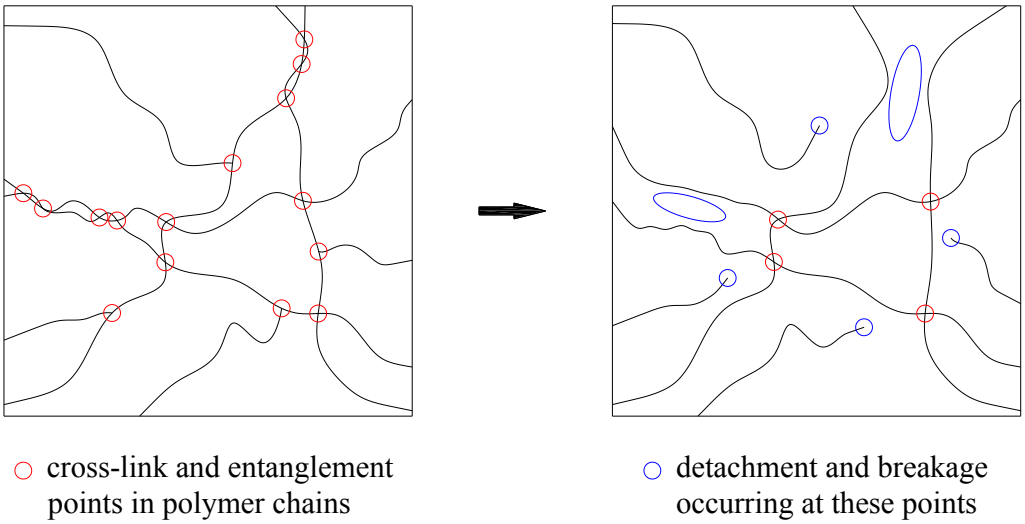

Fig.3-4 Diagram of cross-link reduction in polymer network attacked by water molecules.

The third microscopic ageing mechanism for the polymer matrix is the chain scission that occurs on polymer chains acted upon by water molecules in the matrix, as presented in Fig.3-5 (Weitsman, 2012; Kari, 2017; Bahrololoumi et al., 2020). The phenomenon of chain scission usually happens along with the cross-link reduction simultaneously (Barbosa et al., 2017; Bahrololoumi et al., 2020; Uthaman et al., 2020). As the cross-link detachment causes the increase in the average length of polymer chain segments between two remaining cross-link points, the cross-link reduction further facilitates the chain scission process, because the polymer chain segment is more susceptible to breakage under attack from water molecules if its unrestricted length becomes longer. Consequently, a portion of polymer chains in the matrix are broken and some branches of the main chain would be cut down from the polymer skeleton. These new chains created from chain scission mechanism are much shorter than before and thus are prone to the separation from the original molecular network structure as well as the subsequent extraction out of the polymer matrix over time, accompanied by the motion, diffusion and migration of water molecules therein, particularly when the polymer matrix is under the moisture saturation condition by means of immersion (Xin et al., 2016). With the

continuous scission and precipitation of short chains, the polymer matrix as a whole would suffer the mass loss over time as well (Uthaman et al., 2020). On top of generating short chains, the chain scission process transforms the original structure of polymer chains by adding the free end. As shown in Fig.3-5, two free ends on the polymer chain are created whenever the chain is broken into two pieces owing to the water-induced chain scission. As a result, water-induced chain scission mechanism damages polymer chains and polymer network, contributing to the dissolution of polymer matrix at the macro level. Similar to cross-link reduction, the polymer matrix ageing by means of chain scission mechanism leads to the degradation of its mechanical performance.

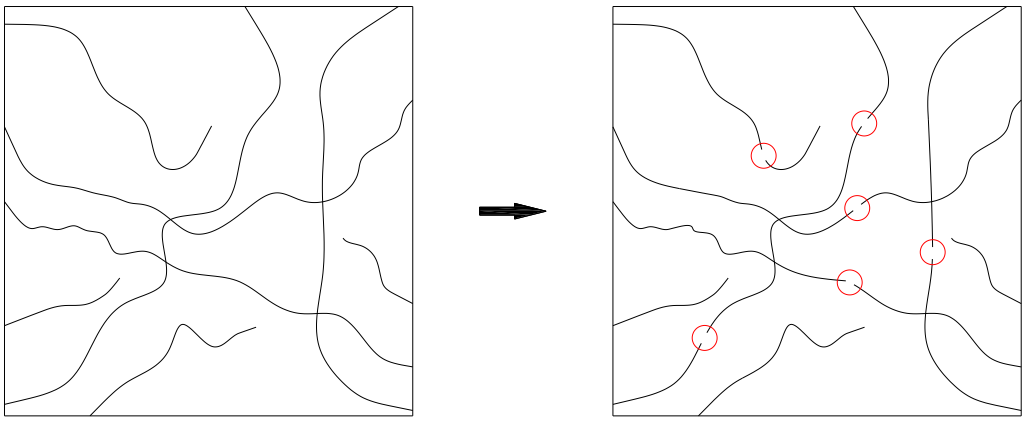

Fig.3-5 Diagram of water-induced chain scission in the polymer matrix.

During the cross-link reduction and chain scission, the original polymer network is also subject to the damage from new link reformation, namely the network rearrangement (Kari, 2017; Bahrololoumi et al., 2020). The breakage and reformation of cross-links in the polymer matrix is a dynamic process. The original network is attacked by water molecules and thus degrades. In the meantime, detached polymer chains can be entangled and linked with other chains again to reform a new polymer network with different structure (Kari, 2017; Bahrololoumi et al., 2020). Likewise, the reformed network present

in the polymer matrix is detrimental to its mechanical properties (Azura and Thomas, 2006; Sun et al., 2011; Padarthi et al., 2021).

In brief, there are four different types of microscopic ageing mechanisms of polymer matrix in total. They include cross-link reduction after water molecules detach those entanglement points inside polymer network, water-induced chain scission on polymer chains, dissolution and rearrangement of the original polymer network. Cross-link reduction and chain scission are two major ageing mechanisms while others are their derivative mechanisms.

The microscopic ageing mechanism of interfacial bonding is related to the polymer matrix ageing aforementioned. With the hardening process of fresh mortar used to cast CFSRM specimen herein, the CFS consisting of carbon fibre and polymer matrix tightly adheres to the surface of the SM substrate by means of producing the firm adhesion between CFS and SM (Lee et al., 2008; Wu et al., 2019). The adhesive force at the interface, or more specifically, the secondary forces of attraction (Ray and Rathore, 2015), can be classified into the intermolecular interactions, including hydrogen bond, van der Waals force and electrostatic force which is also called Coulomb force, wherein hydrogen bond predominates (Pan et al., 2015; Wang et al., 2021). Once moisture molecules migrate to the interface, they weaken the interfacial adhesion and gradually destroys the interfacial integrity in two ways as follows.

On the one hand, moisture molecules generate hydrogen bonds with silica on the surface of SM substrate (Pan et al., 2015; Wang et al., 2021). The presence of these new hydrogen bonds occupies the interfacial adsorption sites which should be used for the molecular adhesion between CFS and SM (Wang et al., 2021). Moreover, hydrogen bonds induced

by moisture molecules are able to aggravate the interfacial damage by replacing the original interfacial hydrogen bonds connecting two sides of the interface initially (Afshar et al., 2016). With more moisture molecules migrating to the interface and creating hydrogen bonds with silica on SM surface, the interfacial interaction would be further impaired and thus the integrity of adhesive interface would be threatened more seriously. In some references, such a microscopic ageing mechanism on interfacial adhesion is characterised as the disruption of interfacial hydrogen bonds under attack from water (Luo et al., 2006; Wang and Petrů, 2021).

On the other hand, as water molecules gradually enter and fill the interfacial space between CFS and SM, they expand the interval between two sides of the interface, and thereby reduce the interfacial interaction which would, in turn, aggravate the increase in intermolecular distance from CFS side to SM side (Pan et al., 2015). With the increased intermolecular distance, those interaction forces, such as the hydrogen bond at the interface, are weakened and prone to breakdown. As a consequence, the interfacial adhesion energy at the interface declines, indicating the decrease in the integral of intermolecular forces over the whole interface (Pan et al., 2015; Wang et al., 2021).

Apart from the direct attack on interfacial adhesion, water molecules worsen it indirectly by means of the polymer network dissolution and rearrangement process as introduced above (Sun et al., 2011). A series of changes occurring in the polymer matrix on account of the moisture intrusion are likely to influence and alter the polymer network structure at its surface boundaries. Then those intermolecular interactions presented at the interface are liable to breakage as a result of the molecular structure change occurring at the polymer matrix side of the interface (Sun et al., 2011).

Based on the aforementioned microscopic ageing mechanisms of interface and polymer matrix, the shear stress transfer between fibre reinforcement and mortar substrate is hindered with the development of water-induced material degradation. Finally, CFSRM material used herein is expected to show the macroscopic shear performance reduction by means of pull-out test, after the water-based ageing treatment.

3.4.3 Elevated-temperature accelerated ageing

Infrastructures, including those located in offshore areas, are usually designed to have a service life for 50 years or longer (Fergani, 2017; Uthaman et al., 2020). However, the history of widely applying FRP reinforced mortar to the construction industry is no more than this time span (Matthys and Triantafillou, 2001; Fergani, 2017). Consequently, if degradation data collected from existent FRP reinforced structures was the only information to study their long-term behaviour in natural environments, it would not be feasible to investigate their durability performance throughout the whole service life. On the other hand, experimental methods used to explore the ageing behaviour of FRP composite are usually limited to the finite period, thereby unrealistic to simulate the material ageing in normal service conditions. Therefore, elevated-temperature accelerated ageing is a commonly used approach to study the durability of FRP reinforced mortar within a limited duration (Ahmed et al., 2020; Gravina et al., 2020; Duo et al., 2021).

The material ageing is actually the result of molecular movements and microstructure changes which damage the material integrity, particular at the interface. Within a certain range, raising temperature can facilitate the current molecular motions and thus accelerate the material ageing process. Many experimental investigations into accelerated ageing of FRP reinforced mortar demonstrated that increasing the ambient temperature moderately

can significantly speed up the ageing reaction rate, while having hardly any influence on the original ageing mechanism (Bank et al., 2003; Huang and Aboutaha, 2010; Spelter et al., 2018).

In order to quantify the internal relationship between temperature setup and accelerated ageing rate, Arrhenius Equation presented in Eq.2-4 is adopted by existing studies to guide the relevant experimental design. Based on measurement results of diverse chemical reactions, Svante Arrhenius in 1880s proposed the Arrhenius Equation to characterise the effect of temperature on the chemical reaction rate (Laidler, 1984). Since Arrhenius Equation was proposed, it has been widely used in scientific research including mass diffusion, chemical reactions, creep relaxation and long-term material degradation (Tant et al., 1995; So et al., 2014; Zhang et al., 2015). Arrhenius Equation has a close relationship to molecular reaction dynamics. The macroscopic reaction rate indicated by the Arrhenius Equation is in accordance with the result of intermolecular collision frequency and interaction (Kovalenko and Dobryakov, 2013). With temperature rising, the intermolecular collision frequency goes up and the intermolecular interaction turns intense. This phenomenon interprets the dependence of ageing reaction rate on the ambient temperature at the micro level. It should be noted that applying the theory about Arrhenius Equation to accelerated ageing research has a premise that the activation energy E_a of ageing reaction stays constant while the environmental temperature changes. Otherwise, it would be equal to the change of ageing reaction mechanism. As mentioned above, many existing studies have conducted a series of experiments to validate that increasing temperature within a certain range wound not affect the ageing reaction mechanism (Bank et al., 2003; Huang and Aboutaha, 2010; Spelter et al., 2018). That is, the activation energy E_a corresponding to the ageing reaction keeps unchanged during the elevated-temperature accelerated ageing treatment. Therefore, it is viable for the

present study to investigate the interfacial ageing of CFSRM material by means of elevated-temperature accelerated ageing approach in compliance with Arrhenius Law.

According to Arrhenius Equation, time-shift factor (TSF) is introduced by the relevant studies to further define the dependence of ageing rate on ambient temperature quantitatively, as shown in Eq.3-17 (Wang et al., 2018; Bazli et al., 2020). By using TSF, the ratio of ageing rate at the prescribed temperature T to the initial temperature T_0 can be calculated.

$$TSF = \frac{k}{k_0} = \frac{Aexp\left(\frac{-E_a}{RT}\right)}{Aexp\left(\frac{-E_a}{RT_0}\right)} = exp\left[\frac{E_a}{R}\left(\frac{1}{T_0} - \frac{1}{T}\right)\right] \quad (3\text{-}17)$$

where k_0 is the ageing reaction rate at the initial temperature T_0.

Note that the ratio of ageing reaction rate between T and T_0, namely *TSF*, is not equivalent to the change in the interfacial ageing rate of CFSRM specimen used herein. Although raising temperature from T_0 to T can speed up the interfacial ageing rate by a certain ratio, this ratio cannot directly decide the reduction in durability performance without substituting it into an appropriate durability prediction model for CFSRM material. The relationship between interfacial ageing and temperature along with the proposed prediction model is discussed in Chapter 6 in more detail.

As regards the temperature selection, existing literature indicates that the accelerated ageing treatment with overly high temperature is more likely to change the degradation reaction mechanism and causes the underestimate of material durability (Robert et al., 2010; Ascione et al., 2016; Ksouri and Haddar, 2018). In view of this, 60 °C is usually adopted by relevant studies as the acceleration temperature which is also recommended by the current durability testing standard such as ACI 440.3R-12 (American Concrete Institute, 2012) and CAN/CSA S806 (Canadian Standards Association, 2021). Many

published experimental results have proved that such a temperature is efficient to facilitate the ageing process and observe the degradation phenomenon of FRP material in a short period (Chen et al., 2006; Al-Lami et al., 2020). Therefore, the accelerated ageing approach used in the present study decides 60 °C as the immersion temperature to age CFSRM specimens. The specific material ageing method and test setup are given in Chapter 6.

3.5 Analytical method of pull-out performance based on bond-slip behaviour

Based on the existing studies on fibre composite reinforced concrete in the last chapter, it is featured as a high tensile property due to fibre composite reinforcement while a poor pull-out property due to the weak interfacial bonding. Under the circumstances, interfacial debonding is a common failure type for fibre composite reinforced mortar materials according to the literature review presented in Section 2.3.4.

In the engineering practice, fibre reinforcement embedded in concrete substrate usually bears tensile force in both directions, especially between two cracks. That is, each end of the fibre reinforcement is acted upon by a pull-out force simultaneously in practical applications. As regards the concrete substrate, it bears axial force at both ends as well, which could be tensile or compressive force.

In order to understand the bond-slip behaviour owing to the loading actions mentioned above, the present study proposes an analytical theory of applying force to both ends of one CFS as well as its mortar substrate simultaneously. The analytical derivation is able to cover the entire interfacial failure process from the initial loading stage to the total failure stage inclusive, and provides the relevant analytical solution.

The analytical derivation provides the theoretical support for later chapters involving experimental and numerical studies that analyse the durability according to the pull-out performance. By means of pull-out test, the long-term degradation in the pull-out performance of CFSRM can be analysed in terms of the changes in the ultimate pull-out resistance along with the related pull-out force-displacement curves.

3.5.1 1D simplified bond-slip behaviour and interface failure mechanism

The ultimate pull-out force is used to assess the deterioration in CFSRM specimens after a variety of ageing treatments. In general, the force-displacement curve rises and then falls with a unique peak point during the whole pull-out process. Before investigating the degradation of pull-out performance, it is necessary for this study to explain the interfacial failure mechanism of CFSRM.

In an idealised mechanical model, it contains only one interface with mortar and fibre reinforcement contacting each other, as shown in Fig.3-6. Mortar and fibre in this model are only acted upon by uniaxial loading along the axial direction. P_1 and P_2 are the loading acting upon right and left end of fibre respectively, whilst P_3 and P_4 are the loading acting upon right and left end of mortar respectively. Note that P_3 and P_4 could be either tensile or compressive force. Compared with the shear deformation along the interface, the deformation along its normal direction can be neglected under such a loading condition. Furthermore, the loading condition at the interface is quite close to the pure shear stress mode (Mode II). Based on the mechanical feature of Mode II, this study assumes that (1) an arbitrary point within mortar or fibre can only have deformation in axial direction when loading is applied on them; (2) an arbitrary point on the interface

can only have pure shear deformation. In this way, the bending deformation would not happen therein.

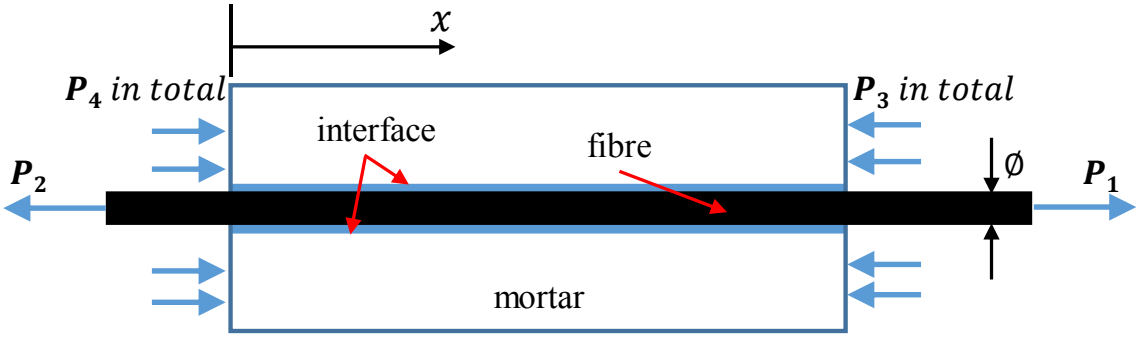

(a) Longitudinal view

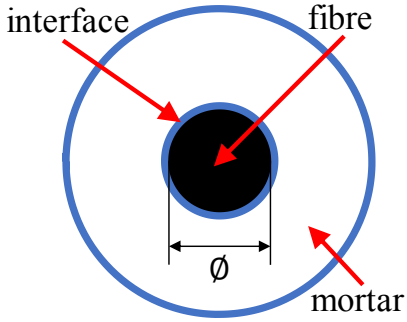

(b) Cross-sectional view

Fig.3-6 1D idealised mechanical model subject to loading at both ends (Cheng et al., 2020).

Before deriving the interfacial failure mechanism, the present study defines a series of material parameters first. In the axial direction, mortar and fibre have the same initial length symbolised by L which means the length of interfacial bond. As shown in Fig.3-6, the perimeter of the interface in the cross-sectional view is $\pi\emptyset$ wherein $\emptyset$ denotes the diameter of fibre. The Young's modulus of fibre and mortar are E_{fi} and E_{mo} respectively. The cross-sectional area of fibre and concrete are A_{fi} and A_{mo} respectively. Besides, the 1D coordinate system is built with the origin at the left end of the model.

During the loading process, the whole model should keep in static equilibrium. Based on conditions of static equilibrium, an arbitrary point at fibre obeys the first order differential equation Eq.3-18 whilst an arbitrary cross section inside the model obeys Eq.3-19 as

$$A_{fi}\frac{d\sigma_{fi}}{dx} - \pi\emptyset\tau = 0 \tag{3-18}$$

$$A_{fi}\sigma_{fi} + A_{mo}\sigma_{mo} = P = P_1 - P_3 = P_2 - P_4 \tag{3-19}$$

where $\sigma_{fi}(x)$ and $\sigma_{mo}(x)$ are the axial stress at arbitrary x in fibre and mortar respectively; and $\tau(x)$ is the bond stress at arbitrary x along the interface.

Now define the interfacial slip $\delta(x)$ as the relative displacement between fibre and mortar at arbitrary x. Then the geometric relationship between δ and the absolute displacement of these two parts at x yields

$$\delta(x) = u_{fi}(x) - u_{mo}(x) \tag{3-20}$$

where $u_{fi}(x)$ and $u_{mo}(x)$ are the absolute displacement at x of fibre and mortar, respectively.

The model should globally satisfy compatibility conditions that the deformation or strain for an arbitrary point is compatible. Thus, calculating the derivative of function $\delta(x)$ with respect to x yields

$$\frac{d\delta}{dx} = \varepsilon_{fi}(x) - \varepsilon_{mo}(x) \tag{3-21}$$

where $\varepsilon_{fi}(x)$ and $\varepsilon_{mo}(x)$ are the strain of fibre and mortar respectively at arbitrary x.

Based on the 1D deformation-strain relation that $\varepsilon_{fi} = \frac{du_{fi}}{dx}$ and $\varepsilon_{mo} = \frac{du_{mo}}{dx}$, Eq.3-21 can be transformed into Eq.3-22 as the compatibility equation controlling the model deformation along its axial direction.

$$\frac{d\delta}{dx} = \frac{du_{fi}}{dx} - \frac{du_{mo}}{dx} \tag{3-22}$$

Assuming that materials comprising the model keep in the elastic stage in the course of loading process, then physical equations used to describe the constitutive relation for these two parts individually can be given based on Hooke's Law, as shown in Eq.3-23 and Eq.3-24 respectively.

$$\sigma_{fi} = E_{fi} \frac{du_{fi}}{dx} \tag{3-23}$$

$$\sigma_{mo} = E_{mo} \frac{du_{mo}}{dx} \tag{3-24}$$

Additionally, this study uses Eq.3-25 to formulate the concept of the constitutive relation located at the interface.

$$\tau = f(\delta) \tag{3-25}$$

Now substituting Eq.3-19, 3-22, 3-23, 3-24 and Eq.3-25 into Eq.3-18, a second order differential equation for arbitrary x along the interface can be obtained as

$$\frac{d^2\delta}{dx^2} - \lambda^2\tau = 0 \tag{3-26}$$

where $\lambda^2 = \pi \emptyset \gamma$ and $\gamma = \frac{1}{E_{fi}A_{fi}} + \frac{1}{E_{mo}A_{mo}}$.

Using factor γ in combination with Eq.3-18, 3-19 and Eq.3-22, σ_{fi} and σ_{mo} from Eq.3-23 and Eq.3-24 can be rewritten as

$$\sigma_{fi} = \frac{1}{A_{fi}\gamma}\left(\frac{d\delta}{dx} + \frac{P}{E_{mo}A_{mo}}\right) \tag{3-27}$$

$$\sigma_{mo} = P - \frac{\sigma_{fi}A_{fi}}{A_{mo}} \tag{3-28}$$

The interfacial bond-slip behaviour is dominated by the local bond-slip relationship, namely $f(\delta)$, for an arbitrary point on the interface between fibre reinforcement and mortar substrate. To date, many viable bond-slip relationships have been proposed and

validated such as the modified Bertero-Eligehausen-Popov (mBEP) model and the Cosenza-Manfredi-Realfonzo (CMR) model (Focacci et al., 2000; Lin and Zhang, 2014). However, it would be difficult for using the simultaneous equations mentioned hereinbefore to obtain a closed form of interfacial bond-slip solution based on those bond-slip relationships, without the method of iterative computations (Cheng et al., 2020). In view of this, simplified trilinear or bilinear (a special case of the trilinear model) local bond-slip relationships are usually adopted by relevant studies and prove to be advantageous (Naaman et al., 1991; Ren et al., 2010; Zhu et al., 2020). In this section, the trilinear local bond-slip relationship is selected to analyse the interfacial failure mechanism. The used relationship has been applied to the model of bond-slip behaviour by many existing studies and validated by them successfully as well (Ma et al., 2016; Yang et al., 2017; D'Antino et al., 2018).

Fig.3-7 illustrates a general form of the linear local bond-slip relationship applicable to the interface inside the idealised mechanical model of fibre reinforced mortar in which the reinforcement may bear the pull-out force at both ends while the mortar may bear either compressive or tensile loading. All stages within the bond-slip process as shown in Fig.3-7 are linear for an arbitrary point on the interface, from its intact stage to its total debonding stage inclusive. During the elastic stage, τ climbs monotonously with δ, until it reaches the peak point with the coordinate value of (δ_1, τ_f) or ($-\delta_1$, $-\tau_f$) which means that the maximum shear stress for arbitrary x at the interface cannot exceed τ_f and the slip corresponding to τ_f is δ_1 at the moment. Subsequently the bond-slip relationship enters a monotonous softening stage. In this stage, the absolute value of δ keeps growing from δ_1 to δ_2 and the absolute value of τ declines linearly from τ_f to τ_r which denotes the residual shear stress. That is, τ_r is defined as the symbol of the final retention of shear stress once the point located on the interface is thoroughly debonded with the interfacial

slip $\pm\delta_2$. As soon as δ exceeds $\pm\delta_2$, this bond-slip relationship enters the total debonding stage and defines that the retention of local shear stress for an arbitrary point on the interface has the constant value of τ_r or $-\tau_r$. It is clear that the complete debonding failure of a local point has already existed since the onset of this stage. Note that if the effect of residual shear stress due to interfacial friction etc. is neglected, the trilinear local bond-slip relationship can be simplified to the bilinear local bond-slip relationship with $\tau_r = 0$.

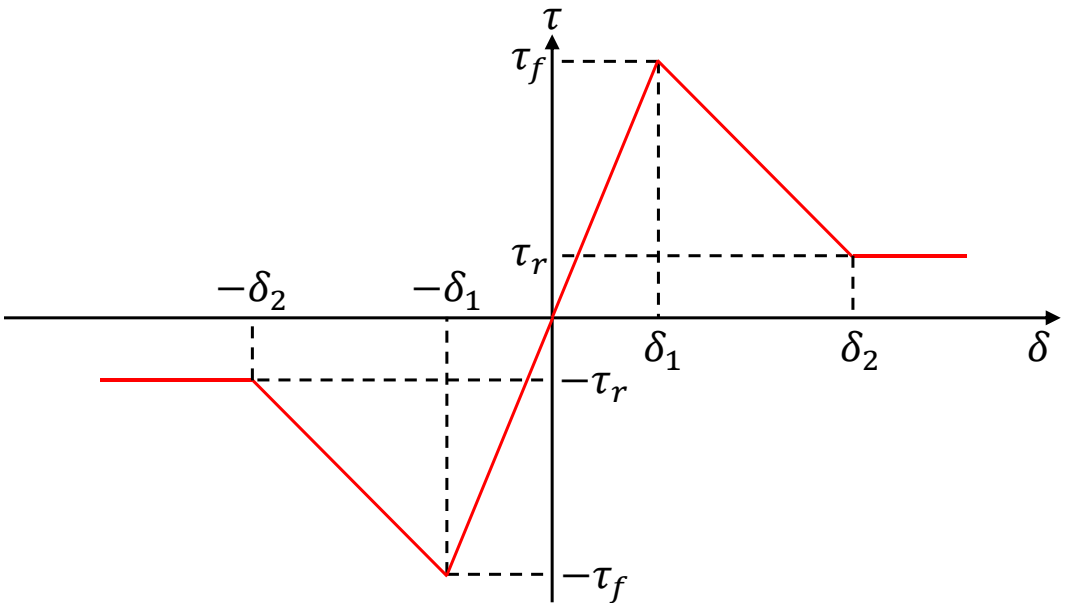

Fig.3-7 Local bond-slip relationship applied to an arbitrary point on the interface.

3.5.2 Analytical solutions to the entire process of interface failure

3.5.2.1 General solutions to the micro-level bond-slip failure process

Based on the different stages of local bond-slip relationship as shown in Fig.3-7, the specific analytical solution to the entire process of debonding failure occurring at the interface is discussed in this section. It provides a mathematical explanation for the interfacial failure mechanism.

As per the curve depicted in Fig.3-7, a piecewise function can be utilised to describe the evolution of local bond-slip relationship in mathematical terms, as shown in Eq.3-29.

$$f(\delta)=\begin{cases}-\tau_r & (\delta \le -\delta_2)\\ -\frac{\tau_f-\tau_r}{\delta_2-\delta_1}\delta-\frac{\tau_f\delta_2-\tau_r\delta_1}{\delta_2-\delta_1} & (-\delta_2 \le \delta \le -\delta_1)\\ \frac{\tau_f}{\delta_1}\delta & (|\delta| \le \delta_1)\\ -\frac{\tau_f-\tau_r}{\delta_2-\delta_1}\delta+\frac{\tau_f\delta_2-\tau_r\delta_1}{\delta_2-\delta_1} & (\delta_1 \le \delta \le \delta_2)\\ \tau_r & (\delta \ge \delta_2)\end{cases} \tag{3-29}$$

Substituting Eq.3-29 into Eq.3-26, δ can be solved at arbitrary x along the interface. Once obtaining the local interfacial slip δ, interfacial shear stress τ can be derived by using the local bond-slip relationship. Then σ_{fi} and σ_{mo}, the axial stress in fibre and mortar respectively, can also be calculated by using Eq.3-27 and Eq.3-28 respectively. According to the specific δ located at both ends of the interface, the load-displacement behaviour during the whole failure process can be acquired eventually. The combination of above mentioned variables and their interrelationships forms the interface failure mechanism for the idealised 1D mechanical model which is subject to loading actions at both ends.

Based on the aforementioned five subfunctions and their different intervals within the domain of Eq.3-29, Eq.3-26 can be transformed into ordinary differential equations (ODE) as expressed from Eq.3-30 to Eq.3-34 in sequence.

$$\frac{d^2\delta}{dx^2}-{\lambda_1}^2\delta=0 \qquad (-\delta_1 \le \delta \le \delta_1) \tag{3-30}$$

$$\frac{d^2\delta}{dx^2}+{\lambda_2}^2\delta={\lambda_2}^2 e \qquad (\delta_1 \le \delta \le \delta_2) \tag{3-31}$$

$$\frac{d^2\delta}{dx^2}+{\lambda_2}^2\delta=-{\lambda_2}^2 e \qquad (-\delta_2 \le \delta \le -\delta_1) \tag{3-32}$$

$$\frac{d^2\delta}{dx^2}-\lambda^2\tau_r=0 \qquad (\delta \ge \delta_2) \tag{3-33}$$

$$\frac{d^2\delta}{dx^2} + \lambda^2\tau_r = 0 \qquad (\delta \le -\delta_2) \tag{3-34}$$

where ${\lambda_1}^2$, ${\lambda_2}^2$ and e are the simplified factors in those equations, defined as ${\lambda_1}^2 = \lambda^2 \frac{\tau_f}{\delta_1}$, ${\lambda_2}^2 = \lambda^2 \frac{\tau_f - \tau_r}{\delta_2 - \delta_1}$ and $e = \frac{\tau_f \delta_2 - \tau_r \delta_1}{\tau_f - \tau_r}$.

By introducing coefficients of C_1 to C_{10}, Eq.3-30 to Eq.3-34 can be solved in general solution terms, as shown from Eq.3-35 to Eq.3-39 sequentially.

$$\delta = C_1 e^{\lambda_1 x} + C_2 e^{-\lambda_1 x} \qquad (-\delta_1 \le \delta \le \delta_1) \tag{3-35}$$

$$\delta = C_3 \cos(\lambda_2 x) + C_4 \sin(\lambda_2 x) + e \qquad (\delta_1 \le \delta \le \delta_2) \tag{3-36}$$

$$\delta = C_5 \cos(\lambda_2 x) + C_6 \sin(\lambda_2 x) - e \qquad (-\delta_2 \le \delta \le -\delta_1) \tag{3-37}$$

$$\delta = \frac{\lambda^2 \tau_r}{2} x^2 + C_7 x + C_8 \qquad (\delta \ge \delta_2) \tag{3-38}$$

$$\delta = -\frac{\lambda^2 \tau_r}{2} x^2 + C_9 x + C_{10} \qquad (\delta \le -\delta_2) \tag{3-39}$$

Once the specific model boundary condition is given within the bond-slip process, C_1 to C_{10} for above general solutions can be determined.

Eq.3-35 to Eq.3-39 are the basic forms of analytical solutions to the micro-level bond-slip failure process in terms of arbitrary x on the interface, where (1) Eq.3-35 indicates the elastic stage which is represented by E State and corresponds to the elastic stage of the local bond-slip relationship plotted in Fig.3-7 with $-\delta_1 \le \delta \le \delta_1$; (2) Eq.3-36 and Eq.3-37 indicate the softening stage which is represented by S State and correspond to the softening stage of the local bond-slip relationship plotted in Fig.3-7 with $\delta_1 \le \delta \le \delta_2$ and $-\delta_2 \le \delta \le -\delta_1$ respectively; (3) Eq.3-38 and Eq.3-39 indicate the debonding stage which is represented by D State and correspond to the debonding stage of the local bond-slip relationship plotted in Fig.3-7 with $\delta \ge \delta_2$ and $\delta \le -\delta_2$ respectively.

3.5.2.2 Bonding states along the interface during bond-slip process

According to the micro-level failure mechanism mentioned above, it is feasible to deduce that the macro-level failure for the entire interface may experience several different states when the idealised 1D mechanical model is subject to the loading actions at two ends of the fibre and the mortar. In terms of the interfacial shear stress distribution, Fig.3-8 lists those possible states that occur along the interface during the bond-slip process, where L_s and L_d symbolise the length of the interface in bond softening state and debonding state, respectively.

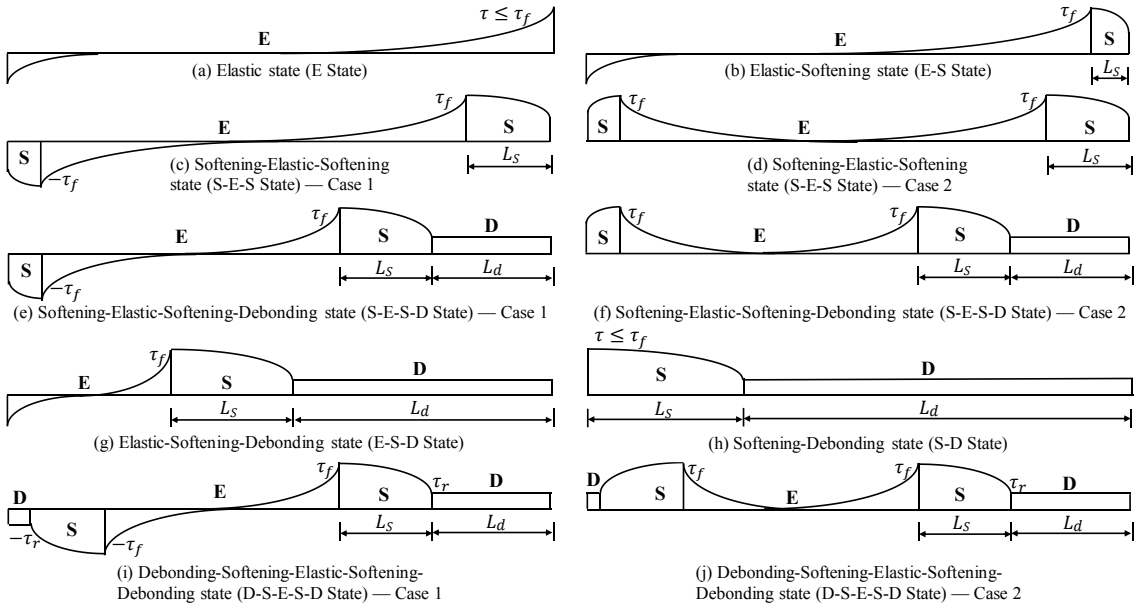

Fig.3-8 Possible bonding states along the interface during bond-slip process.

The interfacial bonding states listed in Fig.3-8 is derived from the analytical bond-slip behaviour under the general condition that both ends are loaded. Since the present study focuses on the pull-out performance of CFSRM specimens and uses pull-out test method, its loading condition and bond-slip behaviour compared with the general analytical solution should be adjusted accordingly. Only one end of fibre is acted upon by a pull-

out force while the reaction force from the support is applied on the mortar at the same end.

Under such a loading condition, the expression of $\delta \geq 0$ holds true throughout the entire pull-out process at an arbitrary point on the interface. Then the possible bonding states given in Fig.3-8 can be further simplified and the types of the bonding states are thus reduced either. In this way, the present study proposes five interfacial bonding states that may occur within the uniaxial pull-out process of CFSRM, containing E State, E-S State, E-S-D State, S State and S-D State.

The interface moves to E State at first with the onset of loading applied to one end of fibre. With the monotonous displacement of the loading end of fibre, the interface goes to E-S State in which the interfacial bond softening phenomenon happens from the loading end while the remaining length of the interface keeps unchanged. With the displacement further increasing, the interface enters E-S-D State if it has enough bond length and thus the interface debonding occurs from the loading end or the whole interface enters S State if its bond length is too short to maintain both elastic bond and debonding existent on the interface at the same time. At last, the interface reaches S-D State in which the debonding length grows continuously until the whole interface is in debonding state, namely the total pull-out failure.

As per the order of the interfacial bond-slip process mentioned above, analytical solutions to all possible interfacial bond states are derived in Table 3-1 which focuses on the process of pull-out test adopted in this study. It provides the theoretical support for later chapters involving experimental and numerical studies that analyse the durability according to the pull-out performance.

Table 3-1 Analytical solutions to interfacial bond states during pull-out test.

Interfacial bond states	Diagram	Region	Analytical solutions		
			δ	τ	σ_{fi}
E State	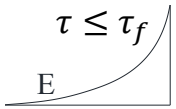	E	$\frac{P\gamma\cosh(\lambda_1 x)}{\lambda_1\sinh(\lambda_1 L)}$	$\frac{\lambda_1 P\gamma\cosh(\lambda_1 x)}{\lambda^2\sinh(\lambda_1 L)}$	$\frac{P\sinh(\lambda_1 x)}{A_{fi}\sinh(\lambda_1 L)}$
E-S State	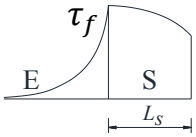	E	$\frac{\delta_1\cosh(\lambda_1 x)}{\cosh[\lambda_1(L-L_s)]}$	$\frac{\tau_f\cosh(\lambda_1 x)}{\cosh[\lambda_1(L-L_s)]}$	$\frac{\delta_1\lambda_1\sinh(\lambda_1 x)}{A_{fi}\gamma\cosh[\lambda_1(L-L_s)]}$
		S	$(\delta_1-e)\cos[\lambda_2(x-L+L_s)]+\frac{\delta_1\lambda_1}{\lambda_2}\tanh[\lambda_1(L-L_s)]\sin[\lambda_2(x-L+L_s)]+e$	$\tau_f\cos[\lambda_2(x-L+L_s)]-\frac{\tau_f\lambda_2}{\lambda_1}\tanh[\lambda_1(L-L_s)]\sin[\lambda_2(x-L+L_s)]$	$\frac{1}{A_{fi}\gamma}\{\lambda_2(e-\delta_1)\sin[\lambda_2(x-L+L_s)]+\delta_1\lambda_1\tanh[\lambda_1(L-L_s)]\cos[\lambda_2(x-L+L_s)]\}$
E-S-D State	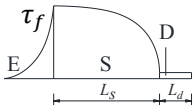	E	$\delta_1\cosh[\lambda_1(x-L+L_s+L_d)]+\frac{\lambda_2}{\lambda_1}\frac{(\delta_2-e)+(e-\delta_1)\cos(\lambda_2 L_s)}{\sin(\lambda_2 L_s)}\sinh[\lambda_1(x-L+L_s+L_d)]$	$\tau_f\cosh[\lambda_1(x-L+L_s+L_d)]+\frac{\lambda_1\lambda_2}{\lambda^2}\frac{(\delta_2-e)+(e-\delta_1)\cos(\lambda_2 L_s)}{\sin(\lambda_2 L_s)}\sinh[\lambda_1(x-L+L_s+L_d)]$	$\frac{1}{A_{fi}\gamma}\{\delta_1\lambda_1\sinh[\lambda_1(x-L+L_s+L_d)]+\lambda_2\frac{(\delta_2-e)+(e-\delta_1)\cos(\lambda_2 L_s)}{\sin(\lambda_2 L_s)}\cosh[\lambda_1(x-L+L_s+L_d)]\}$

Interfacial bond states	Diagram	Region	Analytical solutions δ	τ	σ_{fi}
		S	$\frac{e-\delta_1}{\sin(\lambda_2 L_s)}\sin[\lambda_2(x-L+L_d)]+\frac{\delta_2-e}{\sin(\lambda_2 L_s)}\sin[\lambda_2(x-L+L_s+L_d)]+e$	$-\tau_f\frac{\sin[\lambda_2(x-L+L_d)]}{\sin(\lambda_2 L_s)}+\tau_r\frac{\sin[\lambda_2(x-L+L_s+L_d)]}{\sin(\lambda_2 L_s)}$	$\frac{1}{A_{fi}\gamma}\left\{\frac{\lambda_2(e-\delta_1)}{\sin(\lambda_2 L_s)}\cos[\lambda_2(x-L+L_d)]+\frac{\lambda_2(\delta_2-e)}{\sin(\lambda_2 L_s)}\cos[\lambda_2(x-L+L_s+L_d)]\right\}$
		D	$\frac{\lambda^2\tau_r}{2}(x-L+L_d)^2+\lambda_2\frac{(e-\delta_1)+(\delta_2-e)\cos(\lambda_2 L_s)}{\sin(\lambda_2 L_s)}(x-L+L_d)+\delta_2$	τ_r	$\frac{1}{A_{fi}\gamma}\left[\lambda^2\tau_r(x-L+L_d)+\lambda_2\frac{(e-\delta_1)+(\delta_2-e)\cos(\lambda_2 L_s)}{\sin(\lambda_2 L_s)}\right]$
S State	$\tau\le\tau_f$ S	S	$-\frac{P\gamma\cos(\lambda_2 x)}{\lambda_2\sin(\lambda_2 L)}+e$	$\frac{\lambda_2 P\gamma\cos(\lambda_2 x)}{\lambda^2\sin(\lambda_2 L)}$	$\frac{P\sin(\lambda_2 x)}{A_{fi}\sin(\lambda_2 L)}$
S-D State	$\tau\le\tau_f$ S D L_s L_d	S	$\frac{(\lambda^2\tau_r L_d-P\gamma)\cos(\lambda_2 x)}{\lambda_2\sin[\lambda_2(L-L_d)]}+e$	$\frac{\lambda_2(P\gamma-\lambda^2\tau_r L_d)\cos(\lambda_2 x)}{\lambda^2\sin[\lambda_2(L-L_d)]}$	$\frac{(P\gamma-\lambda^2\tau_r L_d)\sin(\lambda_2 x)}{A_{fi}\gamma\sin[\lambda_2(L-L_d)]}$
		D	$\frac{\lambda^2\tau_r}{2}(x-L+L_d)^2+(P\gamma-\lambda^2\tau_r L_d)(x-L+L_d)+\delta_2$	τ_r	$\frac{P}{A_{fi}}+\frac{\lambda^2\tau_r(x-L)}{A_{fi}\gamma}$

3.5.3 Validation

The analytical solutions presented in Table 3-1 have been validated by existing studies with similar composite materials, as shown in Fig.3-9 (Cheng et al., 2020). It can be found that force-displacement curves in Fig.3-9 match well with the result given by Teng et al. (2006) which focused on the FRP laminate strengthened concrete, and Liu et al. (2019) which focused on FRP strengthened joint.

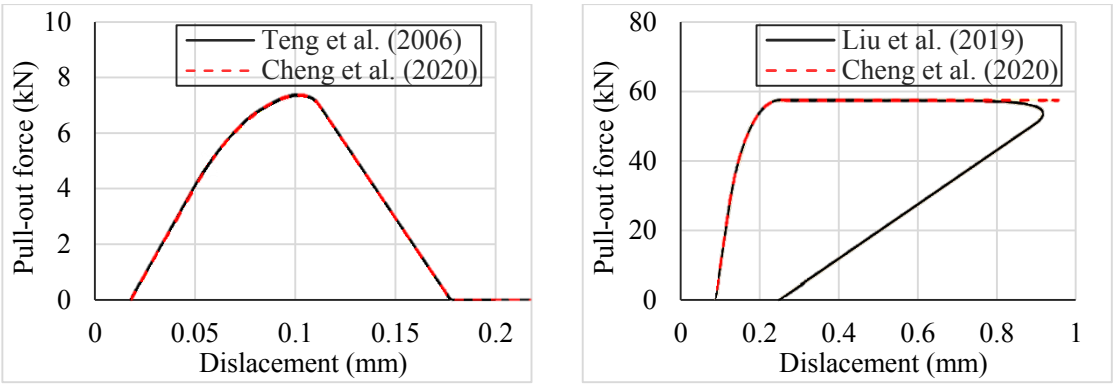

(a) (b)

Fig.3-9 Validation of the present theoretical solutions (Cheng et al., 2020)

The integration of above analytical solutions to all states reveals the closed-form piecewise expression of the interfacial failure mechanism that controls the bond-slip behaviour for the entire interface of CFSRM. It provides the theoretical support for conducting pull-out tests as well as simulating pull-out processes in the later chapters that involve the in-depth studies on the durability of pull-out performance by experimental and numerical methods respectively.

3.6 Summary

This chapter gives a detailed exposition of the theoretical mechanisms for pull-out performance degradation of CFSRM specimens and a general analytical solution of the full interfacial failure process to study the interfacial degradation in later chapters.

According to Fick's Law, it is a long-term and slow process for seawater to diffuse into the interior of CFSRM. Unlike the homogeneous SM substrate, CFS is an orthotropic material and has different diffusion coefficients in axial and radial directions respectively, namely the orthotropic water diffusion mechanism. Using time-temperature superposition based on Arrhenius Law, immersion temperature of 60 °C can accelerate the water diffusion process from the outside to the interior CFSRM, without changing its degradation mechanism or causing the underestimate of material durability. That is, raising temperature from room temperature to 60 °C helps fulfil the water diffusion test within a limited experimental duration.

With water molecules diffusing into CFS/SM interface and the interior of CFS, they cause the pull-out performance degradation of CFSRM in two aspects, containing hygroscopic expansion and interfacial ageing. In order to observe the related experimental phenomenon within the limited conditioning period, the treatment method of elevated-temperature accelerated ageing in compliance with Arrhenius Law is practical to adopt by the present study.

This chapter also proposes a general analytical solution (Eq.3-35 to Eq.3-39) to describe the bond-slip behaviour during the pull-out test in terms of the interfacial failure mechanism.

The degradation mechanisms for pull-out performance in the present study are assumed as the combination of hygroscopic expansion and interfacial ageing. They can be used to analyse the long-term durability of CFSRM under marine environments. Chapter 6 will discuss it in more detail.

4 EXPERIMENTAL STUDY ON PHYSICAL AND MECHANICAL PROPERTIES OF CFSRM

4.1 Overview

This chapter describes the experimental investigation into the physical and mechanical properties of SM, CFS and CFSRM. The experimental results will serve as the basic physical and mechanical parameters not only used in the later numerical modelling but also on the long-term durability performance prediction of CFSRM. The chapter is arranged in four aspects, containing specimen preparation, test setup, test results and related analyses. Focusing on SM, this study measures its density, compressive strength, splitting tensile strength, Young's modulus and flowability. Focusing on CFS, its cross-sectional area, tensile strength and Young's modulus are measured. In addition, the present study measures the diffusion coefficient of CFS and SM immersed in seawater according to the method introduced in Chapter 3. Finally, static pull-out test is conducted for CFSRM to acquire its initial pull-out performance, acting as the baseline data for the long-term durability analysis hereinafter.

4.2 Mortar test setup

4.2.1 Specimens preparation and curing

In this section, there were 65 specimens prepared for mortar tests in total. 24 mortar cubes with standard size (100 mm) were used to test the compressive strength. 24 mortar cylinders with standard size (200×100 mm height/diameter) were used to test the splitting tensile strength. Three prisms of mortar specimens (40×40×160 mm) were used to test

the Young's modulus. Six fresh mortar samples were used to conduct the flowability test. Eight small mortar cylinders (50×20 mm height/diameter) were used to carry out the water uptake test.

Table 4-1 summarises the mortar mix design that was used to cast SM in the study group and freshwater mortar (FM) in the control group.

Table 4-1 The mortar mix design.

Mortar type	Binder materials (kg/m^3)				Dosage of mortar constituents (kg/m^3)				
	Cement	FA	GGBS	SF	Binder	Sea sand	Seawater	Freshwater	Water reducer*
SM	383.9	139.6	139.6	34.9	698	1396	209.4	0	7.6
FM	383.9	139.6	139.6	34.9	698	1396	0	209.4	7.6

* ROCKBOND ADMIX 201 (brand) powder has been used as the water reducer in this study.

In this study, the mortar mix design has a considerably low water/binder ratio of 0.3. The binder consists of normal Portland cement and three types of admixtures, including PFA, GGBS and SF. It is necessary to mix those dry components uniformly before adding water into the binder, as shown in Fig.4-1.

(a) (b)

Fig.4-1 Dry mix of components in mixer: (a) before mixing; (b) after mixing.

Before casting, the fine aggregate used herein was dried in the oven under 80 °C for at least 24 hours. Then casting was carried out under the following sequences: (1) weigh out the exact amount of each ingredient in the mortar mix design; (2) mix all water reducer powder with seawater until no visible powder remains; then let the solution stand still until all bubbles disappear; (3) use wet wipe to wet the inner surface of the mortar mixer; (4) mix all dry components together for 3 min in the mixer; (5) add the water reducer solution to the already mixed dry components, and mix for another 4 minutes in total; (6) stop the mixer and fill the fresh mortar into prepared moulds; (7) vibrate the fresh mortar for 5 minutes.

Bubbles were generated when mixing the water reducer powder with seawater (Fig.4-2a). Thus the solution needs to stand still for 15 minutes until those bubbles disappear as shown in Fig.4-2b. Otherwise bubbles would enter the fresh mortar and cause excessive air content inside mortar specimens, which may reduce the strength of hardened mortar (Zhang et al., 2018).

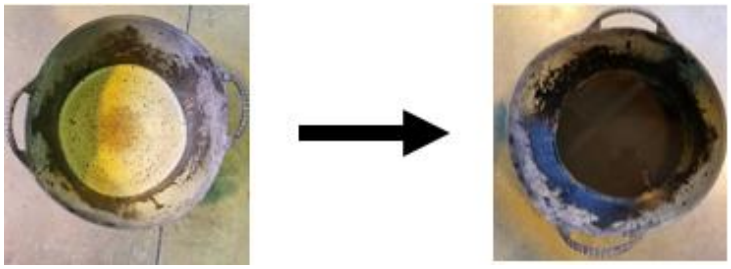

(a) (b)

Fig.4-2 Water reducer solution preparation: (a) mixing in seawater; (b) stand still until bubbles disappear.

Complied with above casting method, the casted specimens are shown in Fig.4-3.

(a) (b) (c) (d)

Fig.4-3 The specimens casting work: (a) the fresh mortar; (b) cubes and cylinders; (c) prisms; (d) small cylinders.

As soon as the specimens were cast, the upper surface of moulds was covered by a plastic sheet to avoid the moisture loss. Specimens were demoulded after 24 hours, and then cured under 20 °C in the curing tanks until testing. SM and FM specimens were cured under seawater and freshwater respectively. Note that the seawater used in the present study came from Marine Station in University of Plymouth.

4.2.2 Physical properties test

This study has adopted the compressive strength test of cubic specimens, the splitting tensile test of cylindrical specimens and the uniaxial compressive elastic modulus test of prism specimens. In addition, flow table test was also conducted to examine the workability of fresh mortar.

According to the standard BS EN 12390-3 (British Standards Institution, 2019a), 100 mm cubic mortar specimens are recommended for testing the compressive strength of the mortar. The standard also recommends 0.3 MPa/s as the loading rate, equivalent to 3 kN/s for the cubic specimen. The compressive strength test can be conducted as follows: (1) apply a small preload to remove any tolerance in the testing machine; (2) start the compressive loading with 3 kN/s; (3) terminate the loading when the cubic specimen is crushed. Fig.4-4 shows the compressive test setup.

Fig.4-4 The compressive strength test of the mortar cubic specimen.

Existing references show that the mortar specimen cast with seawater usually has a different strength growth curve compared with freshwater (Xiao et al., 2017). The usage of admixtures also influences both the short-term strength and long-term strength (Xie et al., 2019). Hence, it is necessary to conduct the test with different curing time to examine

its strength change over time. In this study, the compressive strength was tested with curing times 7d, 14d, 28d and 90d. Three specimens were tested for each condition.

The tensile strength of the mortar was measured using the splitting tensile test of cylindrical specimens. According to BS EN 12390-6 (British Standards Institution, 2009), mortar cylinders with 100 mm diameter and 200 mm length have been used. The standard also recommends a loading rate as

$$R_{ts} = \frac{1}{2}(S_{ts} \times \pi \times L_{ts} \times d_{ts}) \quad (4\text{-}1)$$

where R_{ts} is the load rate (kN/s); S_{ts} is the splitting stress rate of 0.05 N/mm^2 per second; L_{ts} and d_{ts} are the length and diameter of the mortar cylindrical specimen, which are 200 mm and 100 mm respectively. Therefore, a load rate R_{ts} of 1.5 kN/s was adopted. The setup of the splitting tensile test is shown in Fig.4-5.

Fig.4-5 The splitting tensile test of mortar cylindrical specimen.

Same as the compressive strength test, specimens with different curing durations (7d, 14d, 28d and 90d) were also adopted for the splitting tensile test.

As shown in Fig.4-6, mortar specimens of the study group were cast by seawater (Fig.4-6a) while specimens of the control group were cast by freshwater (Fig.4-6b).

(a) Study group (b) Control group

Fig.4-6 Specimens used in the experimental programme about mortar strength tests.

Measuring the uniaxial compressive Young's modulus of mortar prisms is similar to the aforementioned compressive strength test method. Following the standard BS EN 1052-1 (British Standards Institution, 1999), the specimens of mortar prism with 40 mm side length and 160 mm height are used to measure the uniaxial compressive Young's modulus along the height direction. The specific testing procedures are described as below: (1) mark the testing region by two small buttons adhering to both front and rear surfaces of the prism; the testing region on the surface of mortar prism is parallel to its height direction and 30 mm away from its top or bottom as shown in Fig.4-7; (2) start the compressive loading with 2 kN/s; (3) use LVDT to collect the axial deformation data within the testing region while the related loading data is recorded by Instron testing machine simultaneously until the loading curve deviates from the linear growth or the testing machine reaches its maximum capacity.

Fig.4-7 Uniaxial compressive Young's modulus test of mortar prism specimen.

The present study tested the Young's modulus of SM after 28 days of curing. Three specimens used for this test are shown in Fig.4-8.

Fig.4-8 Prism specimens of SM for testing Young's modulus

Slump tests and flow tables test are usually conducted in order to check the fresh mortar workability, especially its flowability. The slump test focuses on the global consistency and the plasticity property of the fresh mortar which contains coarse aggregates, while the flow table test is more recognised for mortar. As the mortar specimens in this study

only contains sand without coarse aggregate, the flowability is similar to the fresh mortar or paste. Thus, flow table test was adopted to check the consistency of the fresh mortar.

Complying with the testing standard BS EN 12350-5 (British Standards Institution, 2019c), the flow table test steps are as follows: (1) prepare a flat and horizontal place to lay the flow table test apparatus; (2) use wet wipe to wet the surface of the flow table and the mould used to form the test sample which possesses a conical frustum shape with base diameter of 100 mm, top diameter of 80 mm, and height of 80 mm; (3) prepare the fresh mortar sample and fill the mould with it; note that filling the entire mould should be completed by two layers of the fresh mortar with the same thickness and a tamping bar should be used to compact the sample during this process; (4) upon the removal of the mould, steadily rotate the handle of the flow table to make it shake manually over one to three seconds for each cycle until 15 cycles is attained in total; (5) measure current maximum diameters of the fresh mortar in two directions perpendicular to each other; (6) decide the flow value as the ratio of average increase of the above two dimensions of the mortar spread to its original base diameter. The flow table test was repeated three times to verify the reliability of test results. Fig.4-9 shows the flow table test setup.

Fig.4-9 Flow table test of the fresh mortar sample.

4.2.3 Water uptake test for mortar

Water uptake test is usually conducted to study its water diffusion behaviour. Several testing methods are recommended in existing standards and references (Alsayed and Amjad, 1996; ASTM International, 2013a; ASTM International, 2013b; British Standards Institution, 2014; Siddique, 2016). ASTM C1585 focuses on the single directional absorption rate, where a single surface of a cubic specimen is exposed to water, while other surfaces are sealed (ASTM International, 2013b; Siddique, 2016). Besides, ASTM C642 focuses on the relationship between specimen internal porosity and its water absorption rate instead of the water diffusion process through a uniform medium (ASTM International, 2013a), which is not the focus of this study. Compared with other specifications, the standard BS 1881-122 was adopted in this study because it targets exactly the same problem as this study is going to explore, using completely immersion method for cylindrical specimen (Alsayed and Amjad, 1996; British Standards Institution, 2014).

As shown in Fig.4-10, the water uptake test used seawater mortar cylinders with the size of 50 mm in height and 20 mm in diameter, which were the same as those used for the subsequent pull-out tests. Seawater used for mortar casting and curing was also used for the long-term immersion during the water uptake test. This test was repeated four times to get reliable results.

Fig.4-10 A set of four SM specimens used for the water uptake test.

Water diffusion through mortar is a considerably slow process, especially for those with low w/b ratio (Nilsson, 2002). In this study, the mortar not only possesses a relatively low w/b ratio with 0.3, but also contains multiple admixtures like PFA, GGBS and SF which improves the particle size gradation of binder components, thereby reducing micro-voids and micropores inside hardened mortar, and increasing its self-compacting capacity and further resisting the internal water mass transport (Gesoğlu et al., 2009). Therefore, the mortar specimen used here has a much lower diffusivity than normal mortar. In order to observe water uptake behaviour and obtain good understanding in a limited period, elevated temperature acceleration method has been adopted, as the water molecules transport mechanism complies with the Arrhenius Law (Takiya et al., 2015; Zehtab and Tarighat, 2018). In this study, 60°C is selected as the accelerated temperature.

The water diffusion test at 20°C was also carried out as the control group in this study. The water diffusion activation energy E_{acW} for SM material in seawater condition can be deduced through test results of these two groups, based on the Arrhenius Law described in Section 3.2.2. The test results are given in Section 4.5.2.

According to the standard BS 1881-122 (British Standards Institution, 2014), the test was carried out as follows: (1) fresh mortar was cast into eight cylinder moulds and cured in

seawater for 28 days; (2) dry specimens in an oven for 72 hours with 80°C; (3) after removing specimens from the oven, cool them for 24 hours in a dry indoor condition; (4) weigh and record the mass of each specimen after cooling; (5) divide specimens into two sets of four; put each set into the curing tank filled by seawater with 20°C and 60°C respectively (Fig.4-11a and Fig.4-11b); note that specimens should be completely immersed; (6) considering uncertain factors during the weight measurement because the mortar specimen used here has a quite slow daily mass growth of water uptake, define the test time interval: specimens should be weighed at two days interval for the first ten days, at ten days interval for the next 80 days and at 30 days interval for the last 90 days; (7) once taking the specimen out from the tank, remove its surface moisture by drying it with a cloth towel until no visible free water can be seen on its surface; (8) weigh each specimen by the digital analytical balance (Fig.4-11c) and record its mass; (9) return the specimens to the curing tank.

(a) (b) (c)

Fig.4-11 Mortar water uptake test: (a) specimens immersed in 20°C seawater; (b) specimens immersed in 60°C seawater; (c) weigh the cylindrical specimen by the digital analytical balance.

4.3 Carbon fibre strand test setup

4.3.1 Physical properties test

This section presents the physical properties measurement of CFS, including the cross-sectional area, uniaxial tensile strength, uniaxial tensile elastic modulus and transverse hygroscopic swelling ratio.

Short CFS samples used for the cross-sectional area measurement were directly cut from the intact carbon fibre mesh. A total of eight samples with a length of 10 mm was used, as show in Fig.4-12. As the cross-sectional area ranges within 1 to 2 mm^2 by a rough estimation, the microscope with magnification power of ten from the objective lens is utilised to conduct the measurement.

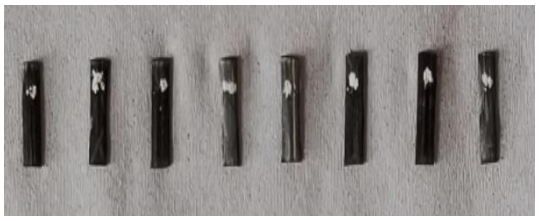

Fig.4-12 Eight CFS samples prepared for the cross-sectional area measurement.

The detailed measurement steps are given as below: (1) randomly cut eight CFS samples with 10 mm length from the intact carbon fibre mesh; note that the cutting direction should be perpendicular to CFS axis; (2) specify the end to measure the area for each sample by marking it with white dot; (3) measure the cross section of each CFS sample under the microscope with magnification power of ten.

Once the average cross-sectional area of CFS was obtained, it can be applied to the later mechanical performance test about the material tensile strength and elastic modulus. Many standards and specifications have been produced to guide relevant tests (Jawaid et al., 2018). ASTM C1557 is for a single filament or a tow made up of a few filaments as it uses a thin mounting tab as the specimen anchorage (ASTM International, 2020a), while BS EN ISO 2307 and ISO 10406-1 aim at fibre ropes and FRP bars respectively (British Standards Institution, 2010; International Organization for Standardization, 2015). As a new type of fibre composite material, currently there is no well recognised testing standard for CFS to measure its uniaxial tensile strength and elastic modulus.

To measure the tensile strength and the elastic modulus of CFS, single strand uniaxial tensile test was adopted in this study. As shown in Fig.4-13, four CFS samples, with a length of 240 mm, have been cut from the carbon fibre mesh that are available in the lab. The testing region of the sample is with 50 mm length in the middle, while a length of 95 mm at both ends will be anchored in an aluminium tube to facilitate the grip at the testing machine.

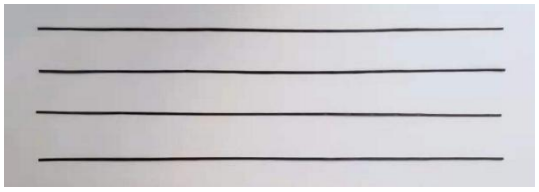

Fig.4-13 Four samples of 240 mm CFS prepared for the uniaxial tensile test.

Carbon fibre commonly features a relatively higher tensile strength and smaller cross-section compared with traditional building materials such as steel bar (Dhoska, 2019; Zhou et al., 2019). Thus, higher anchorage stress is needed for CFS material during its tensile test. However, the normal tensile jig provided by Instron testing machine does not

have a matched geometric shape to sufficiently hold those quite thin CFS materials. Furthermore, the sharp edge of the jig is more likely to cause excessive stress concentration and cause undesirable failure at the grip ends. Taking into account of those adverse conditions, the present study used epoxy resin to anchor the two ends of CFS into an aluminium tube, with 3 mm in diameter and 95 mm in length. The specimens were cured for seven days under ambient room temperature before tensile testing. Fig.4-14 shows the CFS samples with aluminium tube anchorage.

Fig.4-14 CFS samples for tensile test.

The sample preparation and test setup procedures can be summarised as follows: (1) cut carbon fibre mesh into four CFS samples of 240 mm in length; (2) prepare eight aluminium tubes with the length of 95 mm; (3) put one end of CFS into the aluminium tube; (4) seal the tube bottom by plasticine and adhesive tape; note that the usage of plasticine can also help fix the CFS end at the central axis of the tube; (5) fill the interior of the tube with epoxy resin; (6) cure this anchorage end at room temperature for seven days; (7) repeat steps three to six for the other end of CFS; (8) install the sample on Instron testing machine as shown in Fig.4-15; ensure that both aluminium tubes are tightly gripped by testing machine jigs; (9) conduct the tensile test using the displacement control method, with a loading rate of 0.05 mm/min; (10) stop the test and collect testing data when the sample is completely ruptured.

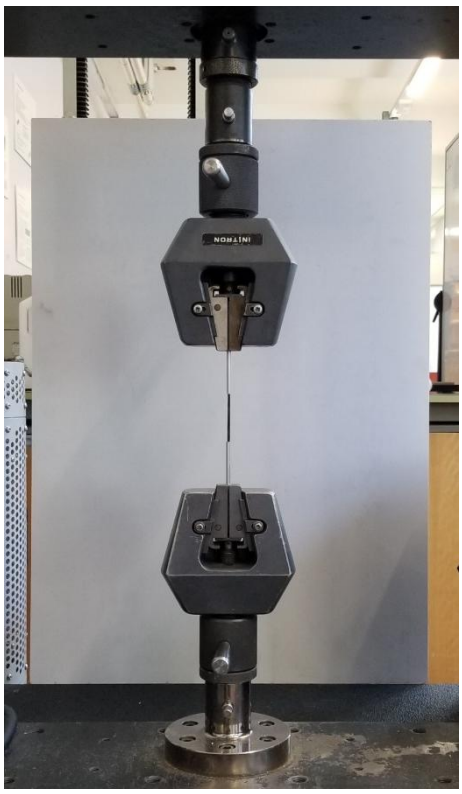

Fig.4-15 CFS tensile test setup.

It is worth mentioning that the aluminium tube used to anchor CFS should have adequate length to provide sufficient bonding strength at the CFS anchorage region during the tensile test. The specific calculation method for CFS physical properties is given in Section 4.6.1.

Hygroscopic swelling of CFS material, mainly due to polymer, is another important physical property in this study. Compared with its swelling in radial direction, its longitudinal swelling can be neglected because the material stiffness of the carbon fibre is vastly higher than the polymer matrix in the axial direction and the global axial swelling deformation of CFS is thus restricted by those fibre filaments (Meng et al., 2015; Dijk et al., 2018). Therefore, the swelling of CFS can be simplified to a 2D behaviour.

The present study only targets at the measurement of its transverse hygroscopic expansion. According to the relevant water absorption trial studies, CFS material in dry condition can reach its moisture saturation after it is immersed in 20 °C seawater for less than 30 days. Based on those short CFS samples that are used for the cross-sectional area measurement as shown in Fig.4-12, the swelling ratio test was carried out by the following steps: (1) after the measurement of initial cross-sectional area for the CFS samples in Fig.4-12, they are taken into a box and placed in 20 °C seawater immersion condition for over 30 days; (3) take out these samples and dry the surfaces; (4) individually measure the current cross-sectional area for each sample at the marked end by microscope; (5) calculate the transverse swelling ratio through the measured area changes before and after immersion.

4.3.2 Water uptake test for carbon fibre strand

To investigate the water absorption behaviour of CFS material, the water uptake test was conducted. To date, there are several relevant testing methods recommended by existing standards and references (ASTM International, 1995; British Standards Institution, 1997; International Organization for Standardization, 2014). Generally, they are all widely applied, depending on material properties and experimental conditions. ISO 3344 is often employed to measure water uptake mass of pure continuous fibres (Gopinath et al., 2013; International Organization for Standardization, 2014; Kasaby and Bdelmagied, 2019). This standard specifies 105 °C as the drying temperature for the specimen before the test and focuses on the moisture content of fibre reinforcement itself that usually possesses a loose structure without any polymer resin impregnation. However, CFS specimens used here involves the polymer matrix which would be prone to damage in overheating. ASTM D570 focuses on the water absorption of plastics including the polymer resin that are used

to impregnate the fibre (ASTM International, 1995; Genna et al., 2017). Although it is appropriate to a wide variety of plastics, this specification is not applicable to composite materials comprised of fibre reinforcement and polymer resin matrix. BS EN 2378 was adopted in this study as it uses completely immersion method for the moisture uptake measurement of fibre reinforced plastics (British Standards Institution, 1997; Onyakora et al., 2017, Onyakora et al., 2020).

Note that the specific testing samples and procedures should consider the following two problems: first, the measuring work should take into account both radial moisture diffusion and axial moisture diffusion inside CFS material, as illustrated in Section 3.2.1; second, an individual CFS is relatively lightweight with around 0.5 g per 200 mm and generally has a quite small water absorption percentage compared with SM material (Pan et al., 2015; Liu et al., 2018), which adds challenges in measurement reliability.

To solve the first problem, two different lengths of CFS samples were chosen for the water uptake test, namely 240 mm and 6 mm. Although water diffuses into the sample radially and axially simultaneously, the diffusion in the axial direction can be ignored for the sample of 240 mm in length because its lateral surface area is more than 100 times larger than its cross-sectional area. However, the diffusion effect from both of axial and radial directions should be considered for the 6mm CFS samples as the axial diffusion plays a crucial role if the length of the sample is less than five times as long as its diameter (Gagani et al., 2018).

To solve the second problem, a bundle of 60 long strands was used in each group composed of 240 mm CFS samples, and approximately 2400 short strands in each group composed of 6 mm CFS samples which are cut by a digital guillotine. In this way, both

types of the test group used have a similar total mass between 32g and 33g, and the water uptake mass has been recorded according to the mass variations in each group during the test.

Like the water uptake test for SM material, four repeat tests were carried out for both 6 mm and 240 mm CFS, as shown in Fig.4-16. The mass measurement is also repeated four times to get reliable results.

(a) (b)

Fig.4-16 A set of four groups of CFS samples used for the water uptake test: (a) 240 mm long strands; (b) 6 mm short strand.

The water uptake test for CFS was also conducted by seawater immersion approach with 60 °C and 20 °C respectively, the same as SM in Section 4.2.3. According to BS EN 2378 (British Standards Institution, 1997), the test was carried out as follows: (1) prepare all groups of CFS samples for both 6 mm short stands and 240 mm long strands; (2) dry them in an oven at 70 °C until the value of their mass is stable for at least 12 hours; (3) upon the removal of them from the oven, immediately weigh and record the mass of each group; (4) take them into the curing tank for the seawater immersion bath at 20 °C and 60 °C respectively; (6) define the test time interval based on the accuracy of the digital analytical balance: for 60 °C immersion, the test groups should be weighed at two-hour intervals

over the first day and at 12-hour intervals over the next three days; with regard to 20 °C immersion, the test groups should be weighed at four-hour intervals over the initial two days, at 24-hour intervals over the next eight days and at five-day intervals over the last 20 days; (7) over the period of immersion, seawater should be refreshed at seven-day intervals to avoid the concentration change; (8) upon the removal of test groups from the curing tank, take them to the covered strainer and dry them until no visible free water remains on their surface; (9) weigh each group and record its mass in 0.1 mg accuracy; (10) return them to the tank and repeat the above mentioned steps until the test completes. Fig.4-17 shows the procedure of the water uptake tests.

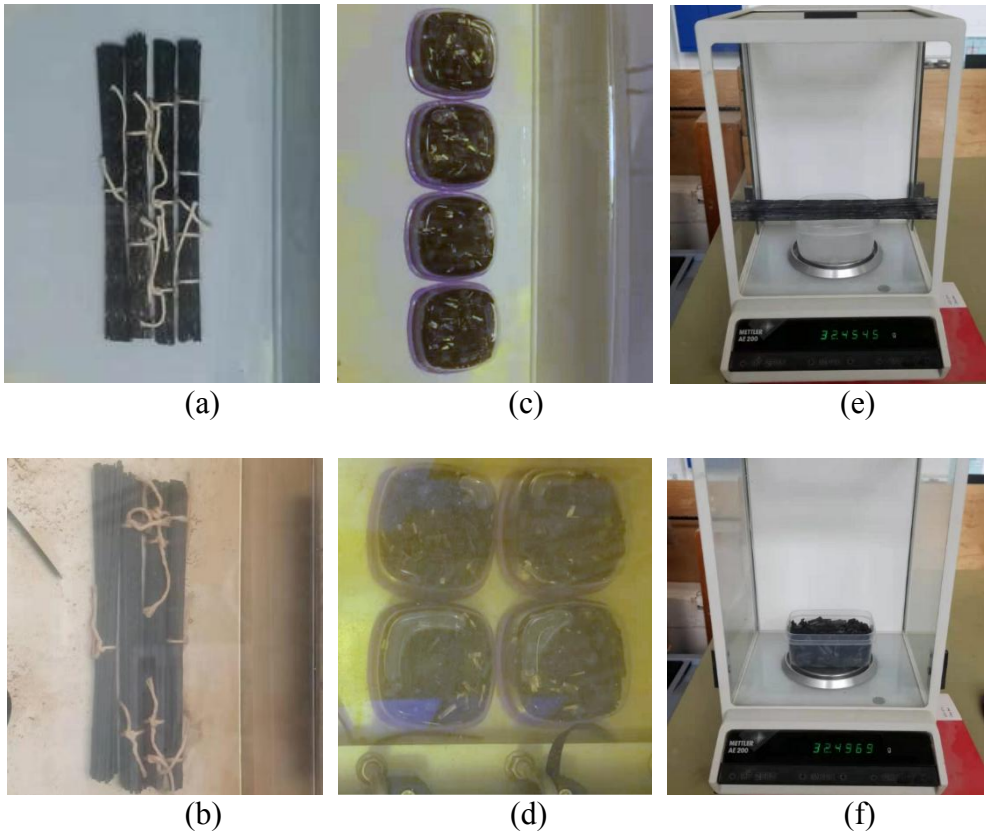

Fig.4-17 Water uptake test for CFS: (a) 240 mm long CFS immersed in 20 °C seawater; (b) 240 mm long CFS immersed in 60 °C seawater; (c) 6 mm short CFS immersed in 20 °C seawater; (d) 6 mm short CFS immersed in 60 °C seawater; (e) weigh 240 mm long CFS by the digital analytical balance; (f) weigh 6 mm short CFS by the digital analytical balance.

4.4 Preparation of cylindrical CFSRM specimens

Pull-out test is conventionally adopted to study the interfacial bond performance of two materials. RILEM-CEB-FIP-RC6 focuses on the bond between the steel rebar and concrete, which suggests that the cubic concrete size of 100*100*100 mm^3 should be used and the steel rebar is up to 12 mm of diameter (RILEM, 1983). CEN–EN 10080 recommends a cubic specimen of 200 mm in length and a rebar with the embedded length five times longer than its diameter (European Committee for Standardization, 2005). ASTM D7913 proposes a test method for bond strength between FRP rebar and its substrate, where the specimen size follows the same as that of pull-out test for steel reinforced material (ASTM International, 2020b).

There have been several pull-out testing guidance for fibre composite materials (ASTM International, 2020b; ASTM International, 2021; Canadian Standards Association, 2021). For instance, CAN/CSA S806 and ASTM D7913 focus on FRP bar, while ASTM D7522 focuses on FRP laminate. These codes highlight the minimum side length of the cubic specimen used to embed FRB bar with 150 mm, because the minimum side length should be five or six times longer than the diameter of FRP bar to avoid splitting.

CFS used herein is much smaller than the rebar, with the diameter of less than 2 mm. Thus the recommended specimen sizes for steel reinforced specimen may not be suitable for CFSRM in this study. To solve such a problem, existing literature has proposed special test methods for pulling out very thin FRP composites from its substrate. Portal et al. (2014) and Bielak et al. (2018) use thin plate samples to conduct pull-out test by embedding the FRP reinforcement in the middle of the plate, as shown in Fig.4-18. The bond length is controlled by saw cutting or drilling hole in this method. Although such a

specimen has its unique advantages of easy gripping by the testing machine, the rather slender geometry of the specimen means that it is prone to damage during its preparation and handling, such as carving notch (Nadiv et al., 2017a), saw cutting and drilling hole (Lorenz and Ortlepp, 2012; Bielak et al., 2018), due to the brittle nature of mortar materials. All those would eventually lead to an underestimation of the bond performance and add uncertainty to test results.

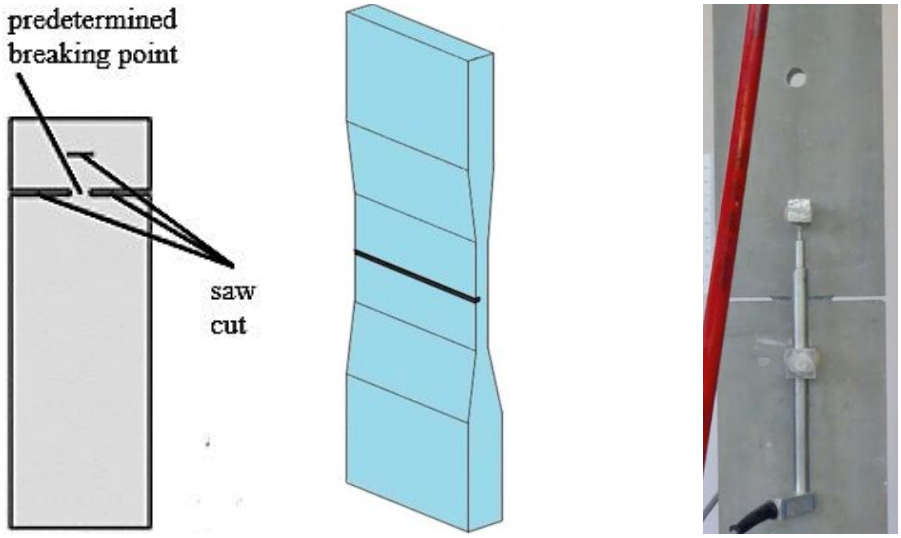

(a) (b) (c)

Fig.4-18 Specimen shapes and preparation methods for fibre strand pull-out test: (a) control the bond length through saw cutting (Lorenz and Ortlepp, 2012); (b) control the position of pull-out happening through carving notch (Nadiv et al., 2017a); (c) control the bond length through drilling hole (Bielak et al., 2018).

In order to simplify the specimen making process and improve its reliability, this research adopted the specimen shape from the classic pull-out test, where the CFS was embedded in a mortar cylinder with a diameter of 20 mm and a length of 50 mm, as shown in Fig.4-19. According to the existing research on interfacial debonding failure (Cheng et al., 2020), the bond behaviour depends on the effective bonding length, namely the local debonding region within a limited length instead of the entire interface. In this study, pull-

out trials with different bond length before the formal tests showed that 50 mm was the effective bonding length which can take the full advantage of bond properties between fibre strand and mortar. Before 50 mm, peak pull-out force increased with bond length, but it would not increase anymore if the bond length continued to increase. Thus the specimen should have its bond region of 50 mm in length, between the mortar substrate and the strand reinforcement.

Fig.4-19 CFSRM specimen used in the pull-out test.

As grain coating is a simple and commonly used method to enhance the bond performance at the interface between fibre based reinforcement and the mortar substrate (Nadiv et al., 2017b; Solyom and Balázs, 2020), this surface treatment method was also adopted in the present study. First the CFS reinforcement was cut into 230 mm in length. Such a length contains four parts with different function regions, including 50 mm of CFS/SM bond region, 10 mm of junction region between SM and aluminium tube, 150 mm of CFS anchorage region embedded in the aluminium tube and 50 mm of CFS/aluminium anchorage end tightly gripped by the jigs of Instron testing machine. Before being embedded in the cylindrical mortar substrate, the CFS surface was coated by a thin layer of epoxy resin and then covered by sprinkled fine sea sand of up to 2 mm in size, as shown in Fig.4-20. The sand coating covered 50 mm length of each CFS from its end,

corresponding to the design bond length of CFSRM specimen. Note that the fine sea sand used here was the same as the sand used in the mortar mix design. After the sand coating treatment, CFS reinforcements were cured in air at the room temperature for seven days before being embedded in the cylinder.

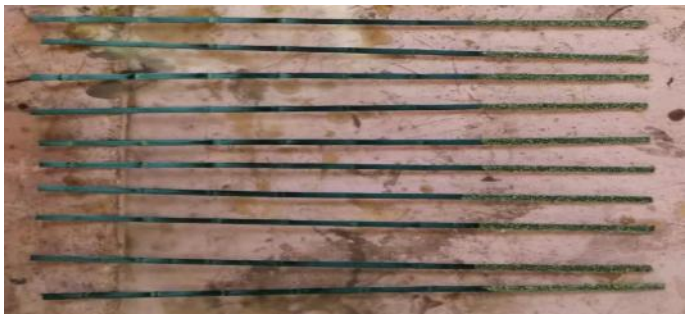

Fig.4-20 Sand coating treatment.

Another essential step was preparing the anchorage end of the specimen. Similar to the CFS tensile test, to improve the anchorage, an aluminium tube (Fig.4-21) of 3 mm in diameter and 170 mm in length was used to glue to the loading end of each CFS. The interior space of the tube was fully injected with epoxy resin to fix CFS inside the tube. The curing time for this step lasted for seven days under indoor ambient conditions before testing.

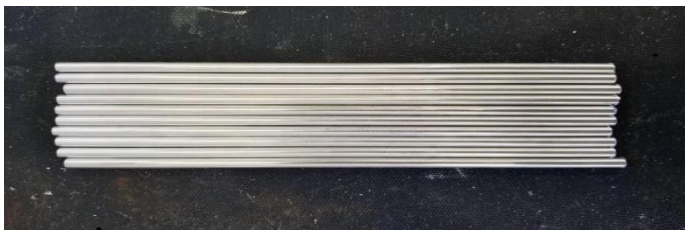

Fig.4-21 Aluminium tubes applied to cover the anchorage region of CFS.

To sum up, the entire making process of CFSRM specimens can be given as follows: (1) cut CFS reinforcements from the carbon fibre mesh to 230 mm in length; (2) apply sand

coating treatment to the CFS surface with the length of 50 mm from one end, and cure it in the air at the room temperature for one week; (3) prepare the fresh mortar and use it to fill the specimen mould; (4) vertically insert the CFS into the centre of the mould filled with the mortar substrate while vibrating; (5) demould after 24 hours and cure these specimens in 20 °C seawater for 28 days; note that the control group of specimens which use freshwater to cast the mortar substrate are cured in freshwater; (6) take out specimens from the curing tank and dry them in the air for 24 hours; (7) anchor the CFS to the aluminium tube using epoxy resin and cure it in the air at the room temperature for another week; (8) mark the free surface of CFS at the junction area, as shown in Fig.4-22, to observe whether or not CFS is pulled out from mortar substrate and in the meanwhile no slip appears between CFS and the aluminium tube during the pull-out process.

After a series of preparation procedures above, the completed CFSRM specimen is displayed in Fig.4-22.

Fig.4-22 The completed CFSRM specimen for the pull-out test.

In order to accommodate the small dimensions of the specimens, a custom made apparatus was designed and manufactured using stainless steel for this study, as shown in Fig.4-23. The upper and the lower plates have identical dimensions, with length, width and thickness of 100 mm, 56 mm and 25 mm respectively. The diameter of the threaded bar is 18 mm.

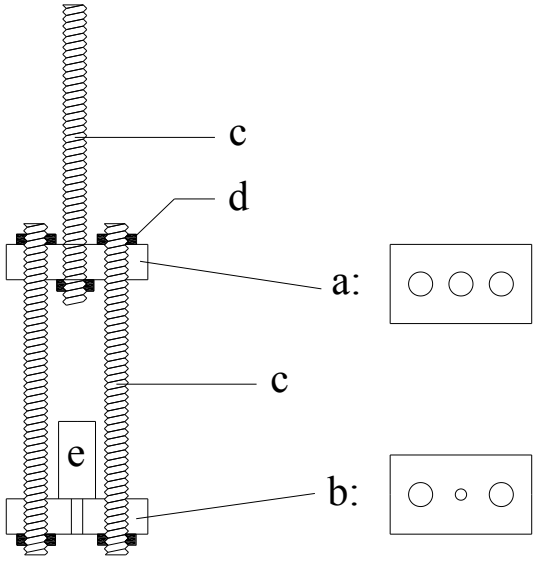

Fig.4-23 The diagram of the stainless steel apparatus used for pull-out test: (a) the upper plate; (b) the lower plate; (c) the threaded bar; (d) nuts; (e) CFSRM specimen.

The stainless steel used for the apparatus has a grade of 304 which is widely used in engineering and scientific research with a Young's modulus ranging from 200 to 250 GPa (Velasco et al., 2009; Rabi et al., 2019). The relevant early trial results indicate that the ultimate pull-out force would not exceed 2.5 kN. Thus the maximum tensile deformation of the apparatus during the loading process can be obtained as follows

$$\Delta l_{tr} = \Delta l_{tr1} + \Delta l_{tr2} = \frac{P l_{tr1}}{A_{tr1} E_{tr}} + \frac{P l_{tr2}}{A_{tr2} E_{tr}} \tag{4-2}$$

where Δl_{tr1} and Δl_{tr2} are the bar tensile deformation at the upper half and the lower half respectively; P is the tensile force provided by the mechanical testing machine; E_{tr} (200 GPa) is the elastic modulus of the stainless steel threaded rebar used in the apparatus; l_{tr1} (the bar length at the upper half) and l_{tr2} (the bar length at the lower half) have the same value of 150 mm; A_{tr1} (the rebar cross-sectional area at the upper half) and A_{tr2} (the rebar cross-sectional area at the lower half) are 254.5 mm^2 and 508.9 mm^2 respectively.

Therefore, the maximum tensile deformation of the apparatus under the loading is only about 11.05 μm, which is much smaller than the expected slip distance between CFS and mortar substrate.

Following the recommendations of RILEM TC 232-TDT combined with the existing studies of pull-out tests (Brameshuber et al., 2016; Raoof et al., 2016), two extensometers was used to measure the pull-out distances at two opposite sides of the sample, as shown in Fig.4-24. The actual pull-out distance was taken as the average of the two readings, to eliminate any bending deformation caused by eccentricity. Displacement control method was used, with a loading rate of 0.05 mm/min. This resulted in a strain rate of 1e-3/min, which was considered adequately to avoid any dynamic effect, and agreed with the existing researches (Butler et al., 2009; Brameshuber et al., 2016; Kabir et al., 2016; Raoof et al., 2016; Schütze et al., 2018).

The pull-out test setup is illustrated in Fig.4-24. The pull-out test follows a procedure: (1) put the stainless steel apparatus into the Instron mechanical testing machine and fix its top end; (2) put the specimen into the apparatus and let the anchorage end of CFS go through the middle hole of the lower plate; (3) use the jig of the Instron to grip the aluminium tube that embeds the anchorage region of CFS; (4) place two digital dial indicators at the front and rear of the lower plate to record the displacement data during the test; (5) start the pull-out loading by 0.05 mm/min; (6) terminate the test when the specimen reaches the complete failure status, i.e. the pull-out force has a sharp drop which suggests that the interface between CFS and mortar has been debonded.

Fig.4-24 Pull-out test setup.

In order to acquire the pull-out test data for the subsequent durability study on CFSRM, two batches of four samples cast by seawater and freshwater (control group) respectively were prepared here for the static pull-out test, as shown in Fig.4-25.

Fig.4-25 Samples used for static pull-out test: seawater batch (PI-1, 2, 3, 4) and freshwater batch (PI-1F, 2F, 3F, 4F).

4.5 Mortar test results and analysis

4.5.1 Physical properties

The failure modes of the mortar specimens for both compressive strength tests and tensile splitting tests are displayed in Fig.4-26. Fig.4-26a and Fig.4-26b show the SM specimens in study group (cast by seawater) with curing duration of 28d and 90d respectively, while Fig.4-26c and Fig.4-26d present the FM specimens in control group (cast by freshwater) with curing duration of 28d and 90d respectively. In spite of different curing durations or the usage of seawater/freshwater, it can be found that the mortar failure mode is similar among those specimens. In addition to those specimens used for strength tests, Fig.4-27 displays the tested SM specimens for the uniaxial compressive elastic modulus test after 28 days of curing.

(a) (b) (c) (d)

Fig.4-26 Tested specimens of the mortar compression test and the splitting tensile test: (a) study group with 28 days curing; (b) study group with 90 days curing; (c) control group with 28 days curing; (d) control group with 90 days curing.

Fig.4-27 Tested specimens of mortar uniaxial compressive elastic modulus test.

The mortar density is calculated using Eq.4-3:

$$\rho_{mo} = \frac{\rho_{water} m_{wa}}{(m_{wa} - m_{ww})} \tag{4-3}$$

where ρ_{mo} is the density of mortar specimens; ρ_{water} is the density of freshwater, with 1000 kg/m^3; m_{wa} and m_{ww} are the specimen mass weighed in the air and water respectively.

Eq.4-4 and Eq.4-5 are used to calculate the cubic compressive strength and the cylindrical splitting tensile strength respectively, according to the testing standard BS EN 12390-3 and BS EN 12390-6 (British Standards Institution, 2009; British Standards Institution, 2019a).

$$f_{mc} = \frac{F_{mc}}{A_m} \tag{4-4}$$

$$f_{mt} = \frac{2F_{mt}}{\pi L_{ts} d_{ts}} \tag{4-5}$$

where f_{mc} and f_{mt} are the compressive strength and the splitting tensile strength of mortar respectively; F_{mc} and F_{mt} are the maximum load of the compressive test and the splitting tensile test; and A_m is the single surface area of the cubic mortar specimen that sustains compressive force.

As a typical linear elastic and brittle material, the force-displacement curves of SM prism compression test feature linear growth before the specimen failure, as shown in Fig.4-28.

Based on the slope of curve, the elastic modulus of SM material after 28 days of curing can be derived as

$$E_{SM} = \frac{F_{pl}L_{pl}}{\Delta l_{pl}A_{pl}} \tag{4-6}$$

where E_{SM} is the SM elastic modulus; F_{pl} and Δl_{pl} are the uniaxial compressive force acting on the specimen and the corresponding axial deformation within the testing zone respectively; $L_{pl} = 100$ mm, denoting the length of the prism specimen; and $A_{pl} = 1600$ mm^2, denoting the cross-sectional area of the prism specimen.

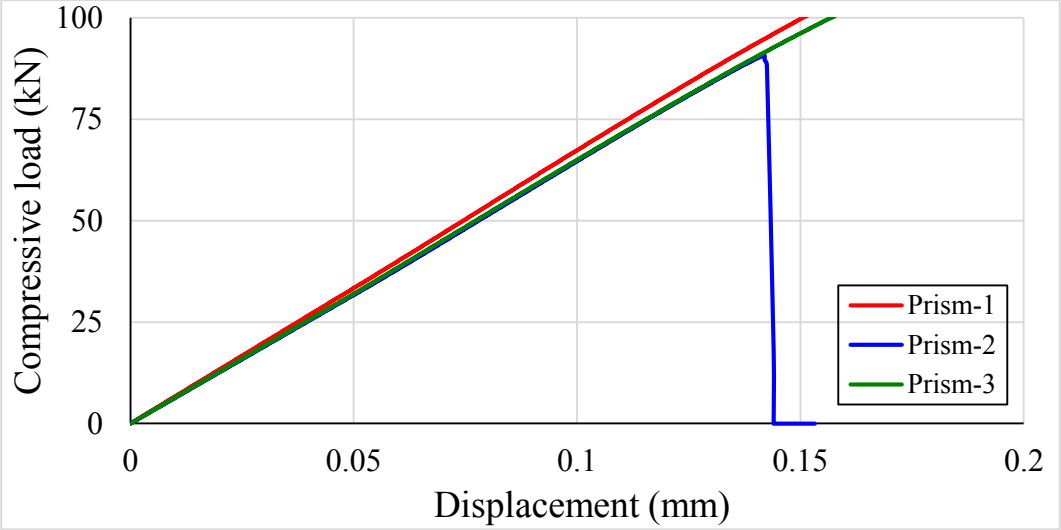

Fig.4-28 Force-displacement curves of SM prism compression test.

Each test has been repeated three times, and the standard deviation (SD) is used to assess the data reliability. Table 4-2 below summarises the average values of all test results based on cubic and cylindrical mortar specimens.

Table 4-2 Test results for cubic and cylindrical mortar specimens.

Type	Group	Curing days	ρ_{mo} kg/m^3 (SD)	F_{mc} & F_{mt} kN (SD)	f_{mc} MPa (SD)	f_{mt} MPa (SD)
Cube	Study group	7	2302 (6.6)	523 (6.0)	52.3 (0.60)	
		14	2301 (5.0)	631 (9.3)	63.1 (0.93)	
		28	2315 (4.9)	699 (4.4)	69.9 (0.44)	
		90	2324 (6.4)	775 (8.0)	77.5 (0.80)	
Cube	Control group	7	2309 (5.5)	464 (4.6)	46.4 (0.46)	
		14	2308 (6.1)	592 (3.2)	59.2 (0.32)	
		28	2309 (4.7)	707 (6.5)	70.7 (0.65)	
		90	2317 (7.8)	801 (14.7)	80.1 (1.47)	
Cylinder	Study group	7	2300 (5.8)	157 (8.1)		5.0 (0.26)
		14	2302 (6.1)	176 (10.9)		5.6 (0.35)
		28	2310 (9.6)	179 (4.8)		5.7 (0.15)
		90	2321 (6.2)	191 (15.4)		6.1 (0.49)
Cylinder	Control group	7	2298 (2.0)	144 (3.7)		4.6 (0.12)
		14	2310 (7.0)	169 (3.3)		5.4 (0.11)
		28	2317 (2.8)	181 (12.9)		5.8 (0.41)
		90	2317 (4.9)	200 (11.5)		6.4 (0.37)

In addition, the uniaxial compressive elastic modulus E_{SM} for SM prism specimens after 28 days of curing can be obtained as per Eq.4-6, with an average value of 40.4 GPa, and standard deviation (SD) of 1.13.

As shown in Fig.4-29, the mortar density of specimens saw a slight rise with curing days. By comparing between the average values of the densities of all specimens cured in 7

days and 90 days, nearly 1% of density growth can be found. As curing days grow, the growth of mortar density can be attributed to the water uptake inside the mortar. Since mortar specimens were continuously cured in seawater/freshwater, the water diffusion into mortar went on constantly until reaching the saturation. In order to investigate such a phenomenon, Section 4.2.3 and 4.5.2 study the water diffusion behaviour of mortar in more detail.

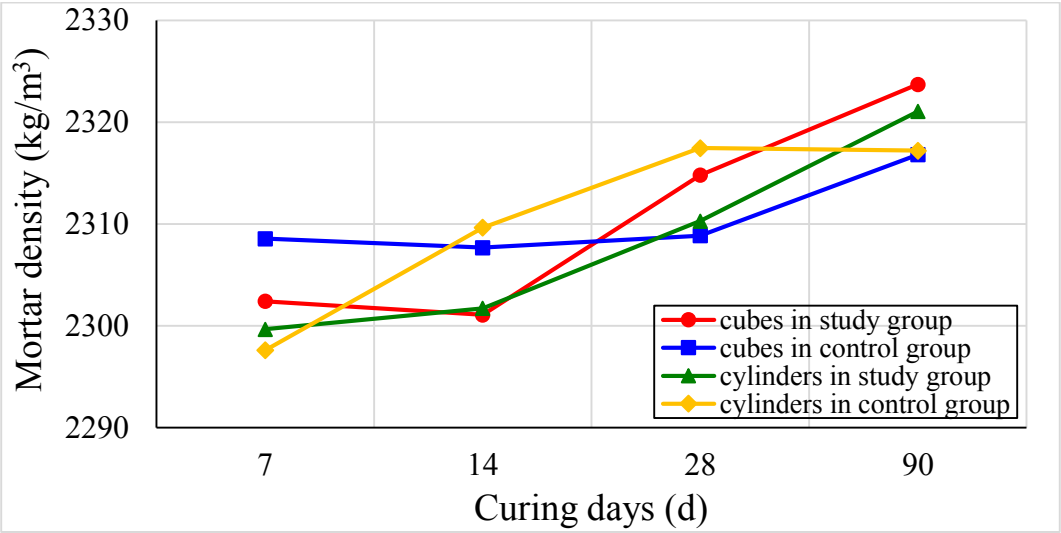

Fig.4-29 The measurement results of mortar density with different curing times.

Fig.4-30 and Fig.4-31 show the test results of mortar compressive strength and splitting tensile strength respectively. Both the compressive strength and splitting tensile strength increased with curing days rising, for both the SM and FM. The 28d standard compressive and splitting tensile strength in study group were 69.9 MPa and 5.7 MPa, while they were 70.7 MPa and 5.8 MPa in control group respectively. Furthermore, their strength growth curves indicate that the increase rate slowed down with the increase of curing time.

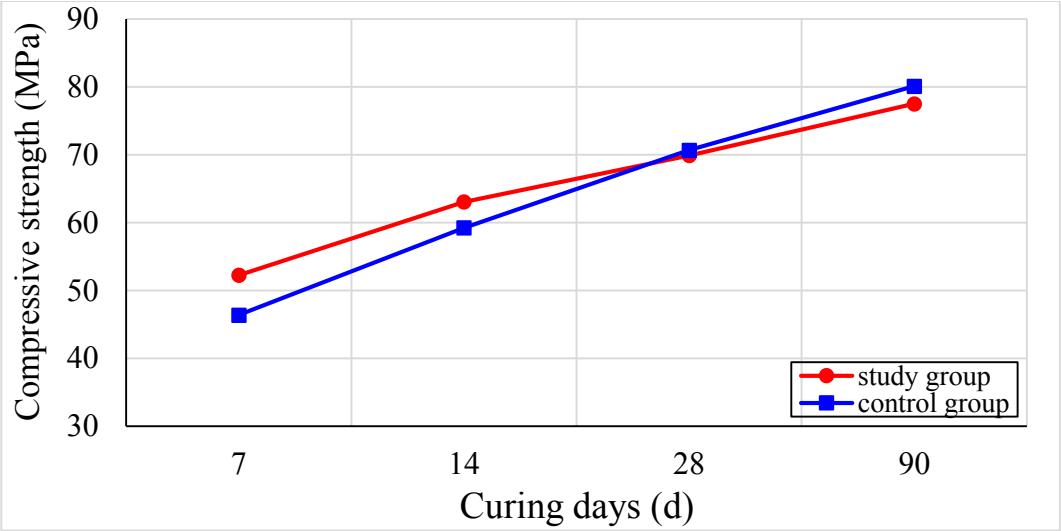

Fig.4-30 Mortar compressive strength with different curing days.

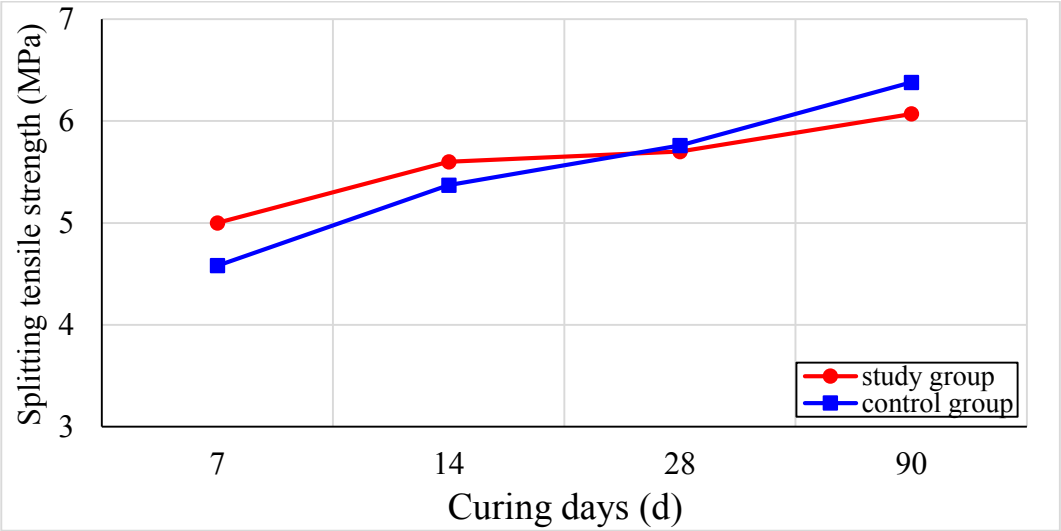

Fig.4-31 Mortar splitting tensile strength with different curing days.

Although strength curves in Fig.4-30 and Fig.4-31 have a similar rising trend for both groups, SM specimens had a higher early strength than FM specimens. For compressive strength, the value in the study group is higher by 12.7% in 7d and 6.5% in 14d compared with the control group. For splitting tensile strength, values in the study group are 9.2% and 4.3% higher than the control group cured in 7 and 14 days respectively.

While tested mortar specimens in both groups had a similar 28d standard strength with the difference around 1%, the long-term strength (90d) of SM specimens was lower than FM specimens by 3.2% in compressive strength and 4.9% in splitting tensile strength as shown in Fig.4-30 and Fig.4-31. This phenomenon indicates the strength growth rate of the study group after 28 days curing is relatively slower than the control group. During the hardening and curing process, chloride ions participate in the mortar hydration reaction in the study group while the control group uses fresh water without any chloride ions. Existing literature has demonstrated that the chloride ion plays a role like the hardening accelerator, as it can facilitate the early hydration up to 28 days but decelerate the later hydration (Ogirigbo and Ukpata, 2017; Han et al., 2021). Based on the 28d standard strength, 90d compressive strength and splitting tensile strength can reach 110.9% and 106.5% in the study group, while they were 113.3% and 110.8% respectively in the control group.

Existing studies revealed similar test results about mortar strength changes (Wegian, 2010; Xiao et al., 2017). Experiments conducted by Wegian (2010) and Xiao et al. (2017) showed that mortar cast by seawater usually had a higher early strength than freshwater. This is because the chloride ion present in seawater can accelerate the mortar setting and hardening process at early stage (Lu et al., 2018; Li et al., 2021). It plays the role like the hardening accelerator as it reacts with tricalcium aluminate in mortar and then generates the Friedel's salt, which accelerates the hydration of tricalcium aluminate and thereby contributes to the increase in the early strength (Li et al., 2021; Zheng et al., 2021). However, its long-term strength was expected to be the same or slightly lower than that of the specimen cast by freshwater (Wegian, 2010; Xiao et al., 2017). In this study, the mortar strength in the study group and the control group had the same development trend during the early stage. For 28d standard strength, test results in the study group were

considerably close to the control group. Thus it can be summarised that the usage of seawater in SM casting had no obvious influence on its mechanical properties in terms of strength, compared with its control group consisting of FM.

Another mortar material property is the flowability of fresh mortar. The present study used flow table, as introduced in Section 4.2.2. The flow table test result of fresh mortar is shown in Fig.4-32. Then the flowability of SM and FM can be evaluated using Eq.4-7 as

$$Fl = \frac{d_{Fl} - d_{ob}}{d_{ob}} \times 100 \tag{4-7}$$

where Fl denotes the value of mortar flowability; d_{Fl} is the average dimension of the spread fresh mortar specimen in two directions perpendicular to each other when the shaking work for the flow table finishes; and d_{ob} represents the original base diameter of the fresh mortar specimen before the removal of the mould used to hold the specimen, with the length of 100 mm.

Fig.4-32 Flow table test result of fresh mortar.

Substituting measured dimension data into Eq.4-7, the flowability for SM is found as $Fl = 41.7$ with the standard deviation of 1.05, while Fl for FM is calculated as 43.4 with the standard deviation of 1.28. There is little difference of flowability between SM and

FM, as Fl value of FM is only 4.1% higher than that of SM. This concludes that the use of seawater has almost no influence on the fresh mortar flowability.

4.5.2 Water uptake behaviour of seawater mortar

4.5.2.1 Results analysis and parameters calculation

In accordance with the water uptake test method for mortar introduced in Section 4.2.3, the mass variation was recorded for four SM cylindrical specimens individually under 60 °C immersion condition over 180 days. Then the water absorption mass growth $M_{SMC}(t)$ for each specimen can be calculated by Eq.4-8 as

$$M_{SMC}(t) = M_{SMCt} - M_{SMCd} \tag{4-8}$$

where M_{SMCt} is the current mass after removing its surface moisture; M_{SMCd} is the initial mass of that specimen after 72 hours of oven drying treatment.

Water uptake test results for all specimens are shown in Fig.4-33. Note that specimens used here are named by WU60-SMC-1, 2, 3, 4 respectively, where WU denotes water uptake test; 60 means the temperature at 60 °C; SMC means cylindrical specimen made of seawater mortar and the last term is the serial number of those specimens.

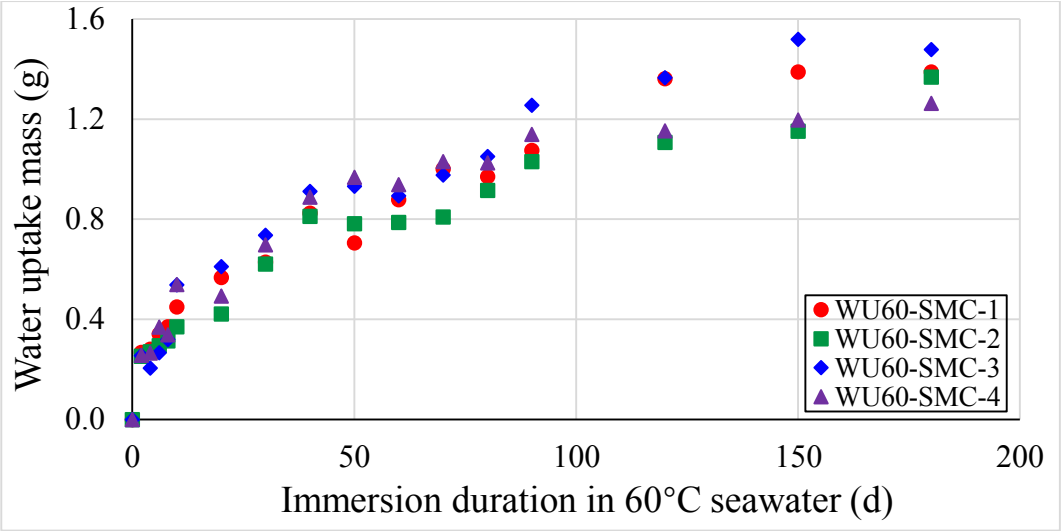

Fig.4-33 Water uptake mass growth of four SM cylindrical specimens up to 180 days of 60 °C seawater immersion.

The water absorption mass varied between 1.26 g and 1.48 g by the 180th day, with an average value of 1.37 g. Although the water absorption speed slowed down over time, it had not yet reached its plateau by the end of the test. The average value of water uptake at the 120th, 150th and 180th day still had an increase of 5.4% and 4.6% at each 30-day interval.

Even using 60 °C elevated temperature immersion method to accelerate the water uptake process, it still did not make those specimens attain their moisture saturation condition by the end of the test. This is because SM used in this study features low porosity and thus strong resistance to the internal water mass transfer. It has a relatively low w/b ratio of 0.3 and a series of admixtures like PFA, GGBS and SF to improve the particle size gradation of binder components and thus reduce its water diffusivity. Considering the time restraint of this study, the maximum water uptake mass and diffusivity of the SM specimens is predicted using Fick's second Law, by assuming homogeneous composition of the mortar materials.

Based on the experimental data of the water uptake test in this study, the maximum moisture absorption at the saturation status (M'_{SMC}) and the water diffusion coefficient of SM material (D_{SM}) can be determined using Eq.3-3, with the value of $M'_{SMC} = 1.97$ g and $D_{SM} = 7.89*10^{-13}$ m^2/s at 60 °C. Then the saturated water absorption of SM material (PA'_{SM}) can be obtained as 5.4%, using Eq.4-9:

$$PA'_{SM} = \frac{M'_{SMC}}{M_{SMCd}} \times 100\% \tag{4-9}$$

where M_{SMCd} has been weighed as 36.15 g.

In addition, the saturation concentration of SM (C'_{SM}) can be derived by Eq.4-10. The value has been found to be 125.38 kg/m^3, or 6965.28 mol/m^3, considering that the molar mass of water molecules is 18 g/mol.

$$C'_{SM} = \frac{M'_{SMC}}{V_{SMC}} \tag{4-10}$$

where V_{SMC} is the volume of the cylindrical SM specimen with 50 mm height and 20 mm diameter.

The moisture saturation of the specimen $S_{SMC}(t)$ at any time t in percentage terms is described as

$$S_{SMC}(t) = \frac{M_{SMC}(t)}{M'_{SMC}} \times 100\% \tag{4-11}$$

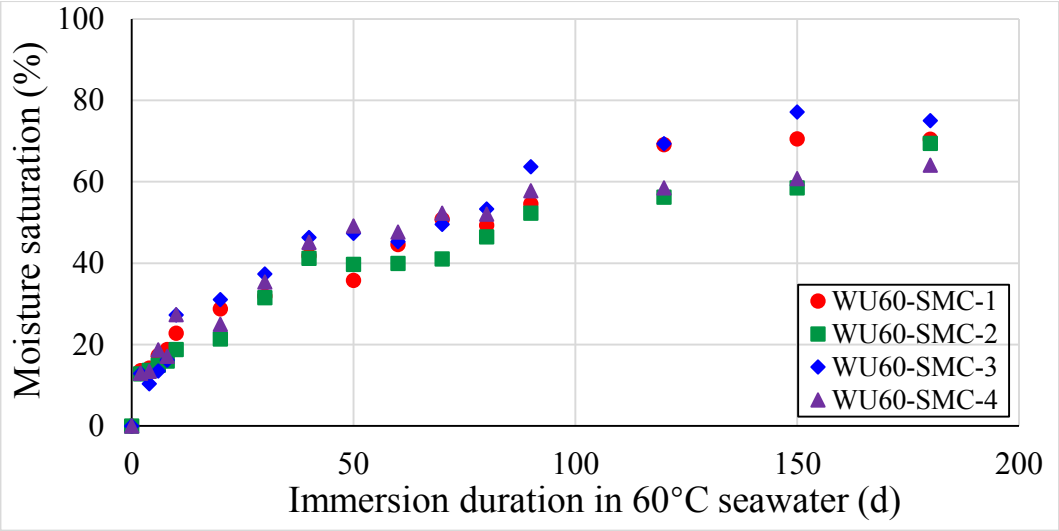

Fig.4-34 The moisture saturation analysis of four specimens immersed in seawater at 60 °C.

By using Eq.4-11, Fig.4-34 reveals the water uptake test results for all specimens in terms of the moisture saturation. From Fig.4-34, it can be found that the average moisture saturation in the water uptake test just attains around 69.8% by the end of the test. According to the analysis results, S_{SMC} has an increase of 57.1% and 12.7% during the first and second 90 days of 60 °C immersion respectively. Obviously, the growth rate of S_{SMC} for the specimen slows down gradually with immersion time.

4.5.2.2 Temperature effect on water diffusion of mortar

By using Eq.4-8, 20 °C water uptake test results for four SM cylindrical specimens are shown in Fig.4-35 wherein the specimens are named by WU20-SMC-1, 2, 3, 4 respectively. The test lasted for 180 days, following the method given in Section 4.2.3.

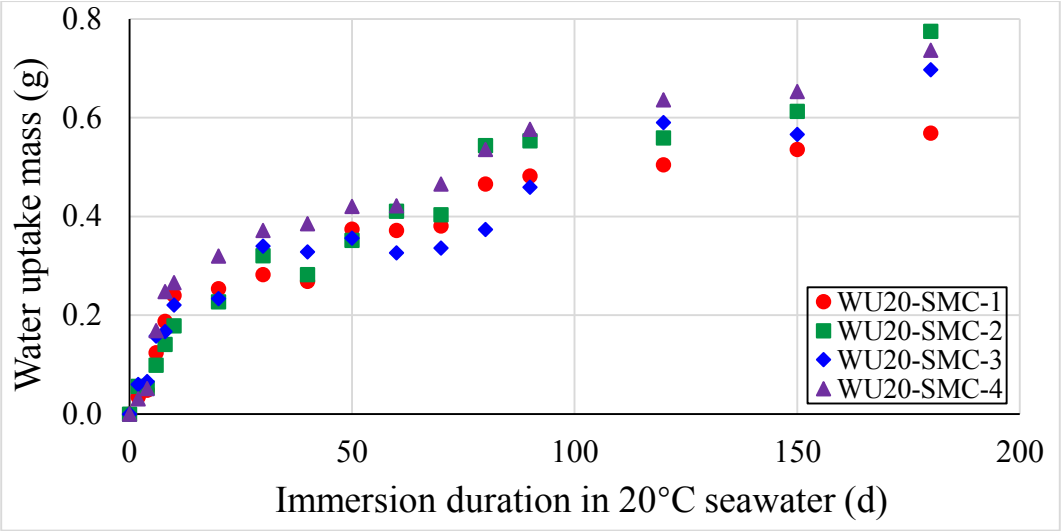

Fig.4-35 Water uptake mass growth of four SM cylindrical specimens up to 180 days of 20 °C seawater immersion.

The average water uptake growth $M_{SMC}(180)$ at 20 °C for all specimens is 0.69 g by the end of the test, nearly 50% lower than the value for the 60 °C test group. Compared with Fig.4-33, the growth rate of water uptake is much slower in Fig.4-35. This phenomenon proves that the water diffusion behaviour is subject to temperature changes and reducing the immersion temperature in a certain scope would retard the rate of water uptake for SM material.

Combined with M'_{SMC} which has been given in Section 4.5.2.1 with the value of 1.97 g, the present study substitutes the test results that constitute Fig.4-35 into Eq.3-3. D_{SM20}, serving as the water diffusion coefficient of SM material at 20 °C, can thus be obtained as $1.30*10^{-13}$ m^2/s.

With temperature rising from 20 °C to 60 °C, the ratio of the diffusion coefficient, D_{SM}/D_{SM20}, is 6.07. In accordance with Arrhenius Law and time-temperature superposition principle introduced in Section 3.2.2, raising temperature can accelerate the water uptake process in the SM cylindrical specimen because there is a unique

relationship between $D_{SM}(T)$ and T (temperature). Upon the decision of the water diffusion activation energy of SM (E_{aMW}), D_{SM} with an arbitrary T can be found out by using α_T which is defined as the shift factor of time-temperature superposition used for water diffusion as per Eq.3-9. Based on Eq.3-3, $M_{SMC}(t)$ at an arbitrary T and t can also be deduced once $D_{SM}(T)$ is acquired. In brief, employing Arrhenius Law along with E_{aMW} makes it viable to evaluate the water uptake behaviour of SM specimens with the variations in temperature ranging from 20 °C to 60 °C.

To derive the value of E_{aMW}, this study substitutes D_{SM} and D_{SM20} into Eq.3-8. Note that D_{SM} along with its corresponding temperature of 60 °C acts as the initial value of the diffusion coefficient D_0 and temperature T_0 respectively in Eq.3-8. Then E_{aMW} is found to be 36.60 kJ/mol.

Fig.4-36 shows the water uptake test results for all specimens under 20 °C. Note that its comparison that records the water uptake test results under 60 °C is given in Fig.4-34 in terms of the moisture saturation. As the immersion temperature declines to 20 °C, the final moisture content only attains 35.3% of the complete saturation by the end of the duration of 180 days, whereas this value at the temperature of 60 °C is approximately twice higher than 20 °C. Under the condition of 60 °C, it only takes the specimens 30 days to attain the same degree of saturation compared with those at the 180th day of immersion at 20 °C.

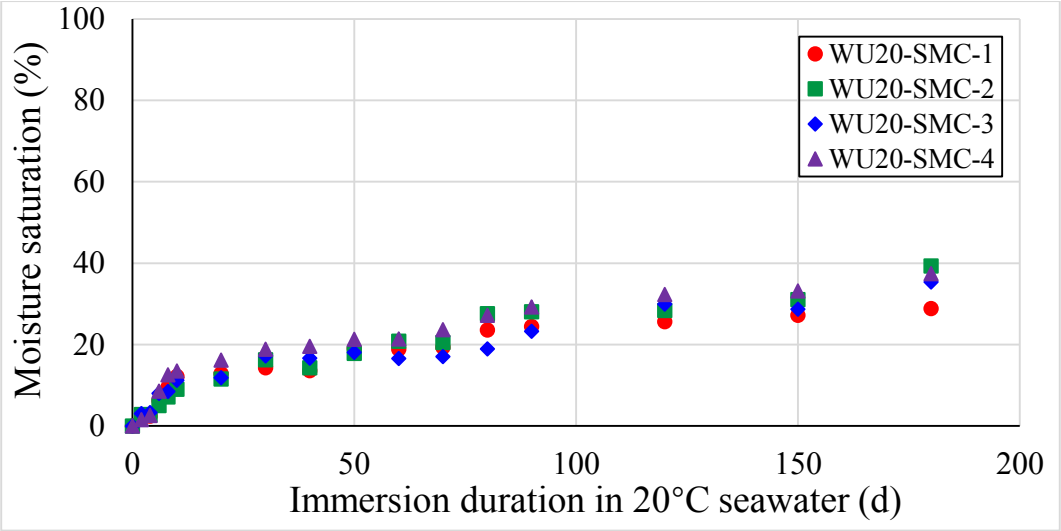

Fig.4-36 The moisture saturation analysis of four specimens immersed in seawater at 20 °C.

Taking the temperature effect mentioned above into consideration, and by employing Arrhenius Law along with E_{acW} that is deemed as the intrinsic property of SM material, its water uptake behaviour at an arbitrary T can be calculated, thereby providing the support for the later numerical and experimental studies on the water-dependent durability performance of CFSRM specimens.

4.6 Test results and analysis of carbon fibre strand (CFS)

4.6.1 Geometric and mechanical properties

This section presents the physical properties of CFS including its cross-sectional geometry, transverse hygroscopic swelling ratio, ultimate tensile strength, and uniaxial tensile elastic modulus. As illustrated in Fig.4-37, eight cross sections stemming from the random selection of CFS samples were measured using the microscope after the material surface polishing treatment. The cross section of eight selected samples has an average area of 1.552 mm^2. The standard deviation of all measured values is 0.09, which indicates

a good consistency of the cross-sectional area of CFS materials used in this study. Table 4-3 presents all the measured CFS cross-sections.

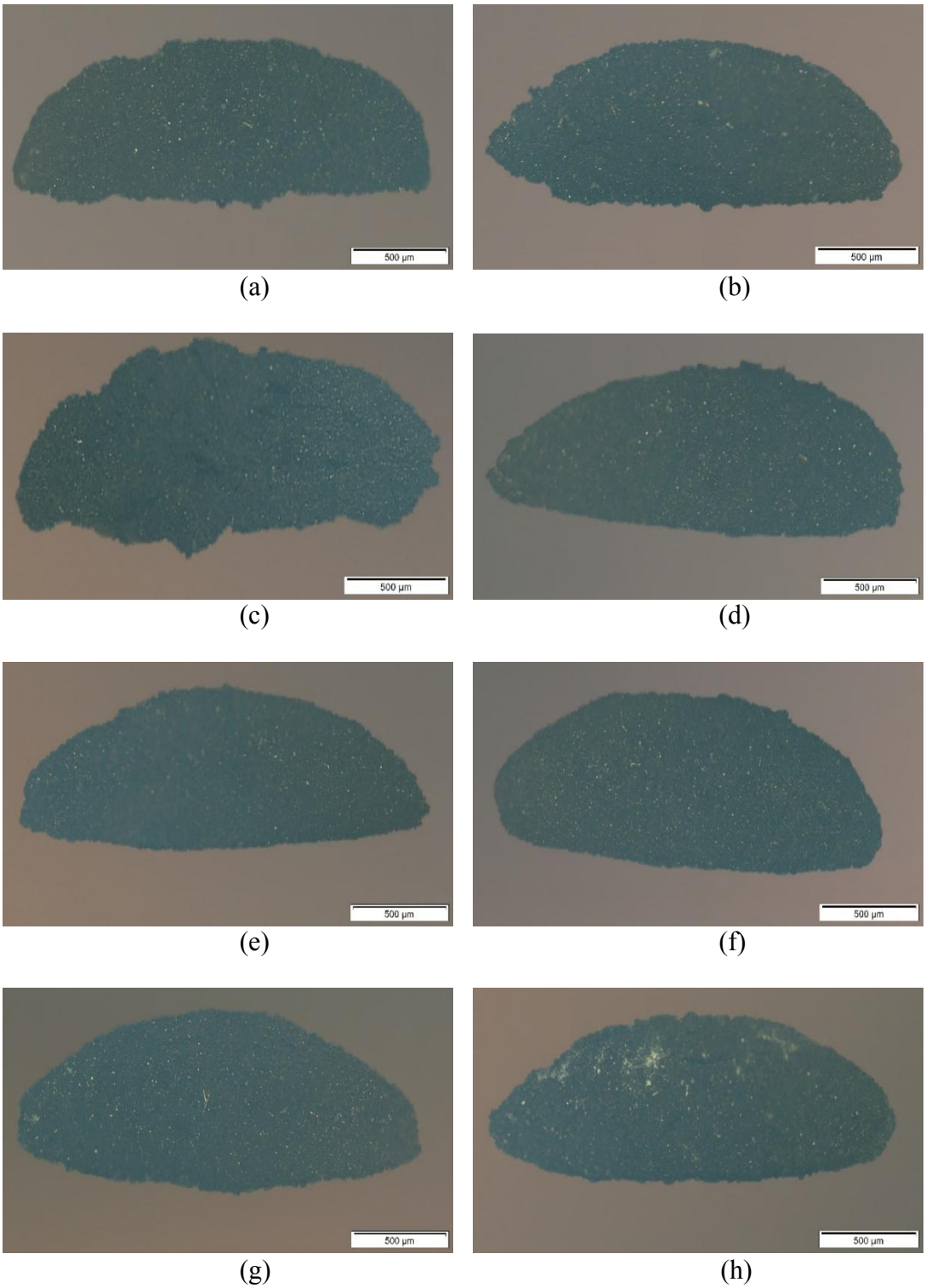

Fig.4-37 Measurement results of the CFS cross section: (a) to (h) correspond to the sample serial number 1 to 8 in Table 4-3 respectively.

Table 4-3 CFS cross-sectional areas in the initial state and after saturated hygroscopic swelling.

	CFS cross-sectional area (mm^2)							
No.	1	2	3	4	5	6	7	8
initial state	1.627	1.402	1.669	1.583	1.456	1.552	1.635	1.492
saturated state	1.640	1.414	1.678	1.597	1.465	1.561	1.647	1.504

In addition to the CFS cross-sectional areas in its initial dry state, Table 4-3 also records the area changes owing to the hygroscopic swelling effect. Once CFS samples reached the moisture saturation condition after immersion into seawater, they were considered to attain the highest transverse hygroscopic swelling strain. The cross-sectional area of CFS samples at moisture saturation has an average value of 1.563 mm^2 with the standard deviation of 0.09.

As shown in Fig.4-37, the shape of CFS cross section can be considered as a circle in the simplified analysis. Let an arbitrary point inside the circular cross section share the same value of the transverse strain. The maximum cross-sectional expansion strain ε'_{HE} under its moisture saturation condition thus can be defined as

$$\varepsilon'_{HE} = \sqrt{\frac{A'_{CFS} - A_{CFS}}{A_{CFS}}} \tag{4-12}$$

where A'_{CFS} and A_{CFS} denote the measured CFS cross-sectional area in the moisture saturation state and the initial dry state respectively. Substituting the measurements shown in Table 4-3 into Eq. 4-12, the average value of ε'_{HE} for all CFS samples used here is found to be $3.60*10^{-3}$.

In order to explore the coupling relationship between the water diffusion and the hygroscopic stress caused by the swelling deformation inside CFS, Section 3.3 introduces the coefficient of transverse hygroscopic expansion β_{CHE} for CFS material. Then its transverse hygroscopic swelling strain ε_{HE} with arbitrary percentage of water absorption that occupies the mass of CFS under its dry condition, namely PA_{CFS}, can be calculated by Eq.3-11 as given in Section 3.3.

Since the maximum expansion strain ε'_{HE} and the related saturated water absorption mass percentage PA'_{CFS} are acquired, the constant β_{CHE} for the CFS material can be determined according to Eq.3-11, with the value of 0.28. As the interior of CFS absorbs moisture continuously over time, its hygroscopic swelling increases simultaneously as per β_{CHE} until reaching the saturation state. For CFSRM specimens used herein, CFS is embedded in SM substrate, therefore its swelling is confined to its original space. Consequently, the swelling deformation causes local stress inside the specimen, which has an effect on the interfacial bonding when conducting the pull-out test for the reinforcement. Section 5.5 and 7.4 further discuss the effect of hygroscopic swelling mechanism on the pull-out behaviour of CFSRM in terms of the numerical simulation and the experimental phenomena.

A typical tensile failure mode of CFS is shown in Fig.4-38. It can be found that the fracture generally happens at the middle testing region, while the breaking surface is uneven, revealing the irregular rupture characteristics for filaments.

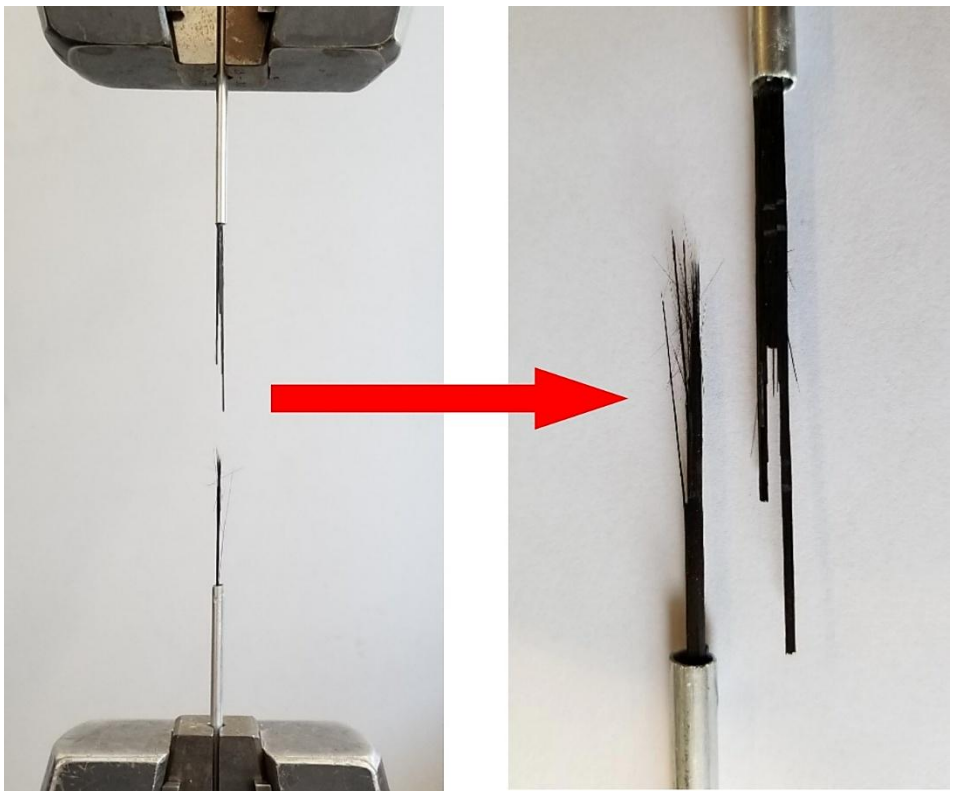

Fig.4-38 Tensile failure of CFS material.

Note that the present tensile test focuses on the basic mechanical properties of CFS specimen including its tensile strength and elastic modulus. The specimens used here all keep in initial state before the test, without any conditioning such as water immersion.

However, plenty of existing studies have indicated that the tensile property changes or any failure mode differences as the results of the tensile test would not occur on the CFS specimen itself before and after immersion treatment (Weitsman, 2012; Kafodya et al., 2015; Heshmati et al., 2016; Benmokrane and Ali, 2018). The ageing treatment of water immersion damages the polymer matrix and the CFS/SM interface, thereby degrading the interfacial bond behaviour and causing the reduction in pull-out performance (Weitsman, 2012). By contrast, carbon fibre is corrosion-free when exposed to moisture (Raman et al., 2020). Unlike the pull-out test, the tensile test is dependent on the tensile behaviour of carbon fibre itself rather than the polymer matrix inside (Spelter et al., 2019). Thus,

the tensile properties including the failure mode of CFS after immersion exposure would not change, compared with the specimen under the initial condition.

Fig.4-39 plots the tensile force-displacement curves for all CFS samples (CFST-1, 2, 3, 4). Contrary to conventional steel reinforcement which has a good ductility, carbon fibre reinforced composite generally can be classified into the brittle material with linear elastic property (Zaidi et al., 2017). From Fig.4-39, it is obvious that the tensile force-displacement curves for all samples have a distinct linear growth with almost the same slope in their early stages. However, with tensile force continuing to go up, these curves experience several modest drops on account of the successive fracture of partial filaments. At last, the tensile force suddenly declines to zero due to the brittle rupture of the main strand. The peak tensile force during the test occurs at the critical point before the fracture failure for all samples. The average value of the peak force is 3.16 kN with the standard deviation of 0.19. Table 4-4 shows the relevant tensile test data for those samples in more detail.

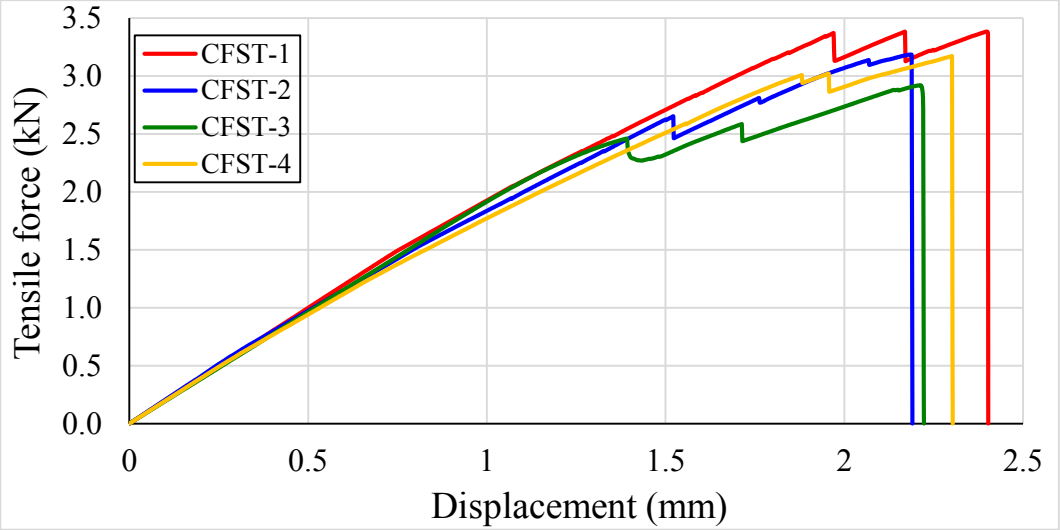

Fig.4-39 CFS tensile test results.

Hooke's Law is applied to calculating fu_{CFS} by substituting the ultimate tensile force Fu_{CFS} during CFS tensile test into Eq.4-13 as

$$fu_{CFS} = \frac{Fu_{CFS}}{A_{CFS}} \tag{4-13}$$

In order to acquire the initial uniaxial tensile elastic modulus of CFS material E_{CFSz}, this study only adopts the testing data at early tensile stage. The testing data within the first 0.5 mm of the tensile displacement is used to calculate E_{CFSz} of CFS material.

As shown in Fig.4-38, the anchorage region embedded in the tube is longer than the testing machine jig by 45 mm at both upper and lower ends, which is necessary to make sure that bond-slip would not occur at the anchorage region during the tensile test. However, such an extra anchorage region also contributes to the tensile deformation in the test. Neglecting this contributing factor would lead to underestimation of E_{CFSz}. As introduced in Section 4.3.1, the anchorage region is comprised of the aluminium tube, epoxy resin and CFS. By using the equation of static equilibrium combined with Hooke's Law, the analytical solution to CFS tensile process within the early stage can be described as

$$\begin{cases} Ft_{CFS} = \frac{\Delta l_{ta}}{l_{ta}}(A_{Al}E_{Al} + A_{es}E_{es} + A_{CFS}E_{CFSz}) \\ Ft_{CFS} = \frac{\Delta l_{tC}}{l_{tC}}A_{CFS}E_{CFSz} \\ \Delta l_t = 2\Delta l_{ta} + \Delta l_{tC} \end{cases} \tag{4-14}$$

where Ft_{CFS} denotes the uniaxial tensile force acting on the sample during the test; $A_{Al} =$ 1.80 mm^2, symbolising the cross-sectional area of aluminium tube of 3 mm in outer diameter and 2.59 mm in inner diameter measured by a digital bore gauge; $A_{es} = 3.72$ mm^2 is the cross-sectional area of internal epoxy resin, which is derived from the tube size and A_{CFS}; E_{Al} is the elastic modulus of aluminium material with the value of 69 GPa (Kouzeli et al., 2001; Khalili et al., 2005); E_{es} is the elastic modulus of epoxy resin, which

adopts the value of 3.1 GPa (Huang et al., 2002; Ayatollahi et al., 2011); Δl_{ta} denotes the tensile deformation of CFS anchorage region beyond jig's grip at upper or lower end; Δl_{tC} denotes the tensile deformation of CFS in the sample testing region; Δl_t denotes the total tensile displacement between a pair of testing machine jigs in CFS tensile test; $l_{ta} =$ 45 mm, representing the length of CFS anchorage region that exceeds the grip range of the upper or lower jig; $l_{tC} = 50$ mm, representing the length of CFS in the testing region of the sample used for the tensile test.

Substituting the data point at 0.5 mm tensile displacement into Eq.4-14, the average uniaxial tensile elastic modulus of CFS is found as $E_{CFSz} = 131.0$ GPa, with the standard deviation of 2.54. Table 4-4 gives the solution to all tested samples as follows.

Table 4-4 Mechanical properties of CFS material.

Sample serial number	1	2	3	4	Average value
Ultimate tensile force Fu_{CFS} (kN)	3.38	3.18	2.92	3.17	3.16
Ultimate tensile strength fu_{CFS} (GPa)	2.18	2.05	1.88	2.04	2.04
Uniaxial tensile elastic modulus E_{CFSz} (GPa)	134.1	131.9	128.3	129.8	131.0

4.6.2 Water uptake behaviour analysis

4.6.2.1 Test results

As discussed in Section 3.2.1, different from the homogeneous diffusion of SM material, the water uptake process inside CFS material features the orthotropic diffusion behaviour. Thus Eq.3-2 should be used here to analyse test results of water mass growth. In order to distinguish between the effect of axial diffusion coefficient D_{CFSz} and the effect of radial diffusion coefficient D_{CFSr} in Eq.3-2, two types of CFS samples with different lengths are designed for the water uptake test under the identical ambient conditions of 60 °C seawater immersion over 96 hours, as introduced in Section 4.3.2. For the 240 mm CFS specimen, the aspect ratio (length/diameter) is more than 100, indicating that the contribution from D_{CFSz} is negligible. Therefore, Eq.3-2 can be simplified as below to describe the water diffusion behaviour in this sample.

$$M_{FSL}(t) = M'_{FSL}\left[1 - 4\sum_{m=1}^{\infty}\frac{1}{{\alpha_m}^2}\exp\left(-{\alpha_m}^2\frac{D_{CFSr}}{{r_{CFS}}^2}t\right)\right] \tag{4-15}$$

where $M_{FSL}(t)$ is the moisture absorption mass growth for a group of 60 CFS samples with 240 mm length at an arbitrary time t; M'_{FSL} is the maximum moisture uptake at the saturation status for this group; r_{CFS} is the radius of the CFS material, with 0.70 mm.

Applying the method similar to Eq.4-8, water uptake test results for four groups of 240 mm CFS samples are obtained by the current mass of each group subtracted from its initial mass, as shown in Fig.4-40. Note that four groups used here all individually comprise 60 of 240 mm CFS samples, named by WU60-FSL-1, 2, 3, and 4 respectively.

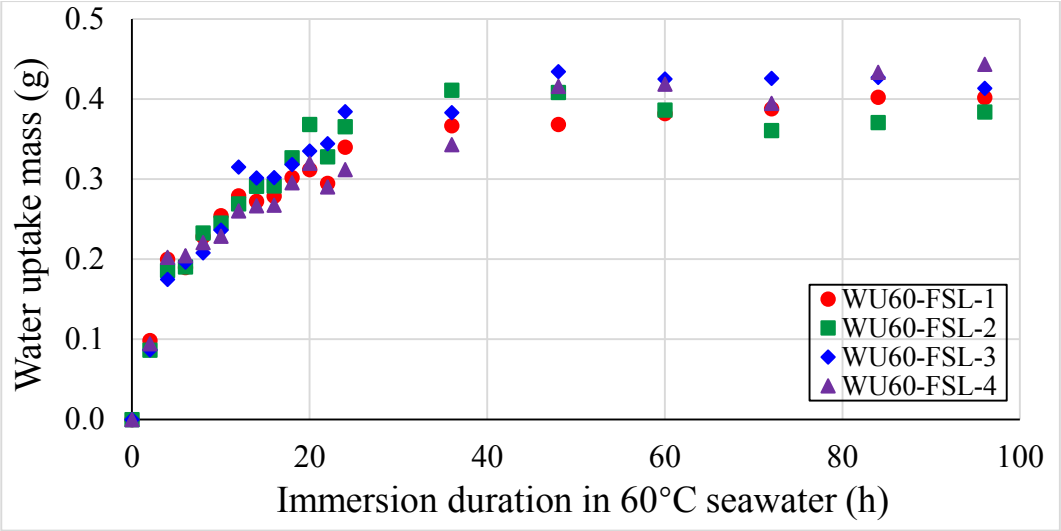

Fig.4-40 Water uptake test results for four groups of 240 mm CFS samples immersed in 60 °C seawater up to 96 hours.

The water absorption mass varied between 0.38g and 0.44g at the 96th hour, with an average value of 0.41g. Throughout the immersion, the mass growth saw a nearly parabolic rise for the first 36 hours and then reached its plateau by the end of the test, indicating that the samples had already approached the saturation status within the period of the test. During the last 60 hours of the test, there was still a slight mass increase from 0.38 g at the 36th hour to 0.41 g at the 96th hour, revealing the water uptake trend that significantly slows down over time.

Substituting the above test records into Eq.4-15, the maximum water uptake mass for those four groups and the radial diffusion coefficient of CFS can be acquired as M'_{FSL} = 0.41 g and D_{CFSr} = 1.33*10^{-12} m^2/s.

Since the maximum moisture uptake at the saturation status M'_{FSL} stems from the data analysis of the test group comprising 60 strands with 240 mm length, this value does not strictly present the water uptake capacity of CFS material universally. Accordingly, the definition of the saturated moisture absorption in mass percentage terms (PA'_{CFS}) is applied to describe the maximum water absorption of CFS material as per Eq.4-16.

$$PA'_{CFS} = \frac{M'_{FSL}}{M_{FSLd}} \times 100\% \quad (4\text{-}16)$$

where M'_{FSL} is known before and M_{FSLd} (the initial mass of the test group consisting of 60 CFS samples with 240 mm length, after complete drying treatment) has already been weighed with 32.21 g. The value of PA'_{CFS} can thus be derived as 1.3%.

In addition, the saturation concentration of CFS material C'_{CFS} can also be obtained based on M'_{FSL} using Eq.4-17.

$$C'_{CFS} = \frac{M'_{FSL}}{V_{FSL}} \quad (4\text{-}17)$$

where V_{FSL} is the net volume of 60 CFS samples of 240 mm in length and 0.70 mm in radius respectively. Then the value of C'_{CFS} is found to be 18.47 kg/m^3, namely 1026.25 mol/m^3 in view of the molar mass of water molecules with 0.018 kg/mol.

Once the specific values of material coefficients M'_{FSL} and D_{CFSr} related to diffusion behaviour of CFS have been determined, they can be substituted into Eq.3-2 in which there is only one unknown diffusion coefficient D_{CFSz} yet to be decided. In accordance with the experimental design introduced in Section 4.3.2, four groups of short CFS samples with 6 mm length are prepared for the water uptake test to calculate D_{CFSz} and distinguish its effect from D_{CFSr}. Fig.4-41 represents the test results of four groups comprised of 6 mm CFS samples where the four groups are named by WU60-FSS-1, 2, 3, 4 and each of them includes about 2400 of 6 mm short CFS samples. Note that it is crucial for this test to control the used material amount of short CFS in each group equal to the foregoing group made up of 60 long CFS samples with 240 mm length, because a series of subsequent data comparison and data analysis all require an invariable value of the used CFS material quantity as a baseline. In addition, as explained in Section 4.3.2, such a test setup can avoid the experimental error. The water uptake amount for a single

CFS is too small to measure, but it is feasible to observe the moisture absorption from a group of 60 long CFS samples whose water uptake amount should be 60 times higher than a single strand theoretically.

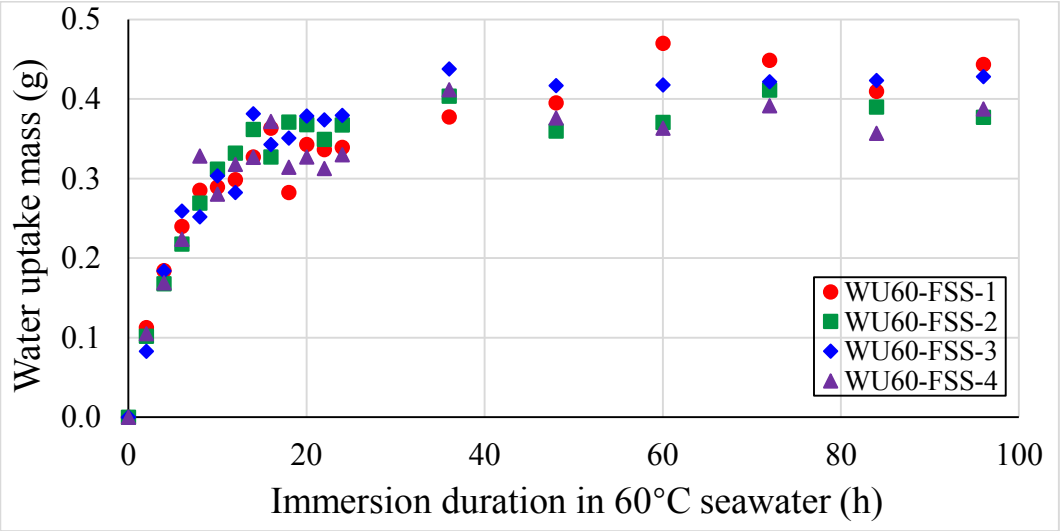

Fig.4-41 Water uptake test results for four groups of 6 mm CFS samples immersed in 60 °C seawater up to 96 hours.

Like the test records in respect of long CFS samples, test results of those groups consisting of short CFS samples had the final water absorption mass ranging from 0.38 g to 0.44 g at the 96th hour, with an average of 0.41 g equal to the value of M'_{FSL}. This implied that the moisture absorption had already attained the saturation state by the end of the test. As shown in Fig.4-41, the mass growth almost entered its plateau after the first day when the water uptake was 0.35 g. Compared with the growth trend in long CFS samples, the water uptake growth of short CFS samples featured a steeper slope at the initial increase stage, revealing the noticeable effect of axial diffusion coefficient D_{CFSz} on the water uptake behaviour of short CFS with 6 mm length.

On account of the same CFS material quantity used in both sample groups mentioned above, M'_{FSL} stemming from the test group made up of long CFS samples can be applied

to the group of short CFS samples directly, serving as the maximum moisture uptake at the saturation status for each group comprising about 2400 short CFS with 6 mm length. Furthermore, D_{CFSr} has also been acquired before. Substituting them into Eq.3-2, the axial diffusion coefficient of CFS material immersed in 60 °C seawater can be obtained as $D_{CFSz} = 1.05*10^{-11}$ m^2/s, nearly eight times the value of D_{CFSr}. This phenomenon results from the orthotropic structural characteristics of CFS material. There tend to be a certain number of micro-voids or pores along its axial direction, especially at the interface between the fibre and the polymer matrix (Bao and Yee, 2002a). Subsequently water molecules become more likely to diffuse through its axis than its radius owing to such a porosity distribution feature (Bao and Yee, 2002b). As a result, its radial diffusion rate D_{CFSr} is markedly lower than its axial diffusion rate D_{CFSz}.

Since the identical material amount is used for both long and short CFS sample groups, the variations in their moisture content during the course of the water uptake test can be directly compared by using $S_{CFS}(t)$ which is defined as the moisture saturation of the test group composed of CFS material at an arbitrary time t. Similar to Eq.4-11, $S_{CFS}(t)$ is derived from the ratio of the current water uptake mass to the maximum water uptake mass M'_{FSL} for an arbitrary test group used here. In terms of the moisture saturation, water uptake test results of long and short CFS samples are presented in Fig.4-42a and Fig.4-42b respectively.

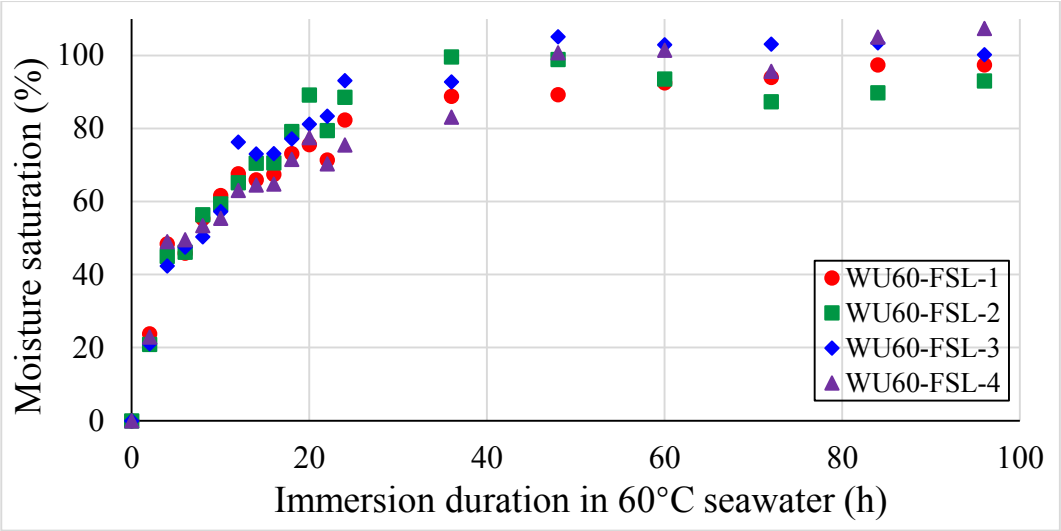

(a)

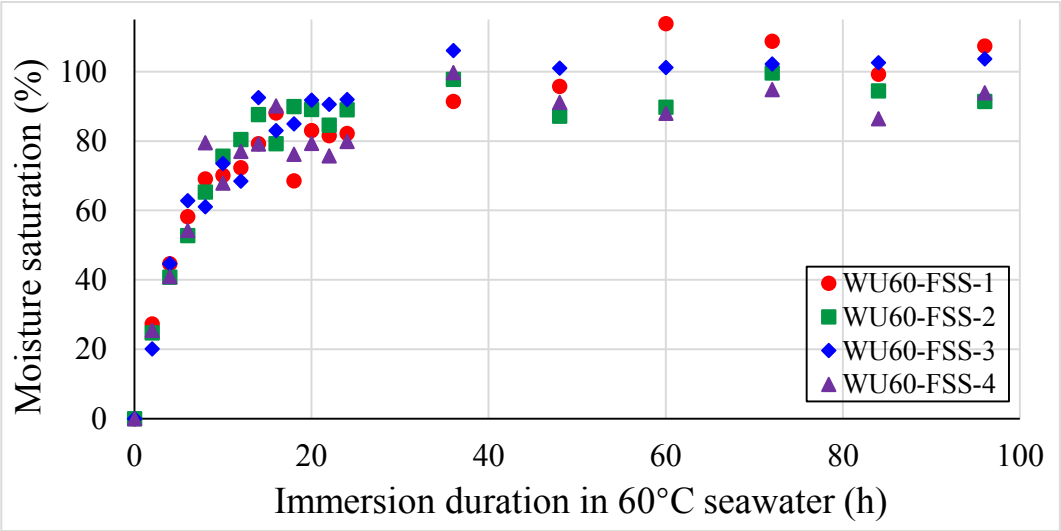

(b)

Fig.4-42 The moisture saturation analysis of four sample groups under ambient conditions of 60 °C seawater immersion up to 96 hours: (a) long CFS samples with 240 mm length; (b) short CFS samples with 6 mm length.

From Fig.4-42, it can be found that the increase in moisture intake of short CFS samples was faster than that of long CFS samples at the beginning, holding a lead of around 2% to 16% over the first 16 hours. However, the difference between them was reduced gradually over time. Finally, the complete saturation was reached at nearly the 48th hour and the 36th hour for long and short CFS samples respectively.

In view of the fact that the radial diffusion coefficient D_{CFSr} is nearly one eighth the value of the coefficient in axial direction D_{CFSz} in this study, but the lateral surface area of CFS is usually much larger than the cross-sectional area, the water uptake behaviour of CFS as shown in Fig.4-42 is featured as the axial diffusion at the beginning and gradually turns to radial diffusion over time. This diffusion behaviour is more evident for short CFS samples of 6 mm in length, accounting for the difference in the saturation changes between long and short CFS samples.

4.6.2.2 Temperature effect

This section studies the temperature effect of CFS in terms of its water diffusion activation energy E_{aFWr} and E_{aFWz} which represent the intrinsic water absorption property of CFS material in radial and axial direction respectively. To investigate the effect of temperature T on water diffusion behaviour of the CFS material used herein, the water uptake test for both 240 mm and 6 mm CFS was conducted at 20 °C seawater with the duration of 30 days. Fig.4-43a and Fig.4-43b demonstrate water uptake test results for four groups of 240 mm and 6 mm CFS individually. Four specimen groups of the former are named by WU20-FSL-1, 2, 3, 4 and each one consists of 60 strands with 240 mm length. As for the latter, they are named by WU20-FSS-1, 2, 3, 4 and every group contains around 2400 of 6 mm short CFS. In this way, the total amount of used CFS material in these two groups is equal to each other.

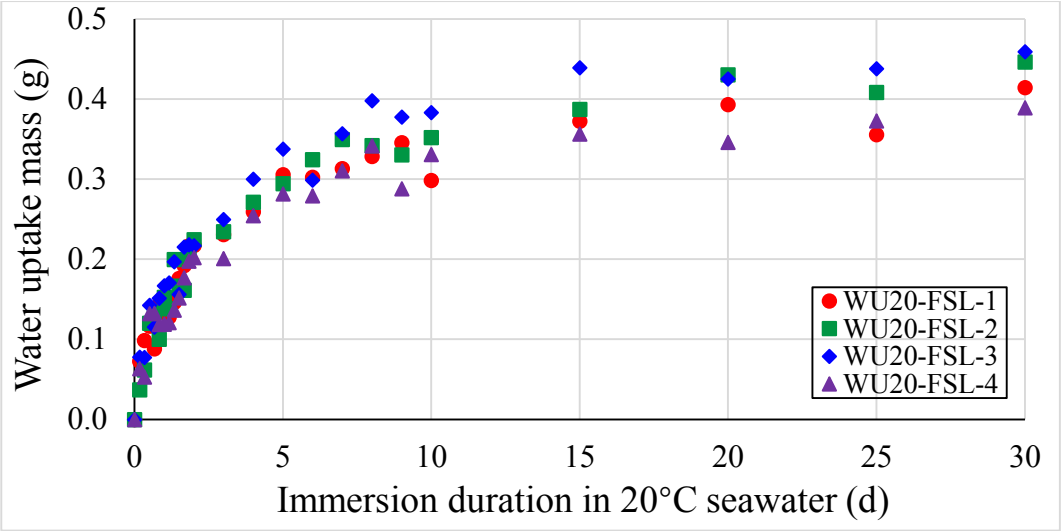

(a)

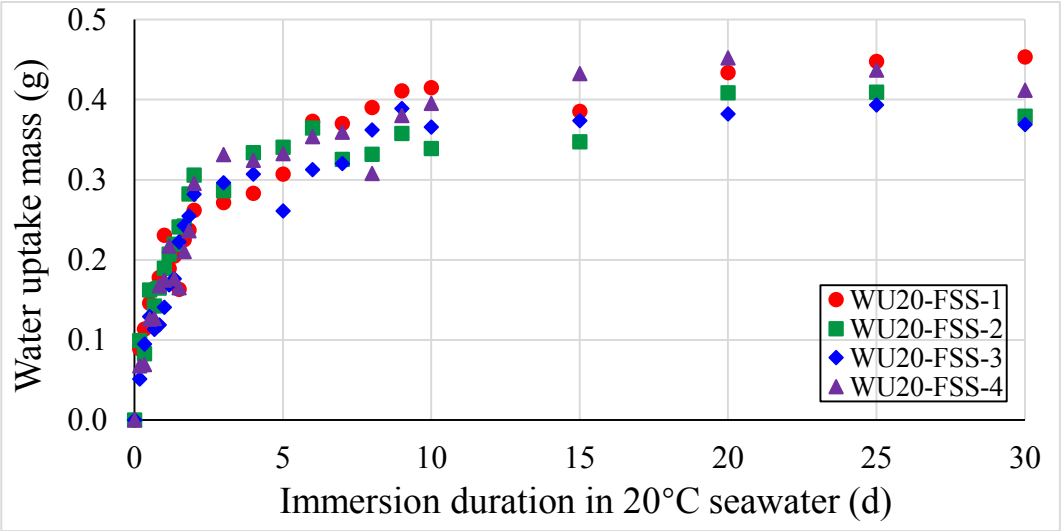

(b)

Fig.4-43 Water uptake test results for four sample groups of CFS immersed in 20 °C seawater up to 30 days: (a) long CFS samples with 240 mm length; (b) short CFS samples with 6 mm length.

By the end of the test, the average water absorption mass on the 30th day was 0.43 g for 240 mm sample groups and 0.40 g for 6 mm sample groups. As shown in Fig.4-43, the water uptake mass in both long and short CFS groups reached a plateau by the end of the test, indicating that all groups in the test attain the saturation stage eventually. By comparing Fig.4-43 with Fig.4-40 and Fig.4-41, it can be found that the water uptake

mass at the saturation stage of the 20 °C immersion is almost the same as the 60 °C immersion, so changing immersion T has little influence on the final water absorption ratio of CFS material at saturation. Furthermore, considering that the amount of CFS material used in each group is almost identical, the total water absorption mass for each group should be the same as well, equal to the value of M'_{FSL} which is 0.41 g derived from Section 4.6.2.1.

Fig.4-44 presents the CFS water absorption process under 20 °C seawater ambient conditions, in terms of moisture saturation. It is found that test specimens attained their 90% saturation on the 15th day for 240 mm samples and on the 9th day for 6 mm samples. It took 240 mm CFS samples under 20 °C immersion ten times longer than that under 60 °C immersion to reach the same saturation level. As regards to 6 mm CFS samples under 20 °C immersion, reaching 90% saturation took them six times the duration of water uptake compared with those under 60 °C immersion. Besides, the mass growth for 20 °C sample groups also experienced an almost linear increase at the beginning and then the uptake rate slowed down gradually with time, which was similar to the growth trend in 60 °C sample groups. After the 15th day, the increment of water uptake as shown in Fig.4-44 became unobvious and the slight fluctuation within 5% was present in the degree of saturation, owing to the statistical discrepancy. Similar trend had been found in the 60 °C sample groups after the second day of immersion.

Substituting M'_{FSL} combined with the test results recorded in Fig.4-43a into Eq.4-15, the radial diffusion coefficient of CFS material immersed in 20 °C seawater D_{CFSr20} can be obtained as $1.65*10^{-13}$ m^2/s. Subsequently, the axial diffusion coefficient of CFS material immersed in 20 °C seawater D_{CFSz20} is found to be $1.55*10^{-12}$ m^2/s by means of Eq.3-2 coupled with the test data presented in Fig.4-43b.

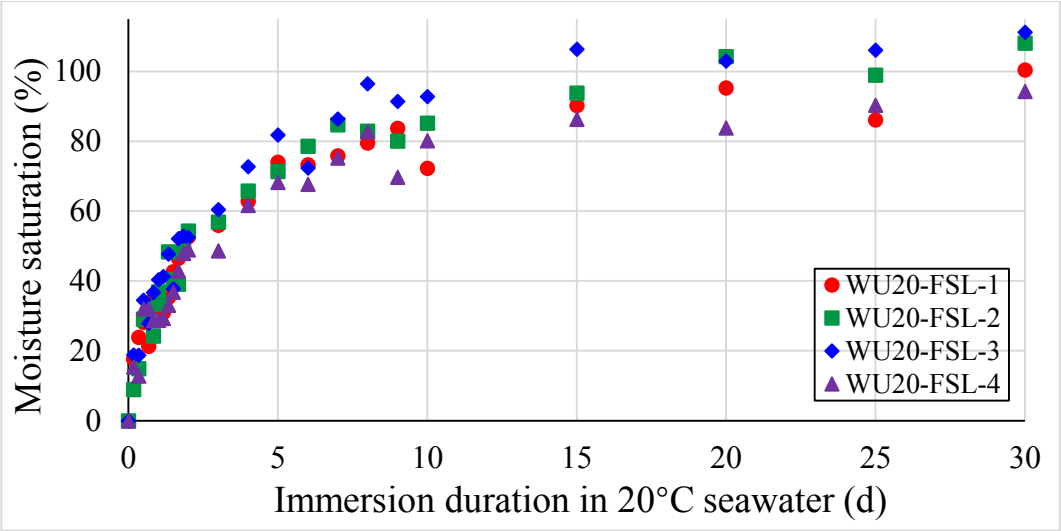

(a)

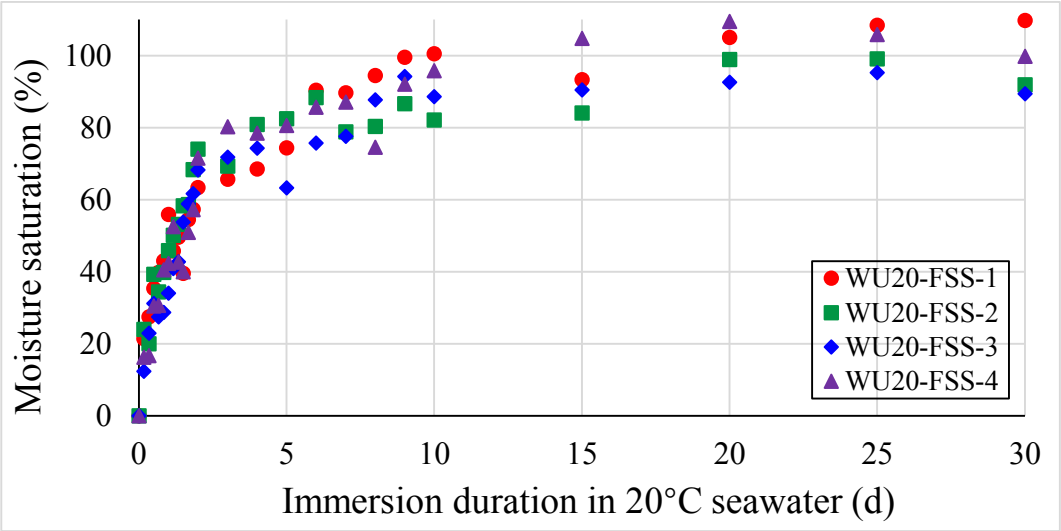

(b)

Fig.4-44 The moisture saturation analysis for four sample groups under ambient conditions of 20 °C seawater immersion up to 30 days: (a) long CFS samples with 240 mm length; (b) short CFS samples with 6 mm length.

With the immersion T drops from 60 °C to 20 °C, a remarkable reduction appears in the water diffusion coefficient of CFS. In its radial direction the ratio of the diffusion coefficient D_{CFSr}/D_{CFSr20} is 8.05, while in its axial direction the ratio D_{CFSz}/D_{CFSz20} is 6.78. These findings lay the foundation in investigating the water diffusion of CFS material using Arrhenius Law.

Compared with 20 °C, elevated temperature of 60 °C significantly increases the water uptake rate and thus effectively reduces the duration for CFS to attain its saturation condition. In accordance with Arrhenius Law, there is a correlation between the diffusion coefficient of CFS and the immersion T. Based on Eq.3-9, α_T is introduced to define the dependence of diffusion coefficient on ambient T quantitatively, namely the ratio of the current diffusion coefficient to the initial diffusion coefficient due to the temperature changes. Once the diffusion coefficient at a certain T is measured, α_T can be used to determine the unique diffusion coefficient at an arbitrary T using Eq.3-9.

To determine α_T at an arbitrary T requires the water diffusion activation energy of CFS, which is an intrinsic material property and independent of temperature changes. Note that there is a difference of the value between D_{CFSr}/D_{CFSr20} and D_{CFSz}/D_{CFSz20}. It suggests that the temperature affects the CFS water diffusion to a different extent between the radial and the axial directions. Substituting the above mentioned four diffusion coefficients into Eq.3-9, the water diffusion activation energy of CFS in radial and axial directions can be obtained as $E_{aFWr} = 42.35$ kJ/mol and $E_{aFWz} = 38.86$ kJ/mol respectively.

In general, the activation energy determines the corresponding chemical reaction or material property change. The higher the value of the activation energy, the more difficult for the material to react. In this study, the difference between E_{aFWr} and E_{aFWz} reveals that it is easier for water molecules to diffuse into the interior of CFS along its axial direction than its radial direction. In terms of the physical structure of CFS, micro-voids or pores are more likely to exist at the interface between the fibre and the polymer matrix. Thus, the CFS is more compact along its radial direction compared with its axial direction,

indicating that the water diffusion is more likely to happen through the axial direction than the radial direction.

As the water uptake mass of CFS at the saturation condition is independent of the ambient temperature variation, the diffusion coefficients for CFS material at an arbitrary T can be calculated theoretically, assuming that the water diffusion activation energy for CFS is independent to temperature.

4.7 Pull-out test results

After 28 days curing in 20 °C water, pull-out tests had been carried out on four specimens (PI-1, 2, 3, 4) using SM and four specimens (PI-1F, 2F, 3F, 4F) using FM. Fig.4-45a and Fig.4-45b plot the force-displacement curves for SM and FM specimens, respectively.

The ultimate pull-out forces are summarised in Table 4-5, using the peak point on the force-displacement curve for each specimen individually. Average ultimate pull-out force with the related standard deviation of each batch is given in Table 4-5 as well.

According to the test results, seawater did not have any obvious effect on ultimate pull-out force. Although the ultimate pull-out force for seawater mortar samples was slightly higher than the freshwater mortar samples, the difference was less than 5%, and thereby can be attributed to the normal statistical variation. Therefore, opting for seawater rather than freshwater to cast the mortar substrate would not be disadvantageous to the pull-out performance for those tested specimens.

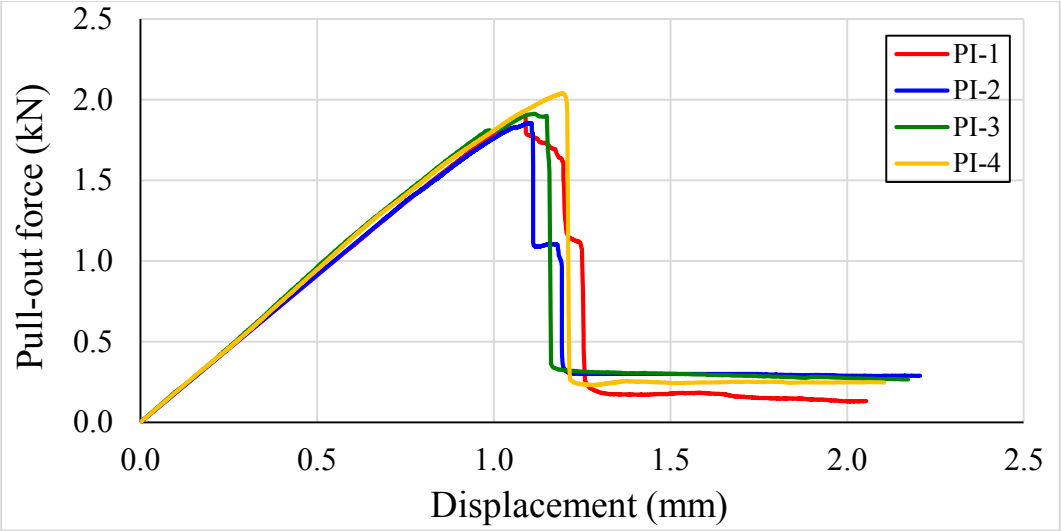

(a) Specimens made of SM: PI-1, 2, 3, 4 respectively

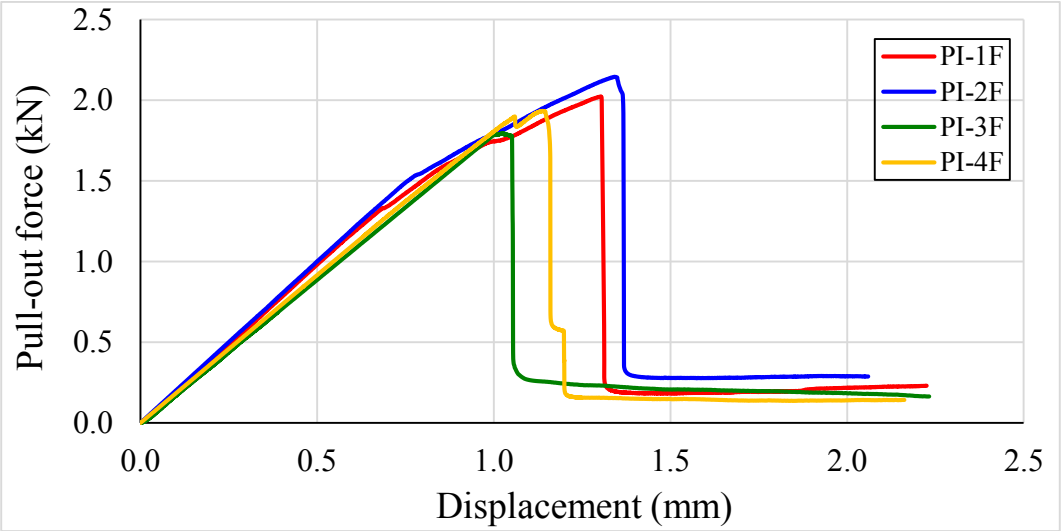

(b) Specimens made of FM: PI-1F, 2F, 3F, 4F respectively

Fig.4-45 Pull-out force-displacement curves.

Table 4-5 Test results of the ultimate pull-out force.

Specimen type	Seawater batch				Freshwater batch			
Serial number	PI-1	PI-2	PI-3	PI-4	PI-1F	PI-2F	PI-3F	PI-4F
Ultimate pull-out force (kN)	1.91	1.86	1.91	2.04	2.02	2.15	1.80	1.93
The average force (kN)	1.93				1.98			
Standard deviation	0.08				0.15			

Fig.4-46 shows the failure modes of the CFSRM specimens. All eight specimens have shown pull-out failure mode, as shown in Fig.4-46a. Fig.4-46b presents all the mortar cylinders after CFS is pulled out from the interior of CFSRM, and Fig.4-46c displays the upper surface of the cylindrical mortar after the test. According to those test records shown in Fig.4-46, the pull-out failure characteristics of CFSRM specimens can be concluded as follows: (1) no longitudinal crack appears in cylindrical mortar surface; (2) no radius crack occurs in cylindrical mortar surface; (3) the embedded CFS reinforcement of 50 mm in length is completely pulled out from the interior of mortar, indicating that the obvious fracture of CFS does not occur during the pull-out process; (5) no visible damage can be found on the pulled out CFS surface.

(a)

(b)

(c)

Fig.4-46 Specimens after the pull-out test: (a) surface of CFS reinforcement fully pulled out from mortar; (b) tested CFSRM of the control group (freshwater mortar) on the left hand and the study group (seawater mortar) on the right hand; (c) upper surface of the cylindrical mortar after pulling out its internal CFS.

As no visible crack can be found on the surface of those mortar cylinders after the test, the mortar mix design is thus believed to be adequate for the present study. In addition, the CFS is found to be sufficiently strong to sustain the pull-out force before the complete debonding failure occurs.

4.8 Summary

This chapter has carried out a series of tests to investigate the physical and mechanical properties of CFSRM with its material components, namely CFS and SM. In brief, those tests contain compressive strength test with cubic mortar specimens, splitting tensile test with cylindrical mortar specimens, Young's modulus test with prism specimens, flow table test with fresh mortar, tensile test with CFS, water uptake tests for both CFS and mortar materials at 60/20 °C respectively and the pull-out test with CFSRM specimens before any ageing treatment. The key results from those tests are concisely presented as below.

The use of seawater in mortar would not influence its strength or flowability, compared with normal freshwater mortar. As regards to CFS used herein, this chapter has acquired its basic material properties including ultimate tensile strength, axial elastic modulus, coefficient of hygroscopic expansion, etc. The water diffusion activation energy, which is a material intrinsic property that does not change by varying temperature, has been found out in this chapter as well, by using Arrhenius Law to analyse test results at 20 °C and 60 °C.

Focusing on the interfacial bond behaviour between CFS and SM, a pull-out test method for CFSRM specimen is proposed in this chapter. Test results suggest that whether using

seawater or freshwater to make the mortar substrate would not affect the pull-out performance of CFSRM. The average ultimate pull-out force is 1.95 kN, which will serve as the baseline to investigate the degradation in pull-out performance after environmental conditioning.

5 NUMERICAL SIMULATION ON PHYSICAL AND MECHANICAL PROPERTIES OF CFSRM SPECIMENS

5.1 Overview

In this chapter the structural behaviour of CFSRM specimens is investigated by using numerical method, including water diffusion, interfacial bonding, hygroscopic expansion and its effect on pull-out resistance. Considering the multi-field coupling nature of the problem, COMSOL Multiphysics software are used as the modelling tool.

The present study directly adopts the material coefficients measured in Chapter 4 to build the numerical water diffusion field. The pull-out behaviour is simulated by adding a stress field using cohesive zone model (CZM), which dominates the gradual failure at the interface between CFS and SM during the pull-out process. The model parameters that govern the interfacial properties of CZM are derived from the pull-out test results. In this way, the simulated pull-out behaviour can be calibrated using the experimental data.

However, the effect of hygroscopic expansion taking placing inside CFSRM specimen cannot be directly observed by the conventional experimental method. This chapter focuses on the mechanism of hygroscopic expansion and its influence on pull-out performance. The present research of the swelling effect can be further broadened to a general analysis applied to FRP and FRP reinforced materials in which the hygroscopic expansion effect cannot be ignored. The relevant details are discussed in Section 5.5.

5.2 Geometrical model

The numerical model in this study adopts the same geometry as the experimental studies, as shown in Fig.5-1.

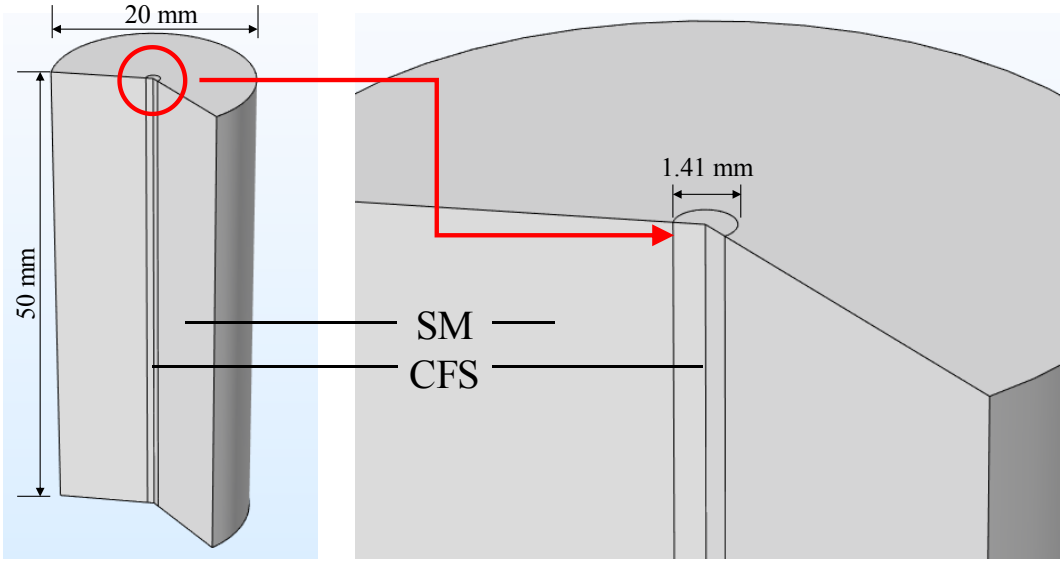

(a)

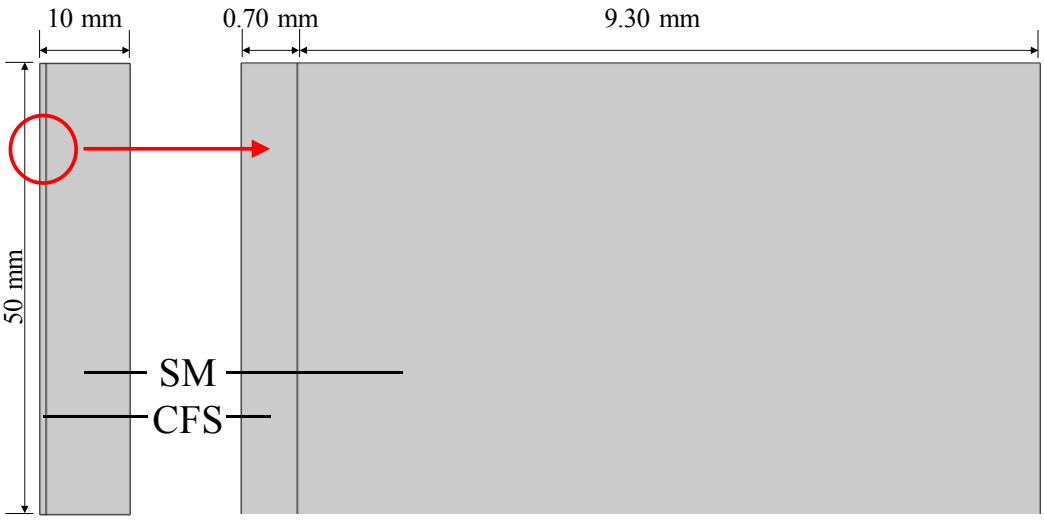

(b)

Fig.5-1 Geometry of the numerical model: (a) 3D geometric profile; (b) 2D axisymmetric geometric model.

The SM substrate of CFSRM has a standard cylindrical geometry with 50 mm height and 20 mm diameter, where the centre is occupied by the CFS reinforcement along the longitudinal axis. Although the cross-section of CFS is measured as a random and irregular round profile as shown in Fig.4-37, an equivalent circular cross-section of 1.41 mm in diameter has been used in the present numerical model. Fig.5-1a depicts the 3D geometry of the numerical model. Taking advantage of the axisymmetric boundary conditions, a two-dimensional axisymmetric model is adopted to improve computational efficiency, as shown in Fig.5-1b.

5.3 Water diffusion model

5.3.1 Boundary conditions based on two-medium diffusion

The diffusion mechanism presented in Section 3.2.1 is for a single material. It cannot be directly used to describe the water uptake process occurring inside CFSRM which is characterised as a composite material consisting of cylindrical SM substrate and embedded CFS reinforcement. On account of such a problem, it is necessary to find out the special model boundary conditions which agree the two-medium diffusion mechanism, in order to simulate the whole water diffusion process inside CFSRM specimen.

Fig.5-2 shows the diagram of the two-medium diffusion mechanism of CFSRM. It indicates that the centrally embedded CFS has an orthotropic diffusion coefficient tensor in axial and radial directions, respectively, whilst the SM substrate features isotropic water diffusion with a coefficient scalar. For the SM substrate, it absorbs moisture from the external environment directly. For the CFS reinforcement, moisture transfers into it

from both the external environment (the two ends) and from the SM medium (the strand wall), as shown in Fig.5-2.

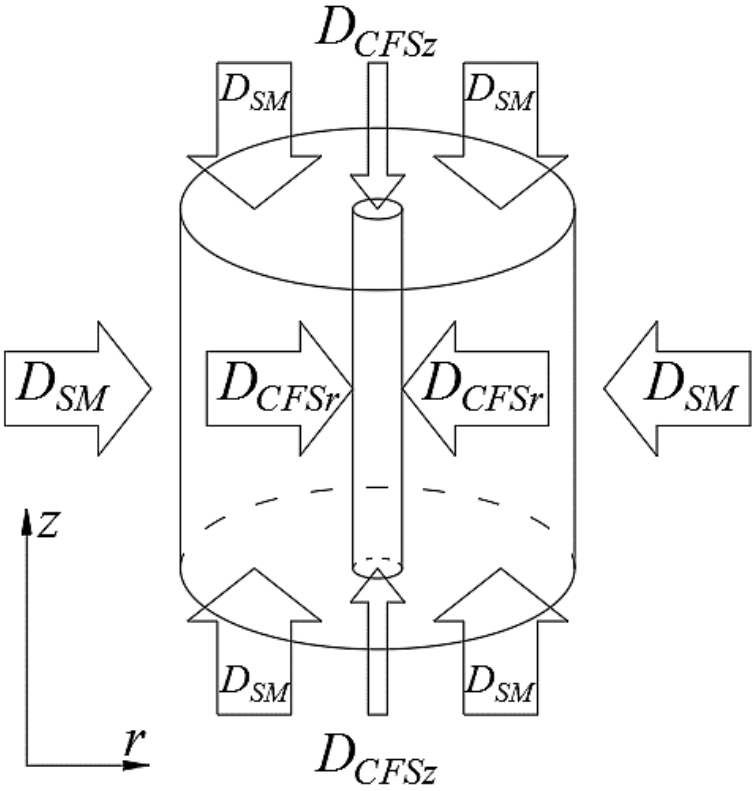

Fig.5-2 The diagram of two-medium diffusion mechanism in CFSRM.

The boundary conditions in accordance with this two-medium diffusion mechanism comprise two parts, including the global boundary condition located at the global solid as well as its exterior surface and the interface boundary condition located at the interface between those two different mediums.

Based on different saturation concentrations of the two mediums, the global boundary conditions can be expressed as

$$\begin{cases} C(r < r_R, |z| < z_h, t = 0) = 0 \\ C(r_R, z, t) = C'_{SM} \\ C(r \le r_{CFS}, z = \pm z_h, t) = C'_{CFS} \\ C(r_{CFS} < r \le r_R, z = \pm z_h, t) = C'_{SM} \\ C(r \le r_{CFS}, z, t_\infty) = C'_{CFS} \\ C(r_{CFS} < r \le r_R, z, t_\infty) = C'_{SM} \end{cases} \tag{5-1}$$

where r_R and z_h are the radius and the half length of CFSRM respectively; r_{CFS} is the radius of CFS; C'_{CFS} and C'_{SM} are the saturation concentration of CFS medium and SM medium respectively.

While the global boundary condition remains unchanged at the outer surface of CFSRM, the interface boundary condition varies over time, controlled by the current concentration at the interfacial point and the total mass of water absorption among each medium.

Fig.5-3 to Fig.5-5 give the graphic exposition of above mentioned variations in terms of Dirichlet (first-type) boundary condition and Neumann (second-type) boundary condition, wherein C_{SM} and C_{CFS} denote the current concentration of the point in SM and CFS medium respectively; M_{SM} and M'_{SM} are the current water absorption and the saturated water absorption within the entire SM medium; M_{CFS} and M'_{CFS} are the current water absorption and the saturated water absorption within the entire CFS medium; N is the diffusion flux of water molecular mass transfer at the point on the interface. Besides, variations described in Fig.5-3 to Fig.5-5 fit any point at the interface between those two mediums. The variations used herein are classified into three stages. Each of them is illustrated by Fig.5-3 to Fig.5-5.

Fig.5-3 shows the initial stage of water diffusion inside CFSRM specimen. Dirichlet boundary condition focuses on the value changes in moisture concentration at the interface. In this stage, water molecular concentration of the point grows from zero at

both sides of the interface simultaneously. This stage ends as long as the right side located in CFS medium attains its saturation concentration C'_{CFS}. To keep the concentration balance between both sides of a point at the interface of those two mediums, $N \neq 0$ exists on those points of which concentration exceeds zero in terms of Neumann boundary condition. The orientation of diffusion flux depends on the concentration gradient ∇C at the specific point.

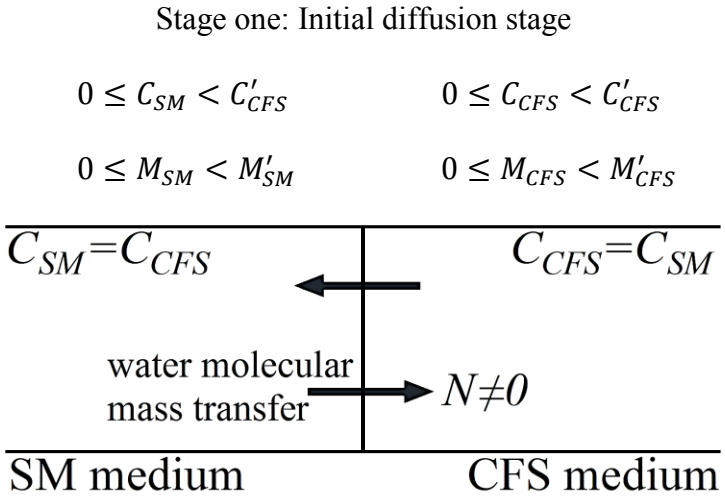

Fig.5-3 The interface boundary condition at initial diffusion stage.

Fig.5-4 shows the one-way diffusion stage at the interface. In terms of Dirichlet boundary condition, concentration of the interfacial point belonging to CFS medium side attains its maximum value C'_{CFS} during this period, while it continues rising for the interfacial point located at SM medium side. This stage will not end until the entire CFS medium attains its saturated water absorption M'_{CFS}. Based on the continuity of moisture mass during its transport, $N > 0$ serves as the Neumann boundary condition always existing on those points that have moved to the second stage. That is, the mass transport of water through the interface within this stage is featured by the direction from SM medium to CFS medium.

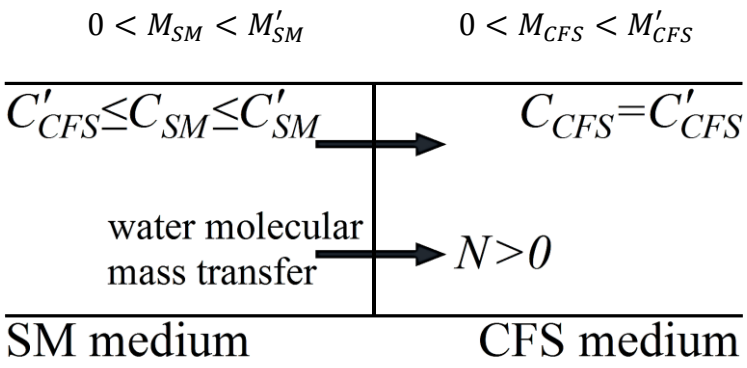

Fig.5-4 The interface boundary condition at one-way diffusion stage.

Fig.5-5 shows CFS medium saturation stage. In this stage, CFS medium reaches its saturation point after the continuous water molecular mass transfer in stage one and two. Hence the entire CFS medium attains its saturated water absorption M'_{CFS}. As no moisture mass transfers into it, Neumann boundary condition can be described as $N = 0$. For Dirichlet boundary condition, an arbitrary point at the interface keeps C'_{CFS} unchanged at CFS medium side while there is a continued increase of the concentration at SM medium side until attains C'_{SM}. Stage three can be seen as the final state for interface boundary condition changes.

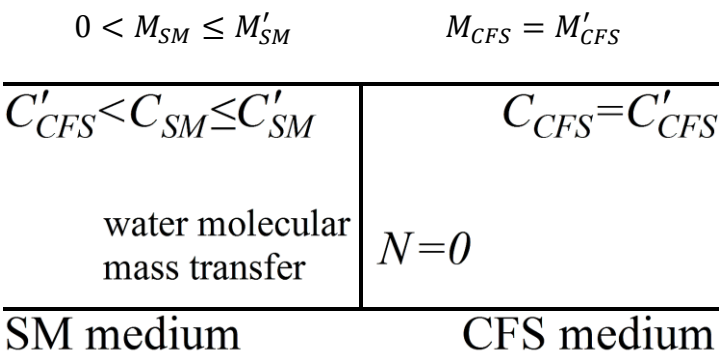

Fig.5-5 The interface boundary condition at CFS medium saturation stage.

The above mentioned three stages cover all variations occurring at the interface from completely dry state to saturation. Coupled with those boundary conditions at the interface and the outer surface, the numerical model can simulate the two-medium diffusion mechanism during the whole process of water diffusion for the CFSRM specimen immersed in seawater.

5.3.2 Cylindrical orthotropic water diffusion model set up

A cylindrical orthotropic water diffusion model is built based on Fick's Law in order to simulate the water diffusion behaviour inside the CFSRM specimen. Diffusion coefficient and concentration are two key parameters when describing a diffusion behaviour. This section dedicates to present how those two parameters are determined.

CFS and SM have different diffusion characteristics. SM has an isotropic diffusion coefficient, while CFS is orthotropic, where the diffusion coefficient in the radial direction is much smaller than that in the axial direction. In addition, the diffusion coefficient is temperature dependent. Arrhenius Law can be employed to investigate the mathematical relationship between temperature and the diffusion coefficient. In order to obtain the diffusion coefficient under a certain temperature, the water diffusion activation energy is required in advance. Moreover, the saturation concentration for CFS and SM in the water diffusion field is also different, although both of them share the same initial water molecular concentration.

As shown in Fig.5-6, the model assumes that its exterior surface reaches the saturation condition at the start of the water diffusion process. Red lines represent boundary conditions of SM domain with the value of C'_{SM} while the blue lines represent boundary

conditions of CFS domain with the value of C'_{CFS}. It is worth mentioning that in the model, rather than setting saturation concentration directly at the boundaries, the concentration value at boundaries quickly rises from 0% to 100% of the saturation concentration over the first hour, which helps avoid convergence problems caused by the sharp concentration discontinuity at the initial step. Fig.5-7 shows the numerical function which is used to control the boundary conditions.

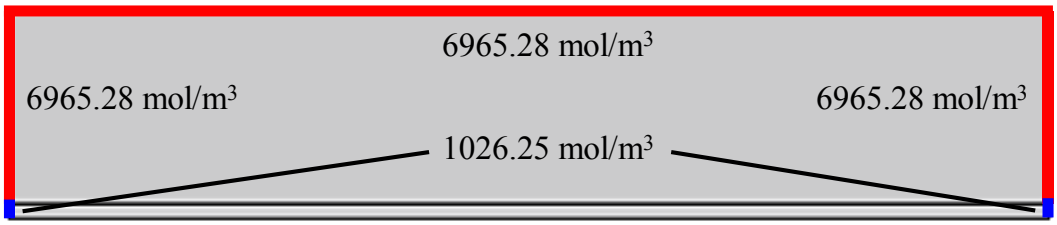

Fig.5-6 Global boundary conditions.

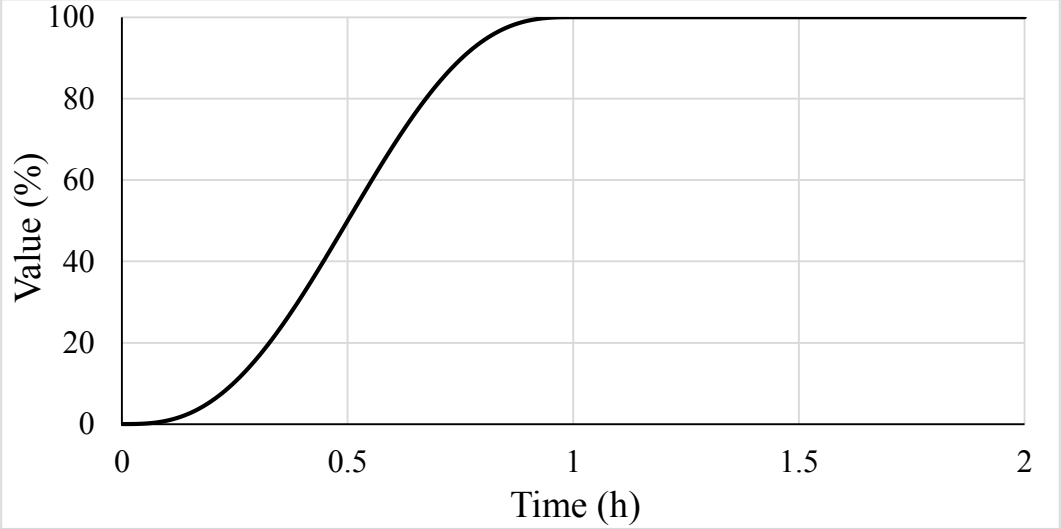

Fig.5-7 A step function utilised to control global boundary conditions.

As shown in Fig.5-8, interfacial boundary conditions between SM and CFS are located on the blue line which represents the CFS/SM interface with zero thickness. Note that such an interface along with the interfacial contact is established by using the interfacial elements based on CZM method which will be introduced in Section 5.4.1 in detail. Based

on Dirchlet boundary condition, the moisture concentration at CFS side is equal to SM side before reaching C'_{CFS}. Afterwards, it becomes discontinuous because the concentration at SM side will further climb until it reaches the value of C'_{SM}. Based on Neumann boundary condition, the total flux at the interface is in equilibrium, i.e. an opposite flux should be defined at SM side, equal to the flux generated from the concentration definition for CFS side.

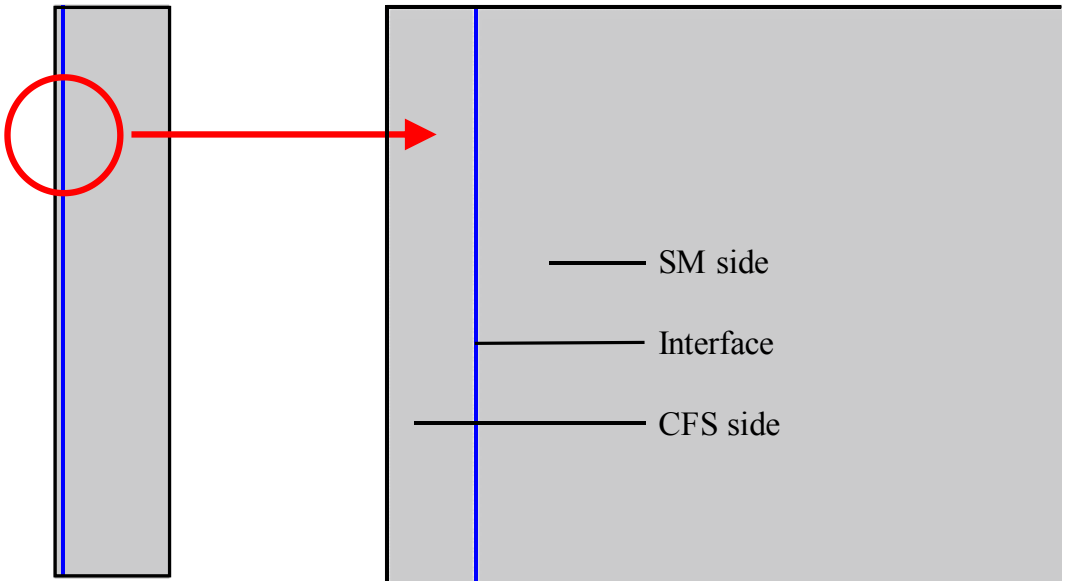

Fig.5-8 Interface boundary conditions.

The finite element mesh used in the present numerical model is shown in Fig.5-9. The mesh size ranges from 0.06 mm to 0.12 mm for CFS, and has a maximum size of 0.25 mm for SM. As shown in Fig.5-9, most of the elements are triangular elements while a small quantity of quadrangular boundary layer elements are present in the exterior surface of the model. The application of the boundary layer element to the model can help prevent the computation non-convergence problem from suddenly raising the boundary concentration from zero to saturation within one hour as mentioned by Fig.5-7.

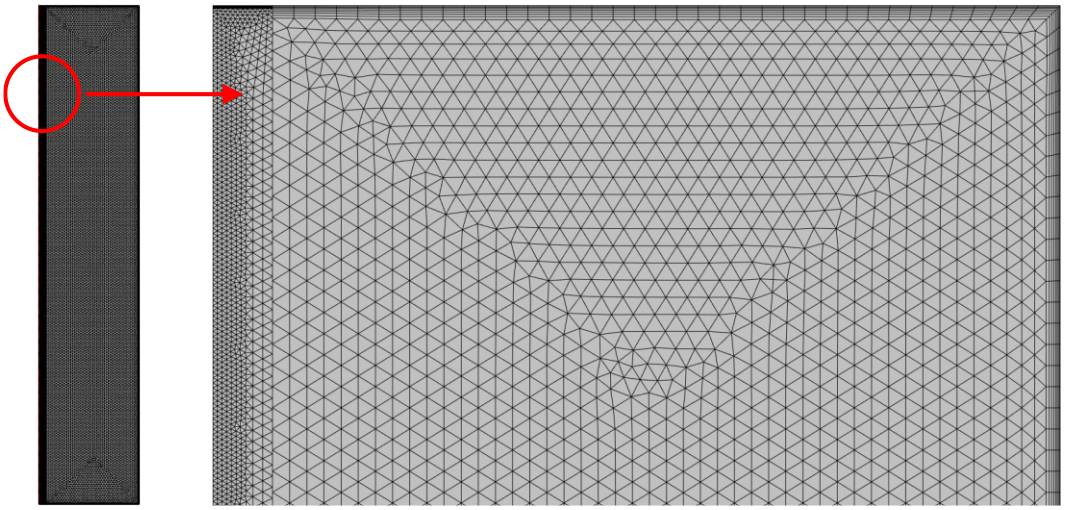

Fig.5-9 The diagram of mesh built for the model.

5.3.3 Diffusion model calibration and data analysis

This section calibrates the diffusion model using the water uptake test results for SM cylindrical specimens at 60 °C. Once calibrated, the numerical model is used to simulate the 60 °C water diffusion process of the CFSRM specimen over 720 days.

The saturated moisture content in CFS domain is nearly three orders less than that in the SM domain, because of the vast differences in volume and the maximum moisture concentration between CFS and SM domain. Therefore, in terms of the total water uptake mass for the whole model, the contribution of CFS can be neglected.

Table 5-1 summarises the calibrated model parameters which are used to control the ultimate moisture content and the diffusion rate of the simulated specimen during the diffusion process. According to the test results in Section 4.5.2 and 4.6.2, the theoretical maximum moisture content of a CFSRM specimen is 1.96 g. Defining this value as 100% of the moisture mass that the whole CFSRM model can absorb, Fig.5-10 compares the simulated water uptake growth of the CFSRM model with experimental results from

specimens under 60 °C seawater immersion over 180 days, in saturation percentage terms. Owing to the fact that the experimental specimens used herein experience oven drying treatment to remove their internal moisture before the water uptake test, the initial moisture concentration of the numerical model used for the calibration work is set to zero accordingly to simulate the initial dry state. After the calibration work, such value returns to 619.63 mol/m^3 that represents the initial moisture content of the experimental specimens on the 28th day of curing. In this way, the subsequent numerical study can be used to analyse the general water diffusion process for CFSRM without the oven drying treatment at the beginning. Note that four experimental specimens used here are named by WU60-SMC-1, 2, 3, 4 respectively. The numerical result has the coefficient of determination $R^2 = 0.9588$ when compared against the experimental data as shown in Fig.5-10, which demonstrates that the numerical model is reliable in predicting the long-term water uptake behaviour of a CFSRM specimen.

Table 5-1 Model parameters used in the water diffusion field.

Model parameters	Symbol	Unit	Value
Water diffusion coefficient of SM material immersed in 60 °C seawater	D_{SM}	m^2/s	7.89*10^{-13}
Water diffusion activation energy of SM	E_{aMW}	kJ/mol	36.60
Saturation concentration of moisture in SM material	C'_{SM}	mol/m^3	6965.28
Initial concentration of moisture in SM material	—	mol/m^3	619.63
Radial diffusion coefficient of CFS material immersed in 60 °C seawater	D_{CFSr}	m^2/s	1.33*10^{-12}
Axial diffusion coefficient of CFS material immersed in 60 °C seawater	D_{CFSz}	m^2/s	1.05*10^{-11}
Radial water diffusion activation energy of CFS material	E_{aFWr}	kJ/mol	42.35
Axial water diffusion activation energy of CFS material	E_{aFWz}	kJ/mol	38.86
Saturation concentration of moisture in CFS material	C'_{CFS}	mol/m^3	1026.25
Initial concentration of moisture in CFS material	—	mol/m^3	619.63

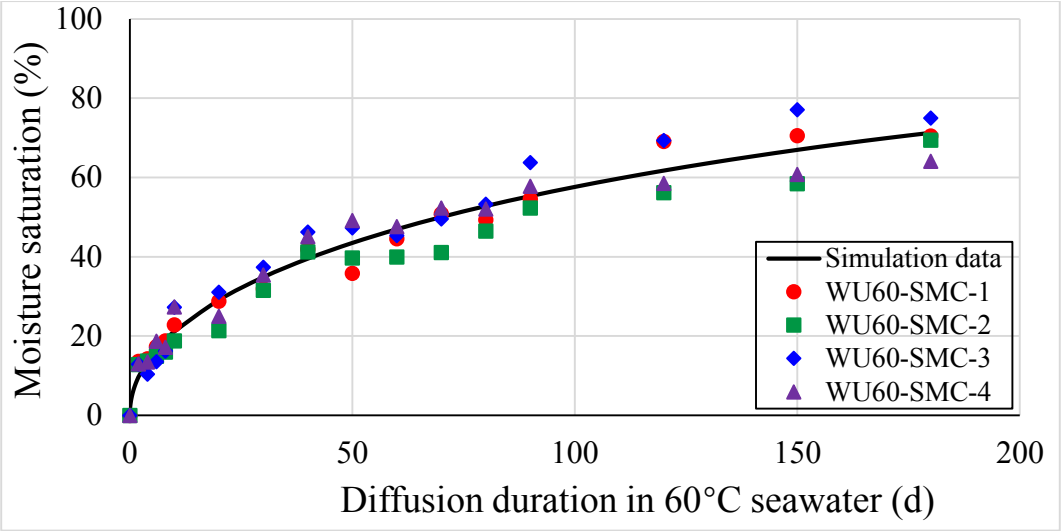

Fig.5-10 The moisture saturation comparison between the simulation data and four CFSRM specimens at 60 °C.

Fig.5-11 predicts the water uptake growth curve up to 720 days. By the end of the simulated duration, the total water uptake is 1.92 g, equal to 97.7% of the moisture saturation of the model. As shown in Fig.5-11, the increase in moisture saturation starts from 8.9%, namely 0.18 g which represents the initial moisture existing in the model. The moisture mass growth rate is comparatively high at the beginning. Subsequently it decreases gradually with time. In the end, it approaches zero and the curve reaches a plateau.

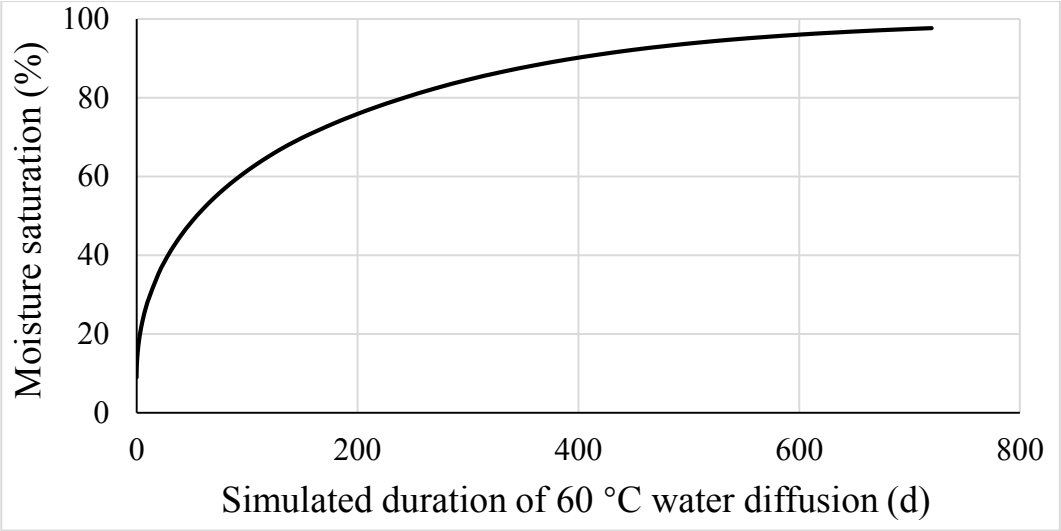

Fig.5-11 Simulated moisture uptake growth under conditions of 60 °C water diffusion for the whole CFSRM model.

Fig.5-12 displays this process in chronological order. The diffusion starts from surfaces and gradually extends inward until it reaches to saturation.

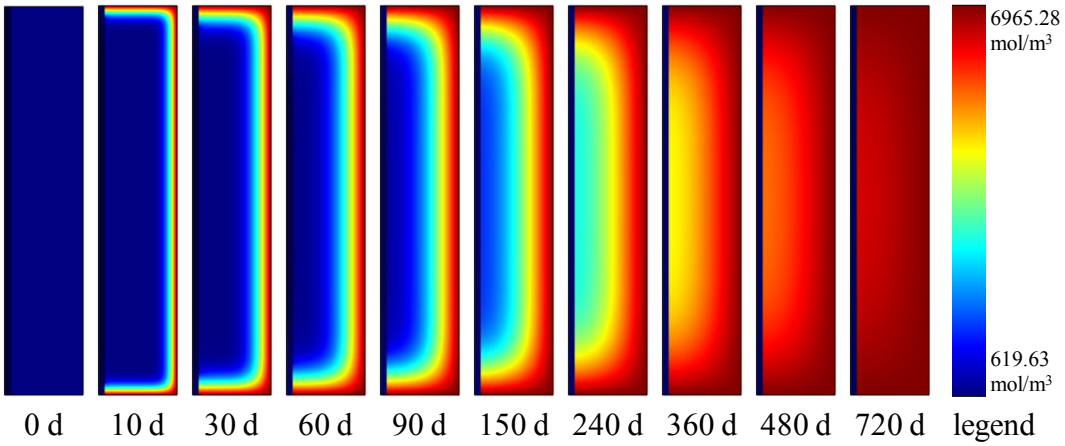

Fig.5-12 The diagram of the simulated diffusion process under conditions of 60 °C immersion.

As the whole model shares a uniform initial moisture concentration in this study, CFS domain has a comparatively higher initial degree of saturation than SM domain due to the much lower saturated concentration of CFS compared with SM. Fig.5-13 plots the water

uptake growth curve for CFS domain of the model, in the degree of saturation terms. As shown in Fig.5-13, the water uptake in CFS domain grows from 60.4% of saturation at the beginning and reaches the complete saturation on the 120th day. Combined with Fig.5-12, it can be found that the water uptake at early stage mainly occurs from both ends of CFS domain. It lasted for nearly 30 days until the absorbed moisture from the outside passes through SM domain and reaches the lateral surface of CFS. Then the water uptake turns to be dominated by its transverse diffusion until it reaches the complete saturation in the next 90 days. During this period, the curve in Fig.5-13 shows a monotonic increase. After 120 days of simulated duration, the curve reaches a plateau, indicating that CFS domain of the model has attained the saturation condition.

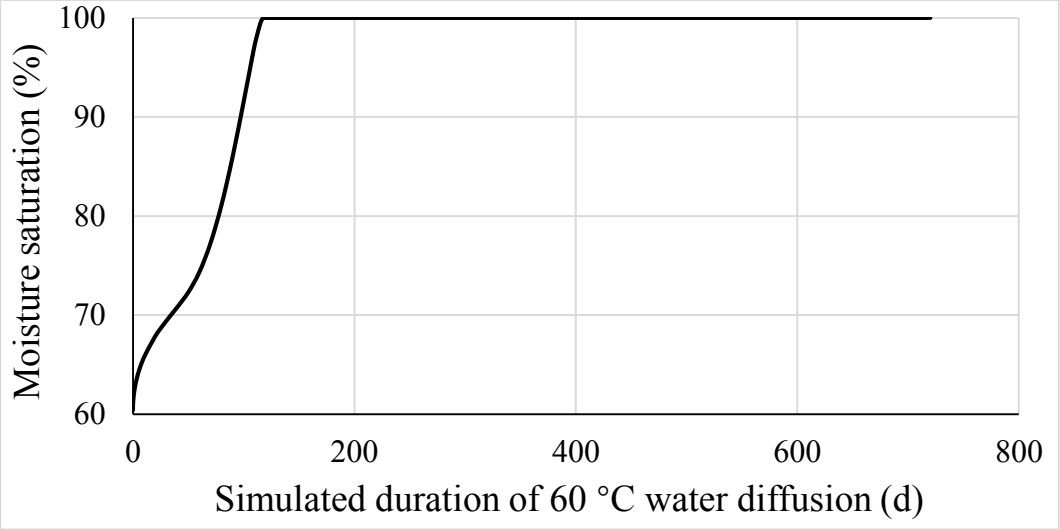

Fig.5-13 Simulated moisture uptake growth under conditions of 60 °C water diffusion for CFS domain in the model.

5.3.4 Effect of immersion temperatures

To investigate the temperature effect on the water diffusion, this section uses the numerical method to study the diffusion phenomenon under three ambient temperatures, namely 20 °C, 40 °C and 60 °C. By using time-temperature superposition principle based

on Arrhenius Law, the model is able to show different water absorption rates under various temperatures.

Before carrying out the numerical investigations, the model of the temperature effect is firstly calibrated under condition of 20 °C ambient temperature using experimental data obtained from the water uptake test as presented in Section 4.5.2. Fig.5-14 plots the calibration of the numerical water diffusion behaviour by using the water uptake test results under 20 °C immersion condition with the CFSRM specimens after oven drying treatment. Hence the model parameter of the initial concentration for Fig.5-14 is set to zero, in agreement with the initial dry state of those experimental specimens. Overall, the numerical results in Fig.5-14 follow the same trend as the experimental data, indicating that the numerical model is reliable in predicting the long-term water uptake behaviour of a CFSRM specimen under different temperatures.

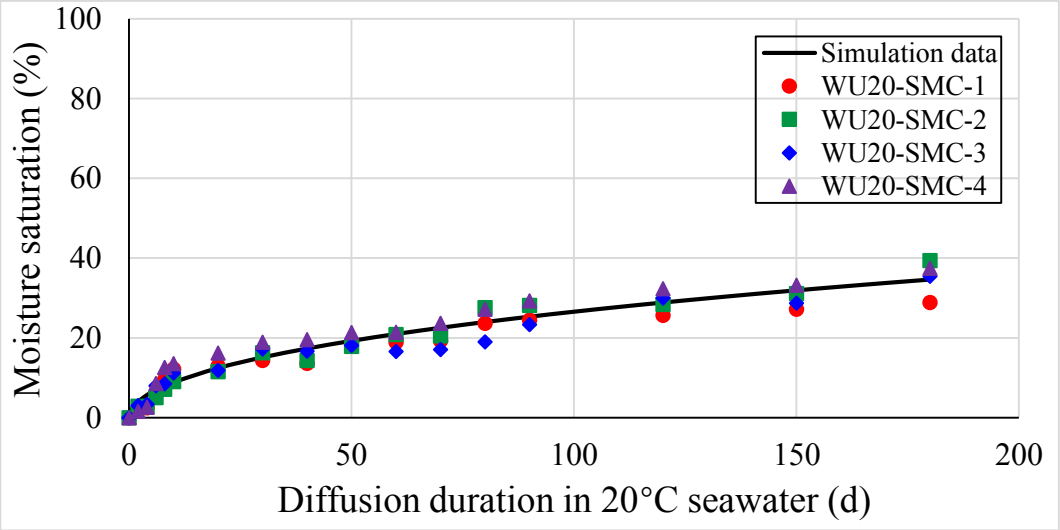

Fig.5-14 The moisture saturation comparison between the simulation data and test records at 20 °C.

After calibration of the numerical model, the temperature effect on water diffusion of CFSRM has been investigated, as plotted in Fig.5-15. Note that the initial moisture

concentration is returned to 619.63 mol/m^3 as given in Table 5-1, in order to analyse the general water diffusion process for CFSRM without the oven drying treatment at the beginning. By comparing the three moisture growth curves shown in Fig.5-15, it is obvious that the water absorption rate for the global model rises steadily with the temperature climbing from 20 °C to 60 °C. To reach 50% saturated condition, it takes the model 55 days at 60 °C, 130 days at 40 °C and 330 days at 20 °C respectively. Compared with the condition of 60 °C moisture diffusion, the period needed by the model to attain its half saturation are 2.4 times and six times longer under conditions of 40 °C and 20 °C individually. Moreover, 90% saturated condition can be reached by 390 days at 60 °C and 910 days at 40 °C. Regarding the 20 °C condition, the model can only reach 88% of the theoretical complete saturation by the end of the simulation duration. The comparison of moisture growth curves ranging from 20 °C to 60 °C clearly demonstrates that higher diffusion temperature can accelerate the water absorption process for CFSRM model.

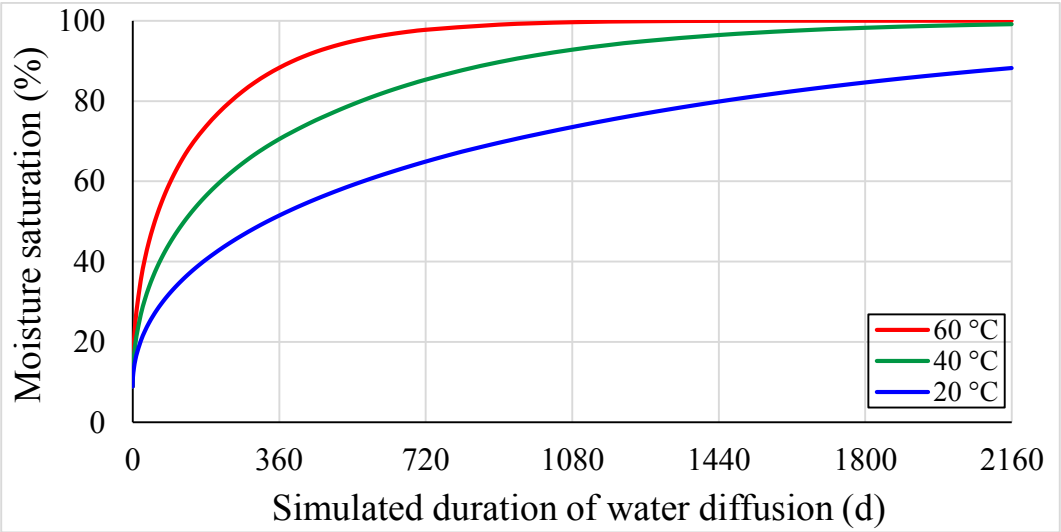

Fig.5-15 Simulated moisture uptake growth up to 2160 days for the global model with different ambient temperatures.

According to the analysis from Section 5.3.3, the water diffusion for the global model is mainly dependent on its SM domain, and the moisture absorption rate of SM is controlled

by its water diffusion coefficient which rises with temperature. With temperature climbing from 20 °C to 60 °C, its diffusion coefficient increases by more than six times as calculated by Section 4.5.2 based on its water diffusion activation energy E_{aMW}. As a result, the period required by the model to reach a certain degree of saturation at 60 °C is reduced by nearly six times when compared with 20 °C.

Fig.5-16 reveals the water diffusion process inside the model at 20 °C. Compared with Fig.5-12, it can be found that variations in temperature between 20 °C and 60 °C have an insignificant effect on the water uptake mechanism including the water diffusion path and the order of concentration changes in the model, although decreasing temperature can significantly slow down the water diffusion process.

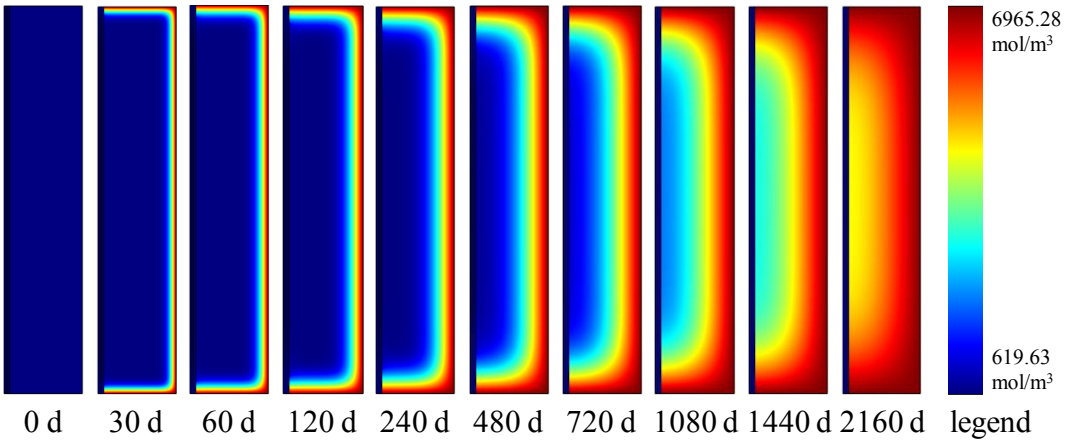

Fig.5-16 Simulated diffusion process under conditions of 20 °C immersion.

Water uptake growth curves for only CFS domain are given in Fig.5-17, which also indicates that raising temperature can noticeably accelerate the moisture absorption rate. While the temperature rises in the sequence of 20 °C, 40 °C and 60 °C, it takes the model 710, 270 and 116 days to reach the saturation condition respectively. Compared with the moisture absorption period at 60 °C, the model takes 2.3 times longer at 40 °C, and 6.1 times longer at 20 °C. Additionally, the comparison with these three curves reveals that

CFS domain under different temperature conditions keeps a similar trend of water diffusion, even though its water absorption rate is subject to temperature changes. The same with SM domain in the model, this phenomenon can also be explained by time-temperature superposition principle. According to intrinsic parameters E_{aFWr} and E_{aFWz} of CFS material given in Table 5-1, the growth in temperature from 20 °C to 60 °C increase its diffusion coefficient by 8.1 times in the radial direction and 6.8 times in the axial direction, leading to the reduction in the duration of its water uptake to reach saturation.

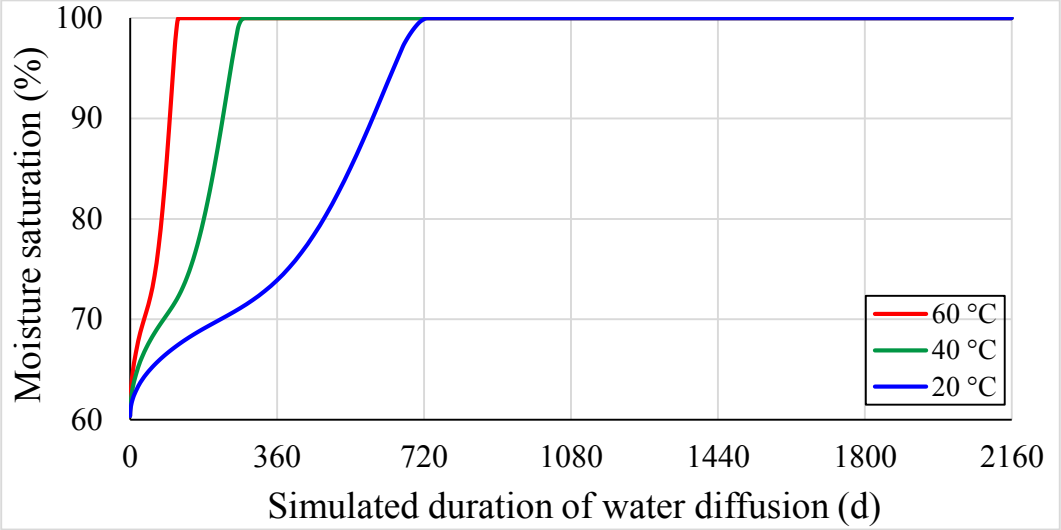

Fig.5-17 Simulated moisture uptake growth for CFS domain with different ambient temperatures.

To sum up, parameters E_{aMW}, E_{aFWr} and E_{aFWz} proved to be valid in the model as the intrinsic properties of CFSRM specimen. By using time-temperature superposition principle complied with Arrhenius Law, the model is able to simulate the temperature effect of water uptake on CFSRM specimen, and further analyse its moisture diffusion process beyond the available test duration between 20 °C and 60 °C.

5.4 Numerical model of pull-out behaviour

5.4.1 Cohesive zone model (CZM) introduction

Subject to environmental conditioning as described in Section 2.3 with diverse temperature and duration, CFSRM that is similar to FRP reinforced concrete is expected to reveal different degradation behaviours in hygroscopic expansion and interfacial ageing (Ray and Rathore, 2015; Maljaee et al., 2016), which lead to the decline in pull-out performance. In view of the fact that hygroscopic expansion and interfacial ageing are always coupled together in reality, each individual effect is impossible to be investigated using experimental studies. Therefore, numerical method is commonly used to investigate the influence of hygroscopic expansion or interfacial ageing on pull-out performance degradation individually (Liu et al., 2016). Hence the present section builds the numerical model to simulate the pull-out process, which will also be applied to the investigation into those complex ageing behaviours involving multi-field coupling effects in later studies.

In order to simulate interfacial bond properties between CFS and SM inside the specimen, a cohesive zone model (CZM) is usually used in the numerical studies and have proved to be able to acquire good simulation results when compared with the bond-slip tests (Wang, 2006; Liu et al., 2020; Mukhtar and Shehadah, 2021). Accordingly, the present study also adopts CZM to simulate the pull-out behaviour of the specimen.

In general, there are three types of possible contact failure modes at the interface subject to the traction force, namely pure tensile failure (Mode I), pure shear failure (Mode II) and mixed failure (Mode III) which is the combination of tensile failure mode and shear

failure mode based on a certain proportion. In this study, the contact failure mode can be classified into Mode II, as the shear stress plays a major role in the interfacial bond-slip behaviour while tensile stress can be generally ignored (Imani et al., 2010; Cheng et al., 2020). Compared with the carbon fibre itself, the interfacial contact between fibre and mortar substrate has proved to be the weakness which controls the bond-slip behaviour, especially when exposed to the harsh environment (Alessi et al., 2014; Cui et al., 2021). While tensile stress dominates the tensile behaviour and eventually causes the fibre fracture failure, shear stress dominates the interfacial bond-slip behaviour and finally causes the interfacial debonding failure (Weitsman, 2012; Kafodya et al., 2015; Heshmati et al., 2016; Benmokrane and Ali, 2018). Under the circumstance, the present study considers that the failure mode of the CFSRM specimen is predominantly Mode II, namely the pure shear failure at the CFS/SM interface under shear stress.

When utilising the CZM approach, there is a zero-thickness layer of CZM elements added between CFS and SM boundaries in the numerical model. These two components contact each other through CZM elements. Shear stress occurs in those interfacial elements as soon as the loading starts. For an arbitrary point in CZM elements, a local relative slip forms as the response to this shear stress (Sakin and Anil, 2019). The interfacial shear stress monotonically climbs until it attains the peak value. From this moment on, the adhesive contact at the point moves to damage state (Campilho et al., 2013). With the evolution of damage of adhesive contact in this state, the deterioration of shear stiffness for those interfacial elements is employed to simulate the delamination propagation at the interface. Then the shear stress reduces while the slip grows continuously. Once it reaches zero, the total decohesion happens at this point in CZM elements and the relevant interfacial shear stiffness falls to zero (Campilho et al., 2013). CZM defines such an interface separation condition as the complete adhesive contact damage.

The above mentioned process of the decohesion development for an arbitrary point in interfacial elements can be illustrated by a bilinear stress-displacement curve as presented in Fig.5-18, which is adopted as the constitutive relation of CZM by the present study, namely the local contact-separation law of CZM (Liu et al., 2019). τ and u in Fig.5-18 denote the local shear stress and the relative slip, respectively for an arbitrary point in interfacial elements. τ_p and u_p are the peak shear stress the point can attain and the related interfacial relative slip respectively. u_{td} is the critical slip value before the total decohesion occurs. G_{el} and G_{so} are the elastic fracture toughness and interface softening fracture toughness of CZM, respectively. D symbolises the adhesive contact damage for an arbitrary point in CZM, ranging from 0 to 1. $D = 0$ represents the intact adhesion state at the interface and $D = 1$ stands for the total decohesion state.

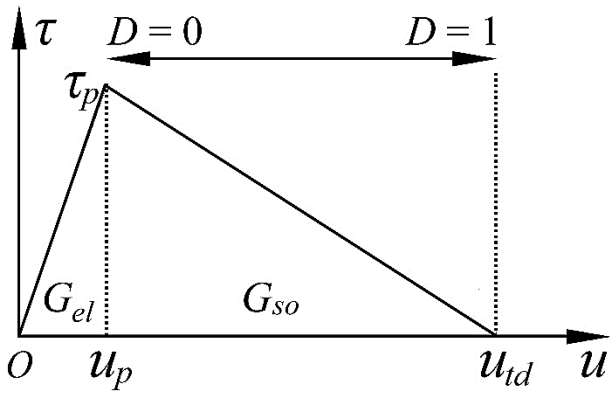

Fig.5-18 Bilinear constitutive relation of CZM adopted by the present study.

As shown in Fig.5-18, three basic CZM parameters, τ_p, u_p and u_{td}, are used to describe the unique interfacial behaviour. Those parameters are usually determined through calibration against experimental bond-slip test curves (Wu et al., 2010; Khoramishad and Zarifpour, 2018). In this study, the pull-out test data of specimens with no treatment, as shown in Section 4.7, has been used to determine these model parameters. When τ_p and u_p are determined, the interfacial shear stiffness K_τ can be obtained by Eq.5-2.

$$K_\tau = \frac{\tau_p}{u_p} \tag{5-2}$$

The total fracture toughness of CZM, G_t, is defined as the area under the bilinear curve of the interfacial contact-separation law in Fig.5-18. It consists of G_{el} and G_{so}, where G_{el} is called the elastic fracture toughness that is equivalent to the area below the upward slope and G_{so} is called the softening fracture toughness that is equivalent to the area below the downward slope (Liu et al., 2019).

Combined with K_τ, G_t can be written as

$$G_t = G_{el} + G_{so} = \frac{\tau_p u_{td}}{2} = \frac{K_\tau u_p u_{td}}{2} \tag{5-3}$$

Another important model parameter in CZM is the interfacial shear energy release rate G_r (Camanho et al., 2003). With the local slip u increasing at a certain point on the interface, G_r can be used to describe its interfacial adhesion energy changes because G_r indicates the area under the current stress-displacement track located at this point:

$$G_r = \int_0^u \tau \, du \tag{5-4}$$

Then the interfacial decohesion failure criterion of CZM can be given based on the relationship between energy release rate and fracture toughness as presented in Eq.5-5. For an arbitrary point in CZM elements, it should comply with Eq.5-5 within the entire contact-separation process. Once the relative slip u goes up to u_{td}, this point reaches the total decohesion state. Meanwhile, its G_r climbs up to the maximum value, namely G_t.

$$\begin{cases} G_r < G_t & (0 \le u < u_{td}) \\ G_r = G_t & (u \ge u_{td}) \end{cases} \tag{5-5}$$

After that, the interfacial adhesion evolution can be further subdivided into intact contact stage and damage development stage in terms of the energy changes (Camanho et al., 2003). When $G_r < G_{el}$, CZM elements remain in the intact contact condition without any adhesive damage emerging, namely $D = 0$. The damage initiation is governed by the criterion of $G_r = G_{el}$. When $G_{el} < G_r < G_t$, CZM elements move to damage development stage as the interfacial adhesive damage grows continuously from $D = 0$ to $D = 1$. In order to include the effect of D on the adhesive contact, CZM uses the adhesive shear stiffness deterioration of interfacial elements to simulate such a damage development process, as shown in Eq.5-6.

$$k_s(u) = (1 - D)K_\tau \tag{5-6}$$

where $k_s(u)$ denotes the current adhesive shear stiffness for an arbitrary point in interfacial elements, corresponding to its relative displacement u as the argument of the function $k_s(u)$.

D is a function of argument u for the whole contact-separation process in CZM. According to the interfacial shear stiffness changes presented in the CZM constitutive relation curve, $D(u)$ is a piecewise function and yields

$$D(u) = \begin{cases} 0 & (0 \le u < u_p) \\ \frac{u_{td}}{u}\left(\frac{u-u_p}{u_{td}-u_p}\right) & (u_p \le u < u_{td}) \\ 1 & (u \ge u_{td}) \end{cases} \tag{5-7}$$

Compared with the theoretical 1D bond-slip process as discussed in Section 3.5, CZM approach simulates this interfacial debonding process in terms of interfacial adhesion energy changes through stiffness deterioration. The published studies according to Cheng et al. (2020) and Zhu et al. (2020) have demonstrated that the residual frictional stress τ_r present at the interface has minimal influence on its bond-slip behaviour before its

complete delamination failure if it possesses a relatively short bond length such as 50 mm adopted in this study. Considering the above-mentioned research conclusion in combination with the fact that τ_r is not the research focus in this study, the trilinear local bond-slip relationship given in Section 3.5 can be further simplified into a bilinear curve while the last segment of the curve which represents the existence of τ_r is neglected. Then the theoretical interface failure mechanism as per the local bond-slip relationship in Section 3.5 is equivalent to the interfacial decohesion evolution defined by the CZM approach in the present section.

5.4.2 Numerical results for pull-out process

Alongside the water diffusion numerical model, a stress field at the interface between SM domain and CFS domain is added to the model for the simulation of CFSRM pull-out behaviour. According to Chapter 4, the uniaxial compressive elastic modulus of SM $E_{SM} = 40.4$ GPa, and the uniaxial tensile elastic modulus of CFS material is measured as $E_{CFSz} = 131.0$ GPa. Poisson's ratio of SM is taken as $\upsilon_{SM} = 0.18$ which is widely used in existing references (Chen et al., 2009; Szmigiera and Woyciechowski, 2013; Wang et al., 2015; Carrillo et al., 2019). Taking account of the orthotropic mechanical properties of CFS material, its Poisson's ratio and shear modulus for both the axial and radial directions are adopted from Camanho et al. (2003) who investigated the material delamination of carbon fibre reinforced polymer matrix composite by CZM approach. Detailed model parameters are shown in Table 5-2.

Table 5-2 Mechanical properties of CFS and SM in the model.

Parameter types	Symbol	Value	Unit
Elastic modulus of SM	E_{SM}	40.4	GPa
Poisson's ratio of SM	υ_{SM}	0.18	—
Axial elastic modulus of CFS	E_{CFSz}	131.0	GPa
Radial elastic modulus of CFS	E_{CFSr}	10.1	GPa
Axial Poisson's ratio of CFS	υ_{CFSz}	0.25	—
Transverse Poisson's ratio of CFS	υ_{CFSr}	0.45	—
Axial shear modulus of CFS	G_{CFSz}	5.5	GPa
Transverse shear modulus of CFS	G_{CFSr}	3.7	GPa

After defining mechanical properties for the material in the model, the model parameters such as τ_p, u_p, u_{td} in the CZM were calibrated using experimental data presented in Section 4.7. However, the testing curves cannot be used here directly because the displacement value includes not only the relative slip taking place at the interface between CFS reinforcement and SM substrate, but also the deformation in the anchorage zone.

Similar to the anchorage structure of the specimen used for CFS tensile test described in Section 4.6.1, the anchorage zone of the pull-out specimen comprised of the aluminium tube, hardened epoxy resin and CFS largely exceeds the length of the testing machine jig by 120 mm as shown in Fig.4-24 and symbolised by l_{pa}, let alone the junction zone of 10 mm in length that is represented as l_{pj} between the cylindrical mortar and the tubular structure of the anchorage. Consequently, the tensile deformation of such anchorage zones acted upon by the pull-out force P is going to contribute to the displacement growth

in the curve as well, in addition to the interfacial slip. In order to find out the actual interfacial slip of the specimens presented in Section 4.7, the tensile deformation of the anchorage zone, Δl_{pe}, is calculated using Eq.5-8, by assuming a linear elastic behaviour in the anchorage:

$$\Delta l_{pe} = \frac{Pl_{pj}}{A_{CFS}E_{CFSz}} + \frac{Pl_{pa}}{A_{Al}E_{Al}+A_{es}E_{es}+A_{CFS}E_{CFSz}} \tag{5-8}$$

where the cross-sectional area and elastic modulus used here are given in Section 4.6.1.

After solving the above-mentioned problems, all CZM parameters used in the numerical model can be summarised in Table 5-3. According to the average measured pull-out curves given in Section 4.7, the basic CZM parameters are determined as $\tau_p = 10.9$ MPa, $u_p = 0.13$ mm, $u_{td} = 0.58$ mm. By using Eq.5-2, the interfacial shear stiffness K_τ for CZM elements is found to be $8.3*10^{10}$ N/m^3. The fracture toughness of CZM is obtained as $G_t = 3.18$ kJ/m^2, derived from τ_p and u_{td} in combination with Eq.5-3. Furthermore, G_t contains elastic fracture toughness G_{el} and softening fracture toughness G_{so} with 0.73 kJ/m^2 and 2.45 kJ/m^2 respectively.

Table 5-3 CZM parameters for interfacial elements in the model.

Parameter types	Symbol	Value	Unit
Peak shear stress	τ_p	10.9	MPa
Relative slip corresponding to peak shear stress	u_p	0.13	mm
Critical relative slip before total decohesion	u_{td}	0.58	mm
Interfacial shear stiffness	K_τ	$8.3*10^{10}$	N/m^3
Fracture toughness	G_t	3.18	kJ/m^2

The boundary condition setup for the numerical model should comply with the actual pull-out test process as shown in Fig.4-24. It is obvious that the surface of the cylindrical SM at its loading end is constrained by the lower plate of the loading frame in its axial direction, while the CFS reinforcement embedded in SM substrate is pulled out on account of the pull-out force *P*. Other area of CFSRM is free without any constraint. As a 2D axisymmetric model, it defines these boundary conditions at an arbitrary longitudinal section as presented in Fig.5-19. In view of the fact that the bond-slip failure only happens at the interface between SM domain and CFS domain, the numerical model defines its internal boundary condition here with CZM element contact mode.

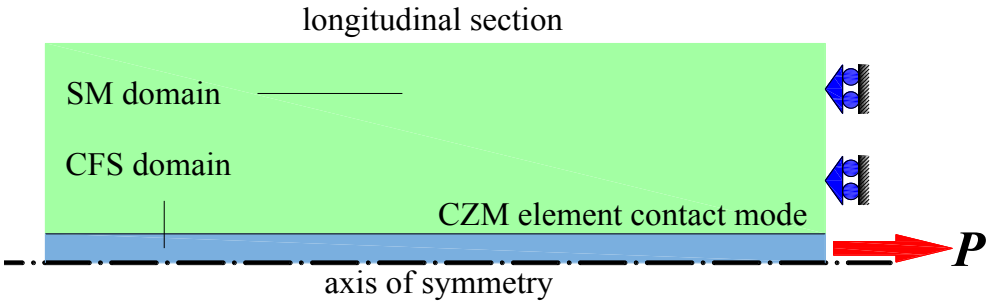

Fig.5-19 The diagram of boundary conditions setup.

The same as the experimental setup, the numerical model is loaded using displacement control method, with an increment of 1 μm each step. The load-displacement curve can be acquired, reflecting the relationship between the pull-out force and the loading end displacement of CFS domain in the numerical model.

Fig.5-20 displays the simulated pull-out curve in red line, along with the experimental test data in black curves after eliminating its extra tensile displacement stemming from the anchorage zone of the specimens. It is shown that the numerical model captures the ascending stage of the pull-out test reasonably well. However, the descending stage of the pull-out test cannot be well simulated in the model, due to the use of the simplified

interfacial bond-slip law by ignoring the residual friction force on the interface after debonding, and the assumption of the linear-elastic behaviour in the anchorage zone. As the experiment only recorded the total displacement of the lower plate, i.e. bottom of the mortar cylinder, the actual displacement of the anchorage zone is unknown. However, as this study only focuses on the maximum pull-out force and the interfacial behaviour beforehand, the descending stage of the pull-out data will not be discussed. Further studies will be necessary if the post-debonding behaviour is focused.

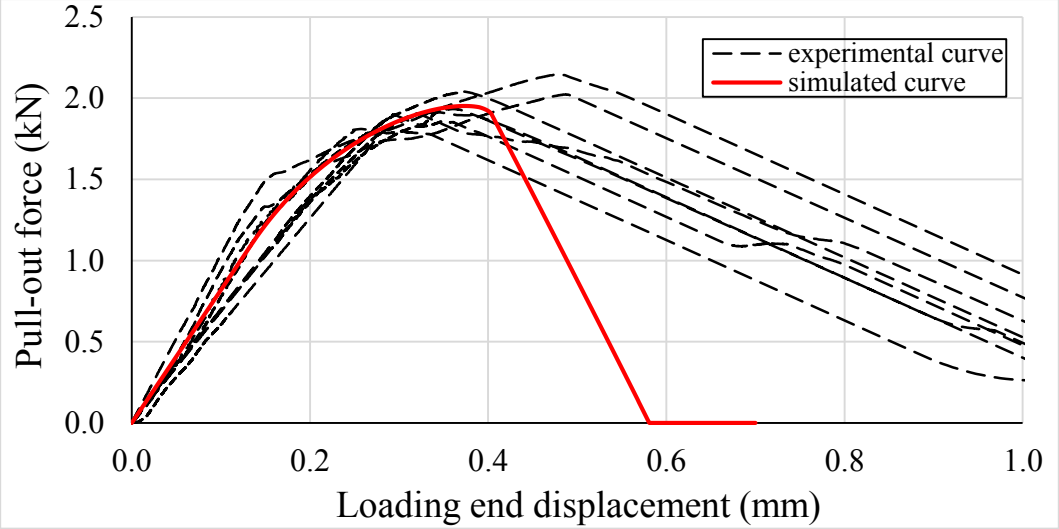

Fig.5-20 The numerical and processed experimental force-displacement curve at the loading end of CFSRM during the pull-out test.

Comparing the numerical and the experimental data, the numerical model is able to capture the experimental pull-out behaviour within its ascending stage, including the measured peak pull-out force of 1.95 kN and the derived interfacial slip of 0.37 mm at the peak point. The numerical model is thus believed reliable in carrying out later studies.

It is worth noting that the simulation result given in this section has not considered the effect of the material hygroscopic expansion or interfacial ageing yet. The actual interfacial behaviour, in fact, is largely dependent on the material durability under the

seawater ambient conditions. With moisture, time and temperature varying, the ultimate pull-out force is not a constant any more. Such a coupling effect on the pull-out behaviour will be investigated in Chapter 6.

5.5 Simulation study on hygroscopic expansion

5.5.1 Numerical results for hygroscopic expansion

As the effect of hygroscopic expansion is hard to calibrate by experimental method, the numerical study on hygroscopic expansion here pays more attention to the analysis of its general mechanical behaviour and the general trend about how the moisture swelling would affect the pull-out performance in terms of the CZM approach.

Based on the numerical model of pull-out behaviour given in Section 5.4.2, a new physical field focusing on the hygroscopic expansion is added into the model to simulate the swelling phenomenon and investigate the swelling stress. While this section revolves around the influence of hygroscopic expansion on CFSRM itself, subsequent sections will further discuss the temperature effect on hygroscopic expansion behaviour and how the hygroscopic expansion mechanism changes the pull-out behaviour.

The hygroscopic expansion field used herein is built based on the swelling mechanism presented in Section 3.3. In this model, Eq.3-13 is used to define the hygroscopic expansion coefficient β_{CHE} in CFS, i.e. the relationship between transverse swelling strain and its current moisture variation. With water diffusing into CFS through SM substrate, the moisture concentration in CFS climbs from the initial concentration until reaching the saturation condition, which causes hygroscopic expansion in CFS. As CFS

dilatation is physically constrained by the surrounding SM, the swelling stress caused by water diffusion can be obtained in this numerical study.

Before conducting the hygroscopic expansion investigations, the simulation method is validated using an experimental study on the free hygroscopic swelling strain of bismaleimide triazine resin (Pyo et al., 2016). Fig.5-21 compares the experimental data (Pyo et al., 2016) and numerical data using the present simulation method. As shown in Fig.5-21, the simulated swelling strain curve agrees well with the experimental results, although the experimental swelling strain in the initial stage is subtly higher than the simulation results. Such a difference may be due to the effect of the initial moisture content existent in the test sample. Overall, it is believed that the simulation method proposed herein is reliable to study the hygroscopic expansion behaviour of CFS embedded in CFSRM specimen.

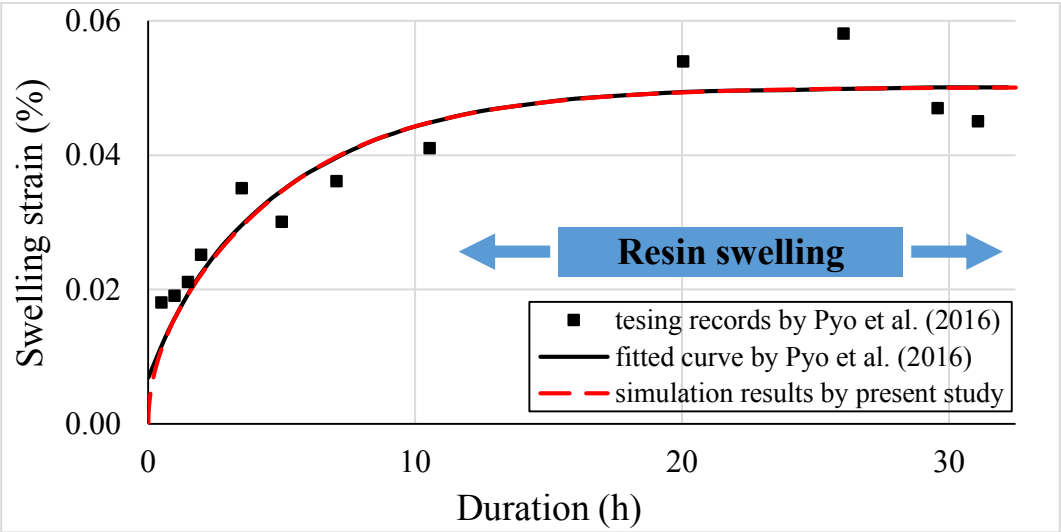

Fig.5-21 Comparison of simulated swelling strain and experimental results.

For CFS material used in the present study, its hygroscopic expansion coefficient, β_{CHE}, is measured to be 0.28 as given in Section 4.6.1. Only the elements in CFS domain are defined with β_{CHE}, while the dilatation is assumed to not occur in SM domain.

Additionally, the moisture concentration of the whole model is adopted from the water diffusion simulation results as discussed in Section 5.3, in order to reveal the actual swelling process in the CFSRM specimen. The mechanical properties, including the stress-strain constitutive relation and the boundary conditions for CFS and SM, comply with the pull-out numerical model presented in Section 5.4.2.

The swelling behaviour with water diffusion inside CFSRM at 60 °C is firstly investigated. The simulation result is illustrated in Fig.5-22 in terms of the variation in the transverse compressive stress σ_r.

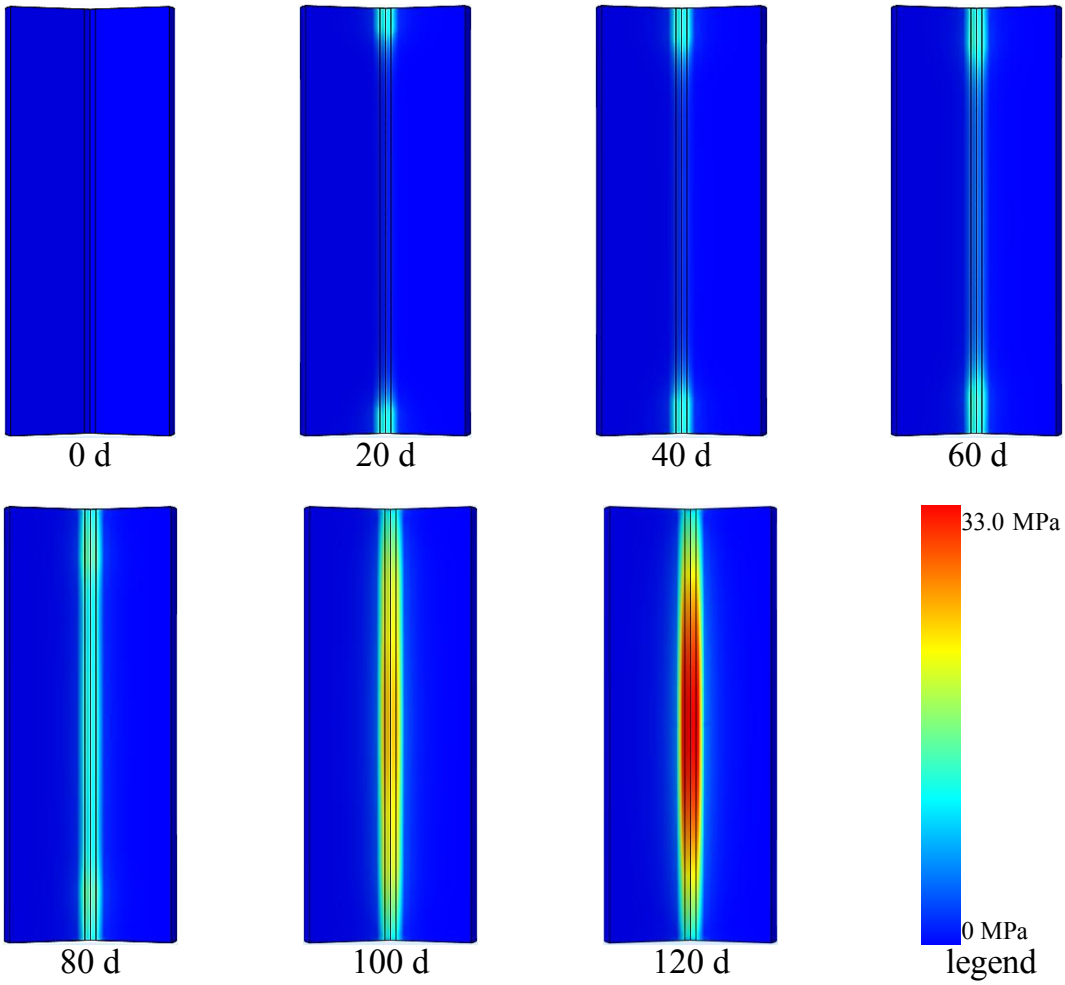

Fig.5-22 Evolution of the transverse stress σ_r induced by the hygroscopic expansion.

Compared with Fig.5-12 and Fig.5-13 which demonstrate the water uptake behaviour in CFS, it is obvious that the evolution of the transverse stress σ_r induced by CFS expansion is simultaneous with the moisture ingress into CFS domain, as explained in Eq.3-16. Water uptake growth in CFS lasted for 120 days. The development of σ_r, likewise, has a gradual increase within this duration and peaks on the 120th day with 33.0 MPa located at the middle region of the cylinder, as shown in Fig.5-22. After CFS reaches saturation, σ_r remains unchanged while SM domain continues to absorb moisture from the outside. Considering that CFS water uptake behaviour is mainly governed by its axial moisture diffusion mechanism at the early stage from 0 d to 60 d, σ_r only occurs at the two ends and propagates towards the middle. Once the moisture crosses from SM substrate to CFS/SM interface since the 60th day and is consequently absorbed by CFS, the radial moisture diffusion mechanism starts to dominate its water uptake and thus makes σ_r go up rapidly over CFS domain until it reaches the saturation.

The stress contour of Fig.5-22 also reveals its transverse stress distribution along the longitudinal orientation. After CFS reaches saturation, namely on the 120th day, it has the highest value of 33.0 MPa in compressive stress at the middle and gradually falls to 11.2 MPa towards both ends symmetrically. Since the transverse swelling of CFS is restrained by the mortar, such deformation tends to convert into the axial expansion of CFS material owing to the effect of Poisson's ratio. However, the closer to the middle of CFS, the more restraints upon the axial deformation of the swell region, thus the higher the transverse compressive stress σ_r. Furthermore, Fig.5-22 suggests that the radial stress σ_r drops drastically along the radial direction in SM domain, while it is almost constant along the radius in CFS domain, which is likely due to its small diameter (1.4 mm) of CFS compared to SM, and the axisymmetric hoop constraint on its lateral surface, leading to the almost uniform elastic compressive strain ε_{CFS}^{el} along its radial direction. Contrary

to CFS, SM has more than ten times the diameter of CFS, and the free boundary on its lateral surface. Thus its internal transverse elastic strain tends to rapidly recover along the radius, resulting in the rapid reduction of σ_r in SM. Fig.5-23 illustrates this phenomenon by slicing a path along the radius of CFSRM model from its centroid to its lateral boundary. As depicted in the graph, σ_r along this path proves to be in accordance with the above mentioned distribution characteristics throughout 120 days of hygroscopic expansion.

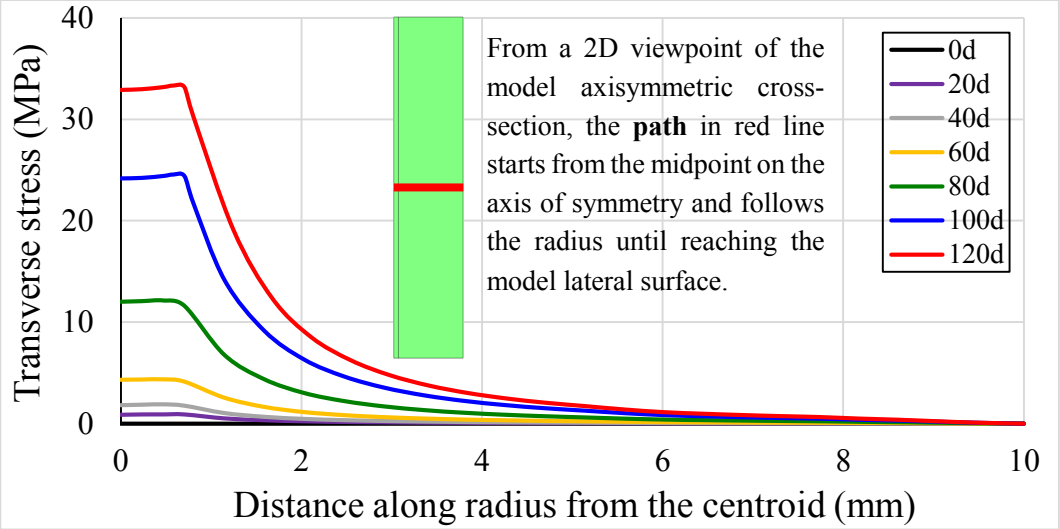

Fig.5-23 Distribution of transverse compressive stress σ_r along the model radius from the model centroid to its lateral boundary up to 120 days of water gain in CFS.

As shown in Fig.5-23, the highest σ_r along the path in SM domain occurs on its inner lateral surface, namely the contact interface with CFS. In addition, the swelling stress along the interface in the longitudinal direction is plotted in Fig.5-24.

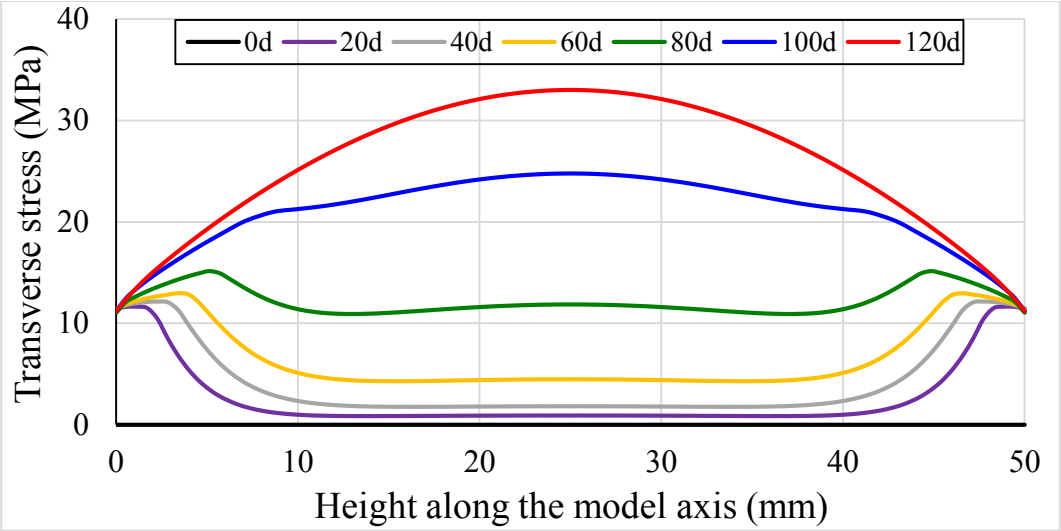

Fig.5-24 σ_r distribution along the interface between CFS and SM up to 120 days of hygroscopic expansion.

According to the water diffusion mechanism, the saturation condition first occurs at both ends of CFS where the swelling strain is hardly constrained in the axial direction. Hence σ_r at both ends is almost totally due to the transverse constraint imposed by the SM hoop. As shown in Fig.5-24, σ_r resulting from the pure transverse constraint is 11.2 MPa at both ends of CFS and remains unchanged over time once C_{CFS} reaches the maximum level. On the 120th day, σ_r at the midpoint of the interface is 33.0 MPa, nearly three times higher than the value located at the CFS end. A relatively high value of σ_r at the middle is attributed to not only the transverse swelling strain restricted by the SM hoop but also the constraint on its longitudinal deformation, as discussed previously. In addition, Fig.5-24 indicates that the global increase of σ_r at the interface strictly follows the water diffusion process. For the first 60 days, σ_r climbs steadily at the end and propagates towards the centre, while its growth at the middle is quite slow (from zero to 4.5 MPa) by the 60th day, with the corresponding C_{CFS} raised by 28.1 mol/m^3. For the later 60 days when C_{CFS} at the middle quickly rises by 378.5 mol/m^3 until reaching the saturation, σ_r there

experiences an increase simultaneously from 4.5 MPa to 33.0 MPa by the 120th day, more than six times the average growth rate of σ_r during the course of the former 60 days.

σ_r is essentially resulted from the transverse hygroscopic deformation of CFS constrained by the surrounding SM. According to the effect of Poisson's ratio, ε_{HE} is expected to convert into the axial strain along CFS under the circumstances of σ_r. However, due to the incompatible elastic modulus and swelling properties of CFS and SM, which are bonded together by their shared interface, interfacial shear stress τ_s will be induced and can be derived based on the bond-slip law defined at the contact interface of the CZM. Fig.5-25 indicates the variations in τ_s acquired along the interface within 120 days of the swelling process.

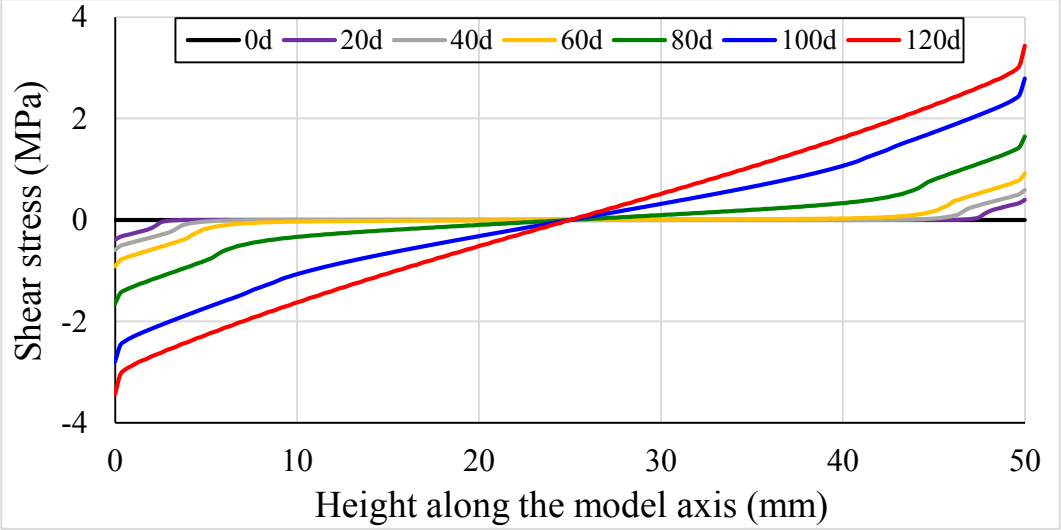

Fig.5-25 Shear stress τ_s distribution along the interface up to 120 days of hygroscopic expansion.

Contrary to σ_r, the distribution of τ_s on the interface has the highest value at both ends and a gradual descending trend towards the midpoint with the zero shear stress. The swelling deformation with time causes the gradually accumulative slip at the interface starting from the ends. In addition, during the first 60 days when the water diffusion effect

only appears at both ends of CFS, τ_s can hardly be found in the middle part. Once the external water starts to move into CFS through the transverse diffusion mechanism, the rapid swelling of CFS makes τ_s climb quickly along the interface, particularly at both ends. During the latter 60 days, τ_s at the end jumps from 0.9 MPa to 3.4 MPa by the 120th day, nearly four times as quick as the average growth rate of τ_s during the course of the former 60 days.

In accordance with the theory of 1D bond-slip mechanism introduced in Section 3.5, the existent τ_s at the interface will further cause the axial stress σ_z both in the SM domain and the CFS domain. In view of the fact that the cross-sectional area of the surrounding SM substrate is more than two hundred times larger than the CFS reinforcement, the axial stress σ_z in SM can be considered insignificant, compared with σ_z in CFS. Fig.5-26 plots the σ_z distribution inside CFS domain and its trend during the hygroscopic expansion.

When CFS reaches the saturation, the maximum σ_z occurs at the midpoint of CFS lateral surface with the axial stress of 102.4 MPa, while σ_z at both ends remains zero throughout the swelling process. The distribution of σ_z in CFS has a gradual ascending trend from the end to the middle as the result of the accumulated interfacial τ_s acting upon the CFS lateral surface. Similar to the evolution of σ_r, the increase in σ_z is not obvious within the first 60 days, as it goes up from zero to 9.7 MPa at the mid-span of CFS. Subsequently it experiences a sharp rise with respect to the later 60 days whereby σ_z climbs from 9.7 MPa to 102.4 MPa, more than ten times faster than the former period.

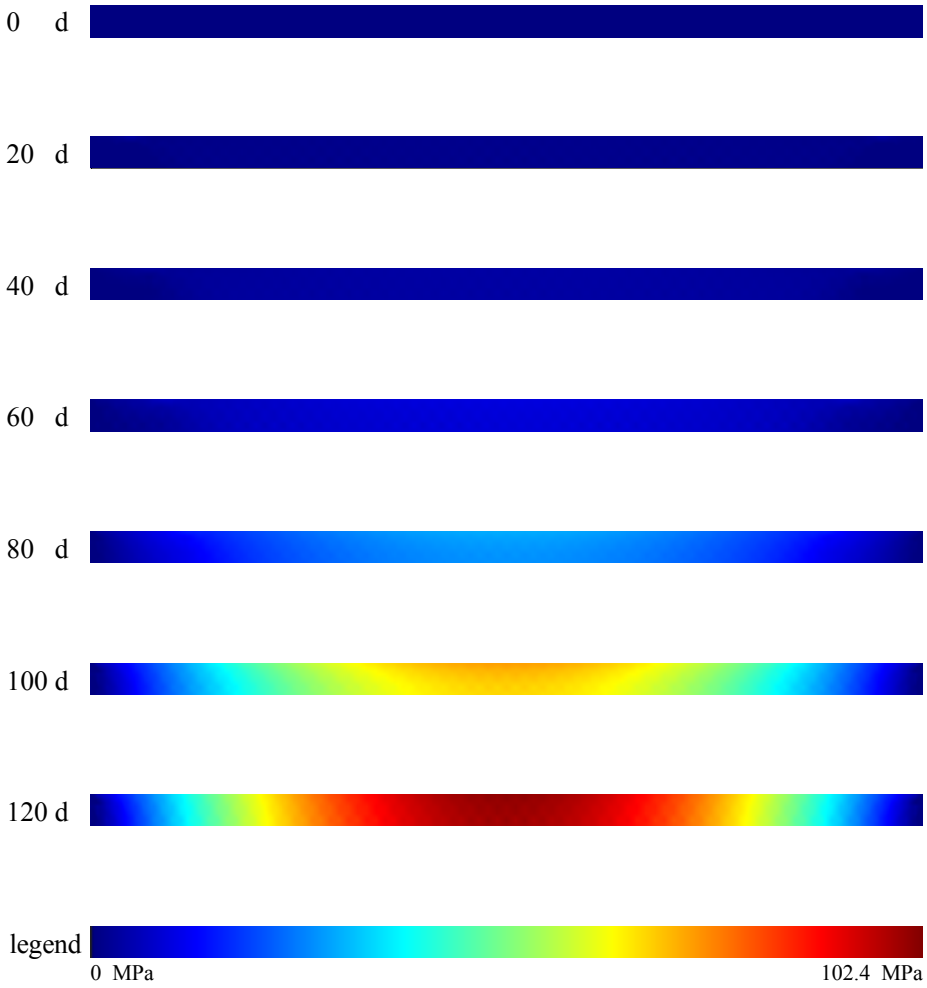

Fig.5-26 Axial stress σ_z distribution inside CFS up to 120 days of hygroscopic expansion.

Integrating σ_z over the cross section of CFS for the whole CFS domain, the axial force distribution along its longitudinal direction can be acquired as presented in Fig.5-27. Acted upon by the interfacial shear force that restrains the axial slip between CFS and SM, the compressive force in CFS longitudinal orientation monotonically increases from the end to the middle. With time passing, CFS axial force along its length has an ascending trend which is consistent with σ_z mentioned above. The maximum axial force located at the middle is 153.6 N on the 120th day, while it keeps zero at both CFS ends over the entire swelling process.

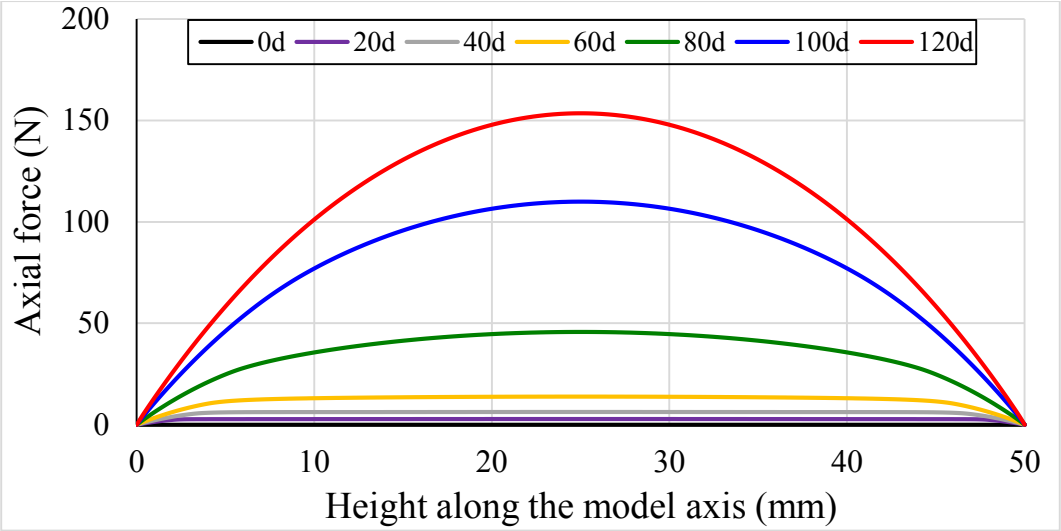

Fig.5-27 Axial force distribution along CFS length up to 120 days of hygroscopic expansion.

5.5.2 Temperature effect on hygroscopic expansion

According to the experimental and numerical diffusion studies on CFS material given in Section 4.6.2 and 5.3.4 respectively, the ambient temperature has a significant effect on the moisture diffusion rate, which will therefore affect the CFS swelling behaviour significantly as the hygroscopic expansion of CFS embedded in SM is entirely governed by the water diffusion process.

In order to investigate the temperature effect, the present numerical model selects five different temperatures varying between 20 °C and 60 °C at 10 °C intervals. Such a temperature range is consistent with the previous temperature effect study on CFSRM water absorption. Temperature is the only control variable for the whole swelling process of the embedded CFS. Based on those simulation results, the present study analyses the temperature effect, in terms of the transverse compressive stress σ_r, CFS/SM interfacial shear stress τ_s and CFS axial force inside the model respectively.

Fig.5-28a illustrates the increase in σ_r located at the midpoint of CFS/SM interface during the course of CFS dilatation with temperature changes. Fig.5-28b shows the comparison of the maximum τ_s between various temperatures over the entire swelling process. Fig.5-28c describes the growth in the axial force located at the middle cross-section of CFS during its hygroscopic expansion on the condition of different temperatures.

According to the simulation results presented in Fig.5-28, variations in temperature do not change the ascending trend in the stresses or the axial force inside the model. Once the embedded CFS reaches its full saturation, the values of σ_r, τ_s and the axial force reach their theoretical maximum owing to the hygroscopic expansion, and likewise remain unchanged afterwards despite the change of ambient temperature, with 33.0 MPa in compressive stress, 3.4 MPa in shear stress and 153.6 N in axial force respectively.

In comparison with the water uptake growth curve of CFS domain from 20 °C to 60 °C given in Section 5.3.4, Fig.5-28 reveals that the evolution of the swelling stress is simultaneous with the water diffusion behaviour in CFS no matter what temperature is. This phenomenon is explained in Section 3.3 with CFS hygroscopic expansion mechanism whereby the swelling stress at an arbitrary point in CFS domain is completely induced by its local moisture concentration growth on the condition that its dilatation strain is constrained by the hoop of the surrounding SM domain.

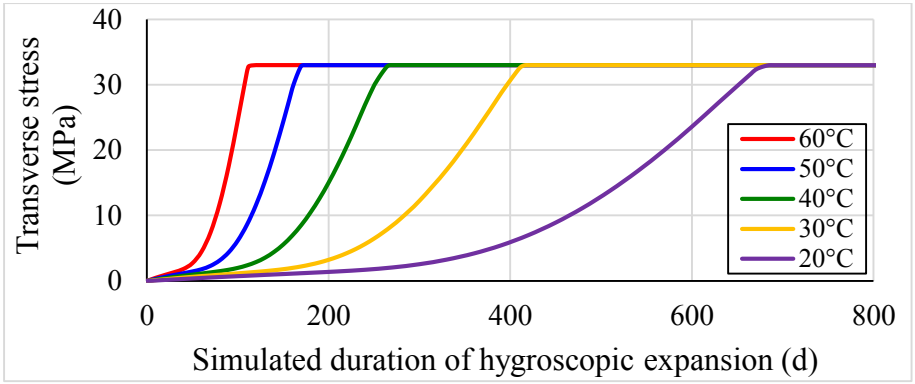

(a) Growth curves of σ_r at the midpoint of CFS/SM interface with different temperatures.

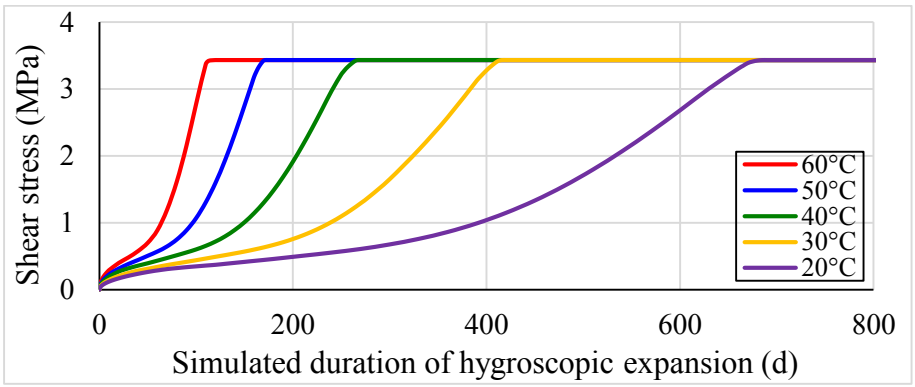

(b) Growth curves of the maximum τ_s at the interface between CFS and SM with different temperatures.

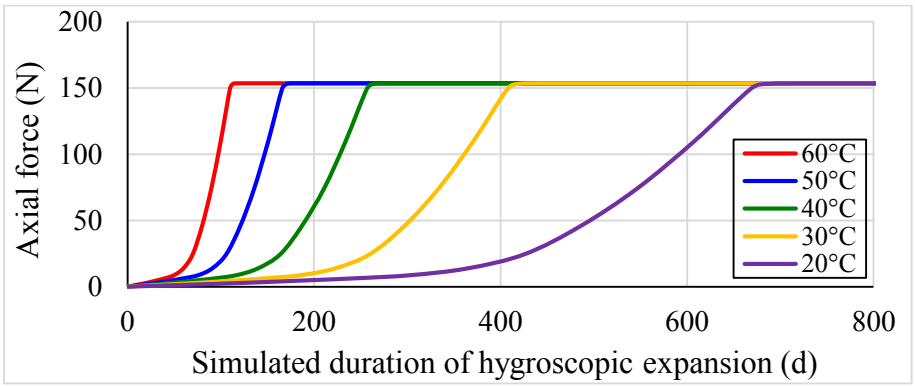

(c) Growth curves of the axial force located at the middle cross-section of CFS with different temperatures.

Fig.5-28 Temperature effect on CFS hygroscopic expansion in terms of the transverse compressive stress, the interfacial shear stress and the axial force.

Furthermore, the change in the ambient temperature can affect the swelling process, thereby controlling the growth rate of σ_r and τ_s in the model. More specifically, for all types of swelling stresses, there is an identical correlation between the prescribed temperature and the duration needed by them to reach their ultimate value. Compared with the entire period of hygroscopic expansion development at 60 °C, it takes 1.5 times, 2.3 times, 3.7 times and 6.1 times longer at 50 °C, 40 °C, 30 °C, and 20 °C respectively. Obviously, the whole swelling duration monotonically increases with the decline in temperature. Fig.5-29 indicates this trend as per the specific days needed for the swelling process at different temperatures.

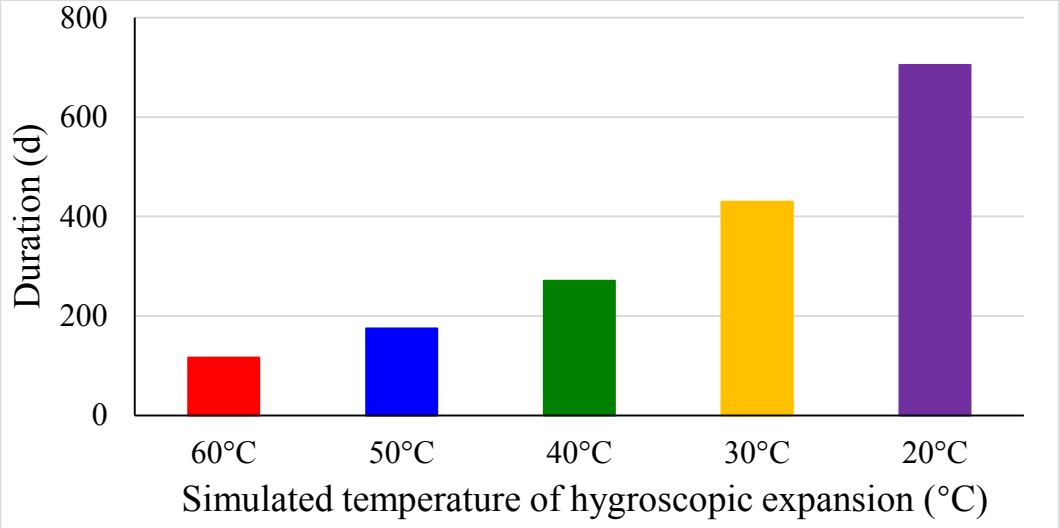

Fig.5-29 The trend of swelling duration going up with the decline in temperature.

To sum up, temperature plays a key role in governing CFS hygroscopic expansion rate by directly controlling the water diffusion rate inside CFS. Based on 60 °C of the ambient temperature, reducing temperature can prolong the swelling duration. Therefore, the temperature effect on hygroscopic expansion cannot be neglected with regard to the further degradation studies focusing on CFSRM pull-out behaviour in later sections.

5.5.3 Influence of hygroscopic expansion on pull-out behaviour

Conventional pull-out test when used for accelerated ageing treated CFSRM specimens immersed under elevated temperature seawater for a period, has its intrinsic limitation, such as that it cannot distinguish the hygroscopic expansion effect from the other contributing factors on the pull-out behaviour degradation. Once the moisture diffuses into the CFS, hygroscopic expansion occurs. In the meantime, such a moisture intrusion is expected to cause the interfacial ageing, namely damaging the adhesive bonding of the polymer matrix among fibres in CFS as well as the interface between CFS and SM. However, by utilising numerical simulation method this problem can be avoided as it can decouple the above accelerated degradation process and thus investigate the influence of hygroscopic expansion or interfacial ageing on CFSRM pull-out behaviour separately. Based on the multi-filed coupled model used hereinbefore, this section focuses on the pure swelling effect on the pull-out performance.

According to the simulation results of the material dilatation with time and temperature introduced in Section 5.5.1 and 5.5.2, the swelling strain recorded in the hygroscopic expansion physical field is extracted as the initial strain of CFSRM material and then added into the numerical model of its pull-out behaviour given in Section 5.4.2. Under the condition that the model has a time and temperature dependent initial strain before simulating the CFS pull-out process from SM domain, the present study can thus investigate how the hygroscopic expansion mechanism influences the pull-out behaviour over the whole swelling duration.

Fig.5-30 illustrates the evolution of the peak pull-out force in the model, revolving around the development of the swelling extent from the original status without any dilatation

deformation to the moisture saturation status with the maximum dilatation deformation of the model. Clearly, the hygroscopic expansion present in the model is detrimental to CFSRM pull-out performance. As the swelling phenomenon develops with time, it makes the peak pull-out force decline gradually until the dilatation process finishes.

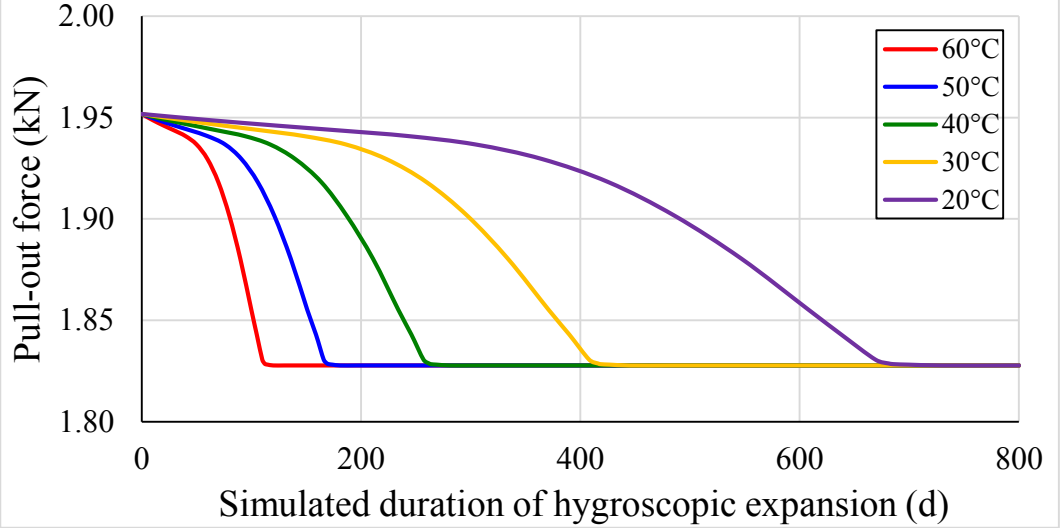

Fig.5-30 The decrease in peak pull-out force with the development of hygroscopic expansion.

As shown in Fig.5-30, the time-dependent pull-out forces at various temperatures ranging from 20 °C to 60 °C share the same starting point of 1.95 kN in pull-out force, representing the initial value of the peak pull-out force for the model before water diffusion or swelling occurs. Note that this value is obtained from the fundamental pull-out mechanical model in Section 5.4.2, consistent with the experimental results given in Section 4.7. Subsequently, the peak pull-out force falls monotonically over time. By the end of the simulated duration, it reaches a plateau no matter what the ambient temperature is. Finally, it is reduced by 6.4% over the entire simulation period, dropping to 1.83 kN.

Compared with the hygroscopic expansion presented in Section 5.5.1, it is found that there is a similar developmental trend between the peak pull-out force decrease and the

model swelling process. Both of them are dominated by the water diffusion level in the model. Taken the curve at 60 °C as an example, at the early stage from 0 d to 60 d, the peak pull-out force only goes down by 1.1%, quite slowly from 1.95 kN to 1.93 kN, while the swelling stress experiences a slight increase at the same time. Then they all enter a period of rapid development. The peak pull-out force quickly falls by 5.2% during the later 60 days, from 1.93 kN to 1.83 kN. Eventually they keep constant after nearly the 120th day when CFS reaches the saturation condition.

Temperature change has been found to affect the pull-out force subject to hygroscopic expansion as the same way as the hygroscopic expansion itself, as shown in Fig.5-30. On the one hand, reducing temperature can remarkably slow down the force reduction, which is equal to the swelling duration under each prescribed temperature condition respectively. On the other hand, the ultimate peak pull-out forces given in Fig.5-30 are identical once CFS reaches the saturation. To sum up, the ambient temperature can only influence the reduction rate of the peak pull-out force based on the temperature effect on hygroscopic expansion, which does not change its descending trend or the ultimate value.

In view of the fact that the mechanism of CFS swelling acting upon CFSRM pull-out behaviour does not alter with temperature, the present study selects the simulation result of pull-out process at 60 °C, serving as the representative model case to do further analysis. Fig.5-31 displays the pull-out curves after zero, 40d, 80d and 120d of 60 °C hygroscopic expansion conditioning respectively.

A continuous drop in the pull-out force can be found over time. The peak point on the curve gradually declines with the onset of CFS swelling, agreeing with the findings in Fig.5-30. The maximum pull-out force is 1.95 kN to begin with, and falls to 1.94 kN, 1.90

kN and 1.83 kN on the 40th, 80th and 120th day respectively. The decrease rate of the pull-out performance is obviously slow at the early stage and accelerates later.

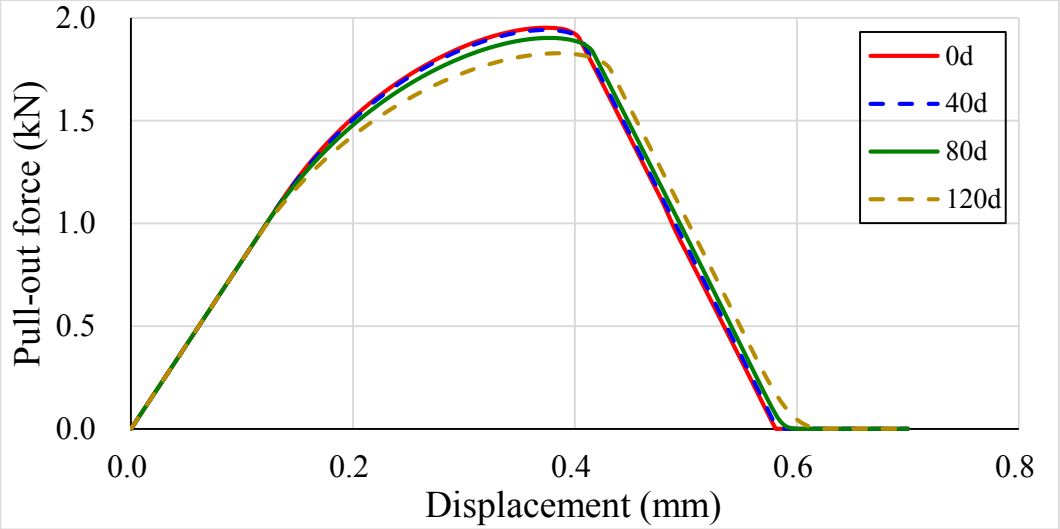

Fig.5-31 Simulated pull-out curves on the starting day, the 40th, 80th and 120th day of 60 °C hygroscopic expansion conditioning respectively.

The pull-out behaviour with the swelling development shown in Fig.5-31 is dependent on the shear stress evolution at the interface between CFS and SM domain. At the beginning, water diffusion inside the model leads to CFS dilatation deformation. Then the increase in deformation is expected to further cause the shear stress and local slip along CFS/SM interface. When simulating CFSRM pull-out behaviour, this interface composed of CZM elements is acted upon by the superposition of the swelling stress and the pull-out shear stress. The initial swelling stress and strain existing in the interface reduces its ultimate mechanical properties for the pull-out behaviour. On the condition that the complete interfacial debonding has not happened yet, the critical interfacial shear stress and the critical local relative slip induced by the pull-out force during the entire pull-out process experience a gradual reduction with the development of hygroscopic expansion.

As a result, the presence of the hygroscopic expansion has an adverse effect on the pull-out behaviour of CFSRM model. Fig.5-32 gives an exposition of such an adverse effect in terms of the interfacial shear stress distribution at 60 °C. Note that all curves depicted in Fig.5-32 record the unique τ_s distribution under the condition that the pull-out force reaches its peak point no matter how long the swelling duration is.

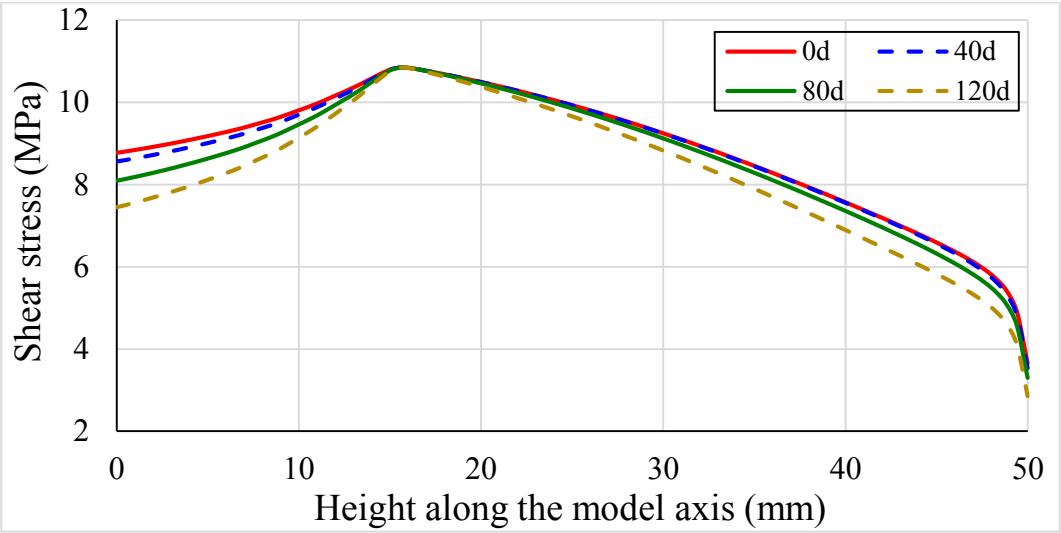

Fig.5-32 Shear stress distribution at the interface acted upon by the peak pull-out force after 0d, 40d, 80d and 120d of 60 °C hygroscopic expansion conditioning respectively.

Overall, τ_s reduces with the increase of the swelling deformation, although its maximum value along the interface keeps unchanged with 10.9 kN, which is the pre-defined interfacial ultimate shear strength τ_p given in Section 5.4.2. By integrating τ_s within the interface, the acquired shear force is consistent with the pull-out force on each corresponding day presented in Fig.5-31. It is reduced to 99.4%, 97.4% and 93.6% on the 40th, 80th and 120th day respectively, indicating the same falling process as the pull-out performance suffering the consequences of hygroscopic expansion. Apart from the τ_s evolution trend with time, Fig.5-32 also reveals that τ_s along the whole interface is subject to the influence of hygroscopic expansion whether it is located in the elastic bond region or the softening region in CZM. Furthermore, the swelling effect on τ_s becomes

more striking if the position of τ_s is closer to the end of the interface, which is due to the accumulative interfacial slip induced by CFS axial deformation under the condition that the surrounding SM domain imposes the physical constraints upon CFS radial dilatation.

By means of changing the specific value of β_{CHE} in the numerical modelling, the present study finds that there is a linear relationship with β_{CHE} versus the reduction in the maximum pull-out force, as shown in Fig.5-33. The simulated ambient temperature is set to be 60 °C here, as the above-mentioned analysis has proved that the variation in temperatures only changes the duration required within the swelling process.

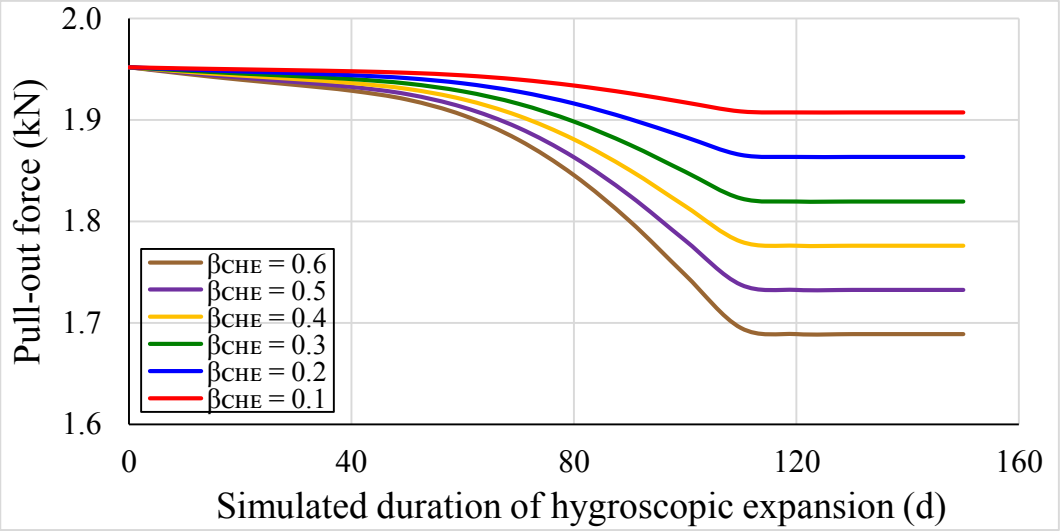

Fig.5-33 Reduction in pull-out force owing to hygroscopic expansion with different β_{CHE}.

Furthermore, from Fig.5-33 it can be found out that such a linear relationship is constant during the entire development process of hygroscopic expansion. With the development of hygroscopic expansion, the reduction in the pull-out force on any given day under the condition of different β_{CHE} has an obvious scaling relationship as per the specific value of β_{CHE}. When the effect of moisture swelling reaches its maximum and the pull-out force reaches a plateau accordingly, the reduction in the pull-out force is 262.8 N with its related

$\beta_{CHE} = 0.6$ or 44.3 N with its related $\beta_{CHE} = 0.1$. The reduction in the pull-out force for the former is six times larger than the latter.

As the simulation results suggest that the reduction in pull-out force is linear to the change of β_{CHE}, the present research of the swelling effect can be further broadened to a general analysis applied to FRP and FRP reinforced materials with diverse coefficients of hygroscopic expansion, instead of being limited by a certain type of material with a particular value of β_{CHE}.

While Section 5.5.3 analyses to what extent the moisture swelling itself can affect the pull-out performance of CFSRM material, Chapter 6 carries out the special study focusing on the influence of hygroscopic expansion coupled with interfacial ageing in terms of the pull-out force decline.

As the degradation in the experimental pull-out force of CFSRM is comprised of two parts from both the hygroscopic expansion effect and the interfacial ageing effect on the adhesive interface between CFS and SM, it should be noted that the experimental results cannot be used directly to validate the numerical model herein. Combined with the interfacial ageing data stemming from the degradation process studies based on TPD model, the decoupled swelling effect can be further analysed, the detail of which is presented in Chapter 6.

5.6 Summary

This chapter carries out the numerical simulation on the physical and mechanical properties of CFSRM specimens, including its interior water diffusion behaviour, interfacial bond behaviour and the hygroscopic expansion behaviour.

Based on Fick's Law and CFS/SM two-medium diffusion mechanism, a cylindrical orthotropic water diffusion model is built to simulate the long-term diffusion process. Simulation results agree well with the test records, proving the accuracy of the numerical model. The simulation of temperature effect on water diffusion shows that the growth in temperature from 20 °C to 60 °C can shorten the required duration of the embedded CFS to reach saturation by 6.1 times. It quantitatively explains the feasibility of raising the temperature to accelerate the water diffusion and the subsequent degradation process of CFSRM specimen within a limited experimental time.

By means of the CZM approach, the numerical model simulates the entire process of the interfacial debonding failure under the uniaxial pull-out loading. The simulated pull-out curve is able to capture the experimental pull-out behaviour within its ascending stage, including the measured peak pull-out force and interfacial shear stiffness.

Based on the numerical model of water diffusion and interfacial bond behaviour, another physical field that simulates the hygroscopic expansion of CFS inside CFSRM is added into the model. The development of the swelling process and the resultant swelling stress are found to be synchronous with the water diffusion process. Accordingly, raising temperature can accelerate the moisture swelling but would not change the maximum swelling stress when CFSRM reaches the saturated condition. The interfacial shear stress

owing to the hygroscopic expansion mechanism has an adverse effect on the pull-out performance. Such an effect has a linear correlation with the coefficient of CFS hygroscopic expansion.

6 LONG-TERM DURABILITY PERFORMANCE OF CFSRM

6.1 Overview

The degradation of bond behaviour of TRM materials is a long-term phenomenon under normal marine environments. Based on Arrhenius Law, the elevated-temperature accelerated ageing was adopted as the conditioning method in the present study in order to observe the interfacial degradation of CFSRM specimen within a limited experimental duration. Pull-out test was used in this chapter to investigate the interfacial degradation of CFSRM specimens after exposure to seawater immersion for a certain period.

In brief, there were 24 CFSRM specimens prepared and tested in Chapter 6, wherein 12 of them were immersed in 60 °C seawater up to 240 days whilst the other 12 were immersed in 20 °C seawater up to the same duration. After ageing treatment, they were used to carry out the pull-out test by means of Instron testing machine. Note that in Chapter 6, the test results of specimens after ageing treatment were compared with the baseline value of the pull-out force which was obtained from the previous pull-out test with eight intact CFSRM specimens as mentioned in Section 4.7.

A multiphysics numerical model which combines water diffusion, hygroscopic expansion, interfacial ageing and pull-out behaviour altogether was also carried out in this chapter. A three-parameter durability (TPD) model was proposed to analyse and predict the long-term interfacial ageing behaviour. In this study, the degradation mechanism of interfacial ageing was simulated by the reductions in local bond-slip relationship which were assumed to be governed by TPD model. Then the multi-field numerical model was used

to investigate the interfacial degradation mechanisms of CFSRM considering both hygroscopic expansion and interfacial ageing.

Following the above-mentioned method, two different degradation modes (Reduction Mode I and Reduction Mode II) in terms of local bond-slip relationship that were used in CZM are discussed. As per each of them, the contributions of hygroscopic expansion and interfacial ageing to the total degradation are separately simulated. After comparing with experimental and numerical data, only Reduction Mode I was adopted in further studies, due to the advantage of enabling decoupling of hygroscopic expansion and interfacial ageing. A simplified hand calculation method was then proposed to predict the long-term pull-out performance of CFSRM under various marine environments. The effects of two key influencing factors, immersion temperature and the moisture concentration, were discussed at the end of this chapter.

6.2 Elevated-temperature accelerated ageing method

In order to investigate the long-term durability of fibre composite materials within a restricted experimental duration, elevated-temperature treatment is commonly used to accelerate material degradation and thus shorten the required duration (Kunioka et al., 2016; Cabral-Fonseca et al., 2018; Nepomuceno et al., 2021). By immersing the FRP reinforced concrete into a high temperature solution, existing studies have focused on their degradation of mechanical properties under various service conditions and predictions of durability performance (Micelli and Nanni, 2004; Silva et al., 2014).

This study targets the long-term interfacial properties of CFSRM specimens. Elevated-temperature accelerated ageing method was adopted by immersing the specimens in the

water tank under the temperature of 60 °C for various periods before carrying out pull-out tests. Using 60 °C as the acceleration temperature can attain the balance between the accelerated ageing efficiency and the allowable critical immersion temperature according to the composite material properties (Robert et al., 2010; Ascione et al., 2016; Ksouri and Haddar, 2018). Both ACI 440.3R-12 (American Concrete Institute, 2012) and CAN/CSA S806 (Canadian Standards Association, 2021) recommend immersion temperature of 60 °C for the accelerated ageing treatment, which is also selected as the highest accelerated temperature in published durability studies of relevant composite materials (El-Hassan et al., 2018; Ghabezi and Harrison, 2020). Therefore, the present study adopted 60 °C as the ambient temperature of seawater immersion during the elevated-temperature accelerated ageing treatment for CFSRM specimens.

A custom-made insulated curing tank, as shown in Fig.6-1, was built for carrying out the accelerated ageing test. A digital thermostatic controller was attached to the tank, as shown in Fig.6-1b, which worked as an automatic switch of heating and keeps the seawater temperature fluctuating within the range of 60±0.5 °C.

(a) (b)

Fig.6-1 Elevated-temperature insulated seawater curing tank: (a) stainless steel curing tank; (b) digital thermostatic controller.

Another control group of specimens was prepared alongside, which were immersed in 20 °C normal temperature seawater for the same duration as for the elevated-temperature treated specimens. It should be noted that the immersion temperature used here is consistent with the previous studies on the water diffusion of CFSRM specimens.

In general, the accelerated ageing period varies from 7 to 240 days (Nepomuceno et al., 2021). For fibre composite materials, existing literature indicates that the material degradation slows down with time (Silva et al., 2014; Wang et al., 2017a), which is more distinct under high temperature accelerated ageing process (Chen et al., 2006; Uthaman et al., 2020). In order to optimise the experimental work, various duration intervals should be adopted. In this study, durations of 30, 60, 120 and 240 days were used for both 20 °C and 60 °C test groups. Based on the aforementioned experimental variable setup, each test with a unique set of experimental variables was repeated three times to ensure the reliable results which were collected from the same test group including three specimens after the same ageing conditioning. The specimen labels used herein indicate the purpose and the conditioning method of specimens as follows: “P” denotes the pull-out test; “60C” or “20C” means the seawater immersion temperature; “30d, 60d, 120d, 240d” represents the ageing treatment duration; the last number in the label symbolises the serial number of specimens conditioned in the same way. In this way, the specimens used for 20 °C test groups are named by P20C-30d-1, 2, 3; P20C-60d-1, 2, 3; P20C-120d-1, 2, 3 and P20C-240d-1, 2, 3 respectively. The specimens used for 60 °C test groups are named by P60C-30d-1, 2, 3; P60C-60d-1, 2, 3; P60C-120d-1, 2, 3 and P60C-240d-1, 2, 3 respectively.

Fig.6-2 shows the overall specimens for the interfacial degradation study.

(a) (b)

Fig.6-2 Specimens prepared for CFSRM degradation investigation.

6.3 Ageing test results

6.3.1 Residual pull-out performance exposed to elevated-temperature accelerated ageing

Fig.6-3 displays all pull-out tested CFSRM specimens after elevated-temperature accelerated ageing treatment at 60 °C, from left to right in chronological order of ageing duration. CFS pull-out failure mode, namely the interfacial debonding failure between CFS and SM, was found for all specimens, and little difference was found among different ageing periods. That is, the fibre reinforcement of all CFSRM specimens presented here was pulled out from the mortar substrate after the test. The same conclusions have been found on the specimens under room temperature as well, as presented in Section 4.7.

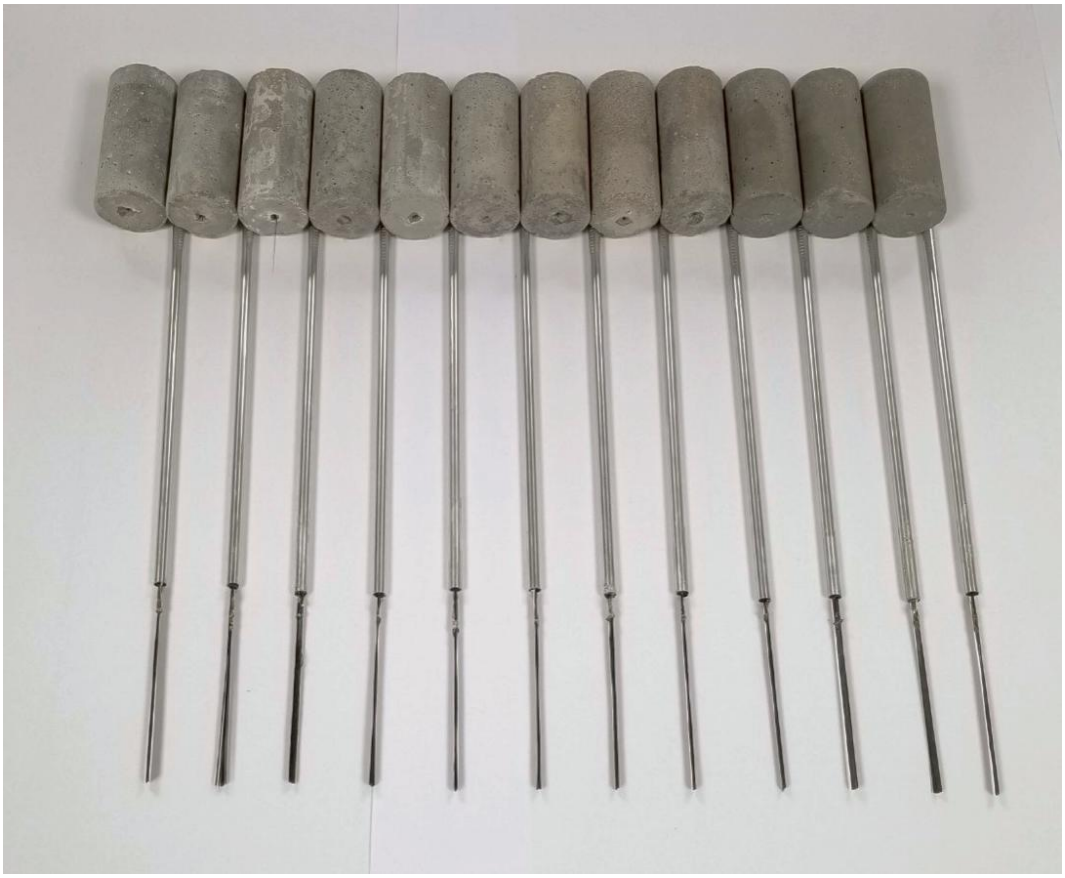

Fig.6-3 Tested CFSRM specimens exposed to elevated-temperature accelerated ageing of seawater immersion at 60 °C.

Fig.6-4 to Fig.6-7 show the pull-out test results of CFSRM specimens after 30, 60, 120 and 240 days of elevated-temperature accelerated ageing respectively. A gradual decline in the residual pull-out performance of CFSRM has been found. The decrease in the peak pull-out force becomes more evident with the increase of the ageing period. Additionally, the ascending stage of the pull-out force-displacement curve becomes more nonlinear with a longer degradation duration, which suggests that the interfacial bonding between CFS and SM is more likely to lose the integrity under longer exposure time.

Although the test results for all specimens complied with the pull-out failure type, it should be noted that the discreteness and the randomness still existed in the test results. As shown in Fig.6-5, the peak pull-out force on the blue curve (P60C-60d-2) has a lower

value than others. It means that the interfacial debonding failure of this specimen occurred earlier than other specimens. The CFS/SM bond of P60C-60d-2 is weaker compared with P60C-60d-1 or P60C-60d-3. Such a lower pull-out performance may result from the specimen making process or the experimental operation process. As shown in Fig.6-6, the pull-out curve of the green one (P60C-120d-3) has a strange shape with fluctuation in half way. The long-term ageing treatment damaged the integrity of adhesive interface between CFS and SM, leading to the problem of uneven shear stress transfer from SM to CFS when the specimen was acted upon by a force (Davalos et al., 2012b). Consequently, partial fibre filaments at the outermost CFS were prone to the early rupture during the loading process. Then the pull-out force experienced a sudden drop at its ascending stage as the interfacial shear stress was redistributed along the remaining continuous fibres. Owing to the fact that the interfacial bond still worked by this moment, the pull-out force continued to go up until reaching the peak point which represented the maximum pull-out force the specimen could sustain.

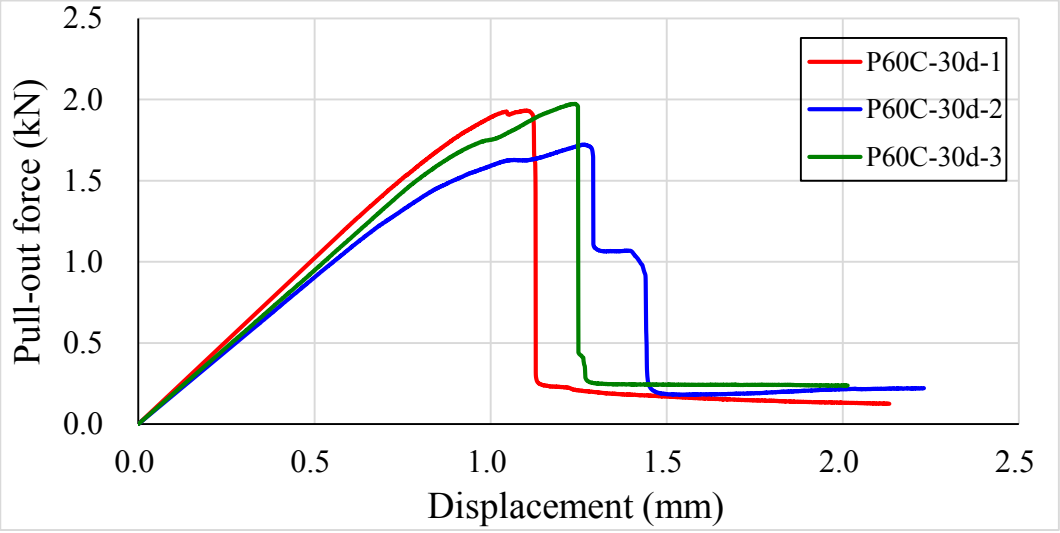

Fig.6-4 Pull-out curves of CFSRM specimens on the 30th day of ageing treatment at 60 °C.

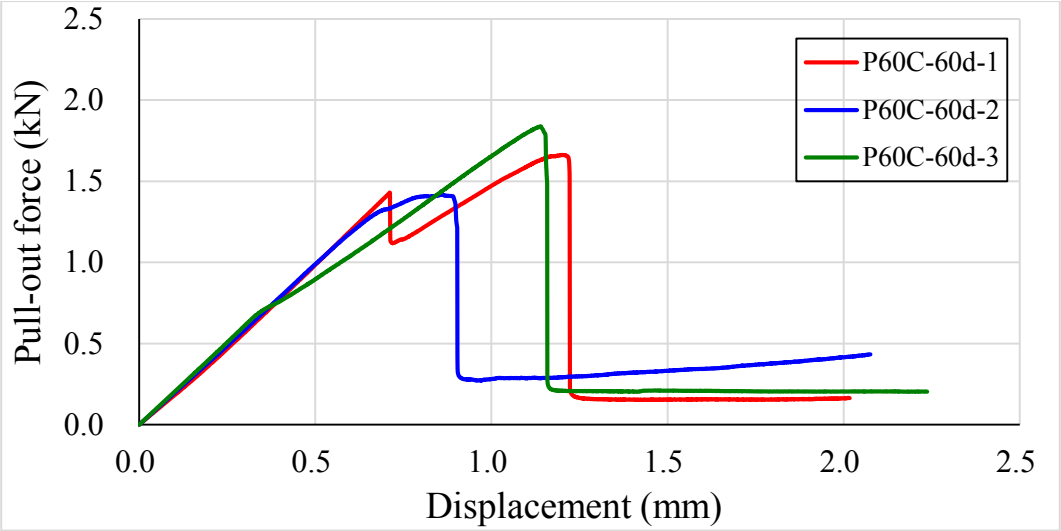

Fig.6-5 Pull-out curves of CFSRM specimens on the 60th day of ageing treatment at 60 °C.

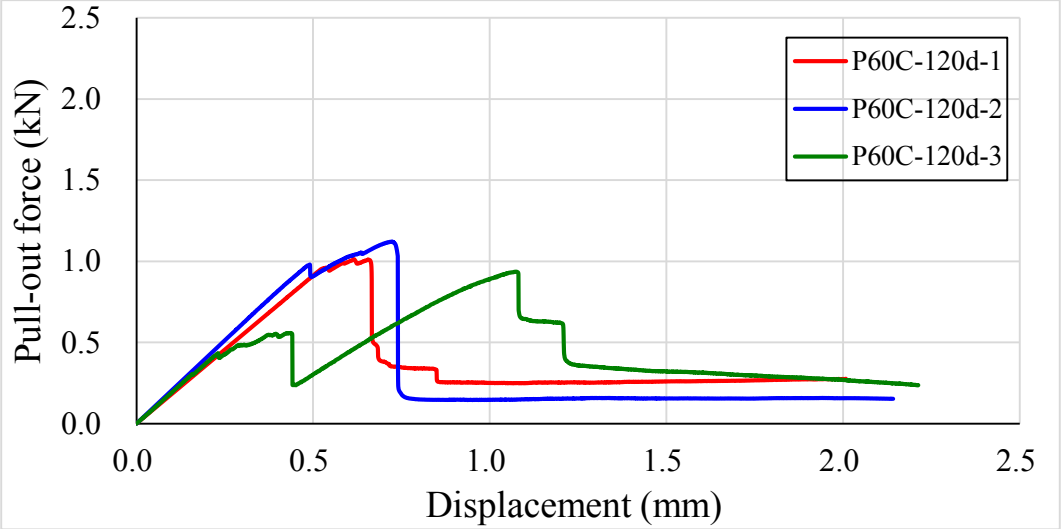

Fig.6-6 Pull-out curves of CFSRM specimens on the 120th day of ageing treatment at 60 °C.

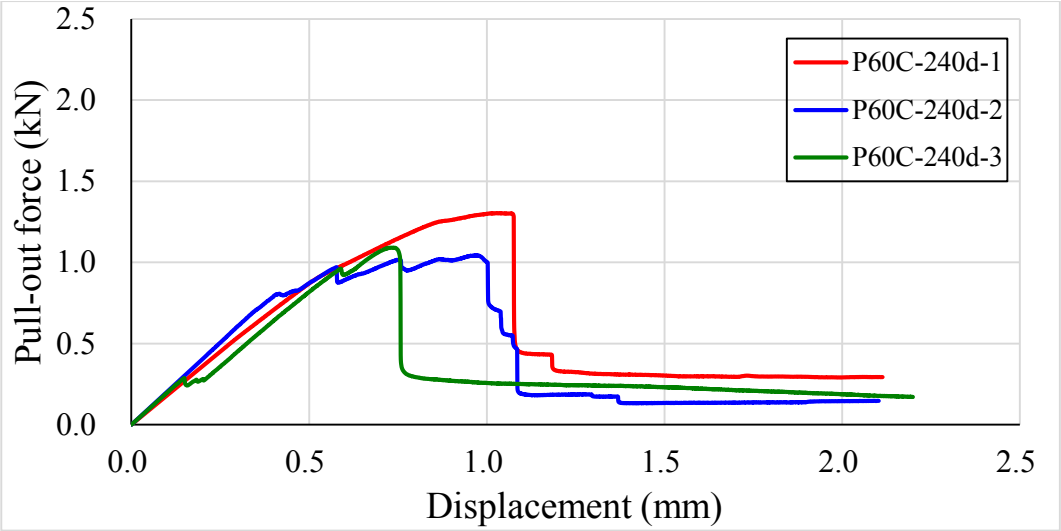

Fig.6-7 Pull-out curves of CFSRM specimens on the 240th day of ageing treatment at 60 °C.

As shown from Fig.6-4 to Fig.6-7 inclusive, although the discreteness and the randomness present in those pull-out curves cannot be avoided, the scatter of the test results is within a small range of 15%. The coefficients of variation for the peak pull-out force of each test group which contains three specimens after 30, 60, 120 and 240 days of treatment have the values of 7.2%, 12.8%, 9.1% and 12.1% respectively. Note that the detailed testing data containing all specimens used in Chapter 6 will be summarised in Table 6-1. The above-mentioned data analysis of test results indicates that the scatter of those pull-out curves will not affect the research conclusions from the present study about the long-term pull-out behaviour of CFSRM.

6.3.2 Residual pull-out performance under normal service condition

Fig.6-8 displays all tested specimens from left to right in chronological order of 20 °C conditioning duration. Little difference in the failure mode of pull-out has been found when compared with those in 60 °C test group. It indicates that the reinforcement rupture

does not happen during the test and the interfacial failure controls the pull-out test results for all specimens in this study.

Fig.6-8 Tested CFSRM specimens exposed to the normal service condition of seawater immersion at 20 °C.

The pull-out force-displacement curves of CFSRM specimens after 30, 60, 120 and 240 days of treatment under normal service conditions are shown in Fig.6-9 to Fig.6-12. Unlike the 60 °C test group, no distinct difference of test results can be observed within the first 120 days of treatment. The variation trend in the peak pull-out force indicates that the deterioration of adhesive interface between CFS and SM under the normal service condition at 20 °C is much slower than the accelerated ageing condition at 60 °C. Consequently, specimens from 20 °C test group maintain the higher pull-out resistance than 60 °C test group when the long-term conditioning is ended at the 240th day. Furthermore, linear increase in the ascent stage of the pull-out curve has been found

among all conditioning time. Compared with specimens from 60 °C test group, environmental conditioning of immersion at 20 °C is deemed less likely to damage the interfacial integrity, which is in agreement with what reported in the literature (Tatar and Hamilton, 2016; Wang et al., 2017a).

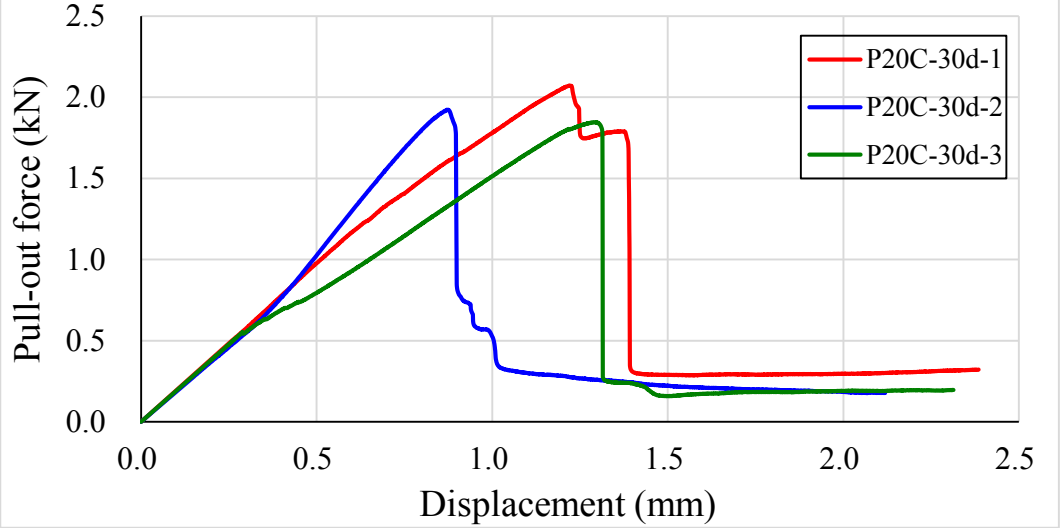

Fig.6-9 Pull-out curves of CFSRM on the 30th day of environmental conditioning at 20 °C.

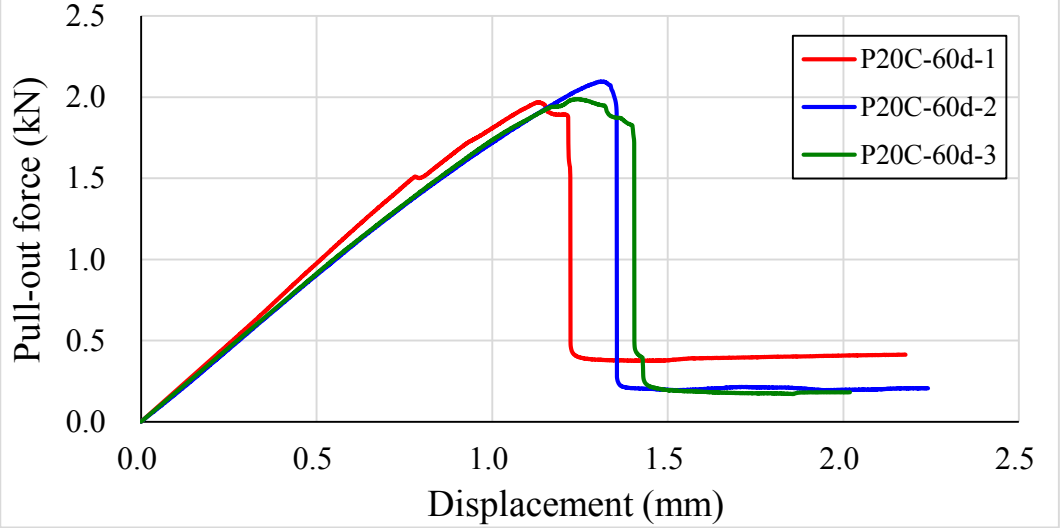

Fig.6-10 Pull-out curves of CFSRM on the 60th day of environmental conditioning at 20 °C.

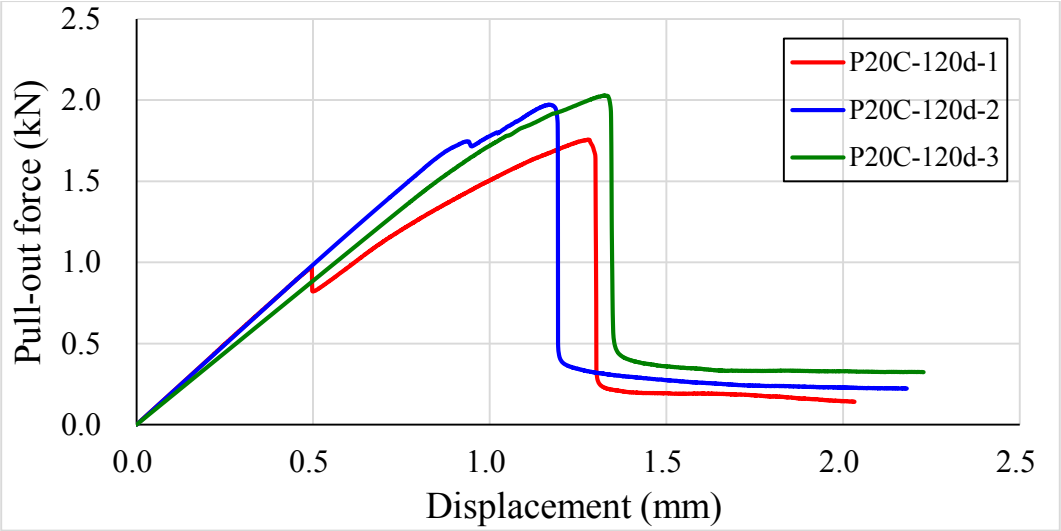

Fig.6-11 Pull-out curves of CFSRM on the 120th day of environmental conditioning at 20 °C.

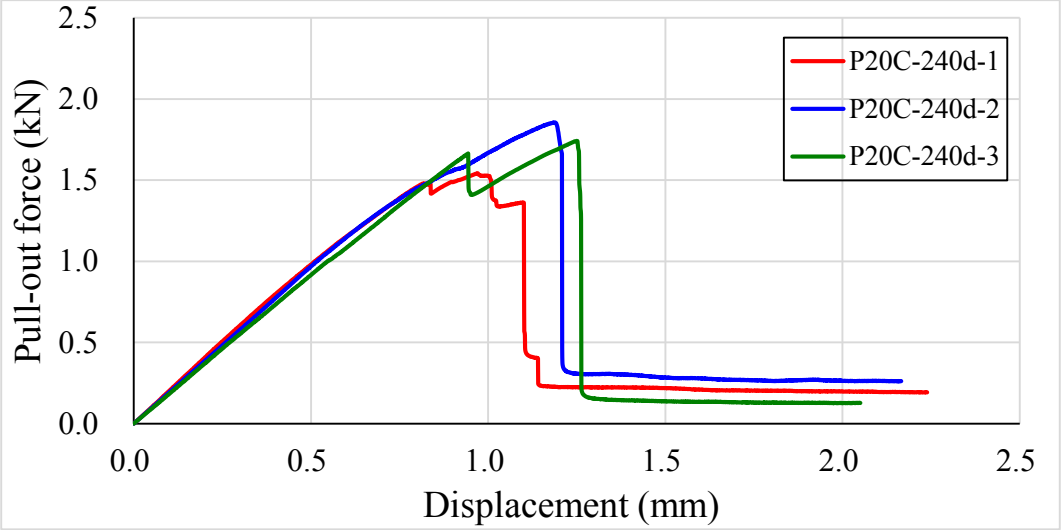

Fig.6-12 Pull-out curves of CFSRM on the 240th day of environmental conditioning at 20 °C.

6.3.3 Comparison between the two immersion conditions

Table 6-1 summarises all pull-out test results of the specimens under both elevated-temperature and normal temperature environment. The percentage of residual performance shown in Table 6-1 is defined as the ratio of the current pull-out force to

1.95 kN that represents the initial pull-out force of CFSRM specimen before any exposure, as derived from Section 4.7.

Table 6-1 The results summary of pull-out test with CFSRM specimens.

Specimen name	Pull-out force (kN)	Residual performance (%)	Mean value (kN)	Standard deviation	Coefficient of variation (%)
P60C-30d-1	1.93	98.9			
P60C-30d-2	1.72	88.2	1.88	0.13	7.2
P60C-30d-3	1.97	101.1			
P60C-60d-1	1.66	85.2			
P60C-60d-2	1.42	72.7	1.64	0.21	12.8
P60C-60d-3	1.84	94.2			
P60C-120d-1	1.01	51.9			
P60C-120d-2	1.12	57.4	1.02	0.09	9.1
P60C-120d-3	0.94	48.0			
P60C-240d-1	1.30	66.8			
P60C-240d-2	1.04	53.5	1.15	0.14	12.1
P60C-240d-3	1.09	55.9			
P20C-30d-1	2.07	106.2			
P20C-30d-2	1.92	98.5	1.95	0.12	5.9
P20C-30d-3	1.85	94.5			
P20C-60d-1	1.97	100.8			
P20C-60d-2	2.10	107.4	2.02	0.07	3.4
P20C-60d-3	1.99	101.9			
P20C-120d-1	1.76	90.0			
P20C-120d-2	1.97	101.0	1.92	0.14	7.5
P20C-120d-3	2.03	103.9			
P20C-240d-1	1.54	79.1			
P20C-240d-2	1.86	95.1	1.71	0.16	9.2
P20C-240d-3	1.74	89.3			

Fig.6-13 plots the reduction in pull-out force of all specimens. The descending trend between the 60 °C condition and 20 °C condition starts to distinguish from the 30th day onwards. The average retention of pull-out force drops to 58.7% (1.15 kN) under accelerated ageing by the end of the experimental duration, in comparison to 87.8% (1.71 kN) for specimens at 20 °C. When the specimens are under 60 °C condition, the pull-out force reduces steadily to its lowest value at the 120th day, and increases slightly afterwards. When the specimens are under 20 °C condition, the pull-out force fluctuates slightly in the first 60 days, since then it reduces monotonically until the end of the test. The slight increase in the pull-out force of specimens under either 60 °C or 20 °C condition could be related to the continuous hydration of the cementitious materials, especially PFA, which has been found to contribute to long-term strength in concrete (Hwang et al., 2004). However, further studies will be needed to prove this hypothesis, as the effect of continuous hydration has been neglected in this study.

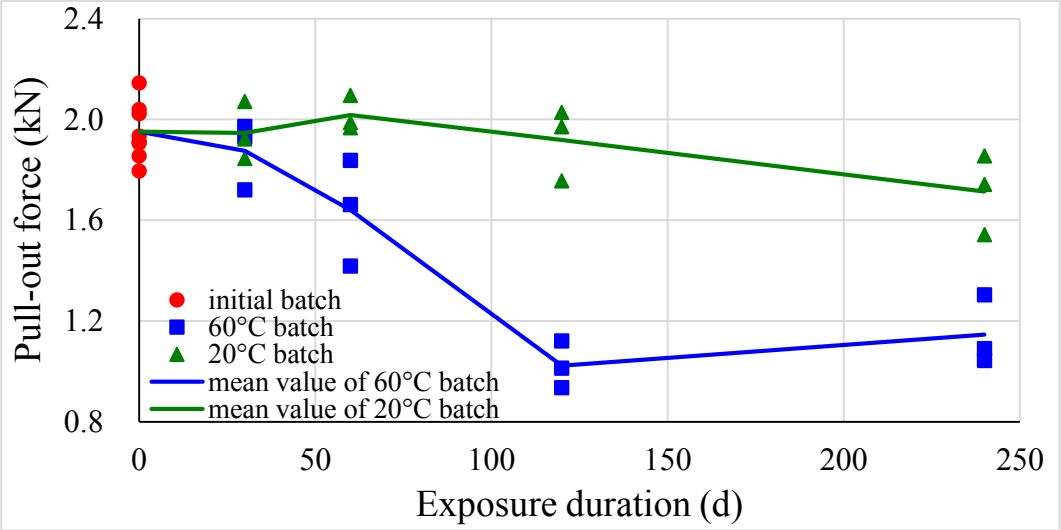

Fig.6-13 Reduction in pull-out force of CFSRM exposed to accelerated ageing condition and normal service condition.

6.4 Multiphysics coupling model for long-term pull-out behaviour

6.4.1 Three-parameter durability (TPD) model for predicting pull-out performance under interfacial ageing

As introduced in Chapter 2, six types of prediction models have been proposed regarding various applications and all have some drawbacks. Overall, Prediction Model IV is most appropriate to this study as it focuses on the reduction to shear-induced interfacial bonding durability. Furthermore, many existing experimental studies have demonstrated that Prediction Model IV is effective to assess the long-term behaviour of interfacial bonding between FRP reinforcement and concrete substrate (Davalos et al., 2012a; Benmokrane and Ali, 2018; Sang et al., 2018). However, Prediction Model IV cannot be directly utilised in this study as the effect of hydroscopic expansion caused by water diffusion is not included. It is believed that the water diffusion and the subsequent moisture concentration growth inside specimen are of significance because the interfacial ageing largely depends on the concentration changes in water molecules as explained in Chapter 2. While immersion only serves as an ageing treatment method in previous research, the present study specifically discusses the effect of water content changes on the interfacial ageing. Therefore, the moisture concentration inside the specimen is no longer a constant like the default condition in former studies. To solve this problem, a modified method based on Prediction Model VI is developed as follows.

If moisture concentration is unchanged over the ageing period, the ageing kinetics at the adhesive interface is equivalent to a pseudo-first-order reaction as shown in Eq.6-1 (Bélan et al., 1997; Farrar, 2008; Dubelley et al., 2018; Borovikov et al., 2019).

$$-\frac{d(Y-Y_\infty)}{dt} = k(Y-Y_\infty)C \tag{6-1}$$

where C represents the concentration of moisture involved in the ageing kinetics.

Within the water uptake process, change in C cannot be ignored. Under this circumstance, Eq.6-1 is no longer a reduced pseudo-first-order reaction but a second-order reaction in terms of ageing kinetics, with both Y and C being time dependent (Bélan et al., 1997; Pickett and Coyle, 2013; Speranza et al., 2014; Borovikov et al., 2019).

Integrating Eq.6-1 yields an integral form as

$$\int -\frac{d(Y-Y_\infty)}{Y-Y_\infty} = \int kC\,dt \tag{6-2}$$

Solving Eq.6-2 in combination with the boundary condition $(Y - Y_\infty) = 1 - Y_\infty$ when $t = 0$, the solution can be obtained in particular integral terms as

$$\ln\left(\frac{Y-Y_\infty}{1-Y_\infty}\right) = -k\int_0^t C\,dx \tag{6-3}$$

where x is an introduced integration variable denoting the physical quantity of time.

Rewriting Eq.6-3 in exponential terms, the expression of Y is subsequently derived as

$$Y = (1 - Y_\infty)exp\left(-k\int_0^t C\,dx\right) + Y_\infty \tag{6-4}$$

Substituting Eq.2-4, namely the basic form of Arrhenius reaction rate constant k, into Eq.6-4, the modified approach to predicting the long-term interfacial ageing of CFSRM can be given as

$$Y = (1 - Y_\infty)exp\left[-\left(\int_0^t C\,dx\right)Aexp\left(\frac{-E_a}{RT}\right)\right] + Y_\infty \tag{6-5}$$

As a refinement proposed by the present study, the prediction model given in Eq.6-5 has three governing parameters including time (t), moisture concentration (C) and

temperature (T). Such three parameters play a dominant role in the interfacial ageing of CFSRM during seawater immersion conditioning. With the real-time changes in the ageing condition, the durability model herein assigns appropriate values to variables of t, C and T synchronously. Then the model can be utilised to analyse the pull-out performance owing to interfacial ageing and thus assess the long-term durability of CFSRM. Hence this model is named three-parameter durability model (TPD model) hereinafter for pull-out performance prediction.

It is worth noting that TPD model has three constant coefficients, namely the final residual bonding performance (Y_∞), pre-exponential factor of Arrhenius Equation (A) and the activation energy for the material and reaction type (E_a), which are determined according to intrinsic properties of the material and the ageing treatment. In the present study, they are derived from the pull-out test results, or more specifically, the reduction in pull-out force owing to the interfacial ageing under different t, C and T conditions after removing the effect of hygroscopic expansion on pull-out behaviour. Table 6-2 summarises the TPD model coefficients that are determined for the specimens used in this study.

Table 6-2 TPD model coefficients.

Material coefficient	Value
Y_∞	57.8%
A	$2.15*10^{-2}$
E_a	51.61 kJ/mol
k	$1.74*10^{-10}$ at 60 °C $1.37*10^{-11}$ at 20 °C

6.4.2 Introduction of the multiphysics coupled modelling

The multiphysics numerical simulation couples the water diffusion field, the water-induced interfacial ageing, the hygroscopic expansion in CFS and the interfacial pull-out mechanical model. When analysing and predicting the durability performance, it takes both hygroscopic expansion mechanism and interfacial ageing mechanism into consideration.

The numerical modelling of interfacial behaviour of CFSRM based on CZM has been calibrated using experimental results given in Section 5.4.2, which has shown to be reliable in predicting pull-out behaviour of CFSRM. Coupled with CZM method, the present study hereinafter proposes a TPD model-based multiphysics model to predict the long-term degradation in pull-out behaviour of CFSRM. As introduced in literature, CZM method based on various bond-slip relationships has been used to study the interfacial ageing (Ouyang, 2007; Yang et al., 2017; Biscaia et al., 2019). Despite the type of bond-slip law the research chooses, the degradation of interface is usually reflected by altering model governing parameters among τ_p, u_p, u_{td}, K_τ and G_t (Mubashar et al., 2011; Liu et al., 2016; Shawa and Andrawes, 2017; Wang and Petrů, 2019; Zaeri and Googarchin, 2019). This study uses the reduction parameter Y derived from the TPD model to describe the degradation of interface. Fig.6-14 gives a flowchart of this multiphysics simulation.

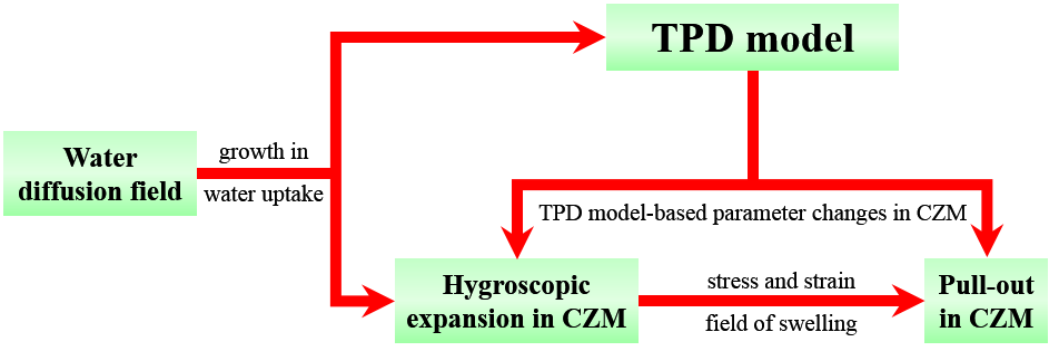

Fig.6-14 TPD model-based multiphysics.

As illustrated in Fig.6-14, the water diffusion field provides information on time and temperature dependant moisture concentration of the CFSRM specimen. Then TPD model calculates the interfacial ageing under the exposure condition, which is then used to update the CZM parameters. Coupled with the initial stress and strain fields incurred by hygroscopic expansion due to water uptake, the long-term degradation in pull-out behaviour, taking into account of both hygroscopic expansion and interfacial ageing, could be simulated.

6.4.3 CZM parameter evaluation based on interfacial ageing

So far, no consensus has been achieved in literature regarding the CZM parameter changes during environmental exposure (Ouyang, 2007; Mubashar et al., 2011; Silva et al., 2013; Sugiman et al., 2013; Shawa and Andrawes, 2017; Emre, 2018; Zaeri and Googarchin, 2019; Li et al., 2020b). Fig.6-15 presents some typical CZM degradation models that have been used so far. All types of evolutionary trends in bond-slip law given from Fig.6-15a to Fig.6-15h are the diagrams taken from the theoretical CZM degradation models in the existing references which is introduced as following.

After exposing to freeze-thaw cycling with salt water, Shawa and Andrawes (2017) found that all parameters related to bond-slip law experienced a decline as shown in Fig.6-15a. Under freshwater exposure at 50 °C, Sugiman et al. (2013) observed the decrease in height of bond-slip path with its base unchanged, whereas the conclusion from Mubashar et al. (2011) was opposite, as shown in Fig.6-15b and Fig.6-15c respectively. When exposed to salt water at room temperature, Li et al. (2020b) found the increase in u_{td} and the decrease in τ_p, G_t and K_τ, as shown in Fig.6-15d. Zaeri and Googarchin (2019) reported the similar result but the interfacial stiffness K_τ did not decline when exposed to tap water at room temperature as shown in Fig.6-15e. Likewise, Fig.6-15f from Ouyang (2007) indicated that all CZM parameters except K_τ dropped by the same ratio, which stayed fixed when exposed to the same ageing condition. Additionally, some or all aforementioned parameters were found to rise during exposure as shown in Fig.6-15g and Fig.6-15h, reported by Silva et al. (2013) who adopted salt fog conditioning at 35 °C and Emre (2018) who adopted conditioning of high humility higher than 90% at the same temperature.

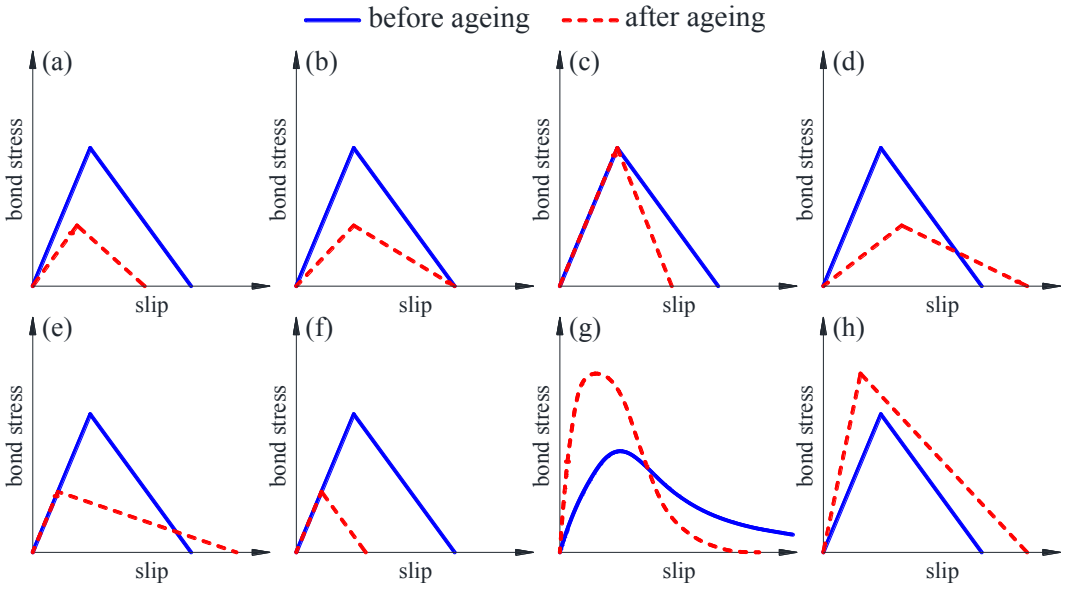

Fig.6-15 Evolutionary trend in bond-slip law of CZM subject to conditioning.

The degradation trend in Fig.6-15f and Fig.6-15e have been adopted in this study due to its simplicity. Furthermore, the present study finds that during the experimental period, the reduction ratio for τ_p, u_p and u_{td} is equal to the interfacial ageing, namely the expression of $(1-Y)$ complied with the TPD model. Therefore, the CZM parameters considering interfacial ageing can be expressed as:

(1) **Reduction Mode I** (Fig.6-15f) denotes that TPD model-based reduction factor (Y_{CZM-I}) governs CZM parameters decreasing in the same ratio, as described from Eq.6-6 to Eq.6-8 inclusive.

$$\tau_p^{age} = \tau_p \cdot Y_{CZM-I} \tag{6-6}$$

$$u_p^{age} = u_p \cdot Y_{CZM-I} \tag{6-7}$$

$$u_{td}^{age} = u_{td} \cdot Y_{CZM-I} \tag{6-8}$$

(2) **Reduction Mode II** (Fig.6-15e) denotes that TPD model-based reduction factor (Y_{CZM-II}) governs CZM parameters decreasing in the different ratio, as described from Eq.6-9 to Eq.6-11 inclusive.

$$\tau_p^{age} = \tau_p \cdot Y_{CZM-II} \tag{6-9}$$

$$u_p^{age} = u_p \cdot Y_{CZM-II} \tag{6-10}$$

$$u_{td}^{age} = u_{td} \tag{6-11}$$

where Y_{CZM-I} is taken as the ageing reduction factor Y, while Y_{CZM-II} has been recalibrated to best describe the pull-out degradation as found from the experiments.

Fig.6-16 compares the numerical results based on both reduction methods against the experimental results.

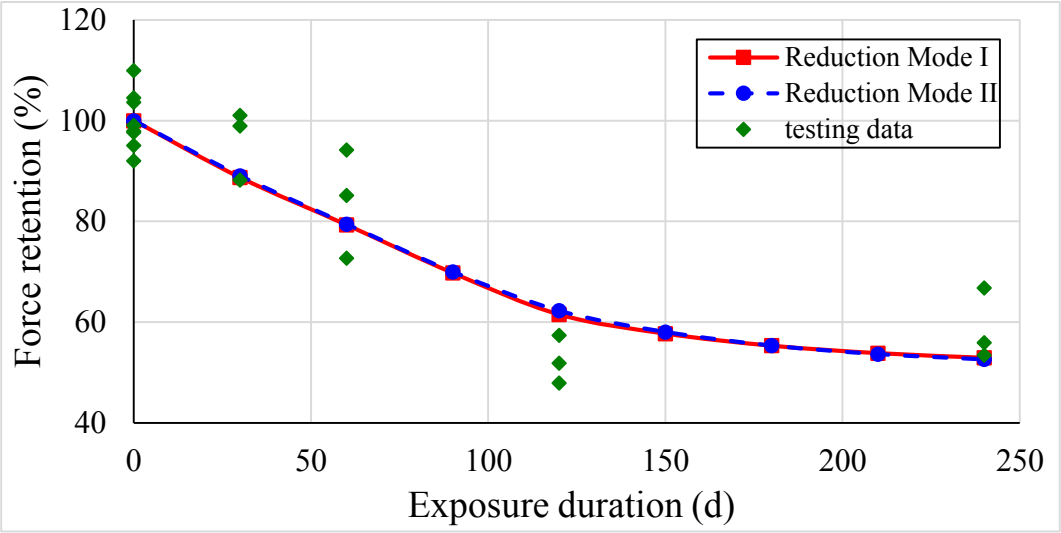

(a) exposure under 60 °C

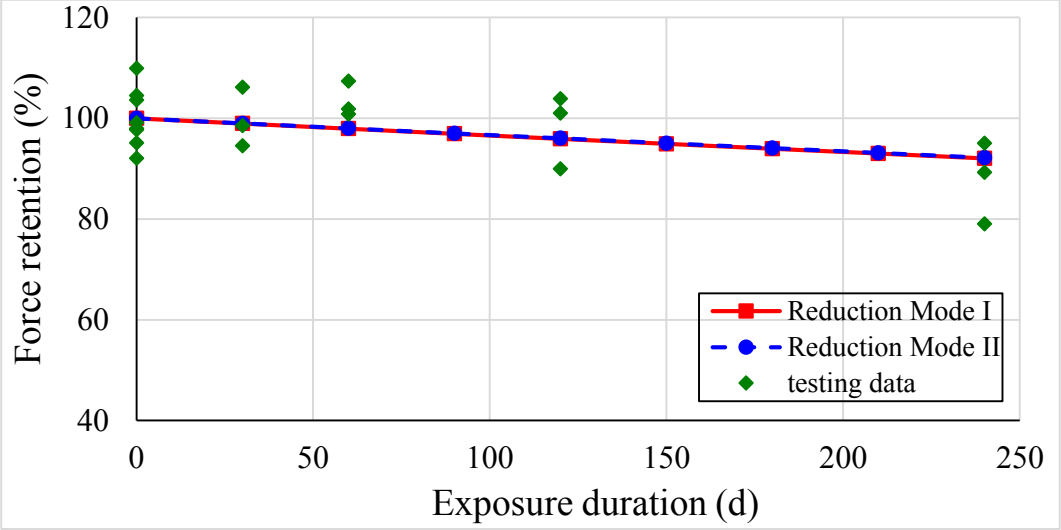

(b) exposure under 20 °C

Fig.6-16 Comparison of test results with simulated results in accordance with two reduction modes.

Overall, the numerical results, coupling both the swelling effect and the interfacial ageing effect, capture the trend of the experimental results very well. Little difference has been found between the two different interfacial bond-slip reduction laws. This is because that,

although the peak interfacial shear stress and the slip at debonding are different, the critical fracture energy, which is the area under the local bond-slip curve, is the same. Therefore, the same pull-out force has been found to cause debonding under the two different interfacial reduction methods. The comparison between experimental and simulated results under the two different exposure temperatures has shown that it is reliable to use the TPD model to analyse the interfacial ageing for CFSRM specimens subject to different ambient temperatures and exposure time.

Fig.6-17 to Fig.6-20 plot the experimental and numerical $P - u_{st}$ curves at different times. As little reduction has been found in experimental pull-out results when the specimens were exposed to the normal service condition within the experimental duration, testing data under elevated-temperature accelerated ageing at 60 °C have been used.

The comparison between the numerical and experimental $P - u_{st}$ curves demonstrates that TPD model-based multiphysics is able to simulate the degraded pull-out behaviour, which is in agreement with the experimental results covering the total ageing duration. Compared with the long-term durability degradation revealed by the experiment, essentially the same trend in pull-out behaviour can be found in the simulation results, although the displacement at the maximum pull-out force for some specimens are relatively longer than that in the numerical model. Overall the numerical model has captured the ascending behaviour and the peak load very well. The descending stage could not be compared due to the noneffective experimental set up, as discussed in Section 5.4.2.

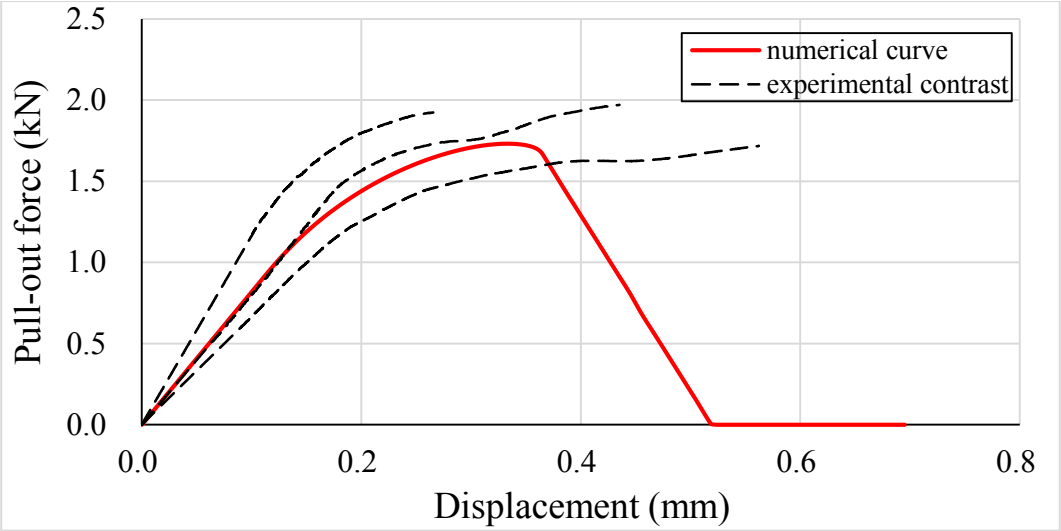

Fig.6-17 Numerical $P-u_{st}$ curve and its experimental contrast for upward slope, on the 30th day of accelerated ageing.

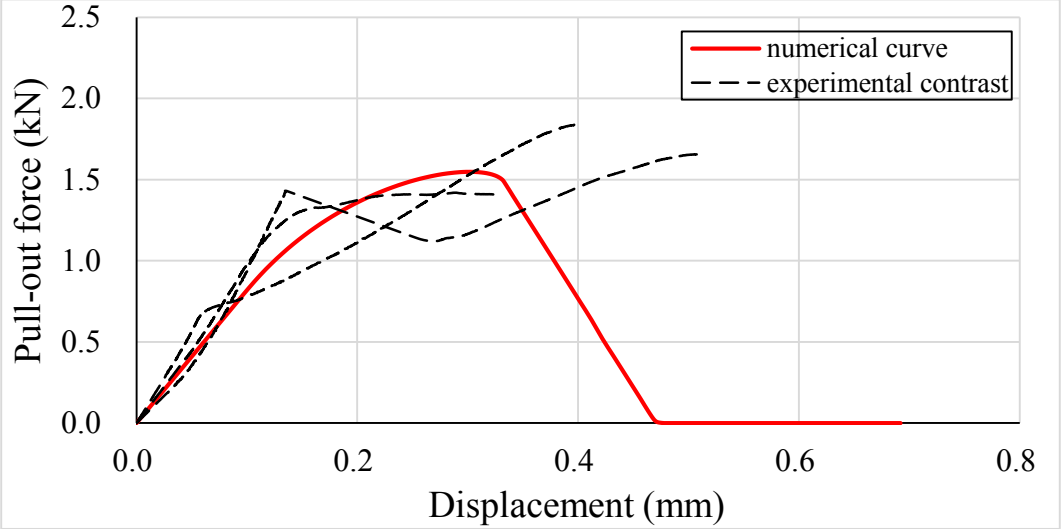

Fig.6-18 Numerical $P-u_{st}$ curve and its experimental contrast for upward slope, on the 60th day of accelerated ageing.

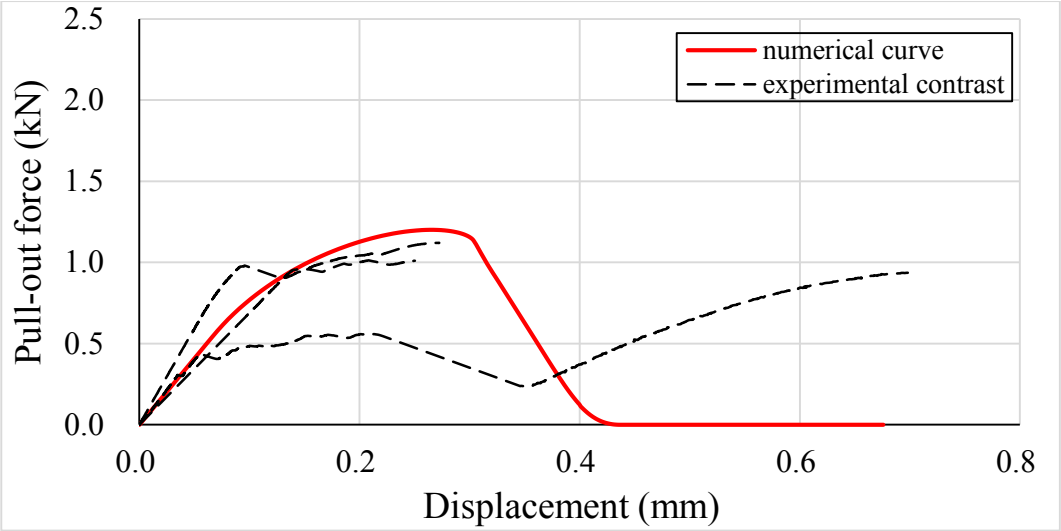

Fig.6-19 Numerical $P-u_{st}$ curve and its experimental contrast for upward slope, on the 120th day of accelerated ageing.

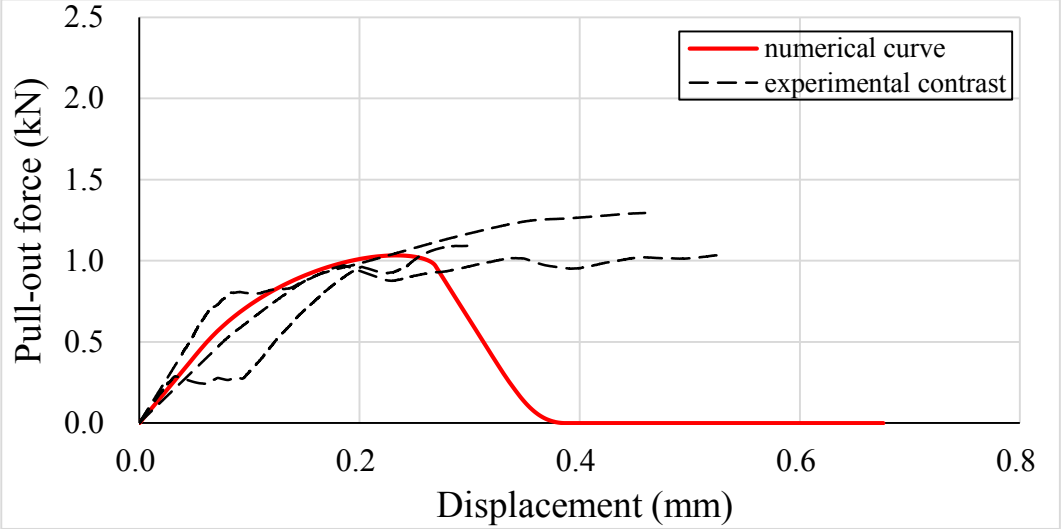

Fig.6-20 Numerical $P-u_{st}$ curve and its experimental contrast for upward slope, on the 240th day of accelerated ageing.

6.5 Long-term pull-out force prediction model

6.5.1 Theoretical derivation of degradation process

By applying the degradation mechanisms discussed in Chapter 3, the reduction in the pull-out resistance of CFSRM can be attributed to both the hygroscopic expansion and the interfacial ageing. On the one hand, the water diffusion in CFSRM causes water molecules to immigrate into CFS reinforcement across SM substrate and thereby induces the swelling stress inside CFS. On the other hand, the long-term immersion weakens the interfacial bond properties between CFS and SM. As a consequence, the pull-out behaviour deteriorates over exposure time, particularly under the accelerated ageing condition. Let the pull-out force retention after a certain duration of conditioning be denoted by F_{PR} and the initial pull-out force of intact specimens be denoted by F_{PI}, the relationship between F_{PR} and F_{PI} in the present study can be given as

$$F_{PR} = F_{PI} - F_{HE} - F_{IA} \tag{6-12}$$

where F_{HE} is the decrease in pull-out force on account of hygroscopic expansion; F_{IA} is the decrease in pull-out force on account of interfacial ageing.

As per the degradation mechanism with respect to interfacial ageing, F_{IA} can be expressed by subtracting the residual pull-out performance from its original value:

$$F_{IA} = F_{PI}(1 - Y) \tag{6-13}$$

Substituting Eq.6-13 into Eq.6-12, F_{PR} can be rewritten as

$$F_{PR} = F_{PI} \cdot Y - F_{HE} \tag{6-14}$$

Fig.6-21 plots the retention of the simulated pull-out forces with and without considering hygroscopic expansion, along with the related ageing reduction factor curves for CZM

parameters. Reduction Mode I and Reduction Mode II are adopted in the numerical modelling respectively.

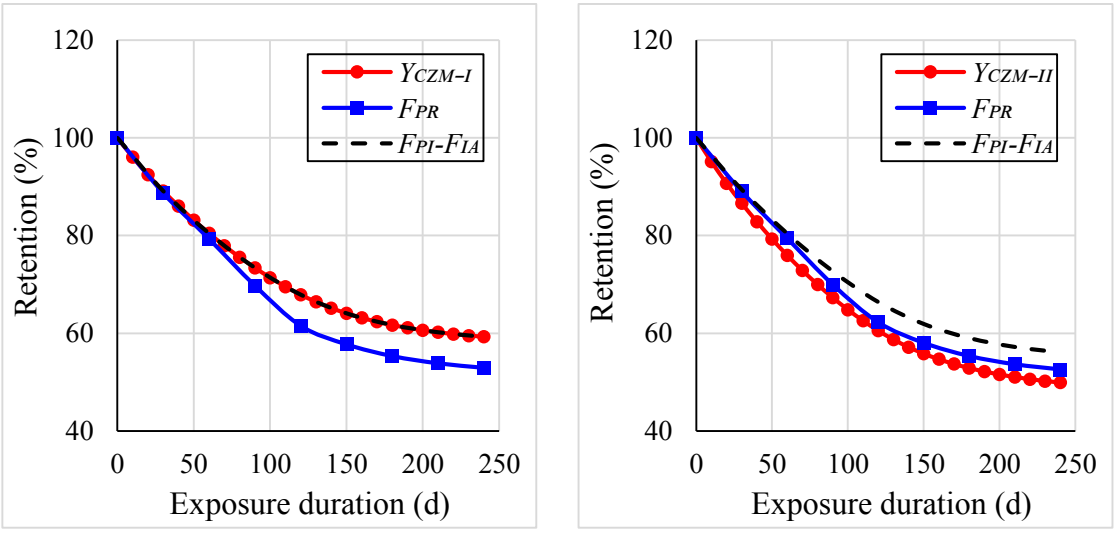

(a) Reduction Mode I under 60 °C (b) Reduction Mode I under 20 °C

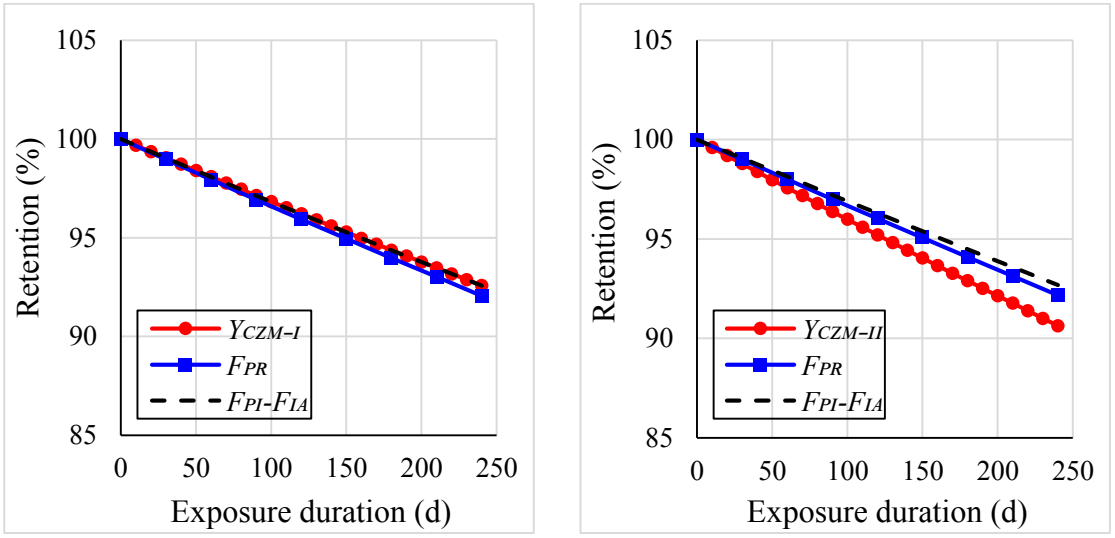

(c) Reduction Mode II under 60 °C (d) Reduction Mode II under 20 °C

Fig.6-21 Retention of the simulated pull-out force with and without considering hygroscopic expansion, along with the related ageing reduction factor curves for CZM parameters.

It is found that the reduction in the pull-out force closely follows the trend of the ageing reduction factor Y, no matter what the ambient temperature is. The effect of interfacial

ageing and hygroscopic expansion could be decoupled using Reduction Mode I in CZM, while they are coupled if Reduction Mode II is used. Further research is needed to investigate the coupling effect if Reduction Mode II is to be used. For simplicity, Reduction Mode I has been used in CZM for the following studies.

6.5.2 Contribution of hygroscopic expansion

This section aims to propose a simplified calculation method to describe the pull-out force degradation due to hygroscopic expansion. Fig.6-22 plots the pull-out forces under different immersion temperature T, immersion time t, and different coefficient of hygroscopic expansion β_{CHE}.

As shown in Fig.6-22, the maximum hygroscopic expansion induced pull-out force degradation F_{HE} is only dependant on the β_{CHE}. The immersion temperature only affects the speed of degradation, rather than the magnitude. Before reaching the maximum value of F_{HE} under a certain β_{CHE}, a parabolic function could be used to describe the time-dependant trend of F_{HE}. After then F_{HE} remains constant with the increase of immersion time because CFS has already reached the saturated condition and the swelling process has stopped. Fig.6-23 gives the diagram of the proposed piecewise function to describe F_{HE}.

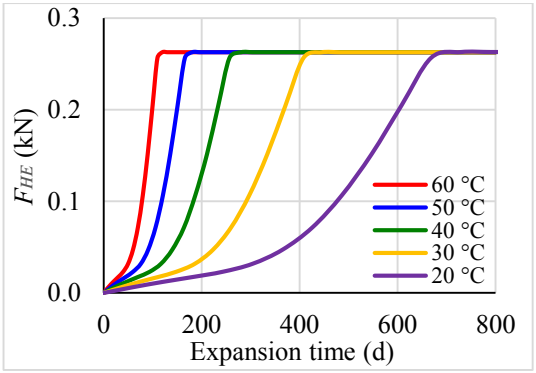

(a) $\beta_{CHE} = 0.6$

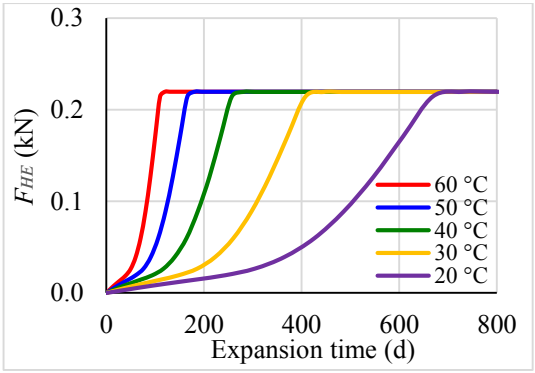

(b) $\beta_{CHE} = 0.5$

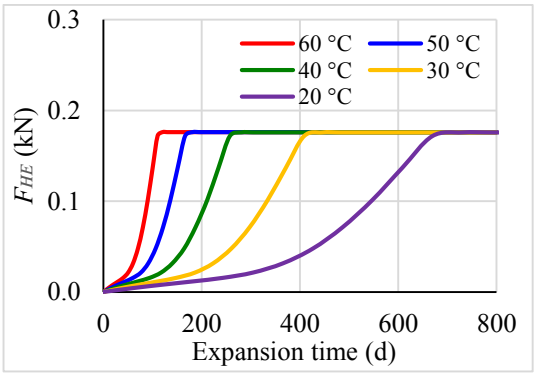

(c) $\beta_{CHE} = 0.4$

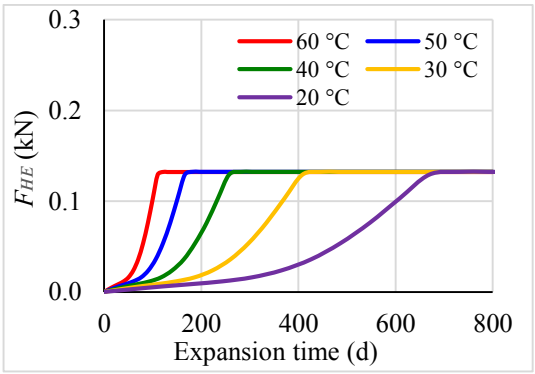

(d) $\beta_{CHE} = 0.3$

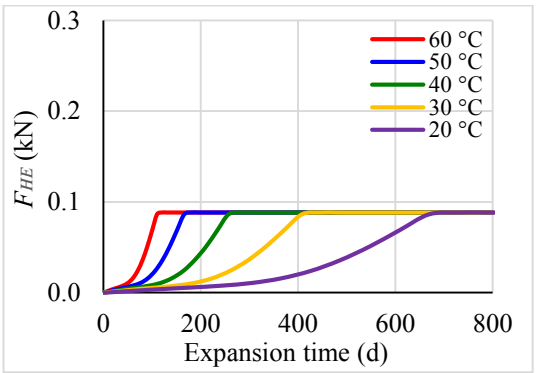

(e) $\beta_{CHE} = 0.2$

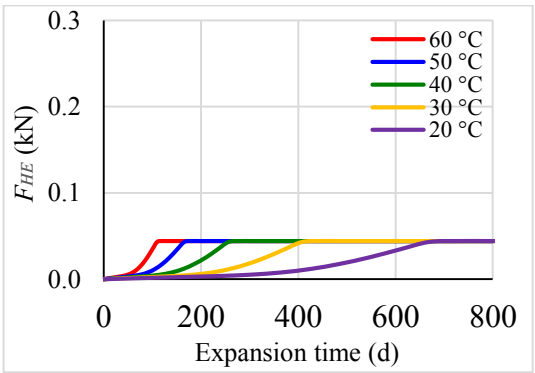

(f) $\beta_{CHE} = 0.1$

Fig.6-22 Simulated changes in F_{HE} with different t, T and β_{CHE}.

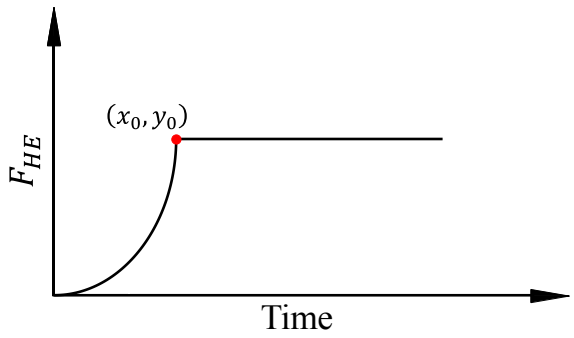

Fig.6-23 The diagram of the piecewise function used to fit simulated F_{HE}.

Complied with Fig.6-23 which demonstrates the increase trend in F_{HE}, Eq.6-15 gives the expression of a piecewise function used to fit such a trend with different t, T and β_{CHE}.

$$F_{HE} = y_0 \left(\frac{t}{x_0}\right)^{\alpha_1} \leq y_0 \tag{6-15}$$

where

$$x_0 = \alpha_2 \cdot \exp\left(\frac{\alpha_3}{T+273.15} - \frac{\alpha_3}{60+273.15}\right) \tag{6-16}$$

$$y_0 = \alpha_4 \beta_{CHE} \tag{6-17}$$

Four coefficients used in the function are derived from fitting the simulation curves shown in Fig.6-22 and Fig.6-24, namely $\alpha_1 = 2.59$, $\alpha_2 = 112$, $\alpha_3 = 4409$, and $\alpha_4 = 0.44$.

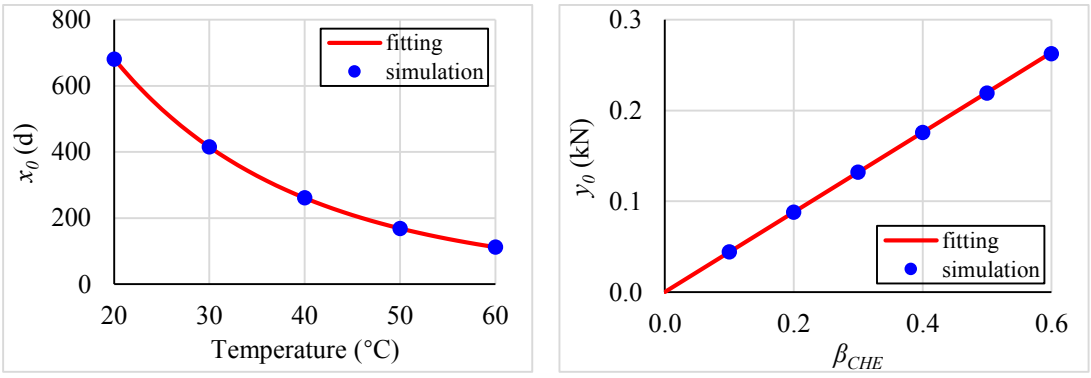

(a) fitting curve of x_0 (b) fitting curve of y_0

Fig.6-24 Derivation of the fitting curve based on (x_0, y_0) along with their coefficients.

6.6 Durability prediction of long-term pull-out performance of CFSRM under marine environment

This section aims to demonstrate the applications of the simplified hand calculation method proposed in Section 6.5. The durability of CFSRM under seawater environment will be assessed in terms of long-term pull-out behaviour. The two key influencing factors, the immersion temperature and the moisture concentration, will be discussed in detail.

6.6.1 Effect of temperatures

Under normal conditions, seawater temperature stays above 0 °C but hardly exceeds 30 °C (Grotefendt et al., 1998; Tompkins, 2001; Ward, 2006; Cárdenas et al., 2018). It can reach around 30 °C at sea surface located in tropical seas (Tompkins, 2001; Ward, 2006). In the meantime, it is close to 0 °C in the Arctic Ocean and the Antarctic Ocean (Grotefendt et al., 1998; Cárdenas et al., 2018). In view of this, the present study focuses on six working conditions for CFSRM used in seawater, with the ambient temperature varying from 5 °C to 30 °C at five-Celsius intervals.

As introduced in Chapter 3, the utilisation of time-shift factor TSF can be used to determine the ageing reaction rate constant under various temperatures. Taking the value of k at 20 °C as the baseline, TSF used to convert the baseline into the corresponding value of k at 5 °C to 30 °C inclusive can be solved according to Eq.3-17 wherein E_a has already been decided in Section 6.4.1.

Based on the above-mentioned calculation method of TSF value, Table 6-3 summarises the TSF of interfacial ageing reaction rate constant as per Arrhenius Law under various

temperatures. It is shown that TSF climbs up steadily with the increase of temperature, and the increase is more rapid under higher temperature.

Table 6-3 Time-shift factor (TSF) in the temperature range of 5 °C to 30 °C.

Temperature (°C)	TSF
5	0.32
10	0.47
15	0.69
20	1
25	1.43
30	2.01

Fig.6-25 plots the hand calculated degradation curves of pull-out resistance following the method proposed in Section 6.5. A variety of undersea environments with ambient temperature from 5 °C to 30 °C is used, given the fact that the seawater temperature around the world can hardly exceed 30 °C (Tompkins, 2001; Ward, 2006). The degradation rate of pull-out performance gradually slows down with the increase of immersion time and the decline in environmental temperatures, finally reaching the plateau. It is expected to take 2.1 years for the retention of pull-out force to fall to 60% of its initial value under the ambient temperature of 30 °C which is expected to occur at sea surface located in tropical seas (Tompkins, 2001; Ward, 2006), whilst it is predicted to take 12.4 years for the retention to drop to the same level at 5 °C, nearly six times longer than the 30 °C condition.

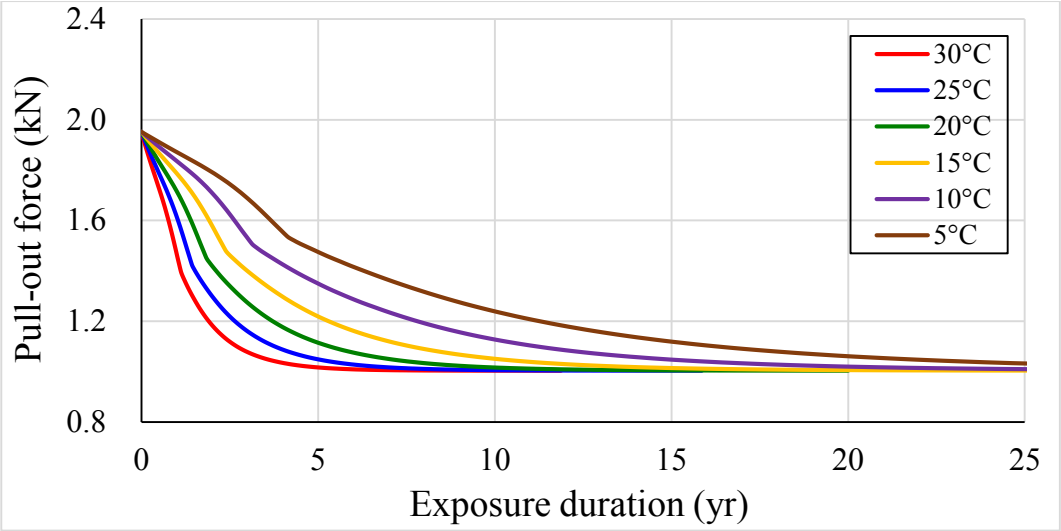

Fig.6-25 Prediction of CFSRM durability in regard to pull-out performance.

6.6.2 Effect of moisture concentration

When a structure is under marine environment, moisture concentration is another key factor to its long-term behaviour. Unlike the underwater structures, offshore platforms are exposed to seawater discontinuously with regular dry-wet cycles or random intervals. As a consequence, CFSRM under such working conditions is less likely to stay saturated during the degradation period. Therefore, the effect of moisture concentration is analysed in this section.

Due to the fact that the real working condition subject to cycles or random intervals of seawater exposure is impractical to reproduce, the present study considers a saturation range likely to occur therein, according to the initial water content and the saturated water content. As shown in Fig.5-13, the initial degree of saturation for CFS is 60.4%. Then this study defines five different saturation levels for the durability prediction, including the initial value (60.4%), 70%, 80%, 90% and 100%. In order to study the effect of different saturation levels, the water uptake process during the discontinuous seawater exposure is simplified to a stable saturation level over the entire service life.

Once the saturation levels are assigned for the whole CFSRM specimen as mentioned above, they are input into the multiphysics coupling numerical model in turn, as the concentration parameter of moisture. Then the simulated retention of pull-out force for the specimen subject to the effect of hygroscopic expansion with different saturation levels is compared with its initial value which comes from the numerical result of the specimen with the initial saturation level of 60.4%. The difference derived from such a comparison is F_{HE}. In this way, the swelling-induced decrease in pull-out force (F_{HE}) at various degrees of saturation can be obtained, as shown in Table 6-4.

Table 6-4 Values of F_{HE} at various degrees of saturation.

Degree of saturation (%)	F_{HE}
60.4	0
70	0.03
80	0.06
90	0.09
100	0.12

Fig.6-26a plots the prediction curves about durability over 25 years on the condition that the ambient temperature remains 30 °C and five different saturation levels therein are in compliance with Table 6-4. Substituting TSF as summarised by Table 6-3 into TPD model approach and repeating the aforementioned prediction procedures, prediction curves of durability among varied saturation levels are obtained as plotted in Fig.6-26b, c, d, e and f, at temperatures of 25 °C, 20 °C, 15 °C, 10 °C and 5 °C respectively.

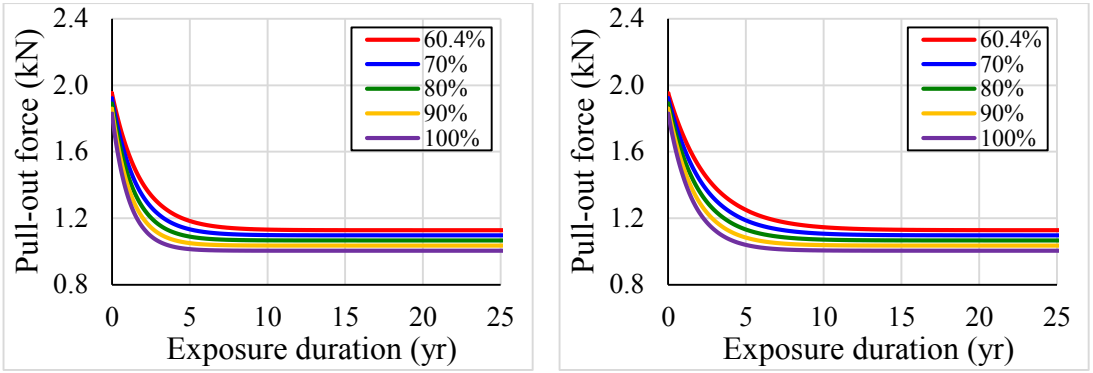

(a) 30 °C (b) 25 °C

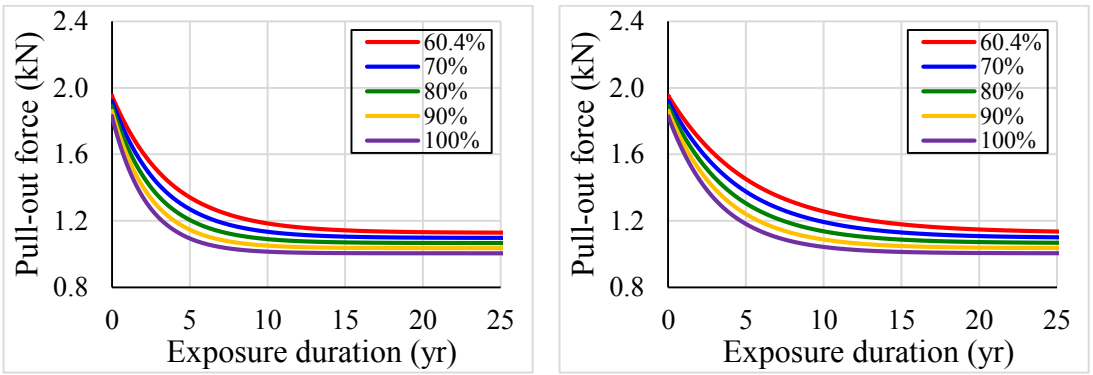

(c) 20 °C (d) 15 °C

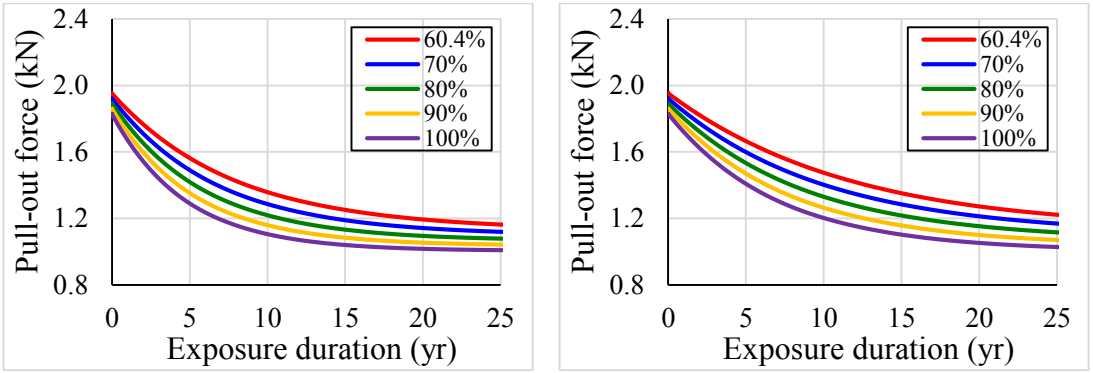

(e) 10 °C (f) 5 °C

Fig.6-26 Prediction curves of durability with different saturation levels from 60.4 % to 100 % inclusive.

The prediction results in Fig.6-26 cannot thoroughly avoid the error, because they are based on assumptions made in Table 6-3 and Table 6-4. The error range is qualitatively discussed as follows.

Table 6-3 gives the theoretical value of TSF that reflects the interfacial ageing reaction rate as per Arrhenius Law under various temperatures. It would agree with the reality if the discreteness of material properties is not taken into account. However, Table 6-4 directly defines the effect of moisture swelling and does not consider the water diffusion process. As explained hereinbefore, it assumes that the moisture can attack the specimen immediately without the intrusion process and the exposure to water attack is continuous without any intervals. Thus, the prediction results based on Table 6-4 would not be identical to the actual situation. Furthermore, the prediction results in Fig.6-26 can be regarded as the worst case which reveals a lower bound of the expected long-term pull-out performance.

Back to the durability prediction as shown in Fig.6-26, it can be found that the influence of moisture factor on the durability is consistent with the theoretical analysis given in Chapter 3. The increase in saturation level compounds the swelling effect and thus reduces the pull-out resistance. On the other hand, the growth in water content is able to speed up the degradation rate during the conditioning time.

Based on the prediction curves as presented in Fig.6-26, the durability of CFSRM specimens subject to offshore environments can be evaluated. Table 6-5 summarises the required period for the pull-out force of CFSRM to reduce to 70%, when it is exposed to various saturation levels at temperatures of 30 °C, 25 °C, 20 °C, 15 °C, 10 °C and 5 °C respectively. It can be found that the required period for the pull-out force degrading to 70% under full saturation condition is 2.5 times shorter compared with the initial saturation level of 60.4%.

Table 6-5 Required time for the residual pull-out property dropping to 70 %.

Degree of saturation (%)	60.4	70	80	90	100
Temperature (°C)	Required time (yr)				
30	2.3	1.8	1.4	1.1	0.9
25	3.2	2.5	2.0	1.6	1.3
20	4.6	3.6	2.8	2.3	1.8
15	6.6	5.2	4.1	3.3	2.7
10	9.7	7.6	6.0	4.8	3.9
5	14.3	11.3	8.8	7.1	5.8

It is worth noting that the calculated degradation duration given in Table 6-5 neglects the water diffusion process and thus would not be identical to the practical application. In fact, the water diffusion process is heavily impacted by the variation in ambient temperatures, moisture concentration, as well as the thickness of mortar cover, which are likely to bring more uncertainties to the durability prediction. As the results in Table 6-5 are calculated based on constant immersion conditions, it can be treated as the worst case, which provides a lower bound prediction for the long-term interfacial behaviour of CFSRM.

6.7 Summary

In accordance with Arrhenius Law, CFSRM specimens exposed to 60 °C accelerated ageing treatment along with the control group at 20 °C are used to conduct pull-out tests in order to measure the retention of pull-out force after the accelerated ageing treatment. Test results show that the pull-out performance of specimens after 240 days of accelerated

ageing has an obvious reduction, to 58.7% of the pull-out force without ageing treatment. Meanwhile, little change is found under normal service condition, retaining 87.8% of the pull-out force by the end of the test.

Based on second-order ageing kinetics in combination with Arrhenius Equation, TPD model is proposed to characterise and predict the long-term effect of interfacial ageing on pull-out performance. Multiphysics numerical simulation is used to couple water diffusion, hygroscopic expansion, interfacial ageing and pull-out altogether, wherein TPD model governs the reduction ratio of local bond-slip relationship that is used in CZM.

The individual contribution of hygroscopic expansion and interfacial ageing to the total degradation is analysed separately by the numerical model. The effect of interfacial ageing and hygroscopic expansion can be decoupled if using Reduction Mode I in CZM, while they are coupled if Reduction Mode II is used.

According to the simulation results based on Reduction Mode I, this chapter proposes a simplified hand calculation method, which enables the long-term durability prediction of TRM exposed to various marine environmental scenarios. Prediction results suggest that if the residual pull-out performance decreases to 60% of its initial performance, raising the immersion temperature from 5 °C to 30 °C can accelerate this degradation process by six times. If the moisture saturation level increases from 60.4% to 100% and the temperature stays unchanged at an arbitrary value, the required time for the pull-out performance degrading to 70% can be shortened by 2.5 times.

7 CONCLUSIONS AND RECOMMENDATIONS FOR FUTURE RESEARCH

7.1 Conclusions

Compared with traditional concrete or mortar materials, carbon fibre TRM investigated in the present study is not only corrosion-resistant against marine environments but also eco-friendly and resource-conserving. The main purpose of the present study is to acquire a better understanding of the interfacial bonding behaviour between CFS and SM within the TRM structure, especially its durability performance under marine environments. CFSRM specimens have been used throughout the study to investigate the interfacial performance of TRM.

7.1.1 Material and mechanical properties of CFSRM

In order to obtain the essential physical and mechanical properties before the durability research, the present study carried out a series of investigations into CFSRM along with its components (CFS and SM) by using experimental and numerical methods. Mortar experiments related to compression, tension and flowability were conducted to acquire the mechanical properties and workability of SM used in this study, while tensile test and pull-out test were used to test the mechanical properties of CFS and CFSRM respectively. Besides, both experimental and numerical studies were conducted to understand the water diffusion behaviour of CFSRM.

The key findings are listed as follows.

- The water diffusion behaviour of CFSRM is temperature-dependent as per Arrhenius Equation. Raising temperature from 20 °C to 60 °C can accelerate the interior diffusion process by nearly six times. Such a process at an arbitrary temperature can be quantitatively analysed by the numerical model of water diffusion field based on the material diffusion coefficients.
- The utilisation of seawater to replace freshwater in the mortar mix design almost has no negative effect on the mechanical properties of the mortar. The ultimate pull-out force of CFSRM was found to be 1.95 kN, regardless of the use of seawater or freshwater to cast the mortar substrate.
- The analytical solution to the 1D analytical model of interfacial failure mechanism theoretically explains the entire process of interfacial failure of CFSRM subject to axial loadings. The solution can be further used to study the debonding failure of fibre composite reinforced materials.
- The numerical model based on CZM approach can simulate the experimental pull-out process of CFSRM. Acting as the foundation, it can be further applied to the numerical study on the long-term pull-out behaviour.

7.1.2 Long-term durability of carbon fibre TRM under marine environments

This study obtains an insight into interfacial degradation of CFSRM specimens in order to assess the long-term durability of carbon fibre TRM under marine environment. The individual effect of hygroscopic expansion on interfacial degradation was studied by the numerical method first. Then both experimental and numerical pull-out tests for specimens after ageing treatment were conducted to understand the coupled mechanisms of hygroscopic expansion and interfacial ageing during the degradation process.

The key findings are listed as follows.

- The moisture swelling is completely synchronous with the water diffusion process. Its effect on pull-out behaviour linearly correlates with the swelling coefficient β_{CHE}. The present research on moisture swelling can be further applied to FRP materials with diverse β_{CHE}.
- Immersion with elevated temperature can accelerate CFSRM degradation. Test results show that the pull-out force drops nearly by half over 240 days under 60°C, but the failure mode remains unchanged.
- Three-parameter durability model (TPD model) is proposed to study the individual effect of interfacial ageing on pull-out behaviour. Furthermore, TPD model-based multiphysics is proposed to analyse the long-term pull-out performance subject to the coupled effects of hygroscopic expansion and interfacial ageing. This multiphysics has proved valid by comparing the related experimental data.
- Based on the aforementioned multiphysics, a hand calculation method of pull-out force retention over time is proposed, which can be applied to the prediction of the durability performance of CFSRM under marine environmental exposure. Prediction results show that raising temperature or internal moisture content accelerates the degradation process.

7.2 Recommendations for future studies

As a new composite material, carbon fibre textile reinforced mortar still has many unsolved questions to be explored in depth before its large-scale applications. Revolving around its long-term durability performance subject to marine environmental exposure, the follows problems need be addressed:

- The effect of regular temperature fluctuations on the long-term durability should be studied, given the fact that TRM applied to marine areas is more likely to work under continuous temperature cycles owing to diurnal cycle and seasonal variation. Under the critical scenario, the temperature changes can be presented in the form of freeze-thaw cycles.
- TPD model proposed herein still requires more long-term test results and in situ engineering data under normal service condition to further calibrate the material coefficients.
- Size effect is expected to be another contributing factor that affects the long-term durability performance of TRM. Further study is needed to find out the specific degradation behaviour according to different structural types and different specimen sizes.
- The long-term fatigue resistance of TRM exposed to marine environments requires in-depth research. Fatigue load stemming from stormy winds and waves plays an important role in its durability assessment and prediction.

8 REFERENCES

ACI 440.3R-12. (2012). Guide Test Methods for Fiber-Reinforced Polymer (FRP) Composites for Reinforcing or Strengthening Concrete and Masonry Structures. American Concrete Institute, Committee 440. Farmington Hills, MI, USA.

ACI PRC-440.1-15. (2021). Guide for the Design and Construction of Structural Concrete Reinforced with Fiber-Reinforced Polymer Bars. American Concrete Institute, Committee 440. Farmington Hills, MI, USA.

Afshar, A., Liao, H.-t., Chiang, F.-p. and Korach, C. S. (2016). Time-dependent changes in mechanical properties of carbon fiber vinyl ester composites exposed to marine environments. Composite Structures, 144, 80-85.

Ahmad, F., Abbassi, F., Hong, J.-W., Chang, S.-H. and Park, M. K. (2017). Hygroscopic effects on the penetration-resistance behavior of a specially-orthotropic CFRP composite plates. Composite Structures, 176, 1073-1080.

Ahmed, A., Guo, S., Zhang, Z., Shi, C. and Zhu, D. (2020). A review on durability of fiber reinforced polymer (FRP) bars reinforced seawater sea sand concrete. Construction and Building Materials, 256, 119484.

Ahmed, J. A. and Ferhadi, R. (2016). Study of Flexural Strength of Ferrocement Slab Panels. 2016 PCI Convention & National Bridge Conference. Nashville, Tennessee, America.

Ako, T. A., Onoduku, U. S., Oke, S. A., Essien, B. I., Idris, F. N., Umar, A. N. and Ahmed, A. A. (2014). Environmental effects of sand and gravel mining on land and soil in Luku, Minna, Niger State, North Central Nigeria. Journal of Geosciences and Geomatics, 2(2), 42-49.

Al-Hamrani, A., Alnahhal, W. and Elahtem, A. (2021). Shear behavior of green concrete beams reinforced with basalt FRP bars and stirrups. Composite Structures, 277, 114619.

Al-Lami, K., D'Antino, T. and Colombi, P. (2020). Durability of Fabric-Reinforced Cementitious Matrix (FRCM) Composites: A Review. Applied Sciences, 10(5), 1714.

Alagirusamy, R. and Das, A. (2010). Technical textile yarns. Woodhead Publishing Limited.

Alessi, S., Pitarresi, G. and Spadaro, G. (2014). Effect of hydrothermal ageing on the thermal and delamination fracture behaviour of CFRP composites. Composites Part B: Engineering, 67, 145-153.

Alsayed, S. H. and Amjad, M. A. (1996). Strength, water absorption and porosity of concrete incorporating natural and crushed aggregate. Journal of King Saud University - Engineering Sciences, 8(1), 109-119.

Amidi, S. and Wang, J. (2016). Deterioration of the FRP-to-concrete interface subject to moisture ingress: Effects of conditioning methods and silane treatment. Composite Structures, 153, 380-391.

Amiri, A., Ulven, C. A. and Huo, S. (2015). Effect of chemical treatment of flax fiber and resin manipulation on service life of their composites using time-temperature superposition. Polymers, 7(10), 1965-1978.

Andrade, C., Cesetti, A., Mancini, G. and Tondolo, F. (2016). Estimating corrosion attack in reinforced concrete by means of crack opening. Structural Concrete, 17(4), 533-540.

Aoki, Y., Yamada, K. and Ishikawa, T. (2008). Effect of hygrothermal condition on compression after impact strength of CFRP laminates. Composites Science and Technology, 68(6), 1376-1383.

Arias, J. P. M., Vazquez, A. and Escobar, M. M. (2012). Use of sand coating to improve bonding between GFRP bars and concrete. Journal of Composite Materials, 46(18), 2271-2278.

Ascione, L., Caron, J.-F., Godonou, P. and Ijselmuijden, K. v. (2016). Prospect for new guidance in the design of FRP: Support to the implementation, harmonization and further development of the Eurocodes. Publications Office of the European Union.

ASTM C642. (2013). Standard Test Method for Density, Absorption, and Voids in Hardened Concrete. ASTM International. West Conshohocken, PA, USA.

ASTM C1557. (2020). Standard Test Method for Tensile Strength and Young's Modulus of Fibers. ASTM International. West Conshohocken, PA, USA.

ASTM C1585. (2013). Standard Test Method for Measurement of Rate of Absorption of Water by Hydraulic-Cement Concretes. ASTM International. West Conshohocken, PA, USA.

ASTM D570. (1995). Standard Test Method for Water Absorption of Plastics. ASTM International. West Conshohocken, PA, USA.

ASTM D7522. (2021). Standard Test Method for Pull-Off Strength for FRP Laminate Systems Bonded to Concrete or Masonry Substrates. ASTM International. West Conshohocken, PA, USA.

ASTM D7913. (2020). Standard Test Method for Bond Strength of Fiber-Reinforced Polymer Matrix Composite Bars to Concrete by Pullout Testing. ASTM International. West Conshohocken, PA, USA.

Awad, Z. K., Aravinthan, T., Zhuge, Y. and Gonzalez, F. (2012). A review of optimization techniques used in the design of fibre composite structures for civil engineering applications. Materials & Design, 33, 534-544.

Ayatollahi, M. R., Shadlou, S., Shokrieh, M. M. and Chitsazzadeh, M. (2011). Effect of multi-walled carbon nanotube aspect ratio on mechanical and electrical properties of epoxy-based nanocomposites. Polymer Testing, 30(5), 548-556.

Azura, A. R. and Thomas, A. G. (2006). Effect of heat ageing on crosslinking, scission and mechanical properties. Elastomers and Components: 27– 38. Woodhead Publishing.

Babar, G., Ghadage, S. S., Pharande, V. A., Bamankar, P. B. and Nikam, P. R. (2019). Investigation of Thermal Properties of Epoxy Composites Filled with Alluminium Nitride (AlN). International Journal of Research and Analytical Reviews (IJRAR), 6(2), 493-502.

Backe, D. and Balle, F. (2016). Ultrasonic fatigue and microstructural characterization of carbon fiber fabric reinforced polyphenylene sulfide in the very high cycle fatigue regime. Composites Science and Technology, 126, 115-121.

Baena, M., Torres, L., Turon, A. and Barris, C. (2009). Experimental study of bond behaviour between concrete and FRP bars using a pull-out test. Composites Part B: Engineering, 40(8), 784-797.

Bahrololoumi, A., Morovati, V., Poshtan, E. A. and Dargazany, R. (2020). A multi-physics constitutive model to predict hydrolytic aging in quasi-static behaviour of thin cross-linked polymers. International Journal of Plasticity, 130, 102676.

Bahrololoumi, A., Morovati, V., Shaafaey, M. and Dargazany, R. (2021). A multi-physics approach on modeling of hygrothermal aging and its effects on constitutive behavior of cross-linked polymers. Journal of the Mechanics and Physics of Solids, 156, 104614.

Baker, I. (2018). Fifty Materials That Make the World. Springer.

Balaguru, P., Nanni, A. and Giancaspro, J. (2008). FRP composites for reinforced and prestressed concrete structures: a guide to fundamentals and design for repair and retrofit. CRC Press.

Bank, L. C., Gentry, T. R., Thompson, B. P. and Russell, J. S. (2003). A model specification for FRP composites for civil engineering structures. Construction and Building Materials, 17(6-7), 405-437.

Bao, L. R. and Yee, A. F. (2002a). Moisture diffusion and hygrothermal aging in bismaleimide matrix carbon fiber composites—part I: uni-weave composites. Composites Science and Technology, 62(16), 2099-2110.

Bao, L. R. and Yee, A. F. (2002b). Moisture diffusion and hygrothermal aging in bismaleimide matrix carbon fiber composites—part II—woven and hybrid composites. Composites Science and Technology, 62(16), 2111-2119.

Barbosa, A. P. C., Fulco, A. P. P., Guerra, E. S. S., Arakaki, F. K., Tosatto, M., Costa, M. C. B. and Melo, J. D. D. (2017). Accelerated aging effects on carbon fiber/epoxy composites. Composites Part B: Engineering, 110, 298-306.

Barjasteh, E. and Nutt, S. R. (2012). Moisture absorption of unidirectional hybrid composites. Composites Part A: Applied Science and Manufacturing, 43(1), 158-164.

Bashir, S. T., Yang, L., Liggat, J. J. and Thomason, J. L. (2018). Kinetics of dissolution of glass fibre in hot alkaline solution. Journal of Materials Science, 53(3), 1710-1722.

Bauer, G. E. and Halim, A. O. A. E. (1987). The performance of geogrid reinforced road bases. Construction and Building Materials, 1(2), 71-75.

Bazli, M., Li, Y. L., Zhao, X. L., Raman, R. K. S., Bai, Y., Al-Saadi, S. and Haque, A. (2020). Durability of seawater and sea sand concrete filled filament wound FRP tubes under seawater environments. Composites Part B: Engineering, 202, 108409.

Bélan, F., Bellenger, V., Mortaigne, B. and Verdu, J. (1997). Relationship between the structure and hydrolysis rate of unsaturated polyester prepolymers. Polymer Degradation and Stability, 56(3), 301-309.

Belarbi, A. and Wang, H. (2012). Bond durability of FRP bars embedded in fiber-reinforced concrete. Journal of Composites for Construction, 16(4), 371-380.

Benli, A., Karatas, M. and Gurses, E. (2017). Effect of sea water and MgSO4 solution on the mechanical properties and durability of self-compacting mortars with fly ash/silica fume. Construction and Building Materials, 146, 464-474.

Benmokrane, B. and Ali, A. H. (2018). Durability and Long-Term Performance of Fiber-Reinforced Polymer as a New Civil Engineering Material. International Congress on Polymers in Concrete. Springer, Cham, 49-59.

Benmokrane, B., Elgabbas, F., Ahmed, E. A. and Cousin, P. (2015). Characterization and Comparative Durability Study of Glass/Vinylester, Basalt/Vinylester, and Basalt/Epoxy FRP Bars. Journal of Composites for Construction, 19(6), 04015008.

Benzecry, V., Rossini, M., Morales, C., Nolan, S. and Nanni, A. (2021). Design of Marine Dock Using Concrete Mixed with Seawater and FRP Bars. Journal of Composites for Construction, 25(1), 05020006.

Bhatt, A. T., Gohil, P. P. and Chaudhary, V. (2018). Primary Manufacturing Processes for Fiber Reinforced Composites: History, Development & Future Research Trends. IOP Conference Series: Materials Science and Engineering, 330(1), 012107.

Bielak, J., Spelter, A., Will, N. and Classen, M. (2018). Anchorage behavior of textile reinforcement in thin concrete components. Beton-und Stahlbetonbau, 113(7), 515-524.

Biscaia, H. C., Chastre, C. and Silva, M. A. G. (2019). A simple method for the determination of the bond-slip model of artificially aged joints. Journal of Composites for Construction, 23(4), 04019028.

Borovikov, P. I., Sviridov, A. P., Antonov, E. N., Dunaev, A. G., Krotova, L. I., Fatkhudinov, T. K. and Popov, V. K. (2019). Model of aliphatic polyesters hydrolysis comprising water and oligomers diffusion. Polymer Degradation and Stability, 159, 70-78.

Brameshuber, W., Hinzen, M., Dubey, A., Peled, A., Mobasher, B., Bentur, A., ... and Jesse, F. (2016). Recommendation of RILEM TC 232-TDT: test methods and design of textile reinforced concrete: Uniaxial tensile test: test method to determine the load bearing behavior of tensile specimens made of textile reinforced concrete. Materials and Structures/Materiaux et Constructions, 49(12), 4923-4927.

BS 1881-122. (2014). Testing concrete - Part 122: Method for determination of water absorption. British Standards Institution. London, UK.

BS EN 1052-1. (1999). Methods of test for masonry - Part 1: Determination of compressive strength. British Standards Institution. London, UK.

BS EN 2378. (1997). Fibre reinforced plastics - Determination of water absorption by immersion. British Standards Institution. London, UK.

BS EN 12350-5. (2019). Testing fresh concrete - Part 5: Flow table test. British Standards Institution. London, UK.

BS EN 12390-3. (2019). Testing hardened concrete - Part 3: Compressive strength of test specimens. British Standards Institution. London, UK.

BS EN 12390-6. (2009). Testing hardened concrete - Part 6: Tensile splitting strength of test specimens. British Standards Institution. London, UK.

BS EN ISO 2307. (2010). Fibre ropes - Determination of certain physical and mechanical properties. British Standards Institution. London, UK.

Butler, M., Mechtcherine, V. and Hempel, S. (2009). Experimental investigations on the durability of fibre-matrix interfaces in textile-reinforced concrete. Cement and Concrete Composites, 31(4), 221-231.

Butler, M., Mechtcherine, V. and Hempel, S. (2009). Experimental investigations on the durability of fibre-matrix interfaces in textile-reinforced concrete. Cement & Concrete Composites, 31(4), 221-231.

Butler, M., Mechtcherine, V. and Hempel, S. (2009). Experimental investigations on the durability of fibre–matrix interfaces in textile-reinforced concrete. Cement and Concrete Composites, 31(4), 221-231.

Butler, M., Mechtcherine, V. and Hempel, S. (2010). Durability of textile reinforced concrete made with AR glass fibre: effect of the matrix composition. Materials and Structures, 43(10), 1351-1368.

Cabral-Fonseca, S., Correia, J. R., Custódio, J., Silva, H. M., Machado, A. M. and Sousa, J. (2018). Durability of FRP-concrete bonded joints in structural rehabilitation: A review. International Journal of Adhesion and Adhesives, 83, 153-167.

Cairns, D. S. and Adams, D. F. (1981). Moisture and Thermal Expansion of Composite Materials. Report UWME-DR-101-104-1. Department of Mechanical Engineering, University of Wyoming. Laramie, Wyoming.

Cairns, D. S. and Adams, D. F. (1983). Moisture and Thermal Expansion Properties of Unidirectional Composite Materials and the Epoxy Matrix. Journal of Reinforced Plastics and Composites, 2(4), 239-255.

Calvo, J. L. G., Moreno, M. S., Carballosa, P., Pedrosa, F. and Tavares, F. (2019). Improvement of the Concrete Permeability by Using Hydrophilic Blended Additive. Materials, 12(15), 2384.

Camanho, P. P., Davila, C. G. and Davila, C. G. (2003). Numerical simulation of mixed-mode progressive delamination in composite materials. Journal of Composite Materials, 37(16), 1415-1438.

Campilho, R. D. S. G., Banea, M. D., Neto, J. A. B. P. and Silva, L. F. M. d. (2013). Modelling adhesive joints with cohesive zone models: effect of the cohesive law shape of the adhesive layer. International Journal of Adhesion and Adhesives, 44, 48-56.

CAN/CSA S806. (2021). Design and construction of building structures with fibre-reinforced polymers. Canadian Standards Association. Mississauga, Canada.

Cárdenas, C. A., González-Aravena, M. and Santibañez, P. A. (2018). The importance of local settings: within-year variability in seawater temperature at South Bay, Western Antarctic Peninsula. PeerJ, 6, e4289.

Carra, G. and Carvelli, V. (2015). Long-term bending performance and service life prediction of pultruded Glass Fibre Reinforced Polymer composites. Composite Structures, 127, 308-315.

Carrillo, J., Ramirez, J. and Lizarazo-Marriaga, J. (2019). Modulus of elasticity and Poisson's ratio of fiber-reinforced concrete in Colombia from ultrasonic pulse velocities. Journal of Building Engineering, 23, 18-26.

CEN EN 10080. (2005). Steel for the reinforcement of concrete - Weldable reinforcing steel - General. European Committee for Standardization. Brussels, Belgium.

Chatzi, E. G. and Koenig, J. L. (1987). Morphology and structure of Kevlar fibers: a review. Polymer-Plastics Technology and Engineering, 26(3-4), 229-270.

Chen, B.-T., Wang, J.-J., Wang, H., Chang, T.-P. and Yang, Z.-R. (2009). Effect of Void Ratio of Concrete on Evaluation of P-wave Velocity by Impact-echo Method. Journal of Applied Science and Engineering, 6(3), 199-205.

Chen, Y. (2007). Accelerated ageing tests and long-term prediction models for durability of FRP bars in concrete. Ph.D. thesis. West Virginia University. Morgantown, West Virginia.

Chen, Y., Davalos, J. F. and Ray, I. (2006). Durability prediction for GFRP reinforcing bars using short-term data of accelerated aging tests. Journal of Composites for Construction, 10(4), 279-286.

Cheng, S., Ji, J. and Meng, M. (2020). Interfacial response of fibre-to-matrix in textile reinforced concrete between two cracks: Analytical solution. Composite Structures, 245, 112380.

Chin, S. C., Shafiq, N. and Nuruddin, M. F. (2015). FRP as strengthening material for Reinforced Concrete beams with openings - A review. Ksce Journal of Civil Engineering, 19(1), 213-219.

Chung, D. D. L. (2019). Carbon Materials: Science And Applications. World Scientific Publishing Co. Pte. Ltd.

CNR-DT 203/2006. (2006). Guide for the Design and Construction of Concrete Structures Reinforced with Fiber-Reinforced Polymer Bars. Italian National Research Council. Rome, Italy.

Cousin, P., Hassan, M., Vijay, P., Robert, M. and Benmokrane, B. (2019). Chemical resistance of carbon, basalt, and glass fibers used in FRP reinforcing bars. Journal of Composite Materials, 53(26-27), 3651-3670.

Cousins, S. (2019). Shifting sand: Why we’re running out of aggregate. Construction Research and Innovation, 10(3), 69-71.

Cui, E., Jiang, S., Wang, J. and Zeng, X. (2021). Bond behavior of CFRP-concrete bonding interface considering degradation of epoxy primer under wet-dry cycles. Construction and Building Materials, 292, 123286.

D'Antino, T., Colombi, P., Carloni, C. and Sneed, L. H. (2018). Estimation of a matrix-fiber interface cohesive material law in FRCM-concrete joints. Composite Structures, 193, 103-112.

Dai, J., Wang, Q., Xie, C., Xue, Y., Duan, Y. and Cui, X. (2019). The Effect of Fineness on the Hydration Activity Index of Ground Granulated Blast Furnace Slag. Materials, 12(18), 2984.

Davalos, J. F., Chen, A., Zahabi, M. and Ray, I. (2012a). Prediction of degradation of interface fracture energy from accelerated aging tests and mode-II loading. Earth and Space 2012: Engineering, Science, Construction, and Operations in Challenging Environments, 722-731.

Davalos, J. F., Chen, Y. and Ray, I. (2012b). Long-term durability prediction models for GFRP bars in concrete environment. Journal of Composite Materials, 46(16), 1899-1914.

Dave, N., Misra, A. K., Srivastava, A., Sharma, A. K. and Kaushik, S. K. (2017). Study on quaternary concrete micro-structure, strength, durability considering the influence of multi-factors. Construction and Building Materials, 139, 447-457.

Deák, T. and Czigány, T. (2009). Chemical Composition and Mechanical Properties of Basalt and Glass Fibers: A Comparison. Textile Research Journal, 79(7), 645-651.

Demirci, M. T. and Düzcükoğlu, H. (2014). Wear behaviors of Polytetrafluoroethylene and glass fiber reinforced Polyamide 66 journal bearings. Materials & Design, 57, 560-567.

Derombise, G., Schoors, L. V. V., Messou, M. F. and Davies, P. (2010). Influence of finish treatment on the durability of aramid fibers aged under an alkaline environment. Applied Polymer, 117(8), 888-898.

Dharmavarapu, P. and S, S. R. M. B. (2021). Aramid fibre as potential reinforcement for polymer matrix composites: a review. Emergent Materials, 1-18.

Dhoska, K. (2019). Testing Analysis of the HRB400 Steel Reinforcement Bar: Tensile Testing Analysis of the HRB400 Steel Reinforcement Bar. International Journal of Innovative Technology and Interdisciplinary Sciences, 2(3), 253-258.

Díaz, A., Alegre, J. M. and Cuesta, I. I. (2016). A review on diffusion modelling in hydrogen related failures of metals. Engineering Failure Analysis, 66, 577-595.

Dijk, Y. L. M. v., Grätzl, T., Abouhamzeh, M., Kroll, L. and Shrof, S. (2018). Hygrothermal viscoelastic material characterisation of unidirectional continuous carbon-fibre reinforced polyamide 6. Composites Part B: Engineering, 150, 157-164.

Divsholi, B. S., Lim, T. Y. D. and Teng, S. (2014). Durability Properties and Microstructure of Ground Granulated Blast Furnace Slag Cement Concrete. International Journal of Concrete Structures and Materials, 8(2), 157-164.

Donev, A., Fai, T. G. and Vanden-Eijnden, E. (2014). A reversible mesoscopic model of diffusion in liquids: from giant fluctuations to Fick's law. Journal of Statistical Mechanics: Theory and Experiment, 14, P04004.

Dong, W., Li, W., Guo, Y., He, X. and Sheng, D. (2020). Effects of silica fume on physicochemical properties and piezoresistivity of intelligent carbon black-cementitious composites. Construction and Building Materials, 259, 120399.

Dong, Z., Wu, G., Zhao, X. L. and Wang, Z. K. (2017). A refined prediction method for the long-term performance of BFRP bars serviced in field environments. Construction and Building Materials, 155, 1072-1080.

Dong, Z., Wu, G., Zhao, X. L., Zhu, H. and Lian, J. L. (2018). Durability test on the flexural performance of seawater sea-sand concrete beams completely reinforced with FRP bars. Construction and Building Materials, 192, 671-682.

Donnini, J., Lancioni, G. and Corinaldesi, V. (2018). Failure modes in FRCM systems with dry and pre-impregnated carbon yarns: Experiments and modeling. Composites Part B: Engineering, 140, 57-67.

Donnini, J., Spagnuolo, S. and Corinaldesi, V. (2019). A comparison between the use of FRP, FRCM and HPM for concrete confinement. Composites Part B: Engineering, 160, 586-594.

Dubelley, F., Planes, E., Bas, C., Pons, E., Yrieix, B. and Flandin, L. (2018). Predictive durability of polyethylene terephthalate toward hydrolysis over large temperature and relative humidity ranges. Polymer, 142, 285-292.

Duo, Y., Liu, X., Liu, Y., Tafsirojjaman, T. and Sabbrojjaman, M. (2021). Environmental impact on the durability of FRP reinforcing bars. Journal of Building Engineering, 43, 102909.

El Kasaby, E. and Bdelmagied, M. F. A. (2019). Performance of Isolated Footings Reinforced Randomly by Glass Fiber. Journal of Engineering Research and Reports, 6(1), 1-8.

Eid, R. and Paultre, P. (2017). Compressive behavior of FRP-confined reinforced concrete columns. Engineering Structures, 132, 518-530.

El-Hassan, H., El-Maaddawy, T., Al-Sallamin, A. and Al-Saidy, A. (2018). Durability of glass fiber-reinforced polymer bars conditioned in moist seawater-contaminated concrete under sustained load. Construction and Building Materials, 175, 1-13.

Emparanza, A. R., Kampmann, R. and Basalo, F. D. C. y. (2017). State-of-the-practice of global manufacturing of FRP rebar and specifications. ACI Fall Convention.

Emre, H. Y. (2018). Long-Term Resistance of Gradient Anchorage for Prestressed CFRP Strips in Structural Concrete Retrofitting. Ph.D. thesis. ETH Zurich. Rämistrasse, Zurich.

Esfandeh, M., Sabet, A. R., Rezadoust, A. M. and Alavi, M. B. (2009). Bond Performance of FRP Rebars With Various Surface Deformations in Reinforced Concrete. Polymer Composites, 30(5), 576-582.

Fan, X. (2008). Mechanics of Moisture for Polymers: Fundamental Concepts and Model Study. EuroSimE 2008-International Conference on Thermal, Mechanical and Multi-Physics Simulation and Experiments in Microelectronics and Micro-Systems. IEEE, 1-14.

Faraj, R. H., Sherwani, A. F. H. and Daraei, A. (2019). Mechanical, fracture and durability properties of self-compacting high strength concrete containing

recycled polypropylene plastic particles. Journal of Building Engineering, 25, 100808.

Farrar, D. (2008). Modelling of the degradation process for bioresorbable polymers. Degradation rate of bioresorbable materials: 183-206. Woodhead Publishing.

Faruk, O., Tjong, J. and Sain, M. (2017). Lightweight and Sustainable Materials for Automotive Applications. Boca Raton: CRC Press.

Feng, J., Sun, J. and Yan, P. (2018). The Influence of Ground Fly Ash on Cement Hydration and Mechanical Property of Mortar. Advances in Civil Engineering, 2018, 4023178.

Fergani, H. A. (2017). Durability and Long-term Structural Performance of GFRP Bars in Concrete. Ph.D. thesis. University of Sheffield. Sheffield, South Yorkshire.

fib Task Group 9.3, Bulletin 40. (2007). FRP Reinforcement in RC Structures. International Federation for Structural Concrete. fib Bulletin 40. Lausanne, Switzerland.

Focacci, F., Nanni, A. and Bakis, C. E. (2000). Local bond-slip relationship for FRP reinforcement in concrete. Journal of Composites for Construction, 4(1), 24-31.

Fonseca, R. P. d., Rocha, J. C. and Cheriaf, M. (2020). Mechanical Properties of Mortars Reinforced with Amazon Rainforest Natural Fibers. Materials, 14(1), 155.

Frank, E., Hermanutz, F. and Buchmeiser, M. R. (2012). Carbon Fibers: Precursors, Manufacturing, and Properties. Macromolecular materials and engineering, 297(6), 493-501.

Fulmali, A. O., Sen, B., Nayak, B. A. and Prusty, R. K. (2021). Effect of repeated hydrothermal cycling on the durability of glass fiber/epoxy composites with and without carbon nanotube reinforcement. Polymer Composites, 42(11), 6160-6172.

Gagani, A., Krauklis, A. and Echtermeyer, A. T. (2018). Anisotropic fluid diffusion in carbon fiber reinforced composite rods: Experimental, analytical and numerical study. Marine Structures, 59, 47-59.

Gemi, L., Madenci, E. and Özkılıç, Y. O. (2021). Experimental, analytical and numerical investigation of pultruded GFRP composite beams infilled with hybrid FRP reinforced concrete. Engineering Structures, 244, 112790.

Genna, S., Trovalusci, F. and Tagliaferri, V. (2017). Indentation test to study the moisture absorption effect on CFRP composite. Composites Part B: Engineering, 124, 1-8.

Gesoğlu, M., Güneyisi, E. and Özbay, E. (2009). Properties of self-compacting concretes made with binary, ternary, and quaternary cementitious blends of fly ash, blast furnace slag, and silica fume. Construction and Building Materials, 23(5), 1847-1854.

Ghabezi, P. and Harrison, N. (2020). Mechanical behavior and long-term life prediction of carbon/epoxy and glass/epoxy composite laminates under artificial seawater environment. Materials Letters, 261, 127091.

Godara, S. S., Yadav, A., Goswami, B. and Rana, R. S. (2021). Review on history and characterization of polymer composite materials. Materials Today: Proceedings, 44, 2674-2677.

Godat, A., Aldaweela, S., Aljaberi, H., Tamimi, N. A. and Alghafri, E. (2021). Bond strength of FRP bars in recycled-aggregate concrete. Construction and Building Materials, 267, 120919.

Godat, A., L'Hady, A., Chaallal, O. and Neale, K. W. (2012). Bond Behavior of the ETS FRP Bar Shear-Strengthening Method. Journal of Composites for Construction, 16(5), 529-539.

Gopinath, S., Murthy, A. R. and Iyer, N. R. (2013). Experimental Investigations on the Glass Fabrics for Confinement of Concrete Specimens. Structural Durability & Health Monitoring, 9(1), 1.

Graham-Jones, J. and Summerscales, J. (2015). Marine applications of advanced fibre-reinforced composites. Woodhead Publishing.

Gravina, R. J., Li, J., Smith, S. T. and Visintin, P. (2020). Environmental durability of FRP bar-to-concrete bond: critical review. Journal of Composites for Construction, 24(4), 03120001.

Grotefendt, K., Logemann, K., Quadfasel, D. and Ronski, S. (1998). Is the Arctic Ocean warming? Journal of Geophysical Research: Oceans, 103(C12), 27679-27687.

Guo, F., Al-Saadi, S., Raman, R. K. S. and Zhao, X. L. (2018). Durability of fiber reinforced polymer (FRP) in simulated seawater sea sand concrete (SWSSC) environment. Corrosion Science, 141, 1-13.

Guo, Y., Zhang, Y. X., Soe, K., Wuhrer, R., Hutchison, W. D. and Timmers, H. (2021). Development of magnesium oxychloride cement with enhanced water resistance by adding silica fume and hybrid fly ash-silica fume. Journal of Cleaner Production, 313, 127682.

Halvaei, M., Jamshidi, M., Latif, M. and Ejtemaei, M. (2020). Experimental investigation and modelling of flexural properties of carbon textile reinforced concrete. Construction and Building Materials, 262, 120877.

Han, S., Zhong, J., Ding, W. and Ou, J. (2021). Strength, hydration, and microstructure of seawater sea-sand concrete using high-ferrite Portland cement. Construction and Building Materials, 295, 123703.

Hartig, J. and Häußler-Combe, U. (2011). A model for Textile Reinforced Concrete under imposed uniaxial deformations. Institute of Concrete Structures, Technische Universität Dresden, Germany.

Hegger, J., Bruckermann, O. and Chudoba, R. (2004). A smeared bond-slip relation for multi-filament yarns embedded in fine concrete. 6th international RILEM symposium on fibre reinforced concretes, 134, 1453-1462.

Heshmati, M., Haghani, R. and Al-Emrani, M. (2016). Effects of moisture on the long-term performance of adhesively bonded FRP/steel joints used in bridges. Composites Part B: Engineering, 92, 447-462.

Hota, G. and Liang, R. (2011). Advanced fiber reinforced polymer composites for sustainable civil infrastructures. Proceedings of the International Symposium on Innovation & Sustainability of Structures in Civil Engineering. Xiamen University.

Huang, J. and Aboutaha, R. (2010). Environmental reduction factors for GFRP bars used as concrete reinforcement: new scientific approach. Journal of Composites for Construction, 14(5), 479-486.

Huang, X. s. (2009). Fabrication and Properties of Carbon Fibers. Materials, 2(4), 2369-2403.

Huang, Y. K., Frings, P. H. and Hennes, E. (2002). Mechanical properties of Zylon/epoxy composite. Composites Part B: Engineering, 33(2), 109-115.

Hukins, D. W. L., Mahomed, A. and Kukureka, S. N. (2008). Accelerated aging for testing polymeric biomaterials and medical devices. Medical engineering & physics, 30(10), 1270-1274.

Huo, Z., Bheemreddy, V., Chandrashekhara, K. and Brack, R. (2015). Modelling of concentration-dependent moisture diffusion in hybrid fibre-reinforced polymer composites. Journal of Composite Materials, 49(3), 321-333.

Hwang, K., Noguchi, T. and Tomosawa, F. (2004). Prediction model of compressive strength development of fly-ash concrete. Cement and Concrete Research, 34(12), 2269-2276.

Ibarra, L. and Chamorro, C. (1991). Short fiber–elastomer composites. Effects of matrix and fiber level on swelling and mechanical and dynamic properties. Journal of Applied Polymer Science, 43(10), 1805-1819.

Imani, F. S., Chen, A., Davalos, J. F. and Ray, I. (2010). Temperature and Water-Immersion Effect on Mode II Fracture Behavior of CFRP-Concrete Interface. CICE 2010 - The 5th International Conference on FRP Composites in Civil Engineering, 557-561.

Ishak, N. I., Johari, M. A. M. and Hashim, S. F. S. (2017). Effects of using blended binder of RHA and GGBS on the properties of concrete: A review. AIP Conference Proceedings, 1892(1), 020027.

Ismail, K. N., Hussin, K. and Idris, M. S. (2007). Physical, chemical and mineralogical properties of fly ash. Journal of Nuclear and Related Technology, 4, 47-51.

ISO 3344. (2014). Reinforcement products - Determination of moisture content. International Organization for Standardization. Geneva, Switzerland.

ISO 10406-1. (2015). Fibre-reinforced polymer (FRP) reinforcement of concrete - Test methods - Part 1: FRP bars and grids. International Organization for Standardization. Geneva, Switzerland.

IStructE-1999. (1999). Interim Guidance on the Design of Reinforced Concrete Structures Using Fibre Composite Reinforcement. Institution of Structural Engineers (IStructE). London, UK.

Ito, M. and Nagai, K. (2007). Analysis of degradation mechanism of plasticized PVC under artificial aging conditions. Polymer Degradation and Stability, 92(2), 260-270.

Jamshaid, H. and Mishra, R. (2016). A green material from rock: basalt fiber - a review. The Journal of The Textile Institute, 107(7), 923-937.

Javaid, U., Khan, Z. M., Khan, M. B., Bassyouni, M., Abdel-Hamid, S. M.-S., Abdel-Aziz, M. H. and Hasan, S. W. u. (2016). Fabrication and thermo-mechanical characterization of glass fiber/vinyl ester wind turbine rotor blade. Composites Part B: Engineering, 91, 257-266.

Jawaid, M., Thariq, M. and Saba, N. (2018). Mechanical and Physical Testing of Biocomposites, Fibre-Reinforced Composites and Hybrid Composites. Woodhead Publishing.

Jiang, J., Jiang, C., Li, B. and Feng, P. (2019). Bond behavior of basalt textile meshes in ultra-high ductility cementitious composites. Composites Part B: Engineering, 174, 107022.

Jiang, X., Kolstein, H., Bijlaard, F. and Qiang, X. (2014). Effects of hygrothermal aging on glass-fibre reinforced polymer laminates and adhesive of FRP composite bridge: Moisture diffusion characteristics. Composites Part A: Applied Science and Manufacturing, 57, 49-58.

Joshi, H. and Purnima, J. (2010). Development of glass fiber, wollastonite reinforced polypropylene hybrid composite: Mechanical properties and morphology. Materials Science and Engineering: A, 527(7-8), 1946-1951.

JSCE-1997. (1997). Recommendation for Design and Construction of Concrete Structures Using Continuous Fiber Reinforcing materials. Research Committee on Continuous Fiber Reinforcing Materials. Japan Society of Civil Engineers (JSCE). Tokyo, Japan.

Kabir, M. I., Shrestha, R. and Samali, B. (2016). Effects of applied environmental conditions on the pull-out strengths of CFRP-concrete bond. Construction and Building Materials, 114, 817-830.

Kabir, R. B. and Ferdous, N. (2012). Kevlar-The Super Tough Fiber. International journal of textile science, 1(6), 78-83.

Kafodya, I., Xian, G. and Li, H. (2015). Durability study of pultruded CFRP plates immersed in water and seawater under sustained bending: Water uptake and effects on the mechanical properties. Composites Part B: Engineering, 70, 138-148.

Kari, L. (2017). Dynamic stiffness of chemically and physically ageing rubber vibration isolators in the audible frequency range. Continuum Mechanics and Thermodynamics, 29(5), 1027-1046.

Katano, K., Takeda, N., Ishizeki, Y. and Iriya, K. (2013). Properties and application of concrete made with sea water and un-washed sea sand. Proceedings of Third International conference on Sustainable Construction Materials and Technologies.

Kaur, J. and Keith Millington, S. S. (2016). Producing high-quality precursor polymer and fibers to achieve theoretical strength in carbon fibers: A review. Journal of Applied Polymer Science, 133(38), 43963.

Kaya, A. I., Kısa, M. and Özen, M. (2018). Effect of natural weathering conditions on the dynamic behavior of woven aramid composites. AIP Conference Proceedings, 1935(1), 020005.

Khalili, S. M. R., Mittal, R. K. and Kalibar, S. G. (2005). A study of the mechanical properties of steel/aluminium/GRP laminates. Materials Science and Engineering: A, 412(1-2), 137-140.

Khan, T., Sultan, M. T. B. H. and Ariffin, A. H. (2018). The challenges of natural fiber in manufacturing, material selection, and technology application: A review. Journal of Reinforced Plastics and Composites, 37(11), 770-779.

Khatib, J. M. (2016). Sustainability of Construction Materials. Woodhead Publishing.

Khayat, K. H. and Meng, W. (2014). Design and performance of stay-in-place UHPC prefabricated panels for infrastructure construction. Missouri University of Science and Technology. Center for Transportation Infrastructure and Safety, No. NUTC R320.

Khoramishad, H. and Zarifpour, D. (2018). Fracture response of adhesive joints reinforced with aligned multi-walled carbon nanotubes using an external electric field. Theoretical and Applied Fracture Mechanics, 98, 220-229.

Khurshid, Z., Najeeb, S., Zafar, M. S. and Sefat, F. (2019). Advanced dental biomaterials. Woodhead Publishing.

Kim, J. E., Park, W. S., Cho, S. H., Kim, D. G. and Noh, J. M. (2012). An Experimental Study on Mechanical Properties for Ternary High Performance Concrete with Fly-ash, Blast furnace slag, Silica fume. Applied Mechanics and Materials, 204, 3699-3702.

Kim, Y., Sim, J. and Park, C. (2012). Mechanical properties of recycled aggregate concrete with deformed steel re-bar. Journal of marine science and technology, 20(3), 274-280.

Kim, Y. J. (2019). State of the practice of FRP composites in highway bridges. Engineering Structures, 179, 1-8.

Kostova, K. Z., Ibell, T. J., Darby, A. P. and Evernden, M. C. (2013). Behaviour of fabric-formed concrete beams reinforced with FRP bars. Advanced Composites in Construction (ACIC) 2013 Conference Proceedings. 6th International ACIC Conference held at the Queen's University Belfast, 286-297.

Kouzeli, M., Weber, L., Marchi, C. S. and Mortensen, A. (2001). Influence of damage on the tensile behaviour of pure aluminium reinforced with ⩾40 vol. pct alumina particles. Acta Materialia, 49(18), 3699-3709.

Kovalenko, S. A. and Dobryakov, A. L. (2013). On the excitation wavelength dependence and Arrhenius behavior of stilbene isomerization rates in solution. Chemical Physics Letters, 570, 56-60.

Krauklis, A. E., Gagani, A. I. and Echtermeyer, A. T. (2019). Prediction of Orthotropic Hygroscopic Swelling of Fiber-Reinforced Composites from Isotropic Swelling of Matrix Polymer. Journal of Composites Science, 3(1), 10.

Ksouri, I. and Haddar, N. (2018). Long term ageing of polyamide 6 and polyamide 6 reinforced with 30% of glass fibers: temperature effect. Journal of Polymer Research, 25(7), 1-12.

Kulagina, G. S. and Zhelezina, G. F. (2022). Physicomechanical Properties of a Unidirectional Organoplast Based on Rusar-NT Aramid Fibers. Polymer Science, Series D, 15(4), 658-662.

Kunioka, M., Shimada, T., Hagihara, H., Funabashi, M., Suda, H. and Horizono, H. (2016). Quick Preparation of Moisture-Saturated Carbon Fiber-Reinforced Plastics and Their Accelerated Ageing Tests Using Heat and Moisture. Polymers, 8(6), 242.

Laidler, K. J. (1984). The development of the Arrhenius equation. Journal of Chemical Education, 61(6), 494-498.

Larner, L. J., Speakman, K. and Majumdar, A. J. (1976). Chemical interactions between glass fibres and cement. Journal of Non-Crystalline Solids, 20(1), 43-74.

Lee, D., Cheng, L. and Hui, J. Y.-G. (2013). Bond Characteristics of Various NSM FRP Reinforcements in Concrete. Journal of Composites for Construction, 17(1), 117-129.

Lee, J. Y., Kim, T. Y., Kim, T. J., Yi, C. K., Park, J. S., You, Y. C. and Park, Y. H. (2008). Interfacial bond strength of glass fiber reinforced polymer bars in high-strength concrete. Composites Part B: Engineering, 39(2), 258-270.

Lekatou, A., Faidi, S. E., Ghidaoui, D., Lyon, S. B. and Newman, R. C. (1997). Effect of water and its activity on transport properties of glass/epoxy particulate composites. Composites Part A: Applied Science and Manufacturing, 28(3), 223-236.

Li, C., Xian, G. and Li, H. (2018). Water absorption and distribution in a pultruded unidirectional carbon/glass hybrid rod under hydraulic pressure and elevated temperatures. Polymers, 10(6), 627-643.

Li, H., Liu, G. j. and Cao, Y. (2014). Content and Distribution of Trace Elements and Polycyclic Aromatic Hydrocarbons in Fly Ash from a Coal-Fired CHP Plant. Aerosol and Air Quality Research, 14(4), 1179-1188.

Li, J., Gravina, R., Visintin, P. and Smith, S. T. (2020b). Durability and long-term performance of FRP-to-concrete joints under environmental conditioning: experimental and analytical study. Journal of Composites for Construction, 24(4), 04020021.

Li, J., Xie, J., Liu, F. and Lu, Z. (2019). A critical review and assessment for FRP-concrete bond systems with epoxy resin exposed to chloride environments. Composite Structures, 229, 111372.

Li, K. L., Tang, X. S., Huang, G. H. and Xu, H. (2009). Experimental research of high performance concrete with multi-elements mineral admixtures. Key Engineering Materials, 405, 24-29.

Li, L., Shao, Y. and Wu, Z. (2010). Durability of wet bond of hybrid laminates to cast-in-place concrete. Journal of Composites for Construction, 14(2), 209-216.

Li, P., Li, W., Sun, Z., Shen, L. and Sheng, D. (2021). Development of sustainable concrete incorporating seawater: A critical review on cement hydration, microstructure and mechanical strength. Cement and Concrete Composites, 121, 104100.

Li, Q. and Xu, S. (2011). Experimental Research on Mechanical Performance of Hybrid Fiber Reinforced Cementitious Composites with Polyvinyl Alcohol Short Fiber and Carbon Textile. Journal of Composite Materials, 45(1), 5-28.

Li, T., Zhu, H., Wang, Q., Li, J. and Wu, T. (2018). Experimental study on the enhancement of additional ribs to the bond performance of FRP bars in concrete. Construction and Building Materials, 185, 545-554.

Li, Y., Zhou, L., Zhang, Y., Cui, J. and Shao, J. (2013). Study on Long-term Performance of Concrete Based on Seawater, Sea Sand and Coral Sand. Advanced Materials Research, 706, 512-515.

Li, Y. L., Zhao, X. L. and Raman, R. K. S. (2018). Mechanical properties of seawater and sea sand concrete-filled FRP tubes in artificial seawater. Construction and Building Materials, 191, 977-993.

Liang, H., Li, S., Lu, Y. and Yang, T. (2018). Reliability Study on FRP Composites Exposed to Wet-Dry Cycles. Applied Sciences, 8(6), 892.

Liang, H., Li, S., Lu, Y. and Yang, T. (2019). The combined effects of wet-dry cycles and sustained load on the bond behavior of FRP-concrete interface. Polymer Composites, 40(3), 1006-1017.

Liang, X. and Yin, S. (2021). Mechanical properties and gas permeability of coral aggregate concrete incorporating supplementary cementitious materials. Construction and Building Materials, 302, 124237.

Liao, J., Zeng, J. J., Bai, Y. L. and Zhang, L. (2022). Bond strength of GFRP bars to high strength and ultra-high strength fiber reinforced seawater sea-sand concrete (SSC). Composite Structures, 281, 115013.

Lim, J. C. and Ozbakkaloglu, T. (2014). Influence of silica fume on stress-strain behavior of FRP-confined HSC. Construction and Building Materials, 63, 11-24.

Lin, H., Feng, P. and Yang, J. Q. (2021). Pressure-dependent bond stress-slip model for sand-coated FRP-concrete interface. Composite Structures, 263, 113719.

Lin, X. and Zhang, Y. X. (2014). Evaluation of bond stress-slip models for FRP reinforcing bars in concrete. Composite Structures, 107, 131-141.

Litherland, K. L., Oakley, D. R. and Proctor, B. A. (1981). The use of accelerated ageing procedures to predict the long term strength of GRC composites. Cement and Concrete Research, 11(3), 455-466.

Liu, J., Liu, J., Huang, Z., Zhu, J., Liu, W. and Zhang, W. (2020). Effect of Fly Ash as Cement Replacement on Chloride Diffusion, Chloride Binding Capacity, and Micro-Properties of Concrete in a Water Soaking Environment. Applied Sciences, 10(18), 6271.

Liu, L., Zhao, Z., Chen, W., Shuang, C. and Luo, G. (2018). An experimental investigation on high velocity impact behavior of hygrothermal aged CFRP composites. Composite Structures, 204, 645-657.

Liu, S., Cheng, X., Zhang, Q., Zhang, J., Bao, J. and Guo, X. (2016). An investigation of hygrothermal effects on adhesive materials and double lap shear joints of CFRP composite laminates. Composites Part B: Engineering, 91, 431-440.

Liu, S., Yuan, H. and Wu, J. (2019). Full-range mechanical behavior study of FRP-to-concrete interface for pull-pull bonded joints. Composites Part B: Engineering, 164, 333-344.

Liu, S., Zhu, M., Ding, X., Ren, Z., Zhao, S., Zhao, M. and Dang, J. (2021). High-Durability Concrete with Supplementary Cementitious Admixtures Used in Corrosive Environments. Crystals, 11(2), 196.

Liu, X., Jiang, J., Wang, G., Wang, J. and Xu, R. (2020). Debonding analysis of curved RC beams externally bonded with FRP plates using CZM. Engineering Structures, 205, 110103.

Lorenz, E. and Ortlepp, R. (2012). Bond Behavior of Textile Reinforcements - Development of a Pull-Out Test and Modeling of the Respective Bond versus Slip Relation. High Performance Fiber Reinforced Cement Composites 6: 479-486. RILEM State of the Art Reports, vol 2. Springer.

Lu, F. and Ayoub, A. (2011). Evaluation of debonding failure of reinforced concrete girders strengthened in flexure with FRP laminates using finite element modelling. Construction and Building Materials, 25(4), 1963-1979.

Lü, Q., Qiu, Q., Zheng, J., Wang, J. and Zeng, Q. (2019). Fractal dimension of concrete incorporating silica fume and its correlations to pore structure, strength and permeability. Construction and Building Materials, 228, 116986.

Lu, Y., Shi, G., Liu, Y., Ding, Z., Pan, J., Qin, D., Dong, B. and Shao, H. (2018). Study on the effect of chloride ion on the early age hydration process of concrete by a non-contact monitoring method. Construction and Building Materials, 172, 499-508.

Lu, Z. (2021). Review on the Precursor Preparation and Carbon Fiber Manufacturing. Journal of Physics: Conference Series, 1798(1), 012003.

Lu, Z., Li, Y. and Xie, J. (2021). Durability of BFRP bars wrapped in seawater sea sand concrete. Composite Structures, 255, 112935.

Lu, Z., Xian, G. and Li, H. (2015). Experimental Study on the Mechanical Properties of Basalt Fibres and Pultruded Bfrp Plates at Elevated Temperatures. Polymers and Polymer Composites, 23(5), 277-284.

Luo, H. L., Lian, J. J., Wan, Y. Z., Huang, Y., Wang, Y. L. and Jiang, H. J. (2006). Moisture absorption in VARTMed three-dimensional braided carbon-epoxy composites with different interface conditions. Materials Science and Engineering: A, 425(1-2), 70-77.

Ma, Q., Salim, M. S. A., Rejab, M. R. M., Bernhardi, O.-E. and Nasution, A. Y. (2020). Quasi-static crushing response of square hybrid carbon/aramid tube for automotive crash box application. Materials Today: Proceedings, 27, 683-690.

Ma, S., Zhao, Z., Nie, W. and Gui, Y. (2016). A numerical model of fully grouted bolts considering the tri-linear shear bond–slip model. Tunnelling and Underground Space Technology, 54, 73-80.

Madhavi, T. C., Raju, L. S. and Mathur, D. (2014). Polypropylene fiber reinforced concrete-a review. International journal of emerging technology and advanced engineering, 4(4), 114-118.

Magna, R. L., Waimer, F. and Knippers, J. (2016). Coreless Winding and Assembled Core - Novel fabrication approaches for FRP based components in building construction. Construction and Building Materials, 127, 1009-1016.

Mahboob, A., Gil, L., Bernat-Maso, E. and Eskenati, A. R. (2021). Flexible Fiber Fabric for FRP-Concrete Connection of Thin Hybrid Slabs. Polymers, 13(17), 2862.

Maljaee, H., Ghiassi, B., Lourenço, P. B. and Oliveira, D. V. (2016). Moisture-induced degradation of interfacial bond in FRP-strengthened masonry. Composites Part B: Engineering, 87, 47-58.

Manaila, E., Stelescu, M. D. and Craciun, G. (2018). Degradation studies realized on natural rubber and plasticized potato starch based eco-composites obtained by peroxide cross-linking. International Journal of Molecular Sciences, 19(10), 2862.

Manu, K. M. S., Raag, L. A., Rajan, T. P. D., Pai, B. C., Petley, V. and Verma, S. N. (2019). Self-lubricating bidirectional carbon fiber reinforced smart aluminum composites by squeeze infiltration process. Journal of Materials Science & Technology, 35(11), 2559-2569.

Mardani-Aghabaglou, A., Karakuzu, K., Kobya, V. and Hatungimana, D. (2021). Durability performance and dimensional stability of road concrete containing dry-shake surface hardener admixture. Construction and Building Materials, 274, 121789.

Marouani, S., Curtil, L. and Hamelin, P. (2012). Ageing of carbon/epoxy and carbon/vinylester composites used in the reinforcement and/or the repair of civil engineering structures. Composites Part B: Engineering, 43(4), 2020-2030.

Masselter, T. and Speck, T. (2011). Biomimetic fiber-reinforced compound materials. Intech.

Mathavan, J. J. and Patnaik, A. (2020). Analysis of wear properties of granite dust filled polymer composite for wind turbine blade. Results in Materials, 5, 100073.

Matos, P. R. d., Junckes, R., Graeff, E. and Jr, L. R. P. (2020). Effectiveness of fly ash in reducing the hydration heat release of mass concrete. Journal of Building Engineering, 28, 101063.

Matthys, S. and Triantafillou, T. (2001). Shear and torsion strengthening with externally bonded FRP reinforcement. Composites in Construction: A Reality, 203-212.

Maxwell, A. S., Broughton, W. R., Dean, G. and Sims, G. D. (2005). Review of accelerated ageing methods and lifetime prediction techniques for polymeric materials. NPL Report DEPC MPR 016.

Melchers, R. E. (2020). Long-Term Durability of Marine Reinforced Concrete Structures. Journal of Marine Science and Engineering, 8(4), 290.

Memon, A. H., Radin, S. S., Zain, M. F. M. and Trottier, J. F. (2002). Effects of mineral and chemical admixtures on high-strength concrete in seawater. Cement and Concrete Research, 32(3), 373-377.

Meng, M., Rizvi, M. J., Grove, S. M. and Le, H. R. (2015). Effects of hygrothermal stress on the failure of CFRP composites. Composite Structures, 133, 1024-1035.

Mesticou, Z., Bui, L., Junes, A. and Larbi, A. S. (2017). Experimental investigation of tensile fatigue behaviour of Textile-Reinforced Concrete (TRC): Effect of fatigue load and strain rate. Composite Structures, 160, 1136-1146.

Micelli, F. and Nanni, A. (2004). Durability of FRP rods for concrete structures. Construction and Building Materials, 18(7), 491-503.

Mo, L., Deng, M. and Wang, A. (2012). Effects of MgO-based expansive additive on compensating the shrinkage of cement paste under non-wet curing conditions. Cement & Concrete Composites, 34(3), 377-383.

Moelwyn-Hughes, E. A. (1936). A theory of electrokinetic effects in solution; reactions between ions. Proceedings of the Royal Society of London. Series A-Mathematical and Physical Sciences, 155(885), 308-315.

Mohammed, M. k. (2015). Multi-scale response of sustainable self-compacting concrete (SCC) to carbonation and chloride penetration. Ph.D. thesis. University of Nottingham. Nottingham, East Midlands.

Mohanta, S., Padarthi, Y., Gupta, J. and Neogi, S. (2021). Insight into the nondestructive performance evaluation of fiber-reinforced polymer composite laminate immersed in produced water using embedded fiber Bragg grating sensor. Polymer Composites, 42(9), 4717-4727.

Mohee, F. M., Al-Mayah, A. and Plumtree, A. (2016). Anchors for CFRP plates: State-of-the-art review and future potential. Composites Part B: Engineering, 90, 432-442.

Monteny, J., Vincke, E., Beeldens, A., Belie, N. D., Taerwe, L., Gemert, D. V. and Verstraete, W. (2000). Chemical, microbiological, and in situ test methods for biogenic sulfuric acid corrosion of concrete. Cement and Concrete Research, 30(4), 623-634.

Motavalli, M. and Czaderski, C. (2007). FRP composites for retrofitting of existing civil structures in Europe: State-of-the-art review. International Conference of Composites & Polycon. American Composites Manufacturers Association Tampa, FL, USA., 17-19.

Mubashar, A., Ashcroft, I. A., Critchlow, G. W. and Crocombe, A. D. (2011). Strength prediction of adhesive joints after cyclic moisture conditioning using a cohesive zone model. Engineering Fracture Mechanics, 78(16), 2746-2760.

Mukhtar, F. M. and Shehadah, M. E. (2021). Experimental verification of 2- and 3-D numerical models for bond-slip behavior of CFRP-concrete. Construction and Building Materials, 287, 122814.

Mumenya, S. W., Tait, R. B. and Alexander, M. G. (2010). Mechanical behaviour of Textile Concrete under accelerated ageing conditions. Cement and Concrete Composites, 32(8), 580-588.

Munck, M. D., Kadi, M. E., Tsangouri, E., Vervloet, J., Verbruggen, S., Wastiels, J., Tysmans, T. and Remy, O. (2018). Influence of environmental loading on the tensile and cracking behaviour of textile reinforced cementitious composites. Construction and Building Materials, 181, 325-334.

Naaman, A. E. (2012). Evolution in Ferrocement and Thin Reinforced Cementitious Composites. Arabian Journal for Science and Engineering, 37(2), 421-441.

Naaman, A. E. (2018). Fiber reinforced cement and concrete composites. Techno press 3000.

Naaman, A. E., Namur, G. G., Alwan, J. M. and Najm, H. S. (1991). Fiber Pullout and Bond Slip. I: Analytical Study. Journal of Structural Engineering, 117(9), 2769-2790.

Nadiv, R., Peled, A., Mechtcherine, V., Hempel, S., Nicke, D. and Schroefl, C. (2017b). Improved Bonding of Carbon Fiber Reinforced Cement Composites by Mineral Particle Coating. International Conference on Strain-Hardening Cement-Based Composites, 392-399.

Nadiv, R., Peled, A., Mechtcherine, V., Hempel, S. and Schroef, C. (2017a). Micro- and nanoparticle mineral coating for enhanced properties of carbon multifilament yarn cement-based composites. Composites Part B: Engineering, 111, 179-189.

Nagavally, R. R. (2017). Composite materials-history, types, fabrication techniques, advantages, and applications. Int J Mech Prod Eng, 5(9), 25-30.

Nanni, A., Luca, A. D. and Zadeh, H. J. (2014). Reinforced Concrete with FRP Bars: Mechanics and Design. CRC Press.

Nepomuceno, E., Sena-Cruz, J., Correia, L. and D'Antino, T. (2021). Review on the bond behavior and durability of FRP bars to concrete. Construction and Building Materials, 287, 123042.

Ng, P. L. and Kwan, A. K. H. (2016). Strategies for improving dimensional stability of concrete. Canadian Journal of Civil Engineering, 43(10), 875-885.

Nguyen, T.-C., Bai, Y., Zhao, X. L. and Al-Mahaidi, R. (2012). Durability of steel/CFRP double strap joints exposed to sea water, cyclic temperature and humidity. Composite Structures, 94(5), 1834-1845.

Nilsson, L. O. (2002). Long-term moisture transport in high performance concrete. Materials and Structures, 35(10), 641-649.

Nolan, S., Rossini, M., Knight, C. and Nanni, A. (2021). New directions for reinforced concrete coastal structures. Journal of Infrastructure Preservation and Resilience, 2(1), 1-12.

Norway Standard NS 3473: 2003. (2003). Concrete structures - Design and detailing rules. Norwegian Council for Building Standardization. Norway.

Ogirigbo, O. R. and Ukpata, J. (2017). Effect of chlorides and curing duration on the hydration and strength development of plain and slag blended cements. Journal of Civil Engineering Research, 7(1), 9-16.

Oguz, Z. A., Erklig, A. and Bozkurt, Ö. Y. (2021). Degradation of hybrid aramid/glass/epoxy composites hydrothermally aged in distilled water. Journal of Composite Materials, 55(15), 2043-2060.

Oncu, G. (2003). Durability and service life prediction of concrete reinforcing materials. MS thesis. University of Wisconsin-Madison. Madison, Wisconsin.

Onyakora, A. N., Abubakre, O. K., Mudiare, E. and Suleiman, M. A. T. (2017). Effect of fibre loading and treatment on porosity and water absorption correlated with tensile behaviour of oil palm empty fruit bunch fibre reinforced composites. Advances in Materials Research, 6(4), 329-341.

Onyakora, A. N., Abubakre, O. K., Mudiare, E. and Suleiman, M. A. T. (2020). Exploitation of coir composites: enhancement of absorbency and impact strength. FUW Trends in Science & Technology Journal, 5(1), 79-82.

Ouyang, Z. (2007). Durability of bond between FRP and concrete in moist environments: Experimental, numerical and analytical study. Ph.D. thesis. Marquette University. Milwaukee, Wisconsin.

Pacheco-Torgal, F., Diamanti, M. V., Nazari, A., Goran-Granqvist, C., Pruna, A. and Amirkhanian, S. (2018). Nanotechnology in eco-efficient construction: materials, processes and applications. Woodhead Publishing.

Padarthi, Y., Mohanta, S., Gupta, J. and Neogi, S. (2021). Assessment of transport kinetics and chemo-mechanical properties of GF/Epoxy composite under long term exposure to sulphuric acid. Polymer Degradation and Stability, 183, 109436.

Page, C. L. (1975). Mechanism of corrosion protection in reinforced concrete marine structures. Nature, 258(5535), 514-515.

Pan, J. and Leung, C. K. (2007). Effect of Concrete Composition on FRP/Concrete Bond Capacity. Journal of Composites for Construction, 11(6), 611-618.

Pan, Y., Shi, J. and Xian, G. (2019). Experimental and numerical study of the CFRP-to-concrete bonded joints after water immersion. Composite Structures, 218, 95-106.

Pan, Y., Xian, G. and Silva, M. A. G. (2015). Effects of water immersion on the bond behavior between CFRP plates and concrete substrate. Construction and Building Materials, 101, 326-337.

Papanicolaou, G. C., Kosmidou, T. V., Vatalis, A. S. and Delides, C. G. (2006). Water absorption mechanism and some anomalous effects on the mechanical and viscoelastic behavior of an epoxy system. Journal of Applied Polymer Science, 99(4), 1328-1339.

Park, S. J. and Seo, M. K. (2011). Interface Science and Composites. Academic Press.

PASĂRE, M. M., LUCA, L. and Radostin, D. (2019). Aspects of composite materials evolution. Fiability Durab./Fiabil. Durabilitate, 2, 55-60.

Patil, A. and Dwivedi, A. K. (2022). Mechanical strength and durability performance of sea water concrete incorporating supplementary cementitious materials in different curing conditions. Materials Today: Proceedings.

Pérez-Pacheco, E., Cauich-Cupul, J. I., Valadez-González, A. and Herrera-Franco, P. J. (2013). Effect of moisture absorption on the mechanical behavior of carbon fiber/epoxy matrix composites. Journal of Materials Science, 48(5), 1873-1882.

Phani, K. K. and Bose, N. R. (1986). Hydrothermal ageing of CSM-laminate during water immersion—an acousto-ultrasonic study. Journal of Materials Science, 21(10), 3633-3637.

Phani, K. K. and Bose, N. R. (1987). Temperature dependence of hydrothermal ageing of CSM-laminate during water immersion. Composites Science and Technology, 29(2), 79-87.

Philip, M. and AlAzzawi, F. (2018). Effects of Natural and Artificial Weathering on the Physical Properties of Recycled Poly(ethylene terephthalate). Journal of Polymers and the Environment, 26(8), 3139-3148.

Pickett, J. E. and Coyle, D. J. (2013). Hydrolysis kinetics of condensation polymers under humidity aging conditions. Polymer Degradation and Stability, 98(7), 1311-1320.

Portal, N. W., Flansbjer, M., Johannesson, P., Malaga, K. and Lundgren, K. (2016). Tensile behaviour of textile reinforcement under accelerated ageing conditions. Journal of Building Engineering, 5, 57-66.

Portal, N. W., Perez, I. F., Thrane, L. N. and Lundgren, K. (2014). Pull-out of textile reinforcement in concrete. Construction and Building Materials, 71, 63-71.

Pradas, M. M., Ribelles, J. L. G., Aroca, A. S., Ferrer, G. G., Antón, J. S. and Pissis, P. (2001). Interaction between water and polymer chains in poly(hydroxyethyl acrylate) hydrogels. Colloid and Polymer Science, 279(4), 323-330.

Preez, A. A. d. and Alexander, M. G. (2004). A site study of durability indexes for concrete in marine conditions. Materials and Structures, 37(267), 146-154.

Prian, L. and Barkatt, A. (1999). Degradation mechanism of fiber-reinforced plastics and its implications to prediction of long-term behavior. Journal of Materials Science, 34(16), 3977-3989.

Prince-Lund Engineering PLC. (2018, August 10). FRP Reinforcement for Structures. https://www.build-on-prince.com/frp-reinforcement.html.

Purnell, P. and Beddows, J. (2005). Durability and simulated ageing of new matrix glass fibre reinforced concrete. Cement and Concrete Composites, 27(9-10), 875-884.

Purnell, P., Short, N. R. and Page, C. L. (2001). A static fatigue model for the durability of glass fibre reinforced cement. Journal of Materials Science, 36(22), 5385-5390.

Pyo, J.-B., Lee, T.-I., Kim, C., Kim, M. S. and Kim, T.-S. (2016). Prediction of time-dependent swelling of flexible polymer substrates using hygro-mechanical finite element simulations. Soft Matter, 12(18), 4135-4141.

Qiao, X. and Chen, J. (2019). Correlation of propagation rate of corrosive crack in concrete under sulfate attack and growth rate of delayed ettringite. Engineering Fracture Mechanics, 209, 333-343.

Qu, F., Li, W., Dong, W., Y.Tam, V. W. and Yu, T. (2021). Durability deterioration of concrete under marine environment from material to structure: A critical review. Journal of Building Engineering, 35, 102074.

Rabi, M., Cashell, K. A. and Shamass, R. (2019). Flexural analysis and design of stainless steel reinforced concrete beams. Engineering Structures, 198, 109432.

Raman, R. K. S., Guo, F., Al-Saadi, S., Zhao, X. L. and Jones, R. (2020). Understanding fibre-matrix degradation of FRP composites for advanced civil engineering applications: an overview. Corrosion and Materials Degradation, 1(1), 27-41.

Rao, P. S., Husain, M. M. and Shankar, D. V. R. (2012). An Investigation on Strength Degradation of Gfrp Laminates Under Environmental Impact. International Journal of Composite Materials, 2(4), 48-52.

Raoof, S. M., Koutas, L. N. and Bournas, D. A. (2016). Bond between textile-reinforced mortar (TRM) and concrete substrates: Experimental investigation. Composites Part B: Engineering, 98, 350-361.

Rashad, A. M., Seleem, H. E.-D. H. and Shaheen, A. F. (2014). Effect of Silica Fume and Slag on Compressive Strength and Abrasion Resistance of HVFA Concrete. International Journal of Concrete Structures and Materials, 8(1), 69-81.

Ray, B. C. and Rathore, D. (2015). Environmental damage and degradation of FRP composites: A review report. Polymer Composites, 36(3), 410-423.

Regazzi, A., Léger, R., Corn, S. and Ienny, P. (2016). Modeling of hydrothermal aging of short flax fiber reinforced composites. Composites Part A: Applied Science and Manufacturing, 90, 559-566.

Ren, F. F., Yang, Z. J., Chen, J. F. and Chen, W. W. (2010). An analytical analysis of the full-range behaviour of grouted rockbolts based on a tri-linear bond-slip model. Construction and Building Materials, 24(3), 361-370.

Richet, P., Conradt, R., Takada, A. and Dyon, J. (2021). Encyclopedia of Glass Science, Technology, History, and Culture. John Wiley & Sons.

RILEM-CEB-FIP-RC6. (1983). Recommendation RC 6: Bond test reinforcement steel. 2. Pull-out test. International Union of Laboratories and Experts in Construction Materials, Systems and Structures. Marne la Vallée, France.

Rizkalla, S., Hassan, T. and Hassan, N. (2003). Design recommendations for the use of FRP for reinforcement and strengthening of concrete structures. Progress in Structural Engineering and Materials, 5(1), 16-28.

Robert, M. and Benmokrane, B. (2013). Combined effects of saline solution and moist concrete on long-term durability of GFRP reinforcing bars. Construction and Building Materials, 38, 274-284.

Robert, M., Cousin, P. and Benmokrane, B. (2009). Durability of GFRP reinforcing bars embedded in moist concrete. Journal of Composites for Construction, 13(2), 66-73.

Robert, M., Wang, P., Cousin, P. and Benmokrane, B. (2010). Temperature as an Accelerating Factor for Long-Term Durability Testing of FRPs: Should There Be Any Limitations? Journal of Composites for Construction, 14(4), 361-367.

Rolland, A., Khadour, A., Benzarti, K., Quiertant, M., Chataigner, S. and Khadour, A. (2020). Analytical and numerical modeling of the bond behavior between FRP reinforcing bars and concrete. Construction and Building Materials, 231, 117160.

Sakin, S. and Anil, Ö. (2019). Nonlinear finite element model for interface between anchoraged carbon fiber reinforced polymer and concrete surface. Structural Concrete, 20(6), 1986-1999.

Saleh, S., Zhao, X. L. and Hamed, E. (2019). Development and mechanical behaviour of ultra-high-performance seawater sea-sand concrete. Advances in Structural Engineering, 22(14), 3100-3120.

Sang, L., Wang, C., Wang, Y. and Hou, W. (2018). Effects of hydrothermal aging on moisture absorption and property prediction of short carbon fiber reinforced polyamide 6 composites. Composites Part B: Engineering, 153, 306-314.

Sang, N. T., Quan, T. M., Dang, V. Q., Ho, L. S. and George, R. C. (2022). Applicability of concrete containing the binary and ternary system of binder materials under natural marine environment. Journal of Applied Science and Engineering, 25(5), 881-891.

Santandrea, M., Imohamed, I. A. O., Jahangir, H., Carloni, C., Mazzotti, C., Miranda, S. D., Ubertini, F. and Casadei, P. (2016). An investigation of the debonding mechanism in steel FRP-and FRCM-concrete joints. 4th Workshop on the new boundaries of structural concrete, 289-298.

Santis, S. d. and Felice, G. d. (2015). Tensile behaviour and durability of mortar-based strengthening systems with glass-aramid textiles. Key Engineering Materials, 624, 346-353.

Saranya, P., Nagarajan, P. and Shashikala, A. P. (2018). Eco-friendly GGBS concrete: a state-of-the-art review. IOP Conference Series: Materials Science and Engineering, 330(1), 012057.

Schumann, A., Michler, H., Schladitz, F. and Curbach, M. (2018). Parking slabs made of carbon reinforced concrete. Structural Concrete, 19(3), 647-655.

Schütze, E., Bielak, J., Scheerer, S., Hegger, J. and Curbach, M. (2018). Uniaxial tensile test for carbon reinforced concrete with textile reinforcement. Beton-und Stahlbetonbau, 113(1), 33-47.

Sen, R. (2015). Developments in the durability of FRP-concrete bond. Construction and Building Materials, 78, 112-125.

Sengul, O. and Tasdemir, M. A. (2009). Compressive strength and rapid chloride permeability of concretes with ground fly ash and slag. Journal of Materials in Civil Engineering, 21(9), 494-501.

Šenšelová, Ž., Borzovič, V. and Baran, J. (2021). Parametric Study of Concrete Members with GFRP Reinforcement Subjected to Bending and Axial Force. IOP Conference Series: Materials Science and Engineering, 1203(2), 022130.

Serbescu, A., Guadagnini, M. and Pilakoutas, K. (2015). Mechanical characterization of basalt FRP rebars and long-term strength predictive model. Journal of Composites for Construction, 19(2), 04014037.

Seymour, R. B., Mark, H. F., Pauling, L., Fisher, C. H., Stahl, G. A., Sperling, L. H., Marvel, C. S. and CarraherJr., C. E. (2012). Pioneers in Polymer Science. Springer Science & Business Media.

Shaafaey, M., Miao, W., Bahrololoumi, A., Nabinejad, O. and Dargazany, R. (2022). Effects of Hydrolytic Aging on Constitutive Behavior of Silicone Adhesives in Seawater and Distilled Water. Experimental Mechanics, 63, 139-162.

Shahrubudin, N., Lee, T. C. and Ramlan, R. (2019). An Overview on 3D Printing Technology: Technological, Materials, and Applications. Procedia Manufacturing, 35, 1286-1296.

Shams, A., Hegger, J. and Horstmann, M. (2014). An analytical model for sandwich panels made of textile-reinforced concrete. Construction and Building Materials, 64, 451-459.

Shawa, I. D. and Andrawes, B. (2017). Finite element analysis of CFRP laminate repairs on damaged end regions of prestressed concrete bridge girders. Advances in Computational Design, 2(2), 147-168.

Shen, B., Liu, H., Lv, S., Li, Z. and Cheng, W. (2021). Acid Aging of CFRP Composite Materials for Solar UAV Structure. International Journal of Aerospace Engineering, 2021, 1664847.

Shen, C. H. and Springer, G. S. (1976). Moisture Absorption and Desorption of Composite Materials. Journal of Composite Materials, 10(1), 2-20.

Sheng, J., Yin, S. p., Wang, F. and Yang, Y. (2017). Experimental study on the fatigue behaviour of RC beams strengthened with TRC after sustained load corrosion. Construction and Building Materials, 131, 713-720.

Shi, F., Su, H., Zhao, L., Yu, X. and Li, S. (2020). Study on the Structure and Properties of Continuous Basalt Fibres. Fibres & Textiles in Eastern Europe, Nr4(142), 52-56.

Shi, S., Liao, Y., Peng, X., Liang, C. and Sun, J. (2019). Behavior of polyurea-woven glass fiber mesh composite reinforced RC slabs under contact explosion. International Journal of Impact Engineering, 132, 103335.

Shirangi, M. H. (2010). Simulation-based Investigation of interface delamination in plastic IC packages under temperature and moisture loading. Cuvillier Verlag.

Shrestha, J., Ueda, T. and Zhang, D. (2015). Durability of FRP Concrete Bonds and Its Constituent Properties under the Influence of Moisture Conditions. Journal of Materials in Civil Engineering, 27(2), A4014009.

Shrestha, J., Zhang, D. and Ueda, T. (2016). Durability performances of carbon fiber–reinforced polymer and concrete-bonded systems under moisture conditions. Journal of Composites for Construction, 20(5), 04016023.

Shrivastava, R. (2018). A Research on FRP: Development and Use in Construction. International Journal of Research and Analytical Reviews, 5(3), 13-17.

Siddique, R. (2014). Utilization (recycling) of iron and steel industry by-product (GGBS) in concrete: strength and durability properties. Journal of Material Cycles and Waste Management, 16(3), 460-467.

Siddique, R. (2016). Compressive strength, water absorption, sorptivity, abrasion resistance and permeability of self-compacting concrete containing coal bottom ash. Construction and Building Materials, 47, 1444-1450.

Silva, M. A. G., Biscaia, H. C. and Marreiros, R. (2013). Bond–slip on CFRP/GFRP-to-concrete joints subjected to moisture, salt fog and temperature cycles. Composites Part B: Engineering, 55, 374-385.

Silva, M. A. G., Fonseca, B. S. d. and Biscaia, H. (2014). On estimates of durability of FRP based on accelerated tests. Composite Structures, 116, 377-387.

Skarendahl, Å. and Petersson, Ö. (1999). PRO 7: 1st International RILEM Symposium on Self-Compacting Concrete. RILEM publications.

So, H. S., Choi, S. H., Seo, K. S., Seo, C. S. and So, S. Y. (2014). The properties of chloride ion diffusion of concrete under high temperature conditions, with implications for the storage of spent nuclear fuel in concrete casks. Ksce Journal of Civil Engineering, 18(7), 2227-2233.

Solyom, S. and Balázs, G. L. (2020). Bond of FRP bars with different surface characteristics. Construction and Building Materials, 264, 119839.

Sonnenschein, R., Gajdosova, K. and Holly, I. (2016). FRP Composites and their Using in the Construction of Bridges. Procedia Engineering, 161, 477-482.

Spadea, S., Orr, J., Nanni, A. and Yang, Y. (2017). Wound FRP Shear Reinforcement for Concrete Structures. Journal of Composites for Construction, 21(5), 04017026.

Spelter, A., Bergmann, S., Bielak, J. and Hegger, J. (2019). Long-term durability of carbon-reinforced concrete: An overview and experimental investigations. Applied Sciences, 9(8), 1651.

Spelter, A., Bielak, J., Will, N. and Hegger, J. (2018). Long-term durability of textile reinforced concrete. Proceedings of the 2018 fib Congress, Melbourne, Australia., 7-11.

Speranza, V., Meo, A. D. and Pantani, R. (2014). Thermal and hydrolytic degradation kinetics of PLA in the molten state. Polymer Degradation and Stability, 100, 37-41.

Springer, G. S. (1984). Environmental Effects on Composite Materials. Vol. 2. Technomic Publishing Company, Inc.

Sugiman, S., Crocombe, A. D. and Aschroft, I. A. (2013). Experimental and numerical investigation of the static response of environmentally aged adhesively bonded joints. International Journal of Adhesion and Adhesives, 40, 224-237.

Sun, M. Q., Liew, R. J. Y., Zhang, M. H. and Li, W. (2014). Development of cement-based strain sensor for health monitoring of ultra high strength concrete. Construction and Building Materials, 65, 630-637.

Sun, P., Zhao, Y., Luo, Y. and Sun, L. (2011). Effect of temperature and cyclic hygrothermal aging on the interlaminar shear strength of carbon fiber/bismaleimide (BMI) composite. Materials and Design, 32(8-9), 4341-4347.

Suresh, D. and Nagaraju, K. (2015). Ground granulated blast slag (GGBS) in concrete–a review. IOSR Journal of Mechanical and Civil Engineering, 12(4), 76-82.

Swaroop, A. H. L., Venkateswararao, K. and Kodandaramarao, P. (2013). Durability Studies On Concrete With Fly Ash & Ggbs. International Journal of Engineering Research and Applications, 3(4), 285-289.

Szmigiera, E. and Woyciechowski, P. (2013). Influence of the compaction method on the bond between steel and concrete in composite columns. Periodica Polytechnica Civil Engineering, 57(2), 129–137.

Tajvidi, M., Falk, R. H. and Hermanson, J. C. (2005). Time–temperature superposition principle applied to a kenaf-fiber/high-density polyethylene composite. Journal of Applied Polymer Science, 97(5), 1995-2004.

Takiya, H., Watanabe, N., Kozaki, T. and Sato, S. (2015). Effects of water-to-cement ratio and temperature on diffusion of water in hardened cement pastes. Journal of Nuclear Science and Technology, 52(5), 728-738.

Tanks, J. D., Sharp, S. R. and Harris, D. K. (2017). Kinetics of in-plane shear degradation in carbon/epoxy rods from exposure to alkaline and saline environments. Composites Part B: Engineering, 110, 204-212.

Tant, M. R., McManus, H. L. N. and Roger, M. E. (1995). High-temperature properties and applications of polymeric materials. ACS Publications.

Tao, Y. and Zhang, Y. (2016). Application of Carbon Fiber Materials in Water Conservancy Project. 2016 International Conference on Architectural Engineering and Civil Engineering. Atlantis Press., 261-264.

Tatar, J. and Hamilton, H. R. (2016). Bond durability factor for externally bonded CFRP systems in concrete structures. Journal of Composites for Construction, 20(1), 04015027.

Tatar, J. and Hamilton, H. R. (2016). Comparison of laboratory and field environmental conditioning on FRP-concrete bond durability. Construction and Building Materials, 122, 525-536.

Tavares, L. R. C., Junior, J. F. T., Costa, L. M., Bezerra, A. C. d. S., Cetlin, P. R. and Aguilar, M. T. P. (2020). Influence of quartz powder and silica fume on the performance of Portland cement. Scientific Reports, 10(1), 1-15.

Tayeh, B. A., Aadi, A. S., Hilal, N. N., Bakar, B. H. A., Al-Tayeb, M. M. and Mansour, W. N. (2019). Properties of ultra-high-performance fiber-reinforced concrete (UHPFRC)—A review paper. AIP Conference Proceedings, 2157(1), 020040.

Techbelt. (2022, April 15). PTFE Coated Kevlar Mesh. https://www.techbelt.com/buy-online/products/ptfe-coated-kevlar-mesh-km-90-na/.

Techno, J. T. S. o. F. S. a. (2016). High-Performance and Specialty Fibers. Springer, Tokyo.

Teh, S. H., Wiedmann, T., Castel, A. and Burgh, J. d. (2017). Hybrid life cycle assessment of greenhouse gas emissions from cement, concrete and geopolymer concrete in Australia. Journal of Cleaner Production, 152, 312-320.

Teng, J.-G., Xiang, Y., Yu, T. and Fang, Z. (2019). Development and mechanical behaviour of ultra-high-performance seawater sea-sand concrete. Advances in Structural Engineering, 22(14), 3100-3120.

Teng, J. G., Yuan, H. and Chen, J. F. (2006). FRP-to-concrete interfaces between two adjacent cracks: Theoretical model for debonding failure. International Journal of Solids and Structures, 43(18-19), 5750-5778.

The University of Southern Mississippi- The Department of Polymer Science. (2022a, April 11). Polymer 3D Molecular Models. https://www.pslc.ws/modelhtms/poly3D.htm.

The University of Southern Mississippi- The Department of Polymer Science. (2022b, April 12). Glass at the Molecular Level. https://pslc.ws/macrog/glass.htm.

Tie, Y., Zhang, Q., Hou, Y. and Li, C. (2020). Impact damage assessment in orthotropic CFRP laminates using nonlinear Lamb wave: Experimental and numerical investigations. Composite Structures, 236, 111869.

Tompkins, A. M. (2001). On the relationship between tropical convection and sea surface temperature. Journal of climate, 14(5), 633-637.

Topçu, İ. B. and Uzunömeroğlu, A. (2020). Properties of corrosion inhibitors on reinforced concrete. Journal of Structural Engineering, 3(2), 93-109.

Toscano, A., Pitarresi, G., Scafidi, M., Filippo, M. D., Spadaro, G. and Alessi, S. (2016). Water diffusion and swelling stresses in highly crosslinked epoxy matrices. Polymer Degradation and Stability, 133, 255-263.

Toumpanaki, E., Lees, J. M. and Terrasi, G. P. (2015). Shear modulus of cylindrical CFRP tendons exposed to moisture. Journal of Composites for Construction, 19(3), 04014059.

Toumpanaki, E., Lees, J. M. and Terrasi, G. P. (2020). Analytical predictive model for the long-term bond performance of CFRP tendons in concrete. Composite Structures, 250, 112614.

Tran, H. V., Truong, G. T. and Choi, K.-K. (2019). Effect of Harsh Conditions on the Tensile Behaviour of Lap-Spliced Carbon Fiber Textile-Reinforced Mortar (TRM) with Different Surface Treatment Methods. Applied Sciences, 9(15), 3087.

Triantafillou, T. (2016). Textile Fibre Composites in Civil Engineering. Woodhead Publishing.

Tsai, S. W. (1988). Composites design. Think Composites. P. O. Box 581, Dayton, Ohio 45419, USA, 1988. 583.

Uthaman, A., Xian, G., Thomas, S., Wang, Y., Zheng, Q. and Liu, X. (2020). Durability of an epoxy resin and its carbon fiber-reinforced polymer composite upon immersion in water, acidic, and alkaline solutions. Polymers, 12(3), 614.

Vaysburd, A. M. and Emmons, P. H. (2004). Corrosion inhibitors and other protective systems in concrete repair: concepts or misconcepts. Cement and Concrete Composites, 26(3), 255-263.

Vazques, E. (1990). Admixtures for Concrete-Improvement of Properties: Proceedings of the International RILEM Symposium. CRC Press.

Velasco, F., Blanco, G., Bautista, A. and Martínez, M. A. (2009). Effect of welding on local mechanical properties of stainless steels for concrete structures using universal hardness tests. Construction and Building Materials, 23(5), 1883-1891.

Vinson, J. R. (1978). Advanced composite materials-environmental effects. ASTM International.

Wang, J. (2006). Debonding of FRP-plated reinforced concrete beam, a bond-slip analysis. I. Theoretical formulation. International Journal of Solids and Structures, 43(21), 6649-6664.

Wang, L., Mao, Y., Lv, H., Chen, S. and Li, W. (2018). Bond properties between FRP bars and coral concrete under seawater conditions at 30, 60, and 80 °C. Construction and Building Materials, 162, 442-449.

Wang, X. and Petrů, M. (2019). Freeze–thaw resistance of epoxy/concrete interface evaluated by a novel wedge splitting test. Construction and Building Materials, 210, 434-441.

Wang, X. and Petrů, M. (2019). Mode I fracture evaluation of CFRP-to-concrete interfaces subject to aggressive environments agents: Freeze-thaw cycles, acid and alkaline solution. Composites Part B: Engineering, 168, 581-588.

Wang, X. and Petrů, M. (2021). Experimental study on fracture properties of CFRP-to-concrete interface subject to salt water. Composite Structures, 258, 113179.

Wang, X. Q., WeiJian, Buyukozturk, O., Leung, C. K. Y. and Lau, D. (2021). Degradation of epoxy/glass interface in hygrothermal environment: An atomistic investigation. Composites Part B: Engineering, 206, 108534.

Wang, Y., Wang, Y., Wan, B., Han, B., Cai, G. and Chang, R. (2018). Strain and damage self-sensing of basalt fiber reinforced polymer laminates fabricated with carbon nanofibers/epoxy composites under tension. Composites Part A: Applied Science and Manufacturing, 113, 40-52.

Wang, Z., Gao, Z., Wang, Y., Cao, Y., Wang, G., Liu, B. and Wang, Z. (2015). A new dynamic testing method for elastic, shear modulus and Poisson's ratio of concrete. Construction and Building Materials, 100, 129-135.

Wang, Z., Xian, G. and Zhao, X. L. (2018). Effects of hydrothermal aging on carbon fibre/epoxy composites with different interfacial bonding strength. Construction and Building Materials, 161, 634-648.

Wang, Z., Zhao, X. L., Xian, G., Wu, G., Raman, R. K. S. and Al-Saadi, S. (2017a). Durability study on interlaminar shear behaviour of basalt-, glass- and carbon-fibre reinforced polymer (B/G/CFRP) bars in seawater sea sand concrete environment. Construction and Building Materials, 156, 985-1004.

Wang, Z., Zhao, X. L., Xian, G., Wu, G., Raman, R. K. S., Al-Saadi, S. and Haque, A. (2017b). Long-term durability of basalt- and glass-fibre reinforced polymer (BFRP/GFRP) bars in seawater and sea sand concrete environment. Construction and Building Materials. Construction and Building Materials, 139, 467-489.

Ward, B. (2006). Near‐surface ocean temperature. Journal of Geophysical Research: Oceans, 111, C02004.

Watson, E. B., Wanser, K. H. and Farley, K. A. (2010). Anisotropic diffusion in a finite cylinder, with geochemical applications. Geochimica et Cosmochimica Acta, 74(2), 614-633.

Webb, S. W. and Pruess, K. (2003). The use of Fick's Law for modeling trace gas diffusion in porous media. Transport in Porous Media, 51, 327-341.

Weber, R. J., Perkins, D. N. and Perkins, D. N. (1992). Inventive minds: Creativity in technology. Oxford University Press on Demand.

Wegian, F. M. (2010). Effect of seawater for mixing and curing on structural concrete. The IES Journal Part A: Civil & Structural Engineering, 3(4), 235-243.

Wei, J., Fu, X. X., Dong, J. H. and Ke, W. (2012). Corrosion evolution of reinforcing steel in concrete under dry/wet cyclic conditions contaminated with chloride. Journal of Materials Science & Technology, 28(10), 905-912.

Wei, L. L., Zhu, J. H., Ueda, T., Su, M. N., Liu, J., Liu, W., Tang, L. P. and Xing, F. (2020). Tensile behaviour of carbon fabric reinforced cementitious matrix composites as both strengthening and anode materials. Composite Structures, 234, 111675.

Weitsman, Y. J. (2011). Fluid effects in polymers and polymeric composites. Springer Science & Business Media.

Weitsman, Y. J. (2012). Effects of Fluids on Mechanical Properties and Performance. Fluid Effects in Polymers and Polymeric Composites. Springer, Boston, MA, 123-144.

Won, J. P., Lee, S. J., Kim, Y. J., Jang, C. I. and Lee, S. W. (2008a). The effect of exposure to alkaline solution and water on the strength–porosity relationship of GFRP rebar. Composites Part B: Engineering, 39(5), 764-772.

Won, J. P., Park, C. G., Kim, H. H., Lee, S. W. and Jang, C. I. (2008b). Effect of fibers on the bonds between FRP reinforcing bars and high-strength concrete. Composites Part B: Engineering, 39(5), 747-755.

Wu, B., Zhang, S., Liu, F. and Gan, T. (2016). Effects of salt solution on mechanical behaviors of aramid fiber–reinforced polymer (AFRP) sheets and AFRP-to-concrete joints. Advances in Structural Engineering, 19(2), 1855-1872.

Wu, G., Dong, Z. Q., Wang, X. and Zhu, Y. (2015). Prediction of long-term performance and durability of BFRP bars under the combined effect of sustained load and corrosive solutions. Journal of Composites for Construction, 19(3), 04014058.

Wu, K., Chen, F., Chen, C. and Zheng, H. (2019). Load-Transfer mechanism and bond-stress components in steel and steel fiber–reinforced concrete structure. Journal of Structural Engineering, 145(12), 04019160.

Wu, Y., Zhou, Z., Yang, Q. and Chen, W. (2010). On shear bond strength of FRP-concrete structures. Engineering Structures, 32(3), 897-905.

Wyrzykowski, M., Terrasi, G. and Lura, P. (2020). Chemical prestressing of high-performance concrete reinforced with CFRP tendons. Composite Structures, 239, 112031.

Xiao, J., Qiang, C., Nanni, A. and Zhang, K. (2017). Use of sea-sand and seawater in concrete construction: Current status and future opportunities. Construction and Building Materials, 155, 1101-1111.

Xie, J., Wang, J., Rao, R., Wang, C. and Fang, C. (2019). Effects of combined usage of GGBS and fly ash on workability and mechanical properties of alkali activated geopolymer concrete with recycled aggregate. Composites Part B: Engineering, 164, 179-190.

Xin, H., Liu, Y., Mosallam, A. and Zhang, Y. (2016). Moisture diffusion and hygrothermal aging of pultruded glass fiber reinforced polymer laminates in bridge application. Composites Part B: Engineering, 100, 197-207.

Xing, D., Xi, X. Y. and Ma, P. C. (2019). Factors governing the tensile strength of basalt fibre. Composites Part A: Applied Science and Manufacturing, 119, 127-133.

Yang, Y., Biscaia, H., Chastre, C. and Silva, M. A. G. (2017). Bond characteristics of CFRP-to-steel joints. Journal of Constructional Steel Research, 138, 401-419.

Yang, Y., Li, Z., Zhang, T., Wei, J. and Yu, Q. (2017). Bond-slip behavior of basalt fiber reinforced polymer bar in concrete subjected to simulated marine environment: effects of BFRP bar size, corrosion age, and concrete strength. International Journal of Polymer Science, 2017, 5156189.

Younis, A., Ebead, U., Suraneni, P. and Nanni, A. (2020). Short-term flexural performance of seawater-mixed recycled-aggregate GFRP-reinforced concrete beams. Composite Structures, 236, 111860.

Yu, H. (2020). Key Technologies for Anticorrosion and Reinforcement of Coastal Building Structures in Alkaline Environment. Journal of Coastal Research, 110(SI), 239-242.

Yu, Q. Q. and Wu, Y. F. (2018). Fatigue retrofitting of cracked steel beams with CFRP laminates. Composite Structures, 192, 232-244.

Zaeri, A. R. and Googarchin, H. S. (2019). Analysis of automotive mixed-adhesive joints weakened by moist conditions: Experimental characterization and numerical simulation using cohesive zone model. Fatigue & Fracture of Engineering Materials & Structures, 42(4), 929-942.

Zaidi, A., Brahim, M. M., Mouattah, K. and Masmoudi, R. (2017). FRP Properties Effect on Numerical Deformations in FRP Bars-Reinforced Concrete Elements in Hot Zone. Energy Procedia, 139, 798-803.

Zehtab, B. and Tarighat, A. (2018). Molecular dynamics simulation to assess the effect of temperature on diffusion coefficients of different ions and water molecules in C-S-H. Mechanics of Time-Dependent Materials, 22(4), 483-497.

Zeng, J. J., Liao, J., Zhuge, Y., Guo, Y. C., Zhou, J. K., Huang, Z. H. and Zhang, L. (2022). Bond behavior between GFRP bars and seawater sea-sand fiber-reinforced ultra-high strength concrete. Engineering Structures, 254, 113787.

Zhang, B., Tan, H., Shen, W., Xu, G., Ma, B. and Ji, X. (2018). Nano-silica and silica fume modified cement mortar used as Surface Protection Material to enhance the impermeability. Cement and Concrete Composites, 92, 7-17.

Zhang, B., Zhu, H., Cao, R., Ding, J. and Chen, X. (2021). Feasibility of using geopolymers to investigate the bond behavior of FRP bars in seawater sea-sand concrete. Construction and Building Materials, 282, 122636.

Zhang, J., Qi, D., Zhou, L., Zhao, L. and Hu, N. (2015). A progressive failure analysis model for composite structures in hygrothermal environments. Composite Structures, 133, 331-342.

Zhang, L., Han, J. g., Guo, Y. h. and Sun, L. (2015). Creep behavior of SnAgCu solders containing nano-Al particles. Journal of Materials Science: Materials in Electronics, 26(6), 3615-3620.

Zhang, P., Li, D., Qiao, Y. and Zhang, S. (2018). Effect of air entrainment on the mechanical properties, chloride migration, and microstructure of ordinary concrete and fly ash concrete. Journal of Materials in Civil Engineering, 30(10), 04018265.

Zhang, Y., Sun, W. and Liu, S. (2002). Study on the hydration heat of binder paste in high-performance concrete. Cement and Concrete Research, 32(9), 1483-1488.

Zhang, Y., Yu, C., Chu, P. K., Lv, F., Zhang, C., Ji, J., Zhang, R. and Wang, H. (2012). Mechanical and thermal properties of basalt fiber reinforced poly(butylene succinate) composites. Materials Chemistry and Physics, 133(2-3), 845-849.

Zheng, D., Monasterio, M., Feng, W., Tang, W., Cui, H. and Dong, Z. (2021). Hydration Characteristics of Tricalcium Aluminate in the Presence of Nano-Silica. Nanomaterials, 11(1), 199.

Zhong, Y., Cheng, M., Zhang, X., Hu, H., Cao, D. and Li, S. (2019). Hygrothermal durability of glass and carbon fiber reinforced composites - A comparative study. Composite Structures, 211, 134-143.

Zhou, F., Liu, H., Du, Y., Liu, L., Zhu, D. and Pan, W. (2019). Uniaxial Tensile Behavior of Carbon Textile Reinforced Mortar. Materials, 12(3), 374.

Zhou, L., Guo, S., Ma, W., Xu, F., Shi, C., Yi, Y. and Zhu, D. (2022). Internal curing effect of saturated coral coarse aggregate in high-strength seawater sea sand concrete. Construction and Building Materials, 331, 127280.

Zhou, Y., Sun, Z., Jiang, L., Chen, S., Ma, J. and Zhou, F. (2020). Flexible and conductive meta-aramid fiber paper with high thermal and chemical stability for electromagnetic interference shielding. Applied Surface Science, 533, 147431.

Zhu, M., Zhu, J. H., Ueda, T., Su, M. and Xing, F. (2020). A method for evaluating the bond behavior and anchorage length of embedded carbon yarn in the cementitious matrix. Construction and Building Materials, 255, 119067.

Živanovic, S., Russell, J., Pavlović, M., Wei, X. and Mottram, J. T. (2019). Effects of Pedestrian Excitation on Two Short-Span FRP Footbridges in Delft. Dynamics of Civil Structures, 2, 143-150.